Investigating Nonlinear Enzyme Kinetics as an Internal Control System for Nanoreactor Drug Release

Stephen Joseph Jones

Submitted in accordance with the requirements for the degree of

Doctor of Philosophy

The University of Leeds
School of Chemistry

Supervisor: Dr Paul Beales

July 2018

The candidate confirms that the work submitted is his/her own and that appropriate credit has been given where reference has been made to the work of others.

This copy has been supplied on the understanding that it is copyright material and that no quotation from the thesis may be published without proper acknowledgement.

The right of Stephen Joseph Jones to be identified as Author of this work has been asserted by him in accordance with the Copyright, Designs and Patents Act 1988.

Acknowledgements

First and foremost, I want to thank my supervisor, Dr Paul Beales – it has been an honour to be his PhD student. In my time here, he has taught me, both consciously and unconsciously, how good experimental research is conducted. I appreciate all his contributions of time, ideas, and funding to make my PhD experience productive and stimulating. The joy and enthusiasm he has for his research was not only motivational, but it was contagious, and I cannot thank him enough.

Secondly, I am extremely grateful to my co-supervisor-come-collaborator, Dr Annette Taylor, for her support, guidance, and intellectual contribution at all stages throughout my PhD experience. Without her expertise and insight, specifically around urea-urease reaction and the associated kinetic modelling, none of this would have been possible.

I would also like to take the time to thank Dave Fogarty for the continued support and friendship over the last 3.5 years. His day-to-day support, technical expertise, and willingness to help others can often go unnoticed, but he is the true unsung hero of the Physical Chemistry department.

Likewise, the members of the Beales group have contributed immensely to my personal and professional time at the University of Leeds. The group, as well as those outside who shared Lab 3.14, have been a source of friendship as well as good advice and collaboration. I am especially grateful to Sanobar Khan, Rashmi Seneviratne, Eleanor (Ellie) McKeating, and Andrew Booth, as well as other past group members that have come and gone, but I have had the pleasure of working with/alongside.

Finally, I would like to thank my family for all their love and encouragement, especially my dad, Steve, who has been the primary source of motivation for all that I have achieved, and my grandparents, Norma and Phil, for their continued encouragement. Most of all, I would like to thank my loving, supportive, and incredibly beautiful fiancée Beth whose faithful support and endurance has not gone unnoticed.

I would also like to take the time to mention my French Bulldog, Chief - I believe if he could read/talk, he would want to be included.

Thank you.

Abstract

The improper administration of therapeutic compounds is not only financially inefficient, but, there exists a very real risk of harmful, or potentially life-threatening effects. To gain control, nano-drug delivery systems provide a discernible option for temporal and spatial regulation of drug bioavailability within the body. In current regimes, temporal control is realised through gradual release over an extended period of time, or triggered release in response to a change in the physiochemical environment. Of course, when considering the design of an ideal drug delivery system, we think of adaptivity – adaptivity to dynamically modulate drug release in response to a changing biological macroenvironment. In nature, this ability to sense, communicate, and respond is fundamental to the existence of any living organism, irrespective of complexity. In most instances, this responsiveness is achieved through feedback-controlled biochemical processes that work to regulate a functional process, and so, any "smart" delivery system would be smart to do the same. Of course, where conventional chemical feedback is concerned, potential toxicity and lack of biocompatibility, caused by inappropriate catalysts, is problematic, however, the emergence and enhanced understanding of enzymatic feedback provides an interesting and more compatible alternative. As such, this doctoral thesis focuses on drawing together two distinct entities of intense scientific focus, nonlinear enzyme kinetics and nanoreactor technology, and works towards the idealism of a feedback-controlled secondary response.

To achieve this, through the utilisation of bottom-up synthetic chemistry, we have successfully built, investigated, and optimised a platform that has allowed up to systematically and extensively investigate the effect of confinement on an enzymatic feedback reaction. Through this process, we have uncovered a system more complicated than first anticipated. This complexity, driven firstly by the fragility of constituents in relatively harsh conditions, but more importantly by the dynamism of the system in terms of membrane transport, and associated pH-linked permeability coefficients. However, by building this platform, we have not only learned how to control the kinetic output of the reaction, but have gained an overview of how the system behaves as a whole. It is this organic discovery, and ultimate understanding, that has allowed us to extend our reach, pushing the functionality of our novel system, to achieve both temporally-controlled drug delivery and nano-motor-based vesicular propulsion.

Table of Contents

List of Figures

CHAPTER FOUR

List of Tables

List of Equations

CHAPTER SIX

CHAPTER SEVEN

CHAPTER NINE

List of Abbreviations

Minimal Effective Concentration (MEC)

Minimal Toxic Concentration (MTC)

Non-Steroidal Anti-Inflammatory Drug (NSAID)

Gonadotropin Releasing Hormone (Gnrh)

Luteinizing Hormone (LH)

Follicle Stimulating Hormone (FSH)

Glyceryl Trinitrate (GTN)

Belousov-Zhabotinskii (BZ)

Methylene Glycol-Sulphite-Gluconolactone (MGSG)

poly(styrene)-poly(acrylic acid) (PS-*b*-PAA)

poly(ethylene glycol) (PEG)

Reticulo-Endothelial System (RES)

Critical Micelle Concentration (CMC)

Giant Unilamellar Vesicles (Guvs)

Food and Drug Administration (FDA)

European Medicines Agency (EMA)

poly(oxyethylene)–poly(oxypropylene)–poly(oxyethylene) (PEO-PPO-PEO)

poly(ethylene oxide)-poly(butadiene) (PEO-*b*-PBD)

poly(ethylene oxide)-poly(ethyl ethylene) (PEO-*b*-PEE)

Superoxide Dismutase (SOD)

Nitric-Oxide (NO)

Nitric Oxide Synthase (NOS)

Mitochondrial Neurogastrointestinal Encephalomyopathy (MNGIE)

Directed Enzyme Prodrug Therapy (DEPT)

Gene-Directed Enzyme Prodrug Therapy (GDEPT)

Green Fluorescent Protein (GFP)

Nicotinamide Cofactor (NADH)

1,2-diphytanoyl-*sn*-glycero-3-phosphocholine (DPhPC)

1,2-dioleoyl-*sn*-glycero-3-phosphoethanolamine-N-(lissamine rhodamine B sulfonyl) (Rhod-DOPE)

8-Hydroxypyrene-1,3,6-trisulfonic acid trisodium salt (HPTS)

4-(2-hydroxyethyl)-1-piperazineethanesulfonic acid (HEPES)

1-palmitoyl-2-oleoyl-*sn*-glycero-3-phosphocholine (POPC)

1,2-dipalmitoyl-*sn*-glycero-3-phosphocholine (DPPC)

Gastroesophageal Reflux Disease (GERD)

Molecular Weight Cut-Off (MWCO)

Adenosine Triphosphate (ATP)

Adenosine Diphosphate (ADP)

Adenosine Monophosphate (AMP)

Hollow Mesoporous Silica Nanoparticles (HMSNPs)

CHAPTER ONE – INTRODUCTION

1.1 Introduction

Pharmacotherapy, described as "the treatment and prevention of illness and disease by means of drugs of chemical or biological origin", is ranked amongst surgery, radiation, psychotherapy, and physiotherapy as one of the most important contributing derivatives of medical treatment [1]. Whilst there are many successful examples of the use of pharmaceuticals and vaccinations to treat, prevent, and in the case of smallpox, completely eradicate illness and disease, the extent to which pharmacotherapy has impacted human health cannot be estimated. There is, however, zero doubt that a combination of improved sanitation, better lifestyles, i.e., diet and housing, and the contribution of pharmacotherapy has improved health, life expectancy, and quality of life.

Rapid advancements in the field of genomics and molecular biology has presented an extensive diversity of new therapeutic targets [2]. Modern pharmacochemical techniques such as combinatorial chemistry and high throughput screening has provided us with a method of producing vast libraries of new drug candidates, and testing their biological or biochemical activity, in very little time. Similarly, a more advanced understanding of the immune system, in conjunction with accelerated developments in microbiology, cell biology, and molecular biology, has allowed for the development of modern vaccines against existing and novel challenges [3].

However, it is important to understand that the discovery of an "active component", be it a more classical small-molecule drug, or a more modern biopharmaceutical compound, e.g., a therapeutic protein, is the beginning of drug development, where considerations of dosage form and appropriate drug delivery is present. As a result, the development of such new and exciting pharmaceutical candidates is both expensive and time-consuming, therefore, efforts can be made to improve the safety and efficacy of existing compounds [4].

Alongside the more obvious methods of achieving this, i.e., therapeutic monitoring, personalised medicine, and dose titration, onus has been placed on the need for advanced drug delivery systems. Of course, the "ideal" drug delivery system is autonomous, capable of releasing its active payload into the body at a specified time, for the optimum duration, and at the correct location, optimising efficacy, and minimising the risk of adverse effects

1.2 Conventional Drug Delivery Systems

There are many ways to categorise drug delivery systems. For example, when thinking about drug delivery in terms of dosage form, a simple and more classical way of differentiating them

is in accordance to their physical state, i.e., solids (e.g., tablets, capsules, powders, etc.), semisolids (e.g., creams, gels, etc.), liquids (e.g., solutions, suspensions, etc.), and, finally, gasses (e.g., anaesthetics). A second outlook, again classical in nature, is to differentiate delivery systems in accordance to route of administration, i.e., through a mucosal membrane (oral, suppositories, nasal sprays, inhalers, etc.), parenteral (e.g., infusion or injection), topical (e.g., ointments, creams, etc.), or transdermal (patches) [1]. A more modern differentiation of drug delivery can be appreciated in terms of the achieved release profile.

It is obvious to say that a relationship exists between the nature of the drug delivery system employed, and the pharmacological effect it can elicit - this can be explained in terms of the pharmacokinetic profile of the compound, the rate in which it is released, the duration in which the drug is active for, the site in which the drug is active at, and, consequently, the associated toxicology profile. In most circumstances, the active compound should hold a concentration within the therapeutic range, i.e., between the minimal effective concentration (MEC) and the minimal toxic concentration (MTC) (Figure 1.1), at the appropriate site of action.
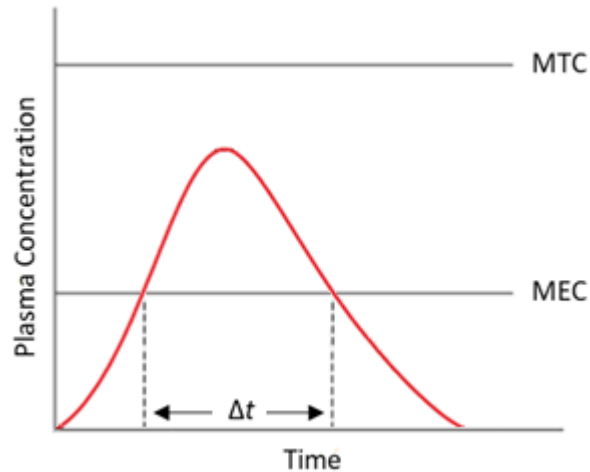
Figure 1.1. Drug plasma concentration over time for oral immediate release therapeutics. Time within (Δt) therapeutic range (MEC ↔ MTC) shown.

1.2.1 Immediate Release

Like many of the most common drugs commercially available to us, a fast onset of therapeutic effect is required. For example, if we take a standard analgesic, such as paracetamol, or a non-

steroidal anti-inflammatory drug (NSAID), such as ibuprofen, we can quickly understand why quick disintegration and rapid uptake are desirable characteristics. In light of this, immediate release forms of drug delivery typically administer the dosage in a single burst, and thus, follows a first-order kinetic profile. What this means is that release/dissolution of a drug compound to its dosage form happens very quickly, resulting in very rapid transport across a mucosal membrane, where drug concentration in the blood plasma can reach its maximum (C_{max}) in the shortest time possible (t_{max}). Once the compound has been absorbed into the body, the process of elimination occurs. Elimination, i.e., the natural process of metabolism and excretion, again displays a first-order kinetics profile [5]. From a pharmacokinetic standpoint, the measurement of drug plasma concentration over time, following initial administration of an immediate release drug, is the sum of first-order absorption and first order elimination (Figure 1.2).
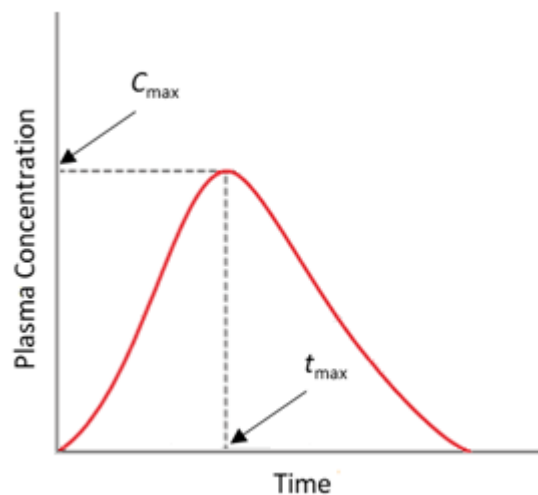
Figure 1.2. Plasma concentration-time curve for oral immediate release. Time taken (t_{max}) to reach maximum concentration (C_{max}) indicated.

The associated downfall of immediate-release dosage is the drugs ability to maintain its blood plasma concentrations within the therapeutic range. If the drug in question has a short biological half-life, i.e., the time taken for drug elimination to hit 50% of C_{max} is quick, then the drug will be limited by its ability to maintain its concentration above the MEC. Although the obvious answer is to increase dosing frequency, in instances where disease onset is not accompanied by debilitating symptoms, i.e., hypertension, a lack of compliance exists, so this may not always be the best answer. Similarly, it may not always be possible to simply increase the dosage of such

therapeutics, due to concern about adverse effects, i.e., blood plasma concentration exceeds MTC. Owing to the importance of maintaining blood plasma concentration levels within the therapeutic range, whilst maintaining patient compliance, a number of alternative drug release systems, largely focused on achieving a degree of temporal control, have been investigated.

1.2.2 Gaining Temporal Control

In its simplest form, temporal control can be obtained in terms of delayed or extended release. In instances of delayed release, the active component of a therapeutic compound is described as being "released at any other time other than immediately after administration" [1]. When discussed in terms of oral therapeutics, delayed release can not only be used to control the ultimate location of drug release, i.e., the small intestine, but to protect degradation or ionisation on its passage through the gastrointestinal system, i.e., the low pH of the stomach. One well-documented way of achieving this is to coat a therapeutic compound in a pH responsive polymer [6]. In this instance, the polymer will be capable of resisting the effects of the stomach's low-pH, but will then dissolve in the higher-pH environment of the small intestine, leading to a pharmacokinetic profile similar to that of immediate release, but shifted along the x-axis (Figure 1.3).
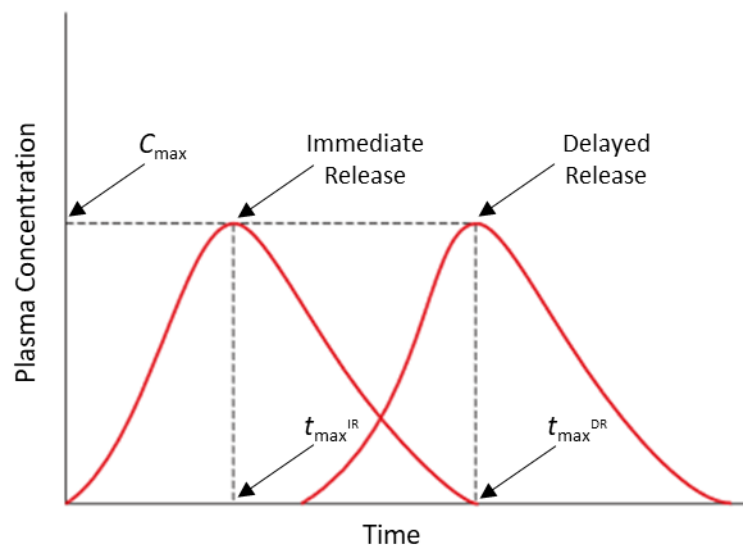
Figure 1.3. Plasma concentration-time curve for oral, immediate and delayed drug release. Time taken to reach C_{max} for immediate (t_{max}^{IR}) and delayed (t_{max}^{DR}) are indicated.

Temporal control can also be obtained by extending the release profile of a drug, thereby reducing the frequency in which medication is administered. This type of control can be achieved in two ways. Firstly, by sustaining the release profile over a longer period of time, which, in a pharmacokinetic sense, is to increase the length of your Δ*t* value (Figure 1.4). Again, this effect is most commonly achieved through a polymer coat [6].
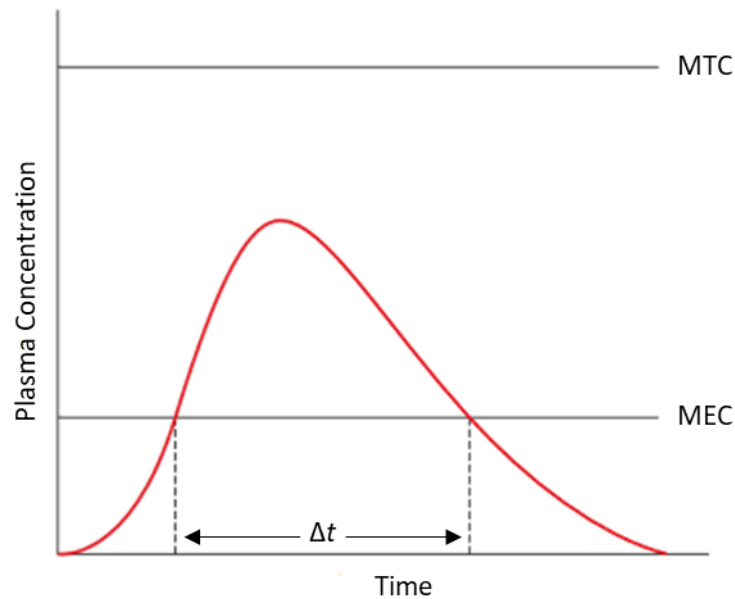
Figure 1.4. Plasma concentration-time curve for oral, sustained drug release, showing extended Δt in comparison to immediate-release profile.

Secondly, controlled release is the preferred approach with regards to temporal control, because it allows for the sustainment of drug plasma levels within the therapeutic range, irrespective of the biological microenvironment at the site of administration [7]. The fundamental difference between controlled- and sustained-release is that controlled release controls the total drug concentration within the body [1], whereas sustained release extends the time period in which a drug quantity is released over. Adding to its increased complexity, controlled release of therapeutics is often mediated by "therapeutic systems", where a therapeutic compound is released in a predetermined fashion over an allocated period of time. The pharmacokinetic release profile of controlled release typically has some zero-order characteristics, for example, layer-by-layer films [8, 9] (Figure 1.5).
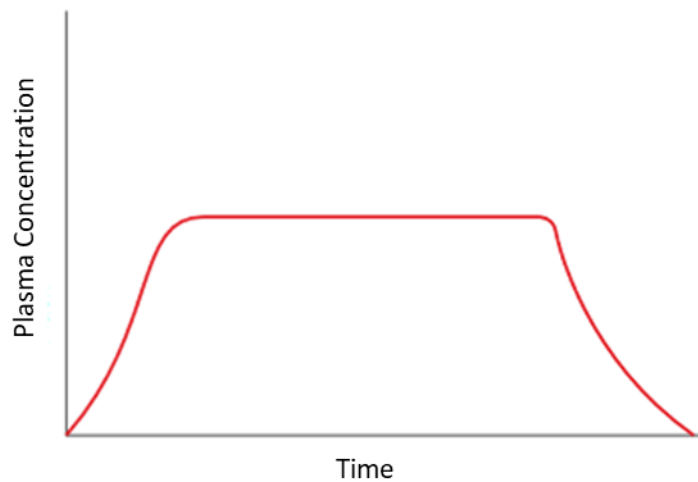
Figure 1.5. Example of plasma concentration-time curve for controlled drug release, showing zero-order release kinetics.

However, irrespective of the advancement we have seen so far, from immediate release to controlled release, important exceptions exist where stronger harmony with biological rhythms and processes would be advantageous.

1.3 Significance of Chronobiology

As we know, the hormone responsible for regulating homeostasis in blood glucose is called insulin. If functioning properly, insulin is secreted from the pancreas in preparation/response to the rise in glucose associated with having a meal. It then functions to transport glucose to the appropriate tissues and organs for utilisation, before a basal level is restored once blood glucose levels fall (Figure 1.6). Type I diabetes is an autoimmune disease, where insulin-producing pancreatic β-cells are destroyed [10]. In this instance, blood glucose is controlled in an exogenous manner, without the above-mentioned "closed-loop". Owing to the responsive nature of insulin release, extensive effort has been focused on the development of a blood delivery system that mimics the biological process of the pancreas [11]. In this instance, where rapid switching of insulin release is necessary, the benefits associated with zero-order release, e.g., improved patient compliance, reduction in the frequency of drug administration, etc., are redundant.
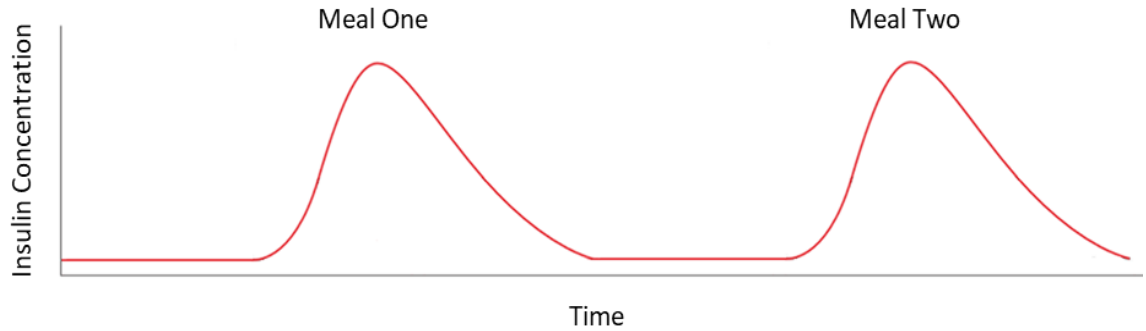
Figure 1.6. Example of a "closed loop" response to a physiological variable, i.e., insulin release in response to increased bloody glucose levels.

There is also huge evidence to suggest that biological processes are not constant, but, instead, conform to a predictable rhythm, measured in time by the frequency of their oscillations, and controlled by endogenous biological clocks [12, 13]. The time taken to complete these cycles can vary dramatically, from the sub-second pulsatile secretions of the neuroendocrine system, to the circadian production of melatonin in sleep-wake cycles, and beyond to longer circamensual cycles associated with ovulation (Table 1.1). The documentation and understanding of such biological rhythms has led to a growing importance being placed on correct drug dosing, and the treatment of certain metabolic conditions, with respect to time.

Table 1.1. Range of biological rhythms and their associated times [12].

Time Category	Rhythm	Example
Short **(t < 30 min)**	Pulsatile (0.1 s < t < 1 s) Pulsatile (t ~ 1 min)	Neural, Cardiac Calcium, Biochemical
Intermediate **(30 min < t < 6 days)**	Ultradian (30 min < t < 20 hours) Circadian (20 hours < t < 28 hours)	Mitotic, Hormonal Sleep-wake, Temperature
Long **(t > 6 days)**	Circaseptan (t ~ 7 days) Infradian (t ~ 30 days) Circannual (t ~ 1 year)	Chronoimmunology Ovarian Seasonal

1.4 Advanced Temporal Control

The need for advanced chronotherapeutics is not only necessitated by the strong association between certain diseases, i.e., asthma, angina, and cancer, and biological rhythms, but, a greater therapeutic efficacy is also achieved when therapeutic compounds aim to mimic the pulsatile release of endogenous peptides, e.g., insulin, gonadotropin releasing hormone (GnRH), somatostatin, etc. [14]. It is interesting to see insulin listed, since common understanding of insulin release is known to be responsive, however, in actuality, discrete pulses of insulin are secreted from a healthy pancreas at an estimated rate of 11–13 minutes [15]. Evidence suggests that administering insulin in an oscillatory pattern, not only reduces the amount of insulin used (in comparison to a continuous release system), but, can also help to alleviate the increased levels of mitosis associated with increased insulin [15] – factors that may be considered in the design of future insulin-delivery systems.

Of the other examples listed, GnRH is another hormone with great clinical significance. GnRH is produced and secreted by the hypothalamus, in a pulsatile fashion. It functions to stimulate the release of other hormones, luteinizing hormone (LH) and follicle stimulating hormone (FSH), from the anterior pituitary gland, which in turn, circulate throughout the body, stimulating the release of reproductive hormones within the gonads [16]. Although both men and women produce LH and FSH, in women, biological feedback of these hormones controls the rate of GnRH, which, in turn, mediates fertility to a monthly cycle [17], whereas in men, the release of GnRH is in low and frequent. In cases of GnRH deficiency, common therapeutic procedure involves the intravenous administration of GnRH in a pulsatile fashion. However, although successful, in chronic cases of GnRH deficiency, the associated downfalls of continuous intravenous administration, i.e., infection and inconvenience, necessitates the long-term need for fully implantable, autonomous alternatives.

Another example of therapeutics that would benefit from pulsatile delivery are agents which show a of tolerance and/or reduced activity, following continuous exposure. This concept is possibly best understood when thinking about exposure to nicotine, and the addiction associated with long-term smoking, however, there are entirely medicinal compounds that exhibit truncated activity following sustained exposure. One clinically available example, is the use of glyceryl trinitrate (GTN) patches. GTN is a vasodilator, which mediates its effects through the nitric oxide pathway, and as such, was developed in a patch for the prevention of angina [18]. However, original GTN patches, which provided a continuous 24-hour dose, were proven to be unsuccessful, following a failure to appreciate associated tolerance [19, 20]. In light of this, the current administration protocol exists of a 12-hour dose [21], followed by a drug-free period

to re-establish GTN sensitivity, before re-patching, however, it is not difficult to appreciate how a rhythmic drug delivery mechanism would enhance both therapeutic-compliance and -outcome. Either way, the oscillations between the drug and drug-free state should conform to the underlying kinetic mechanisms associated with drug tolerance onset, i.e., receptor down-regulation, and subsequent recovery [22, 23].

A final contribution, to complete this quick review on the relationship between intermittent hormone release, and associated treatment strategies, is a mention of the well-known circadian rhythm. This 24-hour oscillation, experienced by many lifeforms, is shown to adapt the organism, changing its behaviour depending on the time. One obvious example is a comparison between diurnal and nocturnal animals, who elicit similar hormonal regulation, during opposite periods, i.e., day vs night, respectively [12]. It has been well-documented that pharmacokinetic and pharmacodynamic factors associated with drug dosing and therapeutic outcome show variation depending on the time of day [12, 14, 24]. It is with this growing appreciation, that drug delivery, especially in the treatment of asthma, cardiovascular problems, and cancer, must evolve to take more heavily into account biological rhythms.

As such, efforts to mimic these natural rhythms in the dominion of drug delivery has led to both "active techniques", whereby an input of external energy, e.g., electrical [25], magnetism [26], ultrasound [27], pressure [28], etc., is used to trigger drug release at the desired time of administration, and, "passive techniques", where drug release is temporally controlled without the need of an external stimuli, i.e., programmed disruption, layering, or through the utilisation of non-linear feedback (oscillations) within the drug delivery system [29].

1.4.1   Chemical Feedback

Feedback is described as "the process by which a system is regulated by its output" [30], and is highly prevalent in biological systems, where a transition in chemical state is needed in response to an external stimuli, i.e., morphogenesis, long-term potentiation (memory formation), signal amplification, etc., [31]. In fact, it was Alan Turing in his seminal paper "the Chemical Basis of Morphogenesis", who put forward the idea of a two-species reaction-diffusion model, where an activator and an inhibitor coalesce to form a single negative feedback loop, and summarised that Turing instability, formed through the spatial heterogeneity of two morphogens with non-equal diffusion coefficients, is an essential part of Turing pattern formation [32]. However, it is the idea that positive and negative feedback can effectuate coaction between complex chemical

reactions and physical processes, to generate a specific function within a chemical system, that has brought the area so much attention in recent years [33].

It is widely understood that chemical oscillators can be generated by combining positive and negative feedback. Positive feedback, or autocatalysis, means that the reaction is catalysed by its products. For example, in an autocatalytic reaction where substrates are converted to products (S → P), the rate law may be defined as $v = k$[S][P], where v is the rate of reaction and k is the rate constant, thus showing that the reaction rate increases as the products are formed. Negative feedback works to remove the autocatalyst, however, for oscillation to arise as a result of kinetic instability, negative feedback must be delayed relative to positive feedback [34].

Chemical oscillators have been well-studied for a very long time, with the most well-characterised being the Belousov-Zhabotinskii (BZ) reaction, where, in the presence a metal-ion catalyst, an acidified bromate solution oxidises an organic substrate (typically malonic acid), in a series of reactions [35, 36]. In recent times, following advancements in soft material science, the BZ reaction has been utilised in the creation of chemoresponsive polymer gels, where autonomous and periodic redox oscillations are the causation of rhythmic volume changes (when immersed in a substrate-rich, acidic solution) [37]. An example of autocatalytic production of a base, is the Methylene Glycol-Sulphite-Gluconolactone (MGSG) reaction, which can be coupled with an acid-consuming step (negative feedback via the ferrocyanide reaction) in a flow reactor, to produce a pH oscillator. However, although a number of pH oscillators are available, and are proposed as tools in drug delivery systems [38], they may not necessarily be suitable, either because of issues surrounding toxicity, or their short oscillatory periods.

One example of a pH oscillator, looked at in more detail because of its relatively mild toxicity and relatively long oscillatory period, is the bromate-sulphite-marble reaction. In this model system, the pH oscillator medium, which contains benzoic acid (pK_a = 4.2), was placed next to a lipophilic ethylene vinyl acetate copolymer membrane. The premise of the experiment was to change the ionisation state of benzoic acid, through oscillations in pH (pH 2-7), and ultimately facilitate the intermittent diffusion of benzoic acid (uncharged) across the lipophilic membrane. However, it was found that inclusion of the "drug" (benzoic acid), even in low concentrations, alters/compromises the behaviour of the pH oscillator, and if drug concentration is increased, oscillations are attenuated, and a steady state pH around the pK_a of the drug is achieved – this is likely attributed to drug-related buffering of the system [39]. This phenomenon has also been witnessed for a Landolt pH oscillator in the presence of benzoic acid [40]. The overriding summary of these results is that the use of inorganic redox reactions as pH oscillators, as well as

being potentially toxic, are limited in their use in potential rhythmic drug delivery systems. So, although we are aware of the great potential held by chemical oscillators in the field of drug delivery, the need for less toxic and biocompatible autocatalysis remains prevalent.

Enzyme-catalysed reactions provide the most discernible option, however, only a low number of robust and reproducible enzyme-catalysed reactions are shown to exhibit feedback instability in vitro [41-43]. One example, studied extensively because of its prevalence throughout nature, is the urea-urease reaction.

1.5   Urea-Urease Reaction

Urease is an metalloenzyme, discovered in a variety of different sources, including bacteria, fungi, and plants, and is responsible for the catalysed hydrolysis of urea to ammonia and carbon dioxide (base-catalysed feedback):

$$CO(NH_2)_2 + H_2O \rightarrow 2NH_3 + CO_2$$
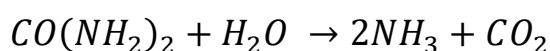
Equation 1.1.. Hydrolysis of urea to ammonia and carbon dioxide.

1.5.1   Mechanism of Action

The structure of urease is dependent on the source from which it is extracted from, however, in terms of the active site, some consistent observations remain; two nickel (Ni_1 and Ni_2) atoms, one carbamylated lysine, four histidines, and one aspartate residue. In addition, a hydroxide ion bridges the two Ni atoms, which along with other three terminal water molecules (W1, W2, W3), forms an H-bonded water tetrahedral cluster in the active site (Figure 1.7) [44, 45]. However, although the components of the urease active site have been successfully elucidated, the mechanism by which catalysis occurs has been of popular debate. At present, strong evidence provided by studies with urease inhibitors [46-48], has led to a harmonisation of opinion. It is proposed that, by replacing water held within the active site (Figure 1.7A), urea binds to the first nickel atom (Ni_1) through the carbonyl oxygen, increasing the electrophilicity of the urea carbon, and increasing its susceptibility to nucleophilic attack (Figure 1.7B). Urea then binds to the second nickel atom (Ni_2), via one of its amino nitrogen atoms, forming a bidentate bond with urease (Figure 1.7C), and ultimately facilitating the water nucleophilic attack on the carbonyl

carbon. Finally, a tetrahedral intermediate is formed (Figure 1.7D), from which NH_3 and carbamate are released (Figure 1.7E) [49].
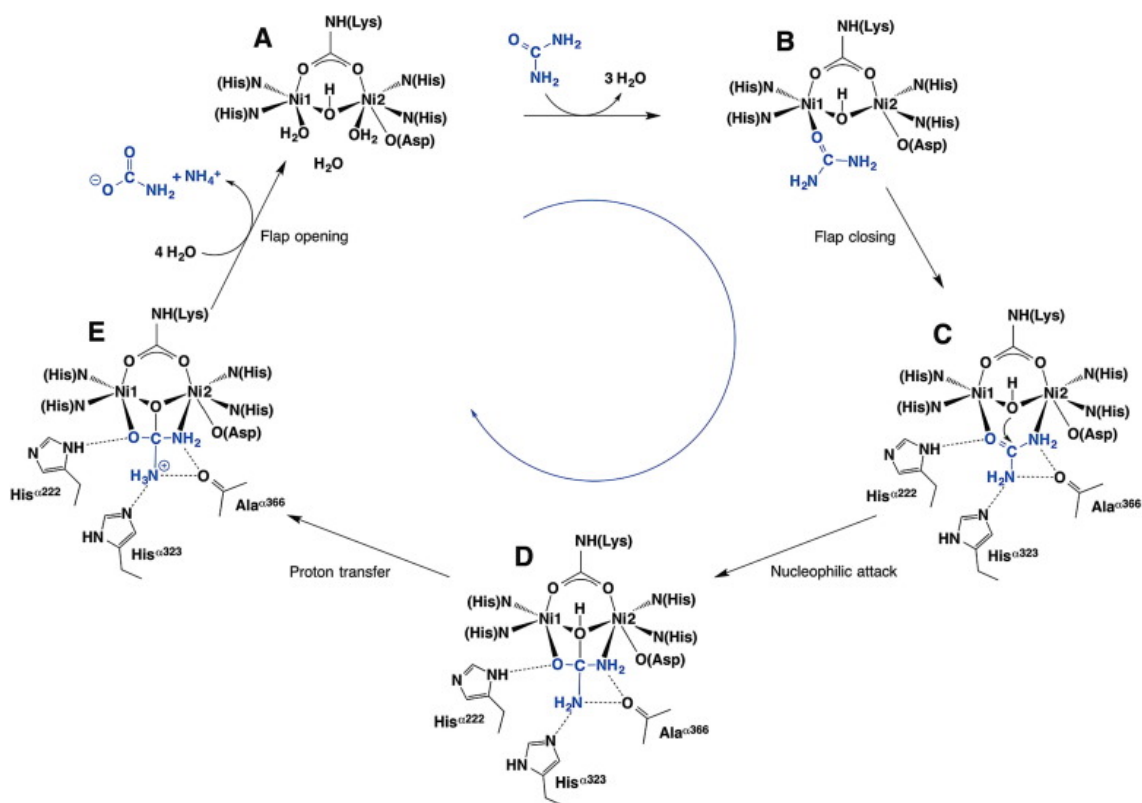
Figure 1.7. Catalytic mechanism of urea hydrolysis by urease, showing structure of nickel-containing urease active site, and associated stepwise reaction scheme, from [49]

1.5.2 Activity

The urea-urease reaction is of the Michaelis-Menten type [44, 50]:

$$EH + U \rightleftharpoons EHU$$

$$EHU \rightleftharpoons P + EH$$
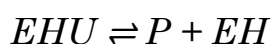
Equation 1.2.. Mechanism/equilibria of enzyme-catalysis for urea-urease reaction.

Where EH is the active protonated form of the enzyme, U is the substrate, urea, EHU is the enzyme-substrate complex and P is $2NH_3$ and CO_2. Applying the steady state approximation to EHU and setting $E_0 = E + EHU$ where E_0 = the total enzyme concentration yields the Michaelis-Menten expression for the rate, where V_{max} represents the maximum rate, and K_M is the Michaelis constant:

$$V = \frac{V_{max}U}{K_M + U}$$

Equation 1.3. Michaelis Menten expression for the rate of enzyme kinetics as applicable to the urea-urease reaction.

Owing to the proficiency of urease activity, and the high stability of urea itself, the reaction rate of urea hydrolysis is shown to be 10^{14} faster in the presence of the enzyme (in comparison to the non-catalysed system) [51]. As such, urease activity and pH are linked. For most ureases, the Michaelis constant (K_M), i.e., the concentration of the substrate when the reaction velocity is equal to one half of the maximal velocity (v_{max}) for the reaction, falls in the range of 1–4 mM [52-56], and has been found to be only slightly dependent on pH [52-56]. In contrast, the v_{max} itself, and by extension the turnover number (k_{cat}), i.e., the number of substrate molecules converted into product per enzyme in a unit time when fully saturated, is known to be strongly dependent on pH. This rate can be expressed as (See Appendix I) [57]:

$$v = \frac{v_{max}U}{\left(K_M + U(1 + \frac{U}{K_S})\right)\left(1 + \frac{[NH_4^+]}{K_P}\right)\left(1 + \frac{K_{es2}}{[H^+]} + \frac{[H^+]}{K_{es1}}\right)}$$

Equation 1.4. Rate of enzyme catalysed hydrolysis of urea by urease.

Where, the v_{max} is the maximum rate, K_M is the Michaelis constant, and K_{es2} and K_{es1} are protonation equilibria of the substrate-enzyme complex. Substrate and product inhibition terms are included: K_s = equilibrium constant for uncompetitive substrate inhibition and K_p = equilibrium constant for non-competitive product inhibition.

Table 1.2. Enzyme constants for the rate of hydrolysis of urea by urease, from [50]

Enzyme Constants	K_M	K_{es1}	K_{es2}	K_s	K_p
	3×10^{-3} M	5×10^{-6}	2×10^{-9}	3	0.002

This dependency, where variations in pH alter the protein binding site conformation, reflects in the speed in which the enzyme is capable of catalysing the reaction, ultimately resulting in the bell-shaped rate-pH curve (characteristic of feedback) (Figure 1.8). The urease-catalysed conversion of urea to a weak base has been shown to have a maximum rate when at pH 7 [30]. This means that if the starting pH is lowered, via the addition of acid, then the reaction accelerates as it advances.
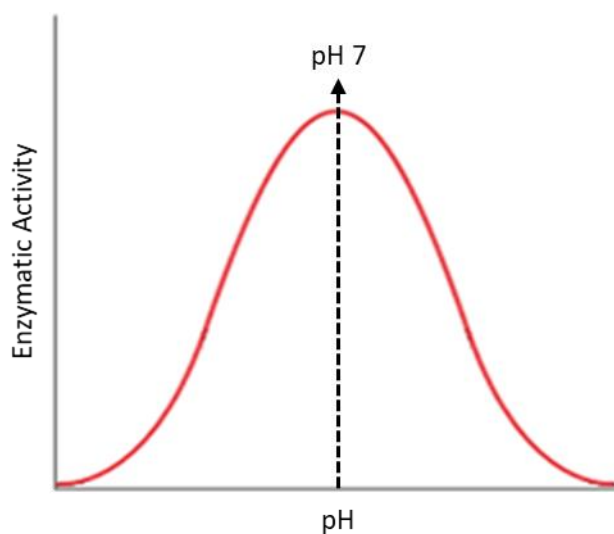
Figure 1.8. pH-activity curve for Jack Bean Urease

1.5.3 "pH Clock" Behaviour

When conducted in a closed reactor, the reaction solution is shown to be stable at an acidic pH (~pH 4) for a particular amount of time, known as the "clock time", before rapidly changing to a basic pH (~ pH 10). Clock reactions are characterised by two indicative features: 1) clock time, and; 2) the maximum reaction rate at a non-zero time point. A study investigating the effects of initial chemical concentrations, i.e., urea, urease, acid, on these features tell us that decreasing urea (Figure 1.9a) and urease (Figure 1.9b) concentrations leads to an increase in clock time and a lower final pH value, whereas, decreasing acid concentration at the start of the reaction (Figure 1.9c) leads to a decrease in clock time, but has no apparent effect on the maximum pH value [51].
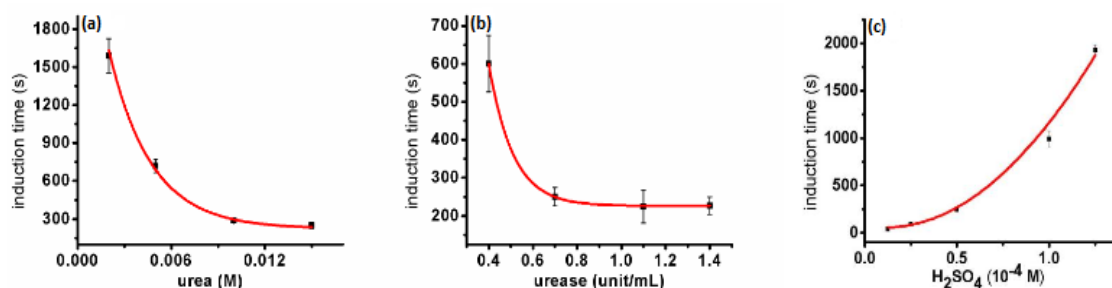
Figure 1.9. Changes in clock time (induction time) as a function of: (a) urea, (b) urease, (c) H_2SO_4, concentrations, from [58]

Aperiodic oscillations (~pH 4 ↔ ~pH 7) have been observed when the urea-urease reaction is conducted in an open (flow) reactor, using a weak acid (acetic acid), as opposed to sulphuric acid [30]. Such oscillations were shown to be slow and responsive to instability in acid/base, and time variations in pH were suggested to be responsive to mixing effects. Currently, all known pH oscillator systems necessitate the need for open flow conditions, because in typical circumstances, at least one of the substrates is fully consumed in the initial pH switch. In the urea-urease system, however, only partial consummation of urea occurs, highlighting its potential as the first batch pH oscillator [30, 59].

1.5.4 Membrane Interaction

Interestingly, these urease metalloenzymes display many biological functions unrelated to their ureolytic activity. For example, *C. ensiformis* is capable of producing three isoforms of urease (Jack bean urease, Jack bean urease II (JBURE-II), and Canatoxin), and in addition to their associated catalytic activity, they have also been reported to induce various other biological responses, i.e., neurotoxicity, exocytosis-inducing and pro-inflammatory effects, activation of blood platelets, and insecticidal and antifungal activities [60-65]. These various effects point to interactions of ureases with cell membranes, either directly or via receptor modulation.

The insecticidal activity of Canatoxin is attributed to the release of an internal peptide, namely pepcanatox, in response to cathepsin-like enzyme-induced hydrolysis in the digestive tract of associated insects [66]. Based on the N-terminal sequence of pepcanatox, through the utilisation of recombinant DNA technology, an analogous Jack bean urease-derived peptide, called Jaburetox, capable of displaying potent entomotoxic activity against insects with either cathepsin- or trypsin-based digestive systems, was expressed [67]. This peptide, shown to elucidate several of the aforementioned biological responses of urease, e.g., insecticidal activity, neurotoxicity, and fungicidal activity [65], highlighted the importance of this region for most of Jack bean urease's "other" biological properties, and this was first demonstrated by Piovesan and co-workers [68], who reported the first demonstration of Jack bean urease and Jaburetox to permeabilise membranes, forming cation-selective ion channels in both zwitterionic and anion lipid membranes.

A higher affinity for negatively charged membranes suggests that anionic lipids may constitute the actual receptors of the toxin in target cells, however, a later study by Micheletto and colleagues [69] showed interaction between Jack bean urease above its isoelectric point (4.5) and a negatively charged lipid membrane, thus inferring that hydrophilic/hydrophobic interactions are more important than the electrostatic attraction in regards to Jack bean urease insertion into a liposome membrane. Interestingly, although the majority of the surface of Jack bean urease is hydrophilic in nature, the Jaburetox sequence is both exposed on the surface and amphiphilic in nature, suggestive of its flexibility to insert itself into a lipid bilayer (Figure 1.10) [69].
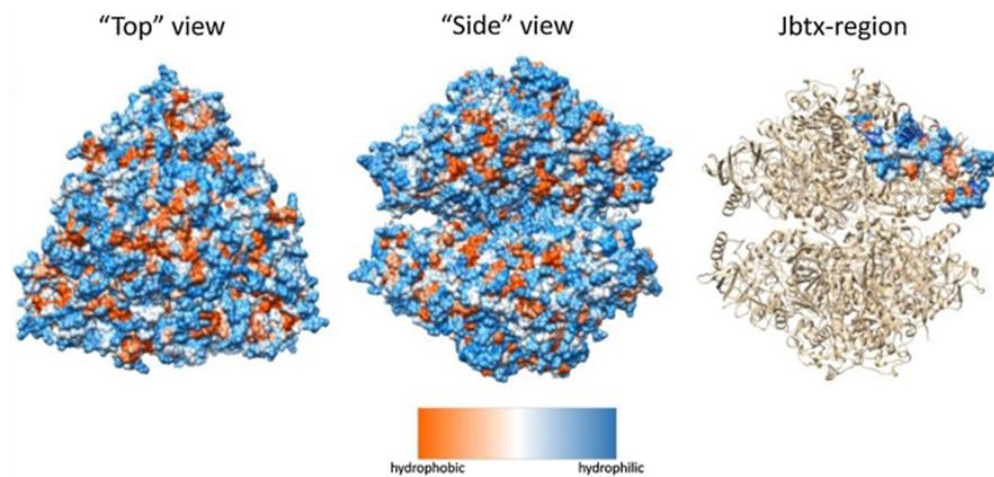
Figure 1.10. Surface hydrophobicity of Jack bean urease, highlighting the Jaburetox (Jbtx)-region, from [69]

It is therefore important to be mindful of this consideration moving forward, even in the presence of neutral charge phosphatidylcholine liposomes (Figure 1.11), e.g., diphytanoyl-phosphatidylcholine, there is potential for encapsulated Jack bean urease, regardless of its pH-induced electrostatic potential, to form cation specific membrane channels, and potentially alter the ion permeation dynamics of our potential system.
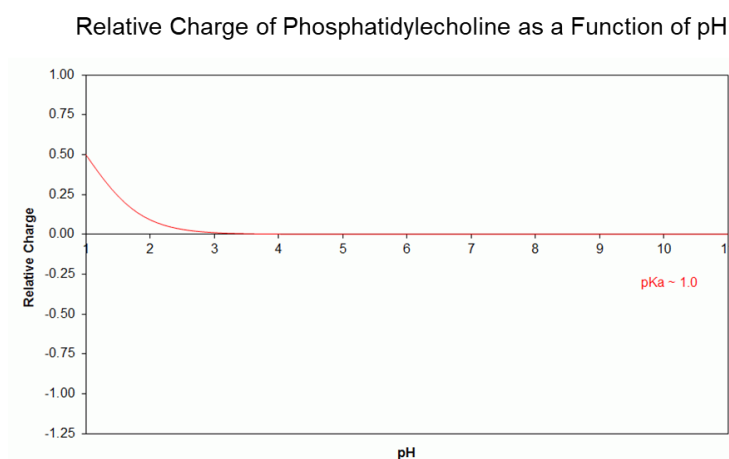
Figure 1.11. Relative charge of phosphatidylcholine as a function of pH (ionic strength = ~0.1 (HCl)), from [70].

39

1.6   Nanoreactors

These vehicles, which allow defined chemical reactions to take place on a nano-scale, have been extensively studied over recent years, not only for their therapeutic potential, but also to better understand the natural counterpart from which they took their inspiration – the human cell. In fundamental terms, the human cell is just a complex reactor, where biological processes are not only protected from the reactive microenvironment of the body, but are kept distinct through function-specific structures called organelles (e.g., mitochondria, endoplasmic reticulum, etc.). This natural form of separation, known as compartmentalisation, provides a suitable platform for signal transduction, facilitating the harmonious regulation of complex biological processes through multiple, simultaneous biochemical cascades [71].

Multiple supramolecular assemblies have been suggested to encapsulate active molecules and generate nanoreactors. These therapeutic nanoreactors can be synthesised using bio- or synthetic-polymers, or a combination of the two. In the field of nanoreactor technology, there exists four groups of natural biopolymers, i.e., lipids, polysaccharides, polypeptides, and polynucleotides, and multiple groups of synthetic polymers, i.e., homopolymers, polyelectrolytes, and block copolymers, etc. [72-75]. However, out of all these, not only are lipid and block copolymer systems the most widely investigated, and best understood, but the use of such supramolecular assemblies is both EMA and FDA approved, e.g. Doxil® [76] and Pluronic® [77].

Comprising of a nanosize reaction compartment, these supramolecular structures allow a multitude of processes and biochemical reactions to take place, e.g., localised production of a drug [78], detoxification [79, 80], monitoring toxic substances [81], enzyme-replacement therapy [82], etc. Their architecture can be comprised from a mixture of "building blocks", including biological or synthetic surfactants, or a combination of the two, and, this architectural versatility allows for active compounds to be entrapped either within the hydrophilic cavity, or within the hydrophobic part of the membrane. Any active components encapsulated within the aqueous core are offered two primary benefits. Firstly, they are provided with a reaction space for *in situ* activity, and secondly, they are protected from the external environment, i.e., proteolytic attack [83]. However, to satisfy the conditions of a nanoreactor, one has to be mindful of the ease in which reaction products can leave. In instances where membrane permeability cannot be facilitated via passive diffusion, the implementation of strategic membrane permeabilisation can be achieved through a variety of means, e.g., manipulation of lipid phase transitions, utilising substrate-permeable membranes, or introducing functional "gate" proteins [83-85].

Liposomes, similarly to naturally occurring membranes (Figure 1.12), contain a lipid bilayer, whereby the hydrophilic head groups are facing the aqueous environment, and the hydrophobic tails face inwards, towards each other. Liposomes, depending on how they are prepared, can contain many (multilamellar), few (oligolamellar), or one (unilamellar) bilayer shell(s). The aqueous solution in which the liposomes are prepared can be found in the lumen of the liposome, however, considerations of osmotic balance between the inside and outside of the vesicle must be employed. The liposome's diameter can be varied, often ranging between approximately 20 nm, and a few hundred micrometres [86].
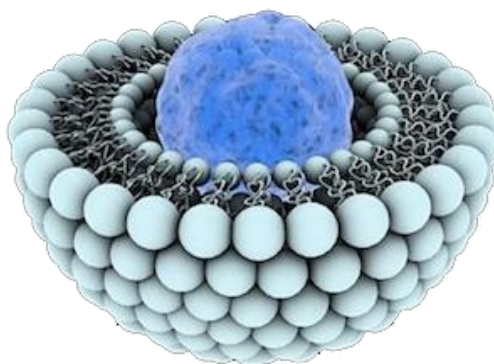
Figure 1.12. Liposome cross-section showing encapsulated enzyme, from [87]

It is worth highlighting that the self-assembly of polymeric amphiphiles, i.e., homopolymers, polyelectrolytes, or block copolymers, can result in a variety of different morphologies, i.e., dendrimers, micelles, capsules, PICsomes, and polymersomes, however, with respect to the research at hand, focus will be aimed at polymersomes. Polymersomes (Figure 1.13), which are comparable to liposomes, are vesicles containing a polymeric membrane. Owing to the diverse library of block copolymers available, where each polymer varies in terms of composition and molecular weight, tighter control over the polymersome's properties can be achieved with regards to membrane thicknesses, permeability characteristics, and stimuli-responsiveness [88-90]. The principle of vesicle self-assembly is covered more extensively by Antonietti and Förster [91], however, the stability of polymer vesicles, mixed with their potential to be both biocompatible and biodegradable, facilitates their usefulness in therapeutic applications.
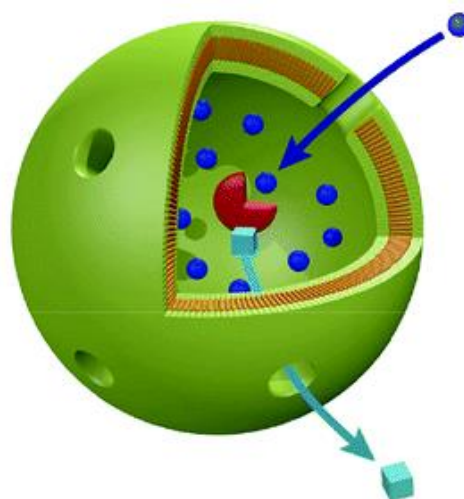
Figure 1.13. Schematic illustration of an enzyme-encapsulating polymersome, showing membrane permeability, adapted from [92]

Introducing poly(ethylene glycol) (PEG) onto the surface of either polymersomes or liposomes vesicles is shown to increase circulation time [93], and in the case of liposomes, increase stability. Liposomes have not only been shown to display a high interaction rate with high and low density lipoproteins in blood plasma, an instability which can cause their constituents to be prematurely released [94], but they are also susceptible to immune system recognition. PEGylation of any composition membrane promotes "stealth-like" characteristics, by minimising the interfacial free energy and increasing steric repulsion, ultimately reducing opsonin recognition and reticulo-endothelial system (RES) uptake [95].

1.6.1 Principles of Self-Assembly

Irrespective of their architecture, it is the balancing of attractive and repulsive forces that causes amphiphiles to self-assemble into supramolecular structures. For example, micelles represent a simple supramolecular assembly, where the individual components are in thermodynamic equilibrium with monomers of the same species in the surrounding medium. When in monomeric form, these surfactant monomers are surrounded by water molecules, forming a "water cage" or "solvation shell", which, in similarity to a clathrate cage, form an ice-like crystal structure, characterised by the hydrophobic effect.

A micelle will then only form when the concentration of surfactant monomers is greater than both the critical micelle concentration (CMC) and the critical micelle temperature (Krafft

temperature) (Figure 1.14). This phenomenon can be described in thermodynamic principles, where it is this balance between entropy and enthalpy that ultimately contributes to the spontaneous formation of micelles. On its own, the assembly of surfactant molecules is unfavourable in terms of both enthalpy and entropy, however, as the concentration of monomers is increased to the point of CMC, the unfavourable entropy contribution, arising from hydrophobic tail clustering, is overcome by a gain in entropy received during the release of their associated solvation shells – at this point, the hydrophobic tail must be distinct from the solvent, and so, form micelles. In summation, where surfactant concentration is above the CMC and Krafft temperature, the gain of entropy due to release of "trapped" water molecules is greater than the loss of entropy due to the assembly of surfactant molecules [96].
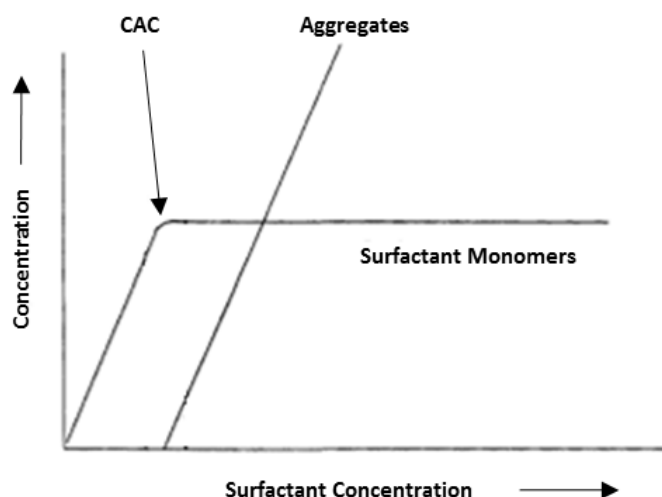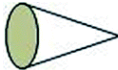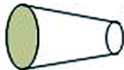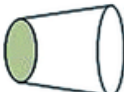
Figure 1.14. Concentration of individual species in a surfactant solution

Following on, the geometry of the surfactant aggregate, i.e., whether it aggregates into a vesicle, micelle, or other, is primarily related to the surfactant's packing considerations. Firstly, it is important to clarify the difference between a vesicle and a micelle; a vesicle contains a bilayer with an aqueous compartment, whereas, a micelle contains a polar head group exterior, and a hydrocarbon interior. In addition, micelles can undertake various different geometries, i.e., spherical, cylindrical, etc. Each amphiphilic molecule has an optimal interfacial area, and supramolecular self-assembly of amphiphiles undertakes considerations of this optimum, in relation to solvent exposure. Where "a_0" is the headgroup area, "v" is the volume, and "l" is the

chain length, then the molecular shape of each structure can be described in terms of the packing parameter (P), where $P = v / a_0 l$ (Table 1.3) [97]. A double-chained amphiphile would (approximately) lead to a doubled v value, and because the optimal "a" and "l" values are constant, this ultimately means that such double-chained amphiphiles tend to form vesicles or cylindrical micelles, whereas single-chained amphiphiles are more likely to form spherical micelles. Vesicle formation can also be aided by other factors, such as hydrophilic head group charge distribution [98].

Table 1.3. Illustration of how surfactant molecular shape affects the critical packing parameter, and ultimately determines aggregate morphology.

Critical Packing Parameter (P)	Surfactant Molecular Shape	Aggregate Morphology
$P \leq \frac{1}{3}$	Cone	Spherical Micelles
$\frac{1}{3} \leq P \leq \frac{1}{2}$	Truncated Cone	Cylindrical Micelles
$\frac{1}{2} \leq P \leq 1$	Truncated Cone	Vesicles
$P \sim 1$	Cylinder	Planar Bilayers
$P > 1$	Inverted Truncate Cone	Inverted Micelles

1.6.2 Membrane Permeability

Phospholipid membranes are permeable to small, uncharged, water-soluble molecules, such as urea or CO_2, via passive diffusion, and in these examples, molecules will travel down their respective chemical concentration gradient, from an area of high concentration, to an area of low concentration. The relative membrane diffusion rate of a given substance is proportional to that substrate's concentration gradient across the lipid bilayer, and to the hydrophobicity of the molecule.

For a molecule to enter a vesicle, first, the molecule must diffuse from the surrounding aqueous solution into the hydrophobic interior of the phospholipid bilayer. Each substance has a partition coefficient (K), determined as the ratio of the molecular concentration inside the hydrophobic bilayer (C^m) to the molecular concentration in the aqueous solutions (C^{aq}), which can be used as a determinant of its hydrophobicity (higher K = greater hydrophobicity and faster diffusion) [99].

$$K = \frac{C^m}{C^{aq}}$$

Equation 1.5. Partition coefficient.

The higher viscosity of the hydrophobic core of a bilayer membrane, in comparison to the aqueous solution surrounding, means that the diffusion rate across the membrane is a lot slower than the associate diffusion rate of the same molecule through the aqueous solution. As such, the diffusion across the cell membrane is determined as the rate-limiting step in the passive diffusion of molecules into the vesicle lumen.

So, if we think about this in a more quantitative fashion, where a membrane with a defined surface area (A) and thickness (x) separates two solutions, of varying concentration, where the concentration outside the vesicle (C_o^{aq}) is greater than the concentration inside the vesicle (C_i^{aq}). In this instance, we can modify Fick's Law [99], stating that the membrane diffusion rate ($\frac{dn}{dt}$) is directly proportional to the permeability coefficient (P), the difference in solution concentrations ($C_o^{aq} - C_i^{aq}$), and to the area (A).

$$\frac{dn}{dt} = PA(C_o^{aq} - C_i^{aq})$$

Equation 1.6. Modified equation to determine diffusion rate

And, the value of P, i.e., the rate of diffusion for any given molecule, is proportional to its partition coefficient:

$$P = \frac{KD}{x}$$

Equation 1.7. Permeability coefficient (P)

Where D represents the diffusion coefficient of the substance whilst inside the membrane, we can combine these two equations to obtain:

$$\frac{dn}{dt} = A\frac{KD}{x}(C_o^{aq} - C_i^{aq})$$

Equation 1.8. Diffusion rate of molecules across a lipid bilayer.

Here, we can see that the diffusion rate is proportional to both the diffusion constant, and the partition coefficient, and inversely proportional to membrane thickness, but, because the membrane thickness, and diffusion coefficient is likely to be similar for all phospholipid bilayers, the real determinant of diffusion is accredited to the substrate-to-substrate differences in partition coefficients, i.e., the degree of hydrophobicity a molecule exhibits.

Now, if we are to consider our potential system, for what at first instance may seem like a relatively straightforward concept, i.e., the encapsulation and subsequent reaction profile of a confined urea-urease reaction, complexity is likely added through the number of reaction species produced, the subsequent equilibria that governs the pH inside and outside the vesicle lumen, and similarly, the transfer of neutral molecules between the vesicles and surrounding solution (Figure 1.15).
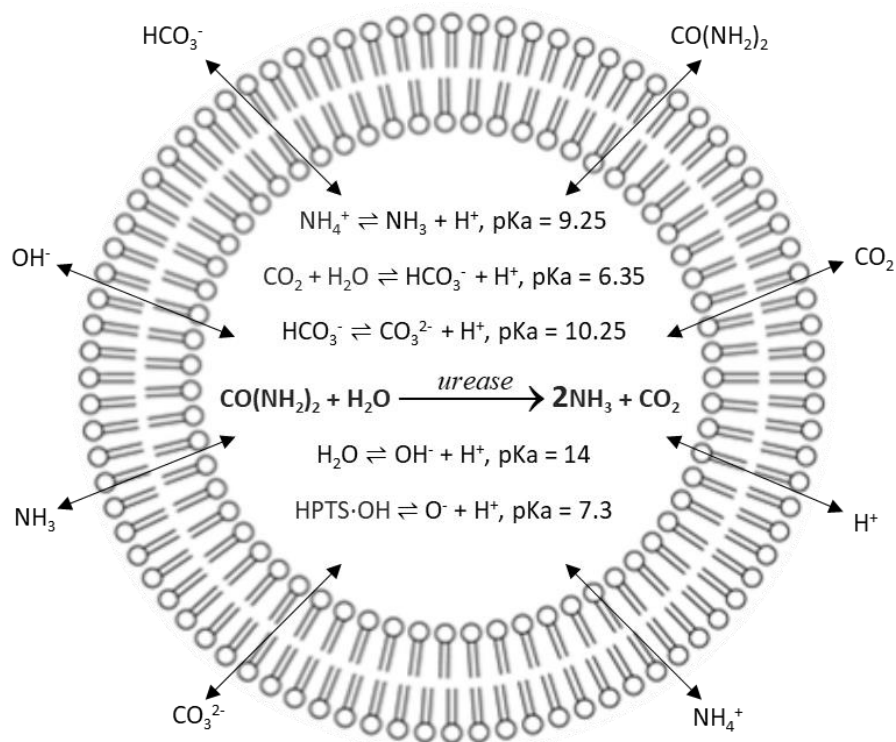
Figure 1.15. Complexity of confined urea-urease reaction in terms of membrane permeation

Of course, where neutral species, e.g., urea, ammonia, and carbon dioxide, do not hold a charge, their relatively smaller partition coefficient infers a greater readiness to cross the lipid bilayer (providing a concentration gradient is present). However, if we are to consider the ions in our system, i.e., H^+, OH^-, NH_3^+, CO_3^{2-}, whose hydrophilicity will be much, much higher than that of the uncharged species, we can begin to see how charge, which is intrinsically linked to pH, affects diffusion rates across the membrane (Table 1.4) [100].

Table 1.4. Permeability rates (m.s⁻¹) across lipid membranes for protons, ammonia, carbon dioxide, and urea [100].

	Neutral			Charged
Chemical Species	NH_3	CO_2	Urea	H^+
Permeability (P) (m.s⁻¹)	10^{-4}	10^{-6}	10^{-8}	10^{-12}

1.6.3 Generating Nanoreactors

Nanoreactor preparation is a complex process, which requires fulfilment of specific requirements with regards to nanoreactor architecture, i.e., building blocks and active constituents, and also the therapeutic application. In addition, generation of therapeutic nanoreactors for intended use in the human body are subject to increased scrutiny in relation to their health and safety. Nanoreactor preparation can be subdivided into two main processes: 1) architecture formation from specific building blocks, and; 2) introducing the active constituent to the architecture. The primary aim is to maintain the active constituent in its functional form; this is both specific to each biomolecule, and also dependent on the preparation method/conditions [73]. As a result, architecture preparation has to be altered to be compatible with the active constituent. Another important consideration is building block treatment with organic solvents. Organic solvents can have a dramatic impact on the activity of biological compounds, and their use should therefore be decreased (where possible) or preferably removed (solvent-free preparation) [90].

There are various methods available for the generation of vesicles with active constituents entrapped from the aqueous phase, which have been extensively reviewed [101], however, for the purpose of this research, two distinct methods are of interest. Firstly, thin film rehydration is one of the most commonly used techniques for the formation of vesicles [102, 103]. Surfactants are dissolved in an organic phase (typically chloroform), and, for this method, that organic phase is removed through evaporation under a high vacuum, to leave a thin, dried lipid film. The thin film is then hydrated with aqueous media, causing it to swell, and subsequently agitated to detach the swelling lamellae from the vessel surface. This ultimately results in the formation of closed, spherical, and multilamellar vesicles, encapsulating the aqueous media, with a typical diameter of several micrometres.

This method represents one of the simplest techniques for liposome formation, however, as a standalone technique, multiple limitations are present. Firstly, there exists a problem with multilamellarity and encapsulation efficiency. It has been shown that subjecting a rehydrated lipid sample to freeze-thaw cycling, not only helps break down multilamellar vesicles into unilamellar vesicles, but, the encapsulation of large macromolecules, such as urease, primarily occurs during this step – this is thought to be the result of membrane-formed ice crystals leaving pores for encapsulant entry [104]. Secondly, extrusion through a polycarbonate filter with a defined nanoscale pore size resolves a lack of homogenisation within the sample [105], as well as further reduces multilamellarity. Finally, unwanted encapsulants outside the vesicle lumen can be removed through a secondary, chromatographic technique, i.e., size-exclusion, etc.

The second method, known as the inverted emulsion technique (Figure 1.16), is of potential interest for the production of giant unilamellar vesicles (GUVs) capable of housing such an enzymatic reaction. In this technique a water-in-oil emulsion is created by agitating a small amount of aqueous solution (containing dissolved encapsulants) in a larger volume of oil containing free surfactants. Within a centrifugation tube, a surfactant-water interface is generated by overlaying free surfactants in oil over a secondary aqueous (collecting) phase. The emulsion is then overlaid on top of the surfactant-in-oil phase, and centrifuged. As the emulsion droplets pass through the interface, they pick up a secondary monolayer.

There are several obvious advantages associated with this technique: firstly, encapsulants remain distinct from the hosting solution throughout the entire process. As a result, encapsulating urease within the emulsion droplets in the first step of process not only increases encapsulation efficiency, but, it keeps the process independent of the type of surfactant used, the size or charge of the encapsulants, or the ionic strength of the hosting solution. This technique also allows for control of vesicle size, which is largely dependent on the rigor of agitation. In addition, the inverted emulsion technique facilitates control over bilayer composition, potentiating the idea of asymmetric vesicles [106]. It is because of this tight control on every aspect of vesicle formation, that these techniques hold such potential in the production of micro- and nanoreactors, which house an enzymatic reaction capable of eliciting a secondary response.
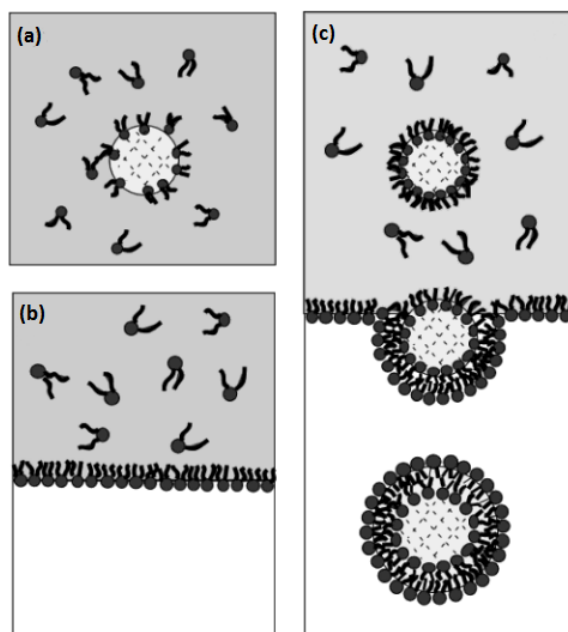
Figure 1.16. Schematic illustration of the inverted emulsion technique showing: a) emulsion droplet formation, b) lipid monolayer formation, and c) vesicle formation [106]

1.6.4 Therapeutic Applications

However, when you step away from the theoretical concept of a nanoreactor and begin to think about their practical use in biomedical applications, different considerations arise. Depending on the function, these considerations can be split into two groups: *in vivo*, e.g., therapeutics, and *ex vivo*, e.g., medical biosensors. The constraints placed on *ex vivo* applications are largely centred on enhancing the system performance via the optimisation of external conditions, whereas, with regard to *in vivo* applications, demands are placed to fulfil strict health and safety regulations governed by the US Food and Drug Administration (FDA), and also the European Medicines Agency (EMA).

For therapeutics, nanoreactors, have been well-received in light of their ability to successfully overcome associated problems of conventional therapeutics, e.g., biocompatibility, biodistribution, toxicity, cellular uptake, and clearance, through their ability to offer a means of protected transport and provide an enclosed reaction space for active biological compounds [73, 107, 108]. As we know, the addition of a biologically inert shell gives the nanoreactor stealth-like properties, increasing circulation time and ultimately boosting efficacy, however, site-specificity can also be achieved through surface-functionalisation with antibodies, peptides, etc., to create recognition points [109-111] or achieve target-specific drug delivery [112-114], and so can stimuli-responsive nanoreactors, whose membrane permeability changes response to physical- (mechanical, temperature, etc.), biological- (enzyme, receptor), or, chemical-stimuli (pH, solvent, etc.) [115, 116].

In this next section, I will give an up-to-date account of the latest advances in vesicle-based drug delivery, and nanoreactor research. As previously mentioned, utilisation of liposomes as drug carriers is already present in the marketplace, with many other research efforts in the clinical trials phase [117]. EMA and FDA approval of such vesicular drug vehicles, as well as the recent approval of triblock copolymer Pluronic® [77] (poly(oxyethylene)–poly(oxypropylene)–poly(oxyethylene), PEO-PPO-PEO), only aids to highlight the potential of nanoreactors for a range of therapeutic applications, such as: prodrug therapy, enzyme-replacement therapy, and also biosensors. Towards the end of the 20th century, considerable advances in lipid-based nanoreactor technology were made and extensively reviewed [86], however, caveats in their relative instability and short systemic circulation time, in conjunction with the first description of polymersomes, led to a distribution of research efforts between liposomes, polymersomes, and lipid-polymer hybrids.

1.6.4.1 Artificial Red Blood Cells

Within the field of oxygen therapeutics, both liposomes [118, 119] and polymersomes [120-123] have been shown to successfully encapsulate haemoglobin. In the hope of creating an artificial red blood cell, haemoglobin-containing lipid vesicles have shown good efficacy in animal studies [124], and multi-compartmental vesicles, co-encapsulating catalase or a reductant, e.g., homocysteine, have been shown to increase oxygen uptake efficiency via the abolition of metheamoglobin formation [125]. However, these lipid-derived systems have shown associated downfalls i.e., liposome stability, compatibility with blood, reticuloendothelial system-induced degradation, and blood circulation time. Polymersome systems have therefore been investigated as a means of protecting the encapsulants whilst working in a biological environment. Poly(ethylene oxide)-poly(butadiene) (PEO-*b*-PBD) and poly(ethylene oxide)-poly(ethyl ethylene) (PEO-*b*-PEE) polymersome nanoreactors have shown to be stable in blood plasma (temperature; 21°C) for up to five days, potentiating their use for successful oxygen replacement therapy [121]. Reduced permeability issues, commonly associated with polymer membranes, significantly reduce oxygen binding potential (in comparison to free haemoglobin) [120], however, impregnation with the OmpF membrane protein was shown to reduce this issue [123]. As is the extensive research effort expended in artificial red blood cell production, as an alternative to transfusion, this topic has been broadly reviewed [119, 126-128].

1.6.4.2 Reactive Oxygen Therapy

Superoxide dismutase (SOD), an antioxidant enzyme known to catalytically degrade the reactive oxygen species (ROS) responsible for the pathogenesis of rheumatoid arthritis, Alzheimer's disease, Parkinson's disease, as well as others, has shown to be successfully encapsulated in lipid- [129] and polymer-based [79, 80] vesicles. In rat models, PEGylation of liposomes was used to enhance blood circulation time, which ultimately resulted in greater SOD accumulation efficiency at targeted sites, and superior therapeutic effects, irrespective of dose quantity or the type of enzyme [94, 130]. A hydrophobic variant of SOD, namely Ac-SOD, resulted in liposomes with SOD enzymes presented on their surface [131]. These Ac-SOD-liposomes were shown to be more efficient, with respect to anti-inflammatory response, in comparison to when the enzyme is encapsulated, due to better surface presentation. In the polymer system, alteration of PMOXA-*b*-PDMS-*b*-PMOXA block lengths were used to tune permeability, ultimately producing SOD-encapsulated nanoreactors with optimal properties [132]. These anti-oxidant-based

nanoreactor-systems are expected to have applications age-associated pathologies, i.e., cataracts [133, 134], cancer, age-associated macular degeneration, Alzheimer's disease, etc.

On the contrary, generation of ROS in high quantities, and in a localised fashion, presents a strategy for photodynamic therapy [135, 136]. Polymersome-based nanoreactor systems containing a photosensitiser linked to bovine serum albumin, were able to, when excited by a specific wavelength of light, to produce ROS and lead to cell death [115]. Such nanoreactor-based systems hold a great advantage over clinical phase photodynamic therapies because ROS are produced in a localised fashion, without the release of the photosensitiser [137, 138].

In addition, this type of advance has been explored in a theranostic capacity, i.e., combining therapeutic and diagnostic qualities within polymeric nanoreactors. In this example, encapsulation of two distinct enzymes, SOD to transform ROS to H_2O_2 and lactoperoxidase to transform H_2O_2 to H_2O and O_2, within a polymeric nanoreactor stimulates an enzymatic cascade, which, in turn, oxidises Amplex Red to its fluorescent product resorufin. This ultimately produces a nanoreactor system capable of removing ROS, whilst simultaneously monitoring ROS-activity through fluorescence [79].

1.6.4.3 Enzyme Replacement Therapy

Nitric oxide (NO) is produced in the arterial endothelial layer and promotes artery wall relaxation, controlling blood flow, and regulating blood pressure. Therefore, being NO deficient is a well-understood cause of a variety of different health challenges e.g., arteriosclerosis, hyperglycemia, impotence, hypertension, etc. [139]. The enzyme responsible for the production of NO is nitric oxide synthase (NOS), which has been successfully encapsulated in a liposomal nanoreactor. These NOS-encapsulated nanoreactors were shown to be stable for a minimum of 15 days, and maintained 75% enzyme activity [139].

Similarly, mitochondrial neurogastrointestinal encephalomyopathy (MNGIE) is a genetic disease, that causes an elevation of thymidine and deoxyuridine in the blood plasma through thymidine phosphorylase deficiency – this leads to toxicity primarily effecting the nervous and digestive systems [140]. The successful encapsulation of thymidine phosphorylase has been documented in polymersomes, where, thymidine phosphorylase-catalysed conversion of thymidine to thymine and deoxyribose 1-phosphate can take place. These nanoreactors were found to be both stable (blood serum, 37°C) and non-toxic (hepatocytes and in macrophages) [73, 82].

1.6.4.4 Prodrug Activation

An example of how nanoreactor systems can be used to enhance an existing cancer therapeutics can be seen with directed enzyme prodrug therapy (DEPT). Here, artificial introduction of enzymes into the body is used as a means of converting a prodrug into an active drug. However, the likelihood of the enzyme invoking an immune response, leading to rapid clearance or potentially harmful adverse effects is high. To circumvent this problem, an advancement on DEPT is gene-DEPT (GDEPT), where an enzyme-encoding gene is delivered to stimulate the enzymatic activation of a prodrug. However, although this strategy has significantly reduced systemic toxicity because toxin production is confined to the tissue to which the gene is delivered [141], a more efficient strategy would be to encapsulate prodrug-activating enzymes within a nanoreactor, which can then be targeted to the cancerous cells, ultimately eliciting their therapeutic effect upon docking. The obvious advantage of enzyme encapsulation is that following intravenous administration, circulation time is to be increased and likelihood of an immune response is greatly reduced.

Again, within the field of cancer therapeutic, encapsulation of an enzyme capable of converting a prodrug to an active drug have been documented. Both lipid [142, 143] and polymer [142] systems have been shown to encapsulate nucleoside hydrolase, an enzyme extracted from the parasite *Tyrpanosoma vivax*, which is capable of converting non-toxic prodrugs 6-methyl-purine riboside and 2-fluoroadenosine to toxically active compounds 6-methylpurine and 2-fluoroadenine, respectively. In each case, incorporation of OmpF channel proteins into the nanoreactor membranes facilitated permeability.

Another promising example, where an element of temporal control was achieved, was shown in penicillin acylase-encapsulating polymeric nanoreactors, capable of successfully converting a prodrug into an active drug. Since the substrate has no antibiotic effect, not only is the risk of adverse reactions reduced, but the localised efficacy of antibiotic effect will be increased. However, temporal control of antibiotic release was only partially achieved through the manipulation of various fundamental parameters, i.e., substrate concentration, vesicle size, and the number of membrane channels present [78].

1.6.4.5 Cell-Level Therapies

The height of nanoreactor technology is rooted in the repair of cell dysfunction, either through the mimicry of cell organelles, or through gene upregulation [114, 144-146]. Further advanced is liposomal DNA delivery, with products such as Lipofectamine already on the market, but these

products are only shown to improve the efficiency of transfection. However, for the cell to express the transgene, it must reach the cell nucleus and undergo transcription [147]. These DNA-carrying nanoreactors are typically generated through the conjugation of a cationic lipid molecules with neutral co-lipid helpers to produce a positively charged liposome, which is then capable of generating electrostatic interaction with nucleic acids and fusing with the negatively charged cell membrane allowing transfer of the genetic material [148].

The idea of mimicking a natural organelle would not only have a resounding impact on the field of artificial cell (protocell) design, but it would also revolutionise medical practice with regards to correcting cell-level disorders, e.g., mitochondrial disease. At this moment in time, there has been no breakthrough in artificial organelle technology where the requirements to achieve such a feat is complicated on many fronts. The nanoreactor needs to be of an appropriate size to be taken into the cell, the *in situ* activity of encapsulated constituents needs to be preserved, the actual nanoreactor architecture must be completely stable. If achieved, this technology would represent a significant milestone in *in vivo* cell organelle replacement, and provide a new frontier in therapeutics.

1.6.5   Artificial Cells

Of course, the potential of this technology stretches beyond that of therapeutic outcomes, to perhaps underpin a pillar of synthetic biology. Cells, often referred to as the "building blocks of life", are the basic structural, functional, and biological unit of all lifeforms. However, on a fundamental level, a cell is just a highly advanced, and efficient microreactor, and it is this fascinating concept that has inspired much research into the field of artificial cell technology. In fact, since there first proposition in 1957 [149], research into these protocells has served many purposes, such as: i) helping shape a plausible theory for the origins of life, ii) providing insight to shape our understanding of cellular life, iii) investigating the connection between the living and non-living world, and; (iv) adding novel functions to biological cells for the development of new applications [150].

At present, the many processes that take place in a natural cell are well-understood. The internal structure, including the function and biochemical characteristics of the internal components have been elucidated [151]. However, the true complexity of a natural cell is owed to understanding how all these individual factors integrate. Advances within synthetic biology tries to bridge the knowledge gap, progressing our understanding of how these processes interconnect, through two distinct yet fundamental approaches:

i.   A top down approach, which involves the systematic breakdown of a living organism's genetic material to leave the minimum number of genes required for essential function [152].

ii.   A bottom-up approach, in which an artificial cell is created through the assembly of non-biotic materials to mimic the aspects of a biological cell [153].

Although yet to be created, an artificial cell, as well as being similar in structure and characteristics to its natural counterpart [153, 154], should be "alive", in the sense that it should be able to self-maintain, self-reproduce, evolve, and die. Given the huge complexity of even the most simple organisms, before any effort is expended trying to synthesise a "living" protocell, one must consider the minimal criteria for cellular life [155]:

i.   A robust and semi-permeable membrane to provide protection to internal constituents and allow selective passage of material/energy

ii.   Genetic material in the form of biomacromolecules, e.g., DNA or RNA, to control the dynamics of the cell, and allow for evolution capabilities

iii. A network of metabolic pathways, providing a means of energy generation, self-maintenance, and self-processing.

iv.   The ability to grow and reproduce, allowing for the survival of the species.

v.   Adaptive characteristics to promote survival in a dynamic and environment.

The integration of such complex and efficient functions into a single synthetic system is an impressive but challenging goal. However, as synthetic biology has advanced, and micro-/nanoreactors have provided an efficient means of housing a variety of macromolecules/functions [156, 157], several groups have successfully mimicked some simple functions of life [158].

Phospholipids have been identified as the primary components of plasma membranes in almost all known living organisms, so liposomes provide one discernible option for the housing of cellular components, but this is not the only option, other examples include polymersomes, lipid-polymer hybrids, colloidosomes, or virus capsids [156]. However, although great control has been achieved in terms of permeability, biodegradability, stimuli-responsiveness, and size, the complex compartmentalised internal structure of eukaryotic cells generates an additional level of difficulty. Within a cell, the separation of microenvironments, housing a variety of distinct chemical reactions and reaction cascades, is appropriated through a number of organelles, however, for this to be replicated in synthetic systems, multi-compartment vesicles must be generated. One example, in the work of Peters and co-workers [159], describes a multi-

compartmentalised vesicle where each compartment was loaded with a different enzymatic reaction cascade step, and communication between such compartments allowed for a signalling cascade to be achieved in an artificial system.

Besides being a basic chemical boundary, a minimal cell should act as an information system. Where all life is coded by DNA, the translation of information held within a gene into a functional product, often a protein, is fundamental to the construction of a minimal cell. However, even the most simple of organisms contains hundreds of delicately regulated genes. Clearly, the task of engineering a complex and communicating synthetic network within a synthetic cell is enormous, however, there have been promising advances. In 2001, Yu and co-workers [160], reported the expression of a functional, mutant green fluorescent protein (GFP) (GFPmutI), through the encapsulation of a protein synthesis reaction mixture. This was built on in 2004, when Ishikawa and colleagues [161] encapsulated both a T7 RNA polymerase gene and a GFP gene, and initiated a two-step reaction cascade, where the product from T7 RNA polymerase promoted the upregulation of the GFP gene. However, in contrary to such relatively simple behaviour, a truer representation of a biological cell would see protein expression regulated through feedback behaviour. To this end, a recently-developed, synthetically-compartmentalised system encapsulating all seven regulatory *E. coli* σ factors has allowed for more complex, and responsive metabolic circuits, where transcriptional activation cascades showing feedback behaviour have been shown to switch between two outputs depending on the inducer [162, 163].

For a cell to function and maintain its activity, it needs a continuous supply of building blocks, and the energy to convert them into functional metabolites. In biological cells, this is supplied through the catabolism of molecules, i.e., ATP $\rightarrow$ ADP, which are continuously recycled as part of the electron transport chain. Here, a series of complexes that transfer electrons from electron donors (nicotinamide cofactor (NADH)) to electron acceptors (Complex I) via redox (both reduction and oxidation occurring simultaneously) reactions, and couples this electron transfer with the transfer of protons (H+ ions) across a membrane. This creates an electrochemical proton gradient that drives the enzyme-catalysed synthesis (ATP synthase) of adenosine triphosphate (ATP), a molecule that stores energy chemically in the form of highly strained bonds [164]. Through the encapsulation of a Baeyer–Villiger monooxygenase, NADH has been shown to be successfully regenerated in nanoreactors [165]. Likewise, the incorporation of Complex I, a membrane protein responsible for the coupling of electron transfer between NADH and ubiquinone to proton translocation across an energy-transducing membrane, to help build the electrochemical potential difference that supports ATP synthesis, into vesicle membranes,

there is clear movement towards an energy producing nanodevice [166]. Finally, encapsulation of ATP synthase, used to produce high-energy ATP, has been reported. [167]. Although not quite there, the potential to combine and expand on such regenerative and energy producing metabolic reactions is huge when looking to achieve a synthetic source of cellular energy. However, in the broader sense of metabolism, in most instances reported to date, the omission of a mechanism to balance such resources results in the cessation of artificial cell metabolism, due to a depletion of nutrients, and where continuous replenishment of nutrients occurs, the accumulation of waste becomes problematic [168].

In order to maintain a living population, cells, whether biological or artificial, must reproduce. In order to proliferate, producing daughter/sister cells of an appropriate size without shrinkage, membrane components must be produced. To do this, an often-adopted approach is to incorporate an amphiphilic molecule-producing catalyst into the vesicle, be it the lumen or the membrane [169]. This catalytic generation of an amphiphile induces budding, and ultimately fission, in response to a disruption in the compartment's surface-to-volume ratio, however, ultimate dilution of the catalyst following growth iterations is problematic. Similarly, to truly reproduce biological cell proliferation, and maintain metabolic function, the associated metabolic machinery must also be replicated – so far, minimal success has been realised in this area [169].

Finally, where we have highlighted the current state of advancement for the first four characteristics of life, finally, we move onto adaptability. In this sense, for a cell to survive in a dynamic environment it must continuously sense and respond to environmental stimuli. In one example [170], dynamic protein-ligand interactions were reversibly controlled by external small-molecule triggers in GUVs. The pH-modifying enzyme, alcohol dehydrogenase, was responsible for the conversion of two different substrates, was used to modulate a pH-specific interaction between the His-tagged luminal protein and the Ni-NTA ligand on the vesicle membrane – this process was also reversible in the presence of an appropriate antagonist. As well dynamic membrane association/dissociation, one of the most important characteristics to replicate would be stimuli-responsive modulation of membrane permeability. In 2013, Li and co-workers [171] successfully showed, albeit in a colloidosome, that they could efficiently regulate an internal reaction through the control of membrane permeability, however, to move towards a total artificial cell, this selectivity should be based on more than just size or charge.

Similar efforts have been expended trying to replicate the natural communication seen between cells when they are coordinating their actions. In the first example of natural-to-artificial cell

signalling, Gardner et al. [172] developed a lipid-bound protocell that could synthesize complex carbohydrates by the autocatalytic sugar-synthesizing formose reaction. It was able to initiate a quorum-sensing mechanism in the marine bacterium *Vibrio harveyi* and cause a bioluminescent response. Since then, a few examples of artificial-to-artificial cell signalling have been described, for example, where hydrogen peroxide formed in one colloidosome induced the formation of a thermoresponsive PNIPAM outer shell on a secondary colloidosome [173]. Despite this progress, reciprocal communication is yet to be achieved; it is this communal communication that could form the foundations of artificial tissue-like structures.

Finally, the importance of motility in natural cells is well documented throughout nature, either by chemotaxis, or through mechanical means. In this sense, motility has been achieved in artificial cell-like systems, via "nanomotors", through a variety of means, i.e., propulsion and chemotaxis. This will be elaborated on in more detail in Chapter Six.

1.7   Overview of Research

So, within this doctoral thesis, we draw together these disciplines of thriving scientific attention, and work towards an idealism, where state-of-the-art nanoreactor technology, is combined with non-linear enzyme kinetics, to generate a secondary outcome.

With regards to a temporally-controlled drug delivery system, although it is obvious to assume that the cooperation between positive and negative feedback is needed to create a system with full autonomy, the inner-workings of how this may be done are still unknown. However, by building a system from the bottom-up, confining enzymatic feedback within a nanoreactor, and investigating the associated nuances, we can begin on a path to better understanding this system, with a view to therapeutic design.

Through this means, we have uncovered a system more complicated than first anticipated. This complexity, driven firstly by the fragility of the constituents in relatively harsh conditions, but more importantly by the dynamism of the system in terms of membrane transport, and associated pH-linked permeability coefficients. However, by building a platform to allow for extensive parameter space exploration, in combination with theoretical modelling, we have not only gained control over the kinetic output but have also pieced together a holistic overview of how the system behaves in totality. It is this organic discovery, and ultimate understanding, that has allowed us to extend our reach, and push the functionality of our novel system, e.g., inter-vesicle communication and vesicular motility.

CHAPTER TWO – OPTIMISATION OF SYSTEM (PRE-CONFINEMENT)

2.1   Introduction

It has previously been suggested [174], through simulations of bistability in alginate beads, that there may be a link between the degree of enzymatic confinement, and the robustness of pH switching, in the urea-urease reaction. However, before attempting to load the urea-urease reaction into a situation of nanoscale, vesicular confinement, a number of considerations and preliminary experiments have to be investigated.

Within this chapter, firstly, a practical and efficient way of monitoring pH switching must be found. Of course, in a regime where pH change must be monitored inside a vesicular lumen, our ideal candidate would not only be pH-sensitive, but also ratiometric, as to mitigate against potential variability in encapsulation efficiency, and membrane impermeant, as to prevent leakage. Once our lead candidate (HPTS), had been identified, specifically owing to its adherence to these characteristics, three questions were asked. Firstly, is HPTS an appropriate pH indicator for the pH-switching range witnessed for the urea-urease reaction, could this switching range be calibrated, allowing for the simple conversion between absorption ratio and pH, and, finally, does HPTS in any way interfere with the catalytic activity, and therefore, pH-switching properties of urease? It is, therefore, within this chapter, that we seek to answer these initial questions, firstly, through the spectroscopic calibration of HPTS, and secondly, through the repetition of a common [174], bulk urea-urease reaction using HPTS as the pH determinant.

Similarly, given the proposed experimental setup, i.e., the reduction of pH in order to obtain a "clock", and the harsh exposure of the system components to freeze-thawing, during the process of thin film rehydration, there are questions to be answered surrounding stability. If we take pH for example, and apply what we know from previous literature [174], including what we know about *H. pylori* [175], we can be assured with a high level of certainty that urease will be able to withstand the proposed reductions in pH, however, can the same be said about the lipid vesicles? Similarly, freeze-thaw cycling is a common technique, coupled to thin-film rehydration, which reduces multilamellarity and increases encapsulation efficiency, however, is urease robust enough to withstand multiple freeze-thaw cycles, or will catalytic activity be severely diminished? This section seeks to answer these questions, aiding a more complete understanding of each component within the proposed system, and reassures us that a confined system will not unravel into a bulk regime due to our harsh preparation techniques.

Finally, owing to the (relatively) massive size of Jack Bean Urease (545 kDa), one of the most crucial and prominent challenges is the successful and efficient removal of unencapsulated entities from the external environment. Of course, the removal of much smaller molecules, e.g.,

HPTS (524 Da), from larger architectures (like vesicles) can be achieved via size-exclusion on a gravity packed column, however, the sheer size of urease may cause unexpected problems with regards to the use of not-so-standard size exclusion media. Therefore, the final part of this chapter is focused on unearthing an efficient and reproducible technique of vesicle purification, exploring the use of different size-exclusion media, and the potential use of peptidases to completely inactivate, or cleave the urease into more manageably removable fragments.

2.2   Experimental

2.2.1   Materials

The lipid, 1,2-diphytanoyl-sn-glycero-3-phosphocholine (DPhPC), and the fluorescent lipid marker (1,2-dioleoyl-*sn*-glycero-3-phosphoethanolamine-N-(lissamine rhodamine B sulfonyl) (ammonium salt)) (Rhod-DOPE), were purchased from Avanti Polar Lipids Inc. The ratiometric pH probe 8-hydroxypyrene-1,3,6-trisulfonic acid trisodium salt (HPTS) and the urease from *Canavalia ensiformis* (Jack Bean) were purchased from Sigma-Aldrich.

2.2.2   Vesicle Preparation (Thin Film Rehydration)

Here is an overview of a non-specific thin film rehydration protocol, however, this process contains multiple variables, i.e., surfactant, encapsulant, pore size, mobile phases, etc., which can be altered to create a desired sample. So, to a known volume of chloroform-suspended lipid stock solution, in this instance, DPhPC (25 mg/mL), 0.5 mol% of the fluorescent marker Rhod-DOPE (0.5 mol%) was added, which will give a final concentration of 2.5 mg/mL when 1 mL of hydrating solution is added, i.e., 70 µL of DPhPC and 30 µL of Rhod-DOPE, and this was then subsequently dried overnight under high vacuum to remove the solvent. The remaining thin lipid film was resuspended in an aqueous solution containing the desired encapsulant, which, for example, could be urease (10 µM) and HPTS (20 mM) in dilute HCl (0.2 mM) (made with distilled water). Following vortex mixing, the samples were subjected to ten cycles of freeze-thawing (nine cycles at 45°C, and the final cycle at 36°C). The samples were then extruded eleven times through a polycarbonate filter with a defined pore size, e.g., 100, 200, 400 nm. The extruded sample was then run down a size-exclusion column, packed with an appropriate medium, e.g., Sephadex G-50, with an appropriate mobile phase, e.g., dilute HCl (0.2 mM), to separate the vesicles from any unwanted, unencapsulated entities.

2.2.3 Calibration of HPTS

2.2.3.1 Ultraviolet-Visible Spectrometer

To cover the range of pH switching (pH 4 – pH 10), a phosphate-citrate buffer, covering a pH range of 2.2 – 8.0, and a glycine-NaOH buffer, covering a pH range of 8.6 – 10.6, were used. The absorption spectra of buffered-HPTS (50 µM) (pH 4.0, 5.0, 6.0, 6.6, 7.0, 7.5, 8.0, 8.6, 9.0, 9.5, and 10.0) were measured using a Cary 100 ultraviolet-visible spectrometer. A calibration curve for HPTS, plotting absorption ratio (450/405 nm) against pH, was created.

2.2.3.2 Fluorometer

The same buffered solutions of HPTS used to calibrate the Ultraviolet-visible spectrometer were used to obtain fluorescent intensity readings, using a FluoroMax-3 fluorometer, for each the known pH solution of HPTS. The solutions were excited at 450 nm and 405 nm, and a fluorescence intensity maxima ratio at 511 nm was plotted against pH, to give a calibration curve for HPTS.

2.2.4 Urea-Urease Reaction – Bulk Conditions

Solutions (500 µL) of urease (6.8 units/mL), HPTS (50 µM), and differing concentrations of H_2SO_4 (0.24 mM, 0.27 mM, and 0.30 mM) were made using distilled water. In a 550 µL micro-cuvette, 250 µL of these solutions were placed, the reaction was initiated through the addition of 250 µL urea (5 mM), and a time course of absorption ratio (450/405 nm) was measured using a Cary 100 Ultraviolet-visible spectrometer.

2.2.5 Acid Stability of Liposomes

2.2.5.1 Carboxyfluorescein-Release Experiment

DPhPC and Rh-DOPE (0.5 mol%) vesicles were prepared via the above described thin film rehydration method. The aqueous medium used to hydrate the lipid film was a 125 mM carboxyfluorescein solution, which had undergone titration using NaOH, until full dispersion of carboxyfluorescein had occurred (pH 7.4). Ten freeze-thaw cycles were conducted before the lipid suspension was passed through a 100 nm polycarbonate pore filter. The carboxyfluorescein-encapsulating liposomes were separated from the external carboxyfluorescein via size-exclusion chromatography, using Sephadex G-50 as the medium, and

deionised water as the mobile phase. A FluoroMax-3 fluorometer was used to monitor changes in fluorescence intensity maxima at 517 nm upon addition of Triton X-100.

2.2.5.2 HPTS-Release Experiment

DPhPC and Rh-DOPE (0.5 mol%) vesicles were prepared via the above described thin film rehydration method. The aqueous medium used to hydrate the lipid film was a 50 mM HPTS solution, adjusted to pH 9.5 with NaOH. Ten freeze-thaw cycles were conducted before the lipid suspension was passed through a 400 nm polycarbonate pore filter. The HPTS-encapsulating liposomes were separated from free HPTS via size-exclusion chromatography, using Sephadex G-50 as the medium, and deionised water as the mobile phase.

A FluoroMax-3 fluorometer was used to monitor changes in fluorescence intensity maxima at 511 nm, when excited at 405 nm, upon addition of increasing concentrations of H_2SO_4 (0.05 mM/pH 4.0, 0.16 mM/pH 3.5, 0.50 mM/pH 3.0, and 1.58 mM/pH 2.5). Two control measures were also taken: 1) no acid, and therefore assumption of no HPTS release, and; 2) addition of Triton X-100 (50 µL, 10% v/v) to cause liposome rupturing, and therefore assume that all encapsulated HPTS is released.

2.2.6   Urease Stability

Two bulk solutions, containing urease (50 U/mL) and HPTS (0.05 mM), were made. One was subjected to ten freeze-thaw cycles, and the other (control), was left untouched. A Cary 100 Ultraviolet-visible spectrometer was then used to measure the absorption ratio of each sample, in terms of HPTS (450/405 nm), over time, following the addition of urea (10 mM).

2.2.7   Purification

Two stock species of DPhPC + Rhod-DOPE (0.5 mol%) vesicles (5 mg/mL) were produced via thin film rehydration. The first species encapsulated urease (11.1 µM) and HPTS (20 mM), the second species were empty, but, once generated, urease (11.1 µM) was added to their external environment. Two samples of the urease-encapsulating vesicles were taken, and were either incubated with pepsin (0.55 µM) for 2 h, then underwent size-exclusion chromatography on a Sephadex G-50 size exclusion column, or vice versa. This was then repeated for the empty vesicles, however, after the size-exclusion step, HPTS (50 µM) was added to the external environment. Finally, two more samples of the empty vesicles were taken, but, this time, they were either incubated with pepsin (0.55 µM) for 2 h *or* underwent size-exclusion

chromatography (Sephadex G-50), before HPTS (50 µM) was added to their external environment. Once the experiment had been initiated by addition 10 mM of urea to each sample, the absorption ratio (450/405 nm) was measured over time using a Cary 100 Ultraviolet-visible spectrometer.

2.3 Results and Discussion

2.3.1 Calibration of HPTS

To allow for pH switching in the urea-urease reaction to be monitored, HPTS was chosen because of its ratiometric pH sensitivity, attributed to pH-responsive shifts in absorption spectra at 450 and 405 nm (Figure 2.1), allowing for ratiometric absorption to be measured at 450/405 nm, and its water soluble and membrane-impermanent properties, owed to the presence of 3 negative charges [176]. The ratiometric nature of HPTS makes it an ideal pH indicator for vesicle encapsulation, because measurements can be taken without regard to encapsulation efficiency. This is in contrast to standard fluorescent pH probes, which typically change absorbance/fluorescence intensity in response to changing pH, and so, in this regime, would exhibit fluctuations in intensity in response to inconsistent encapsulation efficiencies across different samples.
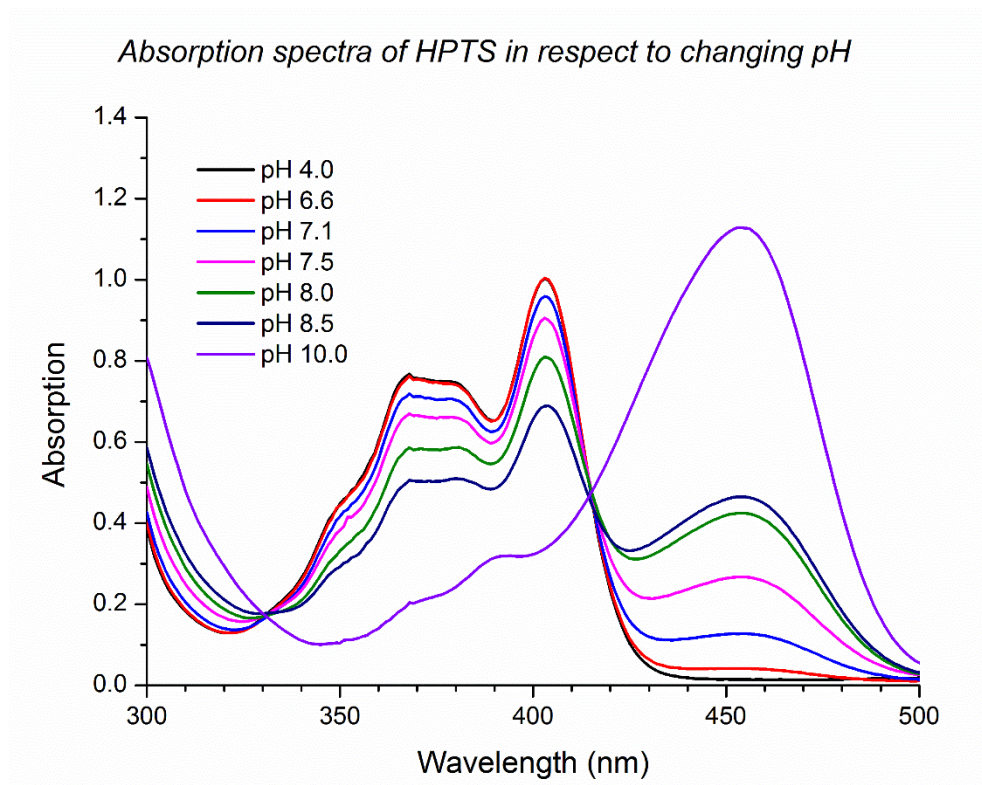
Figure 2.1. Absorption spectra of HPTS with respect to changing pH
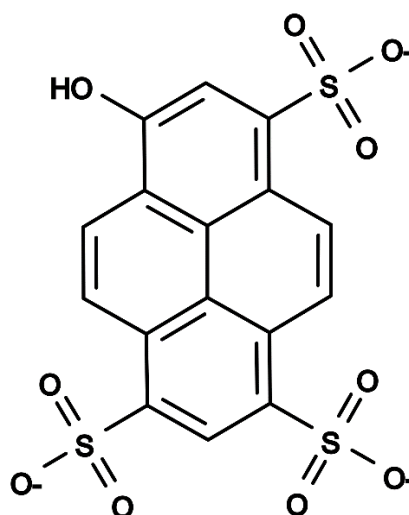
Figure 2.2. Chemical structure of 8-hydroxypyrene-1,3,6-trisulfonic acid (HPTS)

2.3.1.1 Ultraviolet-Visible Spectrometer

To create a calibration curve capable of converting an absorption ratio value to a pH value, buffered solutions (phosphate-citrate and glycine-NaOH) of HPTS (50 μM) were calibrated to known pHs between pH 4 and pH 10, and their absorption was read. A calibration curve, plotting absorption ratio against known pH (Figure 2.3), was shown to be sigmoidal in shape – this was consistent with the literature, where confidence in calculated pH was fallible below pH 6.6. By applying an appropriate fit to the data (Figure 2.3), we can extract the equation of the curve, where x is the pH, y is the absorption ratio (450/405 nm), and x_c, k, and a are fitting parameters, which, when rearranged (Equation 2.1), allows us to directly convert absorption ratio (450/405 nm) into pH, providing it is within the range of the pH probe (approximately pH 6.6 – pH 10).

$$y = \frac{a}{1 + e^{-k(x - x_c)}}$$
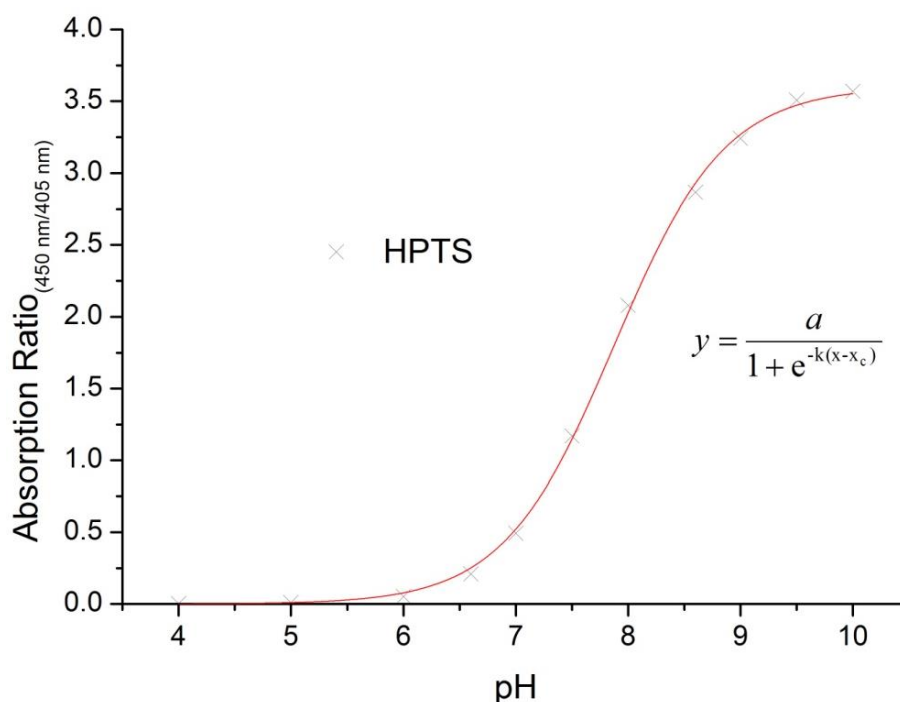
Figure 2.3. Calibration curve of known pH HPTS buffered solutions (Ultraviolet-visible spectrometer).

$$x = x_c - \frac{1}{k} \ln\left(\frac{a}{y} - 1\right)$$

Equation 2.1. Rearranged sigmoidal fit equation from HPTS calibration to allow for prediction of pH based on absorption ratio (450/405 nm)

2.3.1.2 Fluorometer

Similarly, the same buffered solutions of HPTS used to calibrate HPTS absorption were used to obtain fluorescent intensity readings, where, sequential excitation at 450 nm and 405 nm, allowed for a fluorescence intensity maxima ratio at 511 nm to be plotted against pH, and a calibration curve generated. By fitting the data (Figure 2.4), where, again x is pH, y is the absorption ratio, and $A1$, $A2$, and p are the fitting parameters, it allows us to convert between fluorescence intensity ratio and pH, providing another form of spectroscopy capable of determining pH change within HPTS-encapsulating vesicles.

It is interesting to note that fluorescence gives a more useable conversion at lower pH (below pH 6), but is less sensitive above pH 8, whereas, absorption (Figure 2.3) is less sensitive at low pH, but more sensitive at higher pH.

$$y = A1 + \frac{A2 - A1}{1 + 10^{(LOGx0 - x)p}}$$
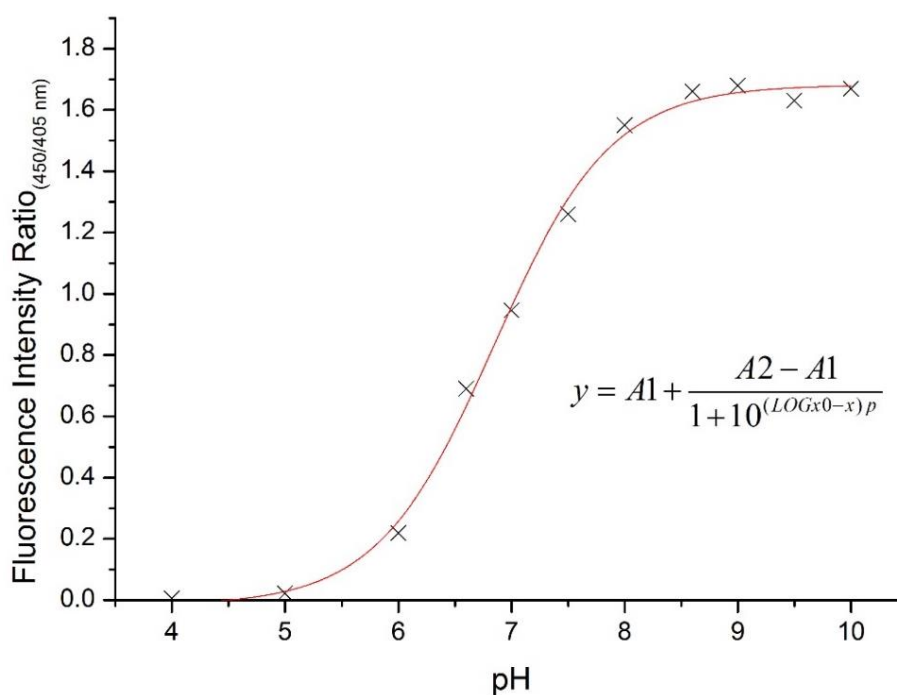
Figure 2.4. Calibration curve of known pH HPTS buffered solutions (Fluorometer).

2.3.2 Urea-Urease Reaction – Bulk Conditions

The intrinsic link between urease activity and pH is widely understood, where changes in pH lead to alterations in the protein binding site conformation, resulting in the bell-shaped rate-pH curve that is an indicative characteristic of feedback [177]. As such, the urease-catalysed conversion of urea to a weak base has been shown to have a maximum rate when at pH 7 [30], meaning that if the starting pH is lowered, through the addition of acid, then the reaction rate accelerates as the reaction progresses. The literature tells us, that when conducted in bulk conditions, the reaction is stable at acidic pH, before rapidly changing to basic pH. As previously mentioned, adjustment of these initial reaction conditions, i.e., urea concentration, urease concentration, and acid concentration, have an effect on clock time and reaction rate, where, increasing urea and urease concentrations leads to a decreased clock time and higher final pH, and increasing acid concentration leads to an increased clock time, but has little effect on the pH maxima [177].

The kinetics of this reaction in bulk conditions are well-studied, and modelled accordingly, however, the use of a ratiometric pH probe (HPTS) in these circumstances is less known. By retesting the system, using HPTS as a pH indicator, this not only allows us to confirm what is reported in the literature, but, it also allows us to: 1) test the usefulness of HPTS within this system, 2) confirm that HPTS plays no interference with pH switching, and; 3) provides a model standard for comparisons with reaction kinetics under confined conditions.

For a urea–urease clock reaction, whereby the initial pH is adjusted by different concentrations of sulphuric acid (0.24 mM, 0.27 mM, 0.30 mM), the clock time is shown to increase in relation to an increase in sulphuric acid (approximately 20 s, 160 s, and 320 s, respectively) (Figure 2.5). The reaction is eventually seen reaching a self-buffering state at a high pH because of the formation of the ammonia-ammonium buffer, however, previous literature [174] dictates that there is a trend between an increased starting acid concentration, and increased width of transition, which can be seen in Figure 2.5, as well as a decrease in final pH, which can also be seen here (Figure 2.6), albeit in one example.
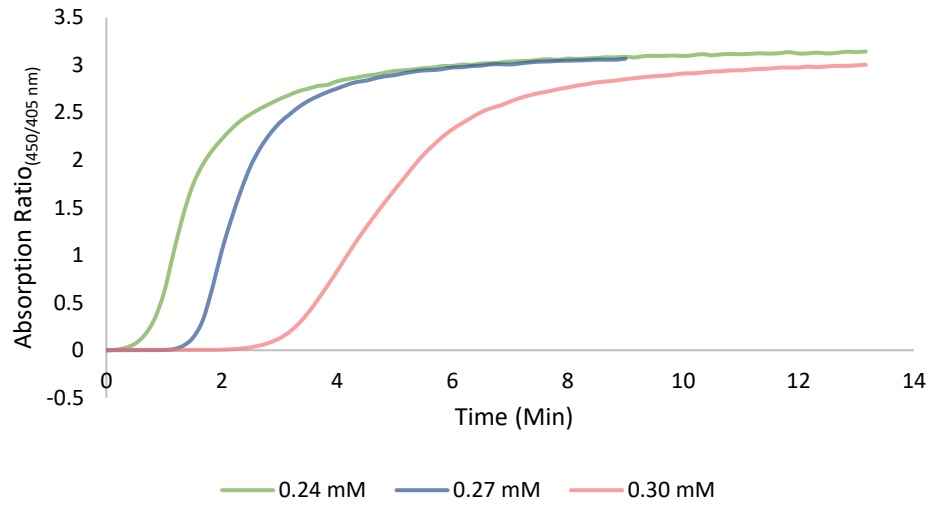
Figure 2.5. Change in HPTS absorption ratio (indicative of pH) when urea (5 mM) is added to bulk urease (6.8 U/mL) and HPTS (50 µM), where the initial pH had been adjusted through addition of H_2SO_4 (0.24 mM, 0.27 mM, 0.30 mM)

Figure 2.6. Final pH of bulk urea-urease reaction, when urease concentration (6.8 U/mL) and urea concentration (5 mM) are held consistent, and initial H_2SO_4 concentration is increased (0.24 mM, 0.27 mM, 0.30 mM)

69

2.3.3 Acid Stability of Liposomes

The nature of the urea-urease reaction means that the liposomes in question may be subjected to relatively strong acidic (pH 3/pH 4) and basic conditions (pH 9/pH 10). Although previous research is indicative of liposomal stability between the ranges of pH 2-9 [178], in our proposed experiments, where the internal pH of a urease-containing liposome will be lowered through the incorporation of H_2SO_4, it is important to ensure the stability of these particular liposomes.

2.3.4 Carboxyfluorescein-Release Experiment

The encapsulation of carboxyfluorescein, a fluorescent dye with pH-dependant solubility around pH 7, and subsequent rupture with a detergent, often Triton X-100, has become a standard technique for testing the mechanical integrity of liposomes. In general, Triton X-100 can be used to determine the rate of leakage displayed by water-soluble substances within a liposome [179]. However, such experimental validity is dependent on two assumptions: 1) encapsulated carboxyfluorescein is self-quenched, meaning that upon release/leakage into the external environment, it is no longer self-quenched, and fluorescence occurs, and; 2) upon addition of Triton X-100, all of the encapsulated carboxyfluorescein is released, and fully dispersed into the external medium. The validity of this technique, in non-buffered solutions, was tested [179].

In typical release studies, when a sufficient volume of Triton X-100 is added to cause all encapsulated carboxyfluorescein to be released, an increase in fluorescent intensity maxima at 517 nm would occur. However, in our scenario (Figure 2.7), the fluorescence spectra has shifted along the x-axis. In the most likely scenario, the reduced pH of deionised water (approximately pH 5.5) caused through dissolution of free CO_2 in the atmosphere, coupled with the pH-dependent solubility of carboxyfluorescein, means that detergent-induced release is causing the carboxyfluorescein to come out of solution. Testing liposome stability to acid using a fluorescent probe with poor solubility at acidic pH makes this approach nonviable.
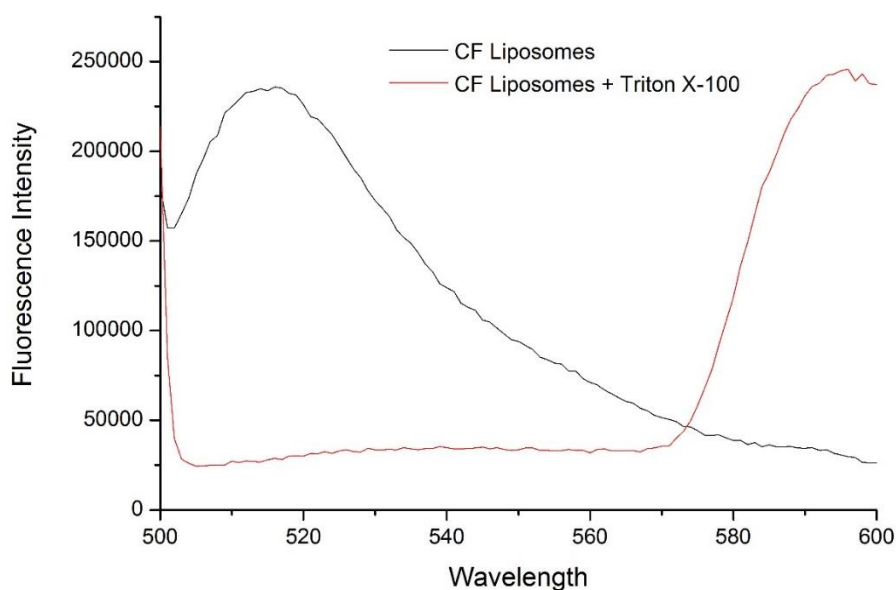
Figure 2.7. Monitoring changes in fluorescence intensity maxima (517 nm) (excitation at 497 nm) when DPhPC + Rh-DOPE liposomes (100 nm) encapsulating self-quenched carboxyfluorescein (125 mM) are completely ruptured with Triton X-100 (50 µL, 10% v/v)

2.3.5 HPTS-Release Experiment

A second approach, using HPTS in place of carboxyfluorescein, was explored to determine the mechanical integrity of liposomes when exposed to acidic environments. As previously mentioned, HPTS is ratiometric, absorbing at 405 nm and 450 nm, and emitting at 511 nm. Therefore, as pH decreases, fluorescence intensity at 511 nm increases when excited at 405 nm and decreases when excited at 450 nm.

In this experiment, HPTS at pH 9.5 was encapsulated, and the external environment was left as deionised water (pH 5.5). The idea was, that if acid-based disruption of membrane integrity occurred, then the HPTS would be diluted into the lower pH external environment, and the fluorescence intensity maxima (excited at 405 nm) would increase. In first instance (Figure 2.8), we can see a trend that suits this hypothesis. In comparison to the baseline (no acid), increasing the concentration of H_2SO_4 is shown to increase fluorescence intensity maxima at 511 nm, and complete rupture (Triton X-100) is shown to cause an expected sharp increase in fluorescence intensity.

However, follow up experiments (see later in Section 3.3.2.1), which determine the rate of proton permeation across the membrane, make it less clear. In these experiments, it was found that through the exchange of ions between the vesicle lumen and the external environment, the internal and external pH would drift towards a state of equilibrium. Given the time taken to prepare and characterise the liposomes, and cross-referencing this time with the time taken to move towards equilibrium, it is likely that before any addition of acid, we are already in this regime.

So, when acid is then added to the external environment to test the mechanical stability of the liposomes, a new proton gradient is introduced, again, with the net flow of protons being directed into the vesicle, and an inevitable decrease in internal pH occurring. As such, the increase in fluorescence intensity witnessed when the concentration of H_2SO_4 is increased, could actually be attributed to the pH of the internal environment becoming lower, not through vesicle leakage/bursting.

Similarly, if we assume that the addition of 0.05 mM H_2SO_4 has, in fact, caused partial release of HPTS, we cannot be certain that addition of further acid is actually causing more release, or the fluorescence intensity increase is the result of the released, now external HPTS pH being decreased further. The reasons outlined make it difficult to ensure the validity of the data, and, in truth, the contributing variables, when trying to use spectroscopy techniques to determine acid stability of liposomes in non-buffered conditions.

However, as we will see when we investigate post-generative stability in Section 3.2.5, given the time taken to produce, purify, and quantify phosphorus concentration, we can safely assume that the vesicles are capable of maintaining their pH gradient over long periods of time in these low pH environments.
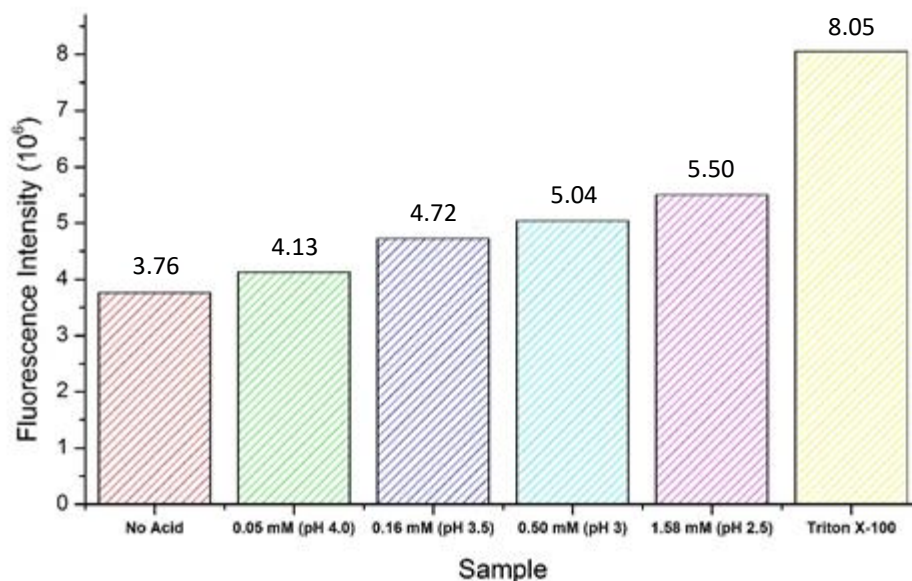
Figure 2.8. Fluorescence intensity change (511 nm) when increasing H_2SO_4 concentrations (0.05, 0.16, 0.50, and 1.58 mM) are added to HPTS-encapsulating (50 mM, pH 9.5) DPhPC liposomes (400 nm). No acid, and addition of Triton X-100 (50 μL, 10% v/v), were controls.

2.3.6 Urease Stability

When it comes to considerations of encapsulation, many of the existing protocols that yield a high encapsulation efficiency, use organic solvents or detergents, and are therefore designed for molecules with considerable chemical stability. However, the delicate nature of biological macromolecules, such as enzymes, means that care is needed in the experimental protocol. As a result, the thin film rehydration method is the most suitable approach for encapsulating enzymes, but, encapsulation efficiency is low. It has been shown that subjecting a rehydrated lipid sample to freeze-thaw cycling, not only breaks down multilamellar vesicles into unilamellar vesicles, but, the encapsulation of large macromolecules primarily occurs during this step – thought to be the result of membrane-formed ice crystals leaving pores for encapsulant entry. However, with each freeze-thaw cycle, there is a likelihood of protein denaturation, and therefore a balance must be struck between encapsulation efficiency and enzyme deactivation. Colletier et al. 2002, reported that the optimum number of cycles to achieve this balance is ten [180]. To confirm this, two identical bulk urease solutions, one left as is, and the other subjected to 10x freeze-thaw cycles, were observed following the addition of urea. It can be seen in Figure 2.9, that in comparison to pH switching in bulk conditions (control), there is little or no difference following exposure to freeze-thaw cycling, and as a result, in the experiments involving enzyme encapsulation, the number of freeze-thaw cycles was fixed to ten.
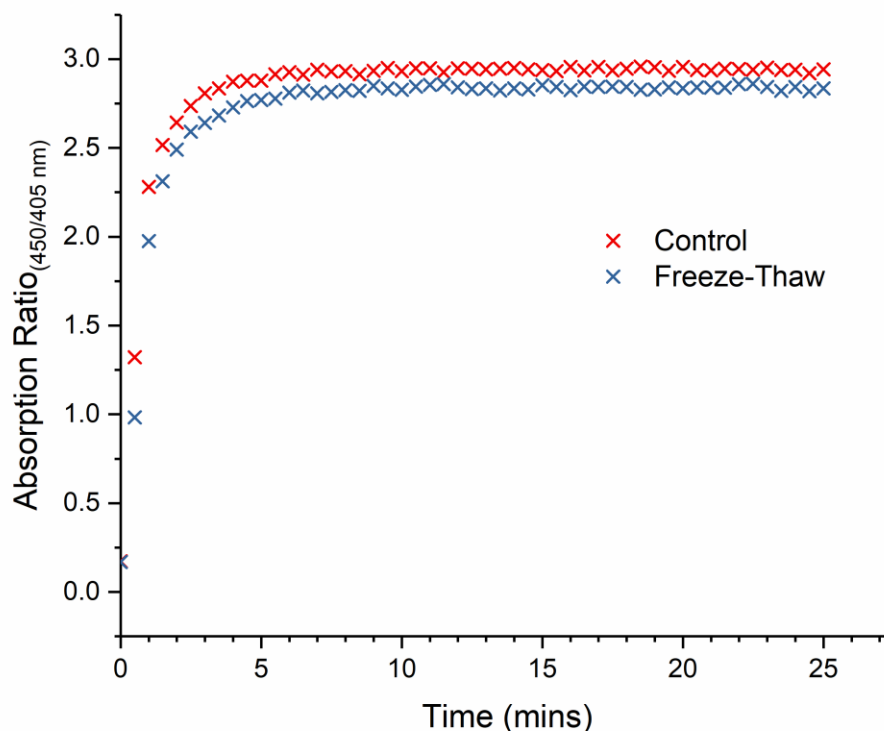
Figure 2.9. pH switching, as shown by change in HPTS (50 µM) absorption ratio (450/405 nm), for bulk urease (1 µM) and bulk urease (1 µM) that has undergone ten freeze-thaw cycles, both suspended in dilute HCl (0.2 mM)

2.3.7 Purification

Owing to the quantitative nature of the data in question, questions may be asked about the location of pH switching, i.e., inside or outside the vesicle. One factor, which may contribute to this uncertainty, is inefficient purification, i.e., inability to successfully remove all external urease from the sample. After failing with a high molecular weight size-exclusion media (Sephacryl S-1000, fractionation range: $M_r = 10^5 - 10^8$), it was hypothesised that using online bioinformatics resources, .e.g., "PeptideCutter" [181] may help. "PeptideCutter" is capable of predicting protease cleavage sites and reporting the subsequent chain lengths of the peptide fragments. Incubation with a protease eliciting high activity at low pH, e.g., pepsin, would break the urease down the urease into fragments capable of being separated from the vesicles using a column gravity-packed with Sephadex G-50 media. As a result, samples were either subjected to 2 hours incubation with pepsin, and then ran down a Sephadex G-50 column, or vice versa, and no pH switching was shown (Figure 2.10).

However, when testing the efficiency of pepsin incubation on its own (Figure 2.10), simulating a biological macroenviroment where free proteases can readily diffuse around the external environment of the vesicle, pH switching was shown to occur upon addition of urea, concluding an inefficiency of pepsin in urease deactivation. In contrast, when testing the efficiency of size exclusion chromatography-only at removing external urease (Figure 2.10), we see in similarly to both iterations of size-exclusion chromatography and pepsin incubation, that no pH switching occurs in response to catalytic activation. This concludes that size-exclusion chromatography is the sole contributor to vesicle purification. Strangely, both the vesicles and the urease were outside the limit of the Sephadex G-50 column, however, this separation may be attributed to the relative size differences between the two entities.
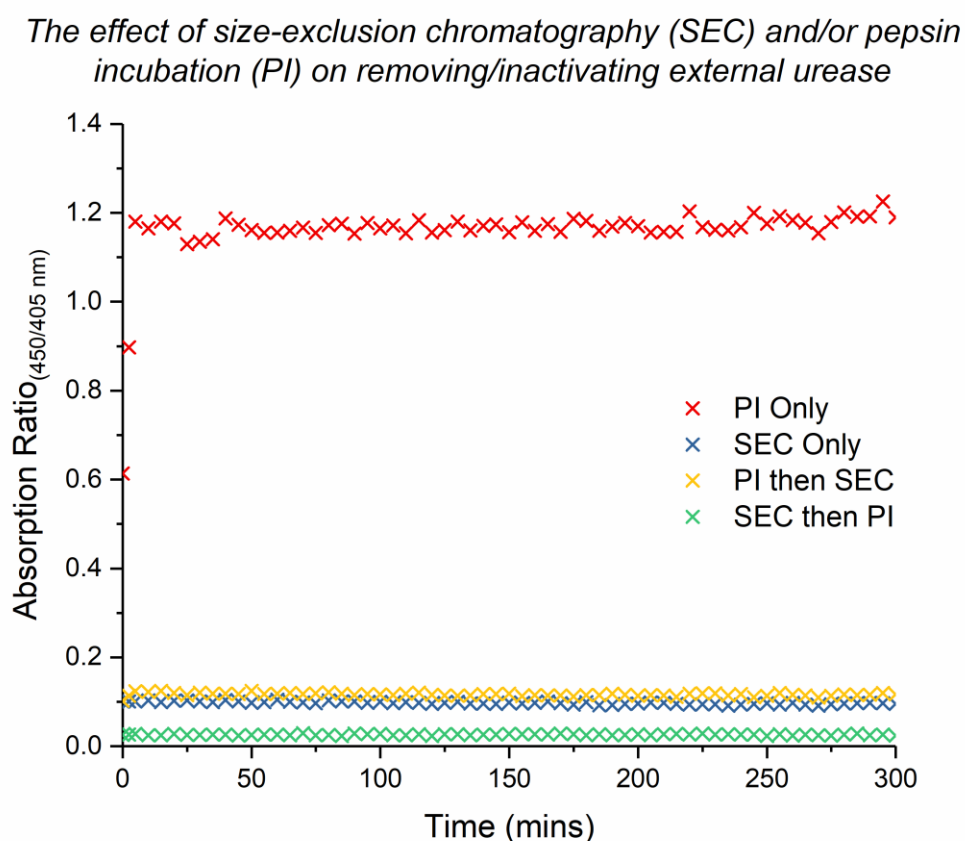
Figure 2.10. Efficiency of size-exclusion chromatography (Sephadex G50) and pepsin (0.55 µM) incubation at purifying DPhPC vesicles from unwanted external urease (11.1 µM) (external environment and mobile phase; dilute HCl (0.2 mM).

2.4 Summary

To summarise, the first aim of pre-loading optimisation was to find a probe capable of monitoring pH-switching from within the vesicle lumen. To satisfy our requirements, the probe had to display characteristics of membrane impermeance, be ratiometric in nature, and work within the desired pH-switching range of the urea-urease reaction, which was found in HPTS. Once identified, we calibrated our pH probe for both fluorescence and absorption spectroscopies, which was consistent with previous literature [182], and successfully investigated its usefulness for tracking pH-switching in our model reaction.

Following on, we tested the robustness of our experimental constituents to the conditions presented in vesicle generation, i.e., low pH and freeze-thaw cycling. We found that, for a 10-fold iteration of freeze-thawing, urease activity is affected very minimally, and for the reported increase in encapsulation efficiency, the cycle number was set at ten. Similarly, we investigated vesicle stability at low pH, however, experimental restrictions made the effect of increased acid concentration, at first instance, difficult to untangle. Despite this initial concern, as we will see in Section 3.2.5, we can be confident in our vesicle's ability to maintain their integrity at large pH gradients, which is also consistent with what is reported in the literature [178].

Finally, and crucially, for urease-confinement to be investigated and understood, an efficient way of removing unwanted, external urease must be found. In our methods, firstly (although not described) we investigated the use of a gel-filtration medium with a molecular cut off range capable of removing urease, however, difficulty with gravity packing disrupted the viability of this technique. Secondly, the use of a protease to either completely inactivate the enzyme, or cleave it into fragments small enough to be purified by gravity-packed Sephadex G-50, was investigated. Unfortunately, the use of pepsin only partially reduced the activity of urease, and, owing to the low pH that we were operating at, a second protease, with a different cleavage behaviour, could not be co-utilised. It was found, however, that a standard, gravity-packed column containing Sephadex G-50 was capable of successfully separating external urease from our vesicle sample, even though urease was above the recommended molecular cut-off weight (~30 kDa), and as such, this technique was used for all further purification.

CHAPTER THREE – OPTIMISATION OF SYSTEM (POST-UREASE CONFINEMENT)

3.1 Introduction

Once an efficient means of tracking pH switching inside vesicles and the potential caveats of adapting thin-film rehydration to suit enzymatic encapsulation had been overcome, i.e., stability of membranes in dilute acid, stability of enzyme to freeze-thawing, and a reliable technique of removing such a large protein from the external environment, we can look encapsulate the urea-urease reaction, and optimise the reaction conditions to build a robust platform for further exploration.

Through our initial failings to obtain a definable pH clock, we begin the consider the effect of membrane permeability, investigating the movement of H^+/OH^- across our vesicle membrane, and taking from literature where appropriate other species permeability coefficients, to build a holistic understanding of the dynamics of our confined system.

In addition, this chapter seeks to optimise the concentration of vesicles needed to obtain a measurable and repeatable reaction profile, especially when scattering and turbidity are present. From this, we build a picture of how vesicle size effects scattering, and look to revisit our HPTS calibration, but this time, in the presence of varying sized vesicles (100, 200, 400 nm), thus allowing us to more accurately define and compare our pH change across varying parameters.

Finally, owing to the unanswered acid stability questions in Chapter Two, we look to confirm the locality of our reaction. To do this, we will compare two sets of identical vesicles, one having been pre-ruptured with detergent prior to enzymatic activation with urea, and one being left as is, whilst asking the question; is the reaction profile we are seeing a result of confinement, or are we simply seeing the disintegration of our vesicle, and bulk-reaction phenomena?

3.2   Experimental

3.2.1   Initial Loading

Urease (12.5 µM) and HPTS (50 µM), suspended in varying concentrations of dilute H_2SO_4 (0.05 mM, 0.16 mM, and 0.50 mM) were subsequently encapsulated in 400 nm DPhPC + Rh-DOPE (0.5 mol%) liposomes, produced via the aforementioned "thin film rehydration" technique (Section 2.2.2). They were purified via size-exclusion chromatography using the corresponding solution of dilute H_2SO_4 used to suspend the urease and HPTS. A Cary 100 Ultraviolet-visible spectrometer was used to monitor changes in the HPTS absorption ratio (450/405 nm), over time, following the addition of urea (5 mM)

3.2.2   Membrane Transport

3.2.2.1 H^+/OH^- Transport

DPhPC and Rh-DOPE (0.5 mol%) vesicles (400 nm), encapsulating HPTS (50 mM) in HEPES (40 mM) and NaCl (20 mM) buffer (pH 7.5), were prepared via thin film rehydration. The mobile phase of size-exclusion was the same buffer used to prepare the vesicles. To initiate the experiment, 3 µL of 1 M NaOH was added to the external environment (1 mL), causing a 0.5 pH unit shift in the buffering point. A Cary 100 ultraviolet-visible spectrometer was used to monitor changes in the HPTS absorption ratio (450/405 nm) over time, and the rate of H^+/OH^- transport across the membrane was extracted.

3.2.2.2   Electrochemical Equilibrium

The same experimental protocol was used as above in the pH-transport experiment (Section 3.3.2.1), however, Triton X-100 (10% v/v) was used to rupture the membrane, once the experiment was complete (equilibrium was reached). A final post-ruptured reading of the absorption ratio (450/405 nm) was taken.

3.2.3   Vesicle Concentration

Urease (10 µM) and HPTS (20 mM), suspended in dilute H_2SO_4 (0.16 mM), was subsequently encapsulated in 400, 200, and 100 nm DPhPC + Rh-DOPE liposomes via "thin film rehydration" (Section 2.2.2). They were purified via size-exclusion chromatography using the corresponding solution of dilute H_2SO_4 used to suspend the urease and HPTS. A phosphorus assay (Section 3.2.3.1) was used to determine the total phosphorus content of the sample, which, in turn, was diluted to 200 and 500 µM. A Cary 100 Ultraviolet-visible spectrometer was used to monitor changes in the HPTS absorption ratio (450/405 nm), over time, when urea (10 mM) and the six

samples (100, 200, 400 nm at a total phosphorus content of 200 and 500 µM) are mixed in equal volumes (250 µL + 250 µL).

3.2.3.1   *Phosphorus Assay*

Stock solutions of H_2SO_4 (8.9 N), ascorbic acid (10% w/v), and ammonium molybdate(VI) tetrahydrate (2.5 % w/v) were made.

Six "standards", which included one "blank" were made by adding the following quantities of phosphorus standard (0.65 mM Phosphorus) into 6 borosilicate test tubes: 0 µmoles (0 µl) blank, 0.0325 µmoles (50 µl), 0.065 µmoles (100 µl), 0.114 µmoles (175 µl), 0.163 µmoles (250 µl), and 0.228 µmoles (350 µl). Sample tubes were made by adding 50 µl of the liposome solution to each test tube (in triplicate, where possible).

To each of the test tubes, 450 µl of H_2SO_4 (8.9 N) was added, and all tubes were heated in an aluminium block at 210°C for 25 minutes. The tubes were then removed from the block, allowed to cool for 5 minutes, before addition of 150 µl of H_2O_2, and placed back in the heating block for a further 30 minutes at 210°C. The tubes were then removed and allowed to cool, before addition of 3.9 mL deionised water, 500 µl of our ammonium molybdate(VI) tetrahydrate stock solution, and 500 µl of our ascorbic acid stock solution. Once complete, each tube was vortexed, and capped with parafilm, before being returned to the heating block for 7 minutes at 100°C.

Once finished, the tubes were removed, cooled, and their contents were transferred to cuvettes. The absorbance of each standard was measured at 820 nm, using a Cary 100 Ultraviolet-visible spectrometer, and a calibration curve was generated. The absorbance of each sample was also measured at 820 nm, and read against the calibration curve to determine the concentration of phosphorus in the sample.

3.2.4   HPTS Calibration (Vesicles Present)

Deionised water-encapsulating DPhPC + Rh-DOPE (0.5 mol%) liposomes (400, 200, 100 nm) were produced via "thin film rehydration" (Section 2.2.2), and a phosphorus assay (Section 3.2.3.1) was used to determine the total phosphorus content of the sample.

As in previous HPTS calibration, a phosphate-citrate buffer (pH 2.2 – 8.0) and a glycine-NaOH buffer (pH 8.6 – 10.6), were used to cover the switching range of HPTS (pH 4-10). The absorbance of each buffered solution (pH 4.0, 5.0, 6.0, 6.6, 7.0, 7.5, 8.0, 8.6, 9.0, 9.5, and 10.0), containing HPTS (50 µM) and deionised water-encapsulating liposomes (400, 200, 100 nm) at a phosphorus

content of 250 μM, was read using a Cary 100 Ultraviolet-visible spectrometer. A calibration curve for HPTS, plotting absorption ratio (450/405 nm) against pH, was created.

3.2.5 Fitting Procedure

From our experimental data, firstly, manual "zero-filling" was performed, introducing negative "dummy" values equating to y at t_0 at 5 minute increments to t_{-25}. Using Origin Pro 2017, the data representing "Absorption Ratio$_{450/405 \text{ nm}}$" versus "Time (mins)" was fitted using the "Hill1" fitting model. From this fit, the final absorption ratio (End), the clock time (k), and an indicator of transition width (n) could be extracted. Finally, using the respective calibration curve from Section 3.2.4, the final absorption ratio value was converted into a final pH value.

3.2.6 Post-Generation Stability

"Thin film rehydration" (Section 2.2.2) was used to encapsulate urease (10 μM) and HPTS (20 mM) inside 200 nm DPhPC + Rh-DOPE (0.5 mol%) liposomes, which were purified via size-exclusion chromatography using the corresponding solution used to suspend the urease and HPTS. A phosphorus assay (Section 3.2.3.1) was then used to determine the total phosphorus content of the sample, which, in turn, was diluted to 2 x 500 μM samples. One sample was left "intact", whilst the other was "ruptured" using Triton X-100 (10% v/v). 250 μL of each sample was placed in a 550 μL micro-cuvette, and a Cary 100 Ultraviolet-visible spectrometer was used to monitor changes in HPTS absorption ratio (450/405 nm), over time, when 250 μL urea stock (100 mM) is added (final urea concentration; 50 mM).

3.3 Results and Discussion

3.3.1 Initial Loading

Data obtained from the initial experimental setup (Section 3.2.1), where urease and HPTS suspended in different concentrations of dilute H_2SO_4 (0.05 mM, 0.16 mM, and 0.50 mM) were loaded into lipid vesicles, but the external environment was deionised water, showed a relationship between increased acid concentration decreased final pH (Figure 3.1). However, although a clear relationship can be seen, there is no distinguishable clock time (as witnessed in bulk).
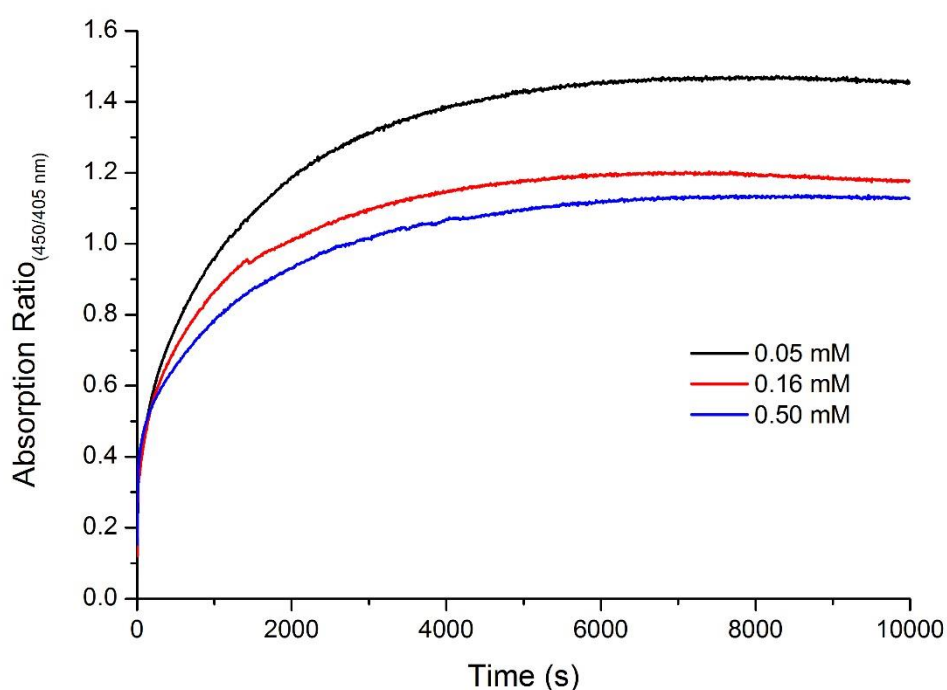
Figure 3.1. Change in absorption ratio, when urea (5 mM) is added to DPhPC + Rh-DOPE liposomes (400 nm), encapsulating urease (12.5 μM), HPTS (50 μM), and a varying initial concentrations of H_2SO_4 (0.05 mM, 0.16 mM, and 0.50 mM)

When trying to better understand why no clock time was witnessed for the above reaction, it could only be assumed that given the strength of the strength of the initial acid concentrations used, in comparison to their bulk counterpart, that the starting pH of the vesicle's lumen had shifted during preparation and purification, and thus, the enzymatic activity of urease was higher than expected – this led us to consider the transport of H^+/OH^- across the vesicle membrane over time.

3.3.2 Membrane Transport

If we consider an empty vesicle (Figure 3.2), where the internal pH is lower than the external pH, it would be sensible to assume, given what we know about ion transport across biological membranes, that there would be a net influx of hydroxyl ions, and a net efflux of protons, along their respective concentration gradients, resulting in an overall increase in internal pH. After all, ion transport across lipid membranes is central to proper cellular functioning, where proton gradients are built, maintained, and dissipated. Of course, such transport of charged species is assumed to be very slow, without the presence of active channels or transporters. In light of this, it would, therefore, not be unrealistic to assume that during the process of production and characterisation, a vesicle with a pH imbalance across its membrane, would move towards a position of equilibrium.
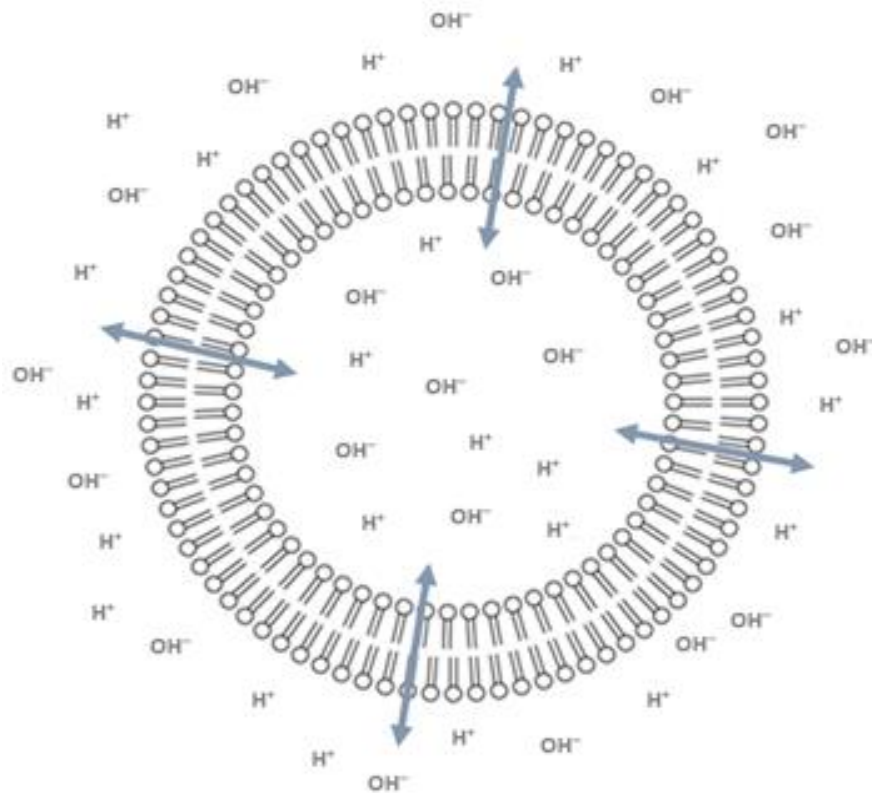
Figure 3.2. H$^+$/OH$^-$ diffusion across a lipid vesicle membrane

3.3.2.1   H⁺/OH⁻ Transport

In this experiment, an increase in pH of the external environment was induced through the addition of NaOH (1 M), creating a pH gradient across the vesicle membrane. As a result, H⁺/OH⁻ will seek to diffuse from respective regions of high relative concentrations, i.e., across the lipid membrane – this can be seen by monitoring the change in absorption ratio (450/405 nm), until a state of equilibrium is achieved (Figure 3.3). A permeability coefficient can then be deduced using a recently reported method [183, 184]. The pK_a of our buffer (7.5) is converted to a K_b value (3.16 x 10⁻⁷), which, in turn, can be used to determine the relative hydroxide and HEPES concentration of the sample throughout the experiment:

$$K_b = \frac{[OH^-] \times [HEPES]}{[HEPES^-]}$$

Equation 3.1. Base dissociation constant for HEPES buffer

The flux of H⁺/OH⁻, J, can then be determined using the equation:

$$J = \frac{[OH^-]_{t=x} + [HEPES^-]_{t=600} - [HEPES^-]_{t=0}}{\Delta t} \times \frac{V}{S}$$

Equation 3.2. Calculating flux of H⁺/OH⁻ across vesicle membrane

Where V is the internal volume and S is the external surface area estimated in line with associated extrusion filter pore size. J uses the amount of OH⁻ ions at t = 0 s or t = 600 s. The net flux of protons and hydroxide ions, $J_{H+/-OH,}$ can be found by subtracting J_{start} from J_{end} To find the permeability constant, P, the net flux, $J_{H+/-OH,}$ is divided by the hydroxide ion concentration gradient (C) formed from the addition of NaOH:

$$P = \frac{J_{end} - J_{start}}{C}$$

Equation 3.3. Permeability coefficient for H⁺/OH⁻ transfer across a membrane

Slow proton leakage with a permeability of 1.1×10^{-10} cm.s⁻¹ was measured for 400 nm DPhPC liposomes, taking approximately 3.5 h to reach equilibrium. As such, in an experimental protocol where sample preparation is long, considerations of proton transport across a membrane hold their own weight. It was therefore important to keep internal and external pH balanced to ensure no movement throughout lengthy sample preparation.
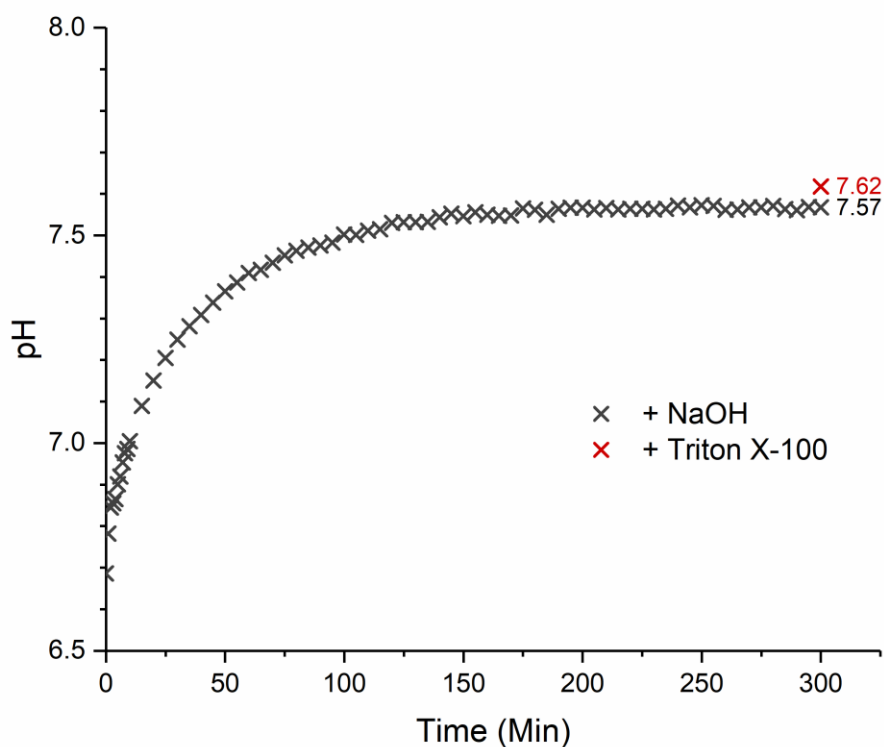
Figure 3.3. Determination of electrical potential across membrane following vesicle rupture after H⁺/OH⁻ equilibria is reached.

3.3.2.2 Electrochemical Equilibrium

However, considerations of pH transport across a membrane does not paint the whole picture, where considerations of electroneutrality are present. As ions move across the vesicle bilayer, along their respective concentration gradients, they may contribute to the build-up of a potential differences across the membrane, and, where such charge separation is present, an electrical gradient will continue to grow in magnitude until it balances exactly with the chemical gradient. Therefore, the rate of exchange between the vesicle lumen and the external environment, i.e., the movement towards chemical equilibrium may not occur if an imbalance of electrical charge is present [185]. By rupturing the membrane with Triton X-100 and seeing a further increase in pH (0.05), it may be assumed that the chemical gradient across the membrane has not quite reached equilibrium, and, in fact, a build-up of electrical potential is preventing further transport. However, given the small increase, and the likely contribution of symport and antiport of M^+/A^-, this does not seem likely (Figure 3.3).

3.3.3 Vesicle Concentration

Of course, to compare two samples of urease-encapsulating vesicles, which may differ by an influencing parameter, i.e., urease concentration, it is imperative to ensure the number of liposomes in each sample is equal. To calculate the total number of liposomes, one must first calculate the number of lipid molecules in a liposome [186]. To do this, we determine the total surface area of the inner and outer monolayers of unilamellar vesicle, where d is the diameter of the liposome, h is the bilayer thickness (~5 nm), and divide that area by the head group of a single lipid molecule (a, ~$0.61 - 0.71$ nm^2) [187]:

$$Area_{outer} = 4\pi \left(\frac{d}{2}\right)^2$$

Equation 3.4. Surface area of outer monolayer

$$Area_{(inner)} = 4\pi \left(\frac{d}{2} - h\right)^2$$

Equation 3.5. Surface area of inner monolayer

$$N_{tot} = \frac{\left[4\pi \left(\frac{d}{2} \right)^2 + 4\pi \left[\frac{d}{2} - h \right]^2 \right]}{a}$$

Equation 3.6. Number of lipid molecules in a unilamellar liposome

On that basis, the total number of lipids that make up a 100, 200, and 400 nm vesicle is 8.09 x 10^4, 3.37 x 10^5, and 1.38 x 10^6 (if a = 0.71 nm^2), respectively. As such, if we know the concentration of lipids (C_{lipid}) in a known volume (V), and the total number of lipids in a single unilamellar vesicle (N_{tot}), then the total number of liposomes (N_{lipo}) can be calculated:

$$N_{lipo} = \frac{C_{lipid} \times V \times N_A}{N_{tot}}$$

Equation 3.7. Determination of liposome number in a sample

So, if we have a 1 mL solution of 100, 200, and 400 nm unilamellar DPhPC (Mr; 818.3) vesicles, at a concentration of 5 mg/mL, the total number of liposomes in each sample would be 4.59 x 10^{13}, 1.09 x 10^{13}, and 2.66 x 10^{12}, respectively.

However, in practicality, it would be naïve to assume that the preparation and purification of two identical samples, would yield exactly the same number of liposomes, due to experimental discrepancies, and, as such, these discrepancies can result in a significant difference with regards to the concentration of active urease within the overall sample. To mitigate against such inter-sample differences, quantitation of lipid concentration can be achieved by calculating the total concentration of phosphorus in the system, where each phospholipid contains a single phosphorus group, by means of a phosphorus assay, and diluting each sample to a standard phosphorus concentration.

However, defining the correct liposome concentration, where considerations of turbidity and scattering are present, was not as simple as first anticipated. When using optical detection methodology, it can be assumed that the two most important parameters are the wavelength (λ) of light, and the refractive index (*n*) of the vesicles (relative to the surrounding medium). Typically, any optical phenomena witnessed is dependent on the relationship between the

wavelength of light and the refractive index, where the larger the difference in refractive index between the particle and its medium, the more light that is scattered [188]. When translated into the practical use, in Ultraviolet-visible spectrometer spectrometry, this means that incident light illuminating a sample of vesicles is partly scattered, and partly absorbed. Determination of scattering through mathematical means has been defined numerous times, i.e., Rayleigh scattering, Fraunhofer diffusion, etc., however, Mie theory, which determines the scattering cross section (σ) of a vesicle, using the diameter, the refractive index of the particle and its medium, and the wavelength of polarised light, can be applied to any relationship between wavelength and particle diameter [189].

To illustrate the relationship between particle size, and associated refractive index, it has been shown that at 488 nm, a single 600 nm polystyrene bead scatters 64,000-fold higher than that of a single 60 nm polystyrene bead. Similarly, when comparing the effect of associated refractive index on scattering, comparisons between similarly sized (300 nm) polystyrene (n = 1.605) and silica (n = 1.445) beads, and a vesicle (n = ~1.42), all in water (n = 1.33), shows a seven-times decrease in scattered light between polystyrene and silica beads, and a four-times decrease between silica beads and vesicles [188].

However, although it is easy to imagine the effects of scattering on a single liposome, in turbid samples, containing millions of vesicles, the summative extend in which light is scattered is more difficult to understand. For instance, if multiple scattering events were to occur, but the final scattering event directed incident light back towards the detector, then that light would be transmitted to the detector. In this instance, a balancing act therefore needs to be found between a sample being dilute enough not to cause associated problems of scattering, but concentrated enough that the encapsulated molecules are efficient at raising the internal pH (urease) and capable of being detected without noise (HPTS).

Cross-comparing 400, 200, and 100 nm vesicles at 100 and 250 µM (Figure 3.4), we can see that the more standard 100 µM vesicle concentration (dashed line), as commonly seen in the literature to reduce turbidity-associated scattering, does not have a clearly-defined switch in pH, the absorption ratio is low (reduced signal), and there is no discernible difference between the three different-sized vesicles. In contrast, increasing the concentration to 250 µM, negates against these concentration-associated problems, giving a clear, and expected difference in reaction profile between the different sized vesicles, and, as a result, 250 µM was chosen as a standard for all future experiments.

Determination of appropriate vesicle concentration (100 µM vs 250 µM)
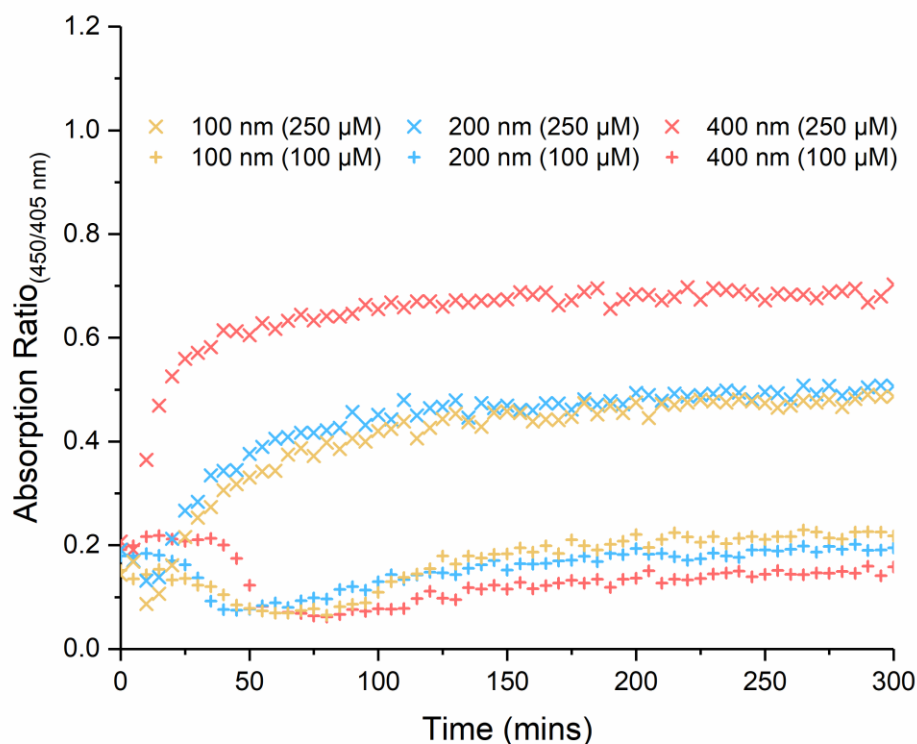
Figure 3.4. Determining optimum concentration (in terms of phosphorus content, 100 vs 250 µM) of urease (10 µM) and HPTS (20 mM)-encapsulating vesicles in dilute HCl (0.2 mM) to ensure efficient switching and characterisation

3.3.4 HPTS Calibration (Vesicles Present)

However, in these circumstances, it is important to understand the effect that turbidity and scattering is having on absorption, and as such, a new HPTS calibration curve, in the presence of vesicles, is needed. As we can see from the data (Figure 3.5), as particle size increases closer to the wavelength of incident light, the amount of scattering also increases, flattening the calibration curve. Through fitting the data at hand (Equation 3.8), where y is the absorption ratio$_{(450/405 \text{ nm})}$, x is the pH, b_{start} and b_{end} is the absorption ratio at the beginning and end, respectively, k is pH at ½ max, and n is the gradient at ½ max, then rearranging the equation, it allows us to directly convert absorption ratio (450/405 nm) into pH for each size vesicle (providing it is within the range of the pH probe).
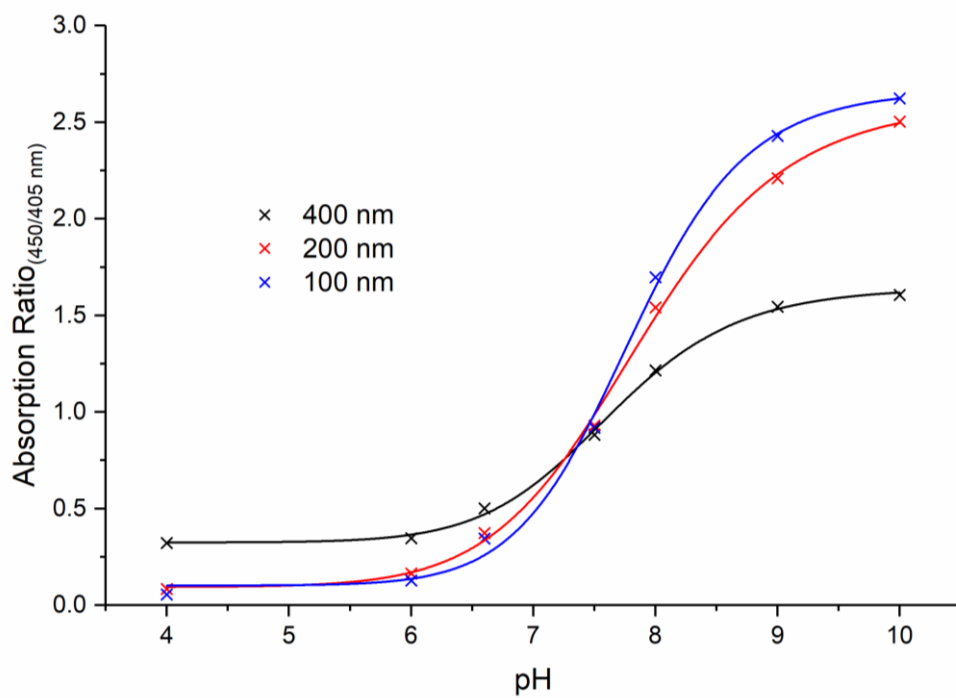
Figure 3.5. Calibration of HPTS, in known pH solutions, when 100, 200, and 400 nm DPhPC vesicles (250 µM phosphorus concentration) are present.

$$y = b_{start} + (b_{end} - b_{start})\frac{x^n}{k^n + x^n}$$

Equation 3.8. Fitting equation (adaptation of "Hill Equation")

$$x = \left(\frac{(y - b_{start})k^n}{b_{end} - y}\right)^{\frac{1}{n}}$$

Equation 3.9. Fitting equation rearranged to make x the subject

Table 3.1. Values extracted from each calibration curve for 100, 200, and 400 nm DPhPC vesicles.

	100 nm	200 nm	400 nm
b_{start}	0.102	0.094	0.325
b_{end}	2.67	2.61	1.64
k	7.80	7.86	7.63
n	16.33	12.85	14.41

To understand how these calibration curves can be used to determine a change in pH, and to ensure the absorption ratio reflects the pH insides the vesicles, the reaction profile for 200 nm vesicles at 250 µM phosphorus concentration from Figure 3.4 (Section 3.3.4) was converted to pH, and plotted (Figure 3.6). From this data, we can confirm that absorption ratio is a representational indicator of pH.

Figure 3.6. Comparison between absorption ratio (450/405 nm) and pH reaction kinetics for 200 nm vesicles (phosphorus concentration; 250 µM) encapsulating urease (10 µM) and HPTS (20 mM) in dilute HCl (0.2 mM), when activated with urea (10 mM).

3.3.5 Fitting Procedure

The fitting equation used above (Equation 3.8) to extract a viable calibration curve can be used to extract kinetic parameters that will allow for comparison between multiple samples. If we consider the kinetic outputs of our reaction profile that we are interested in, i.e., the clock time, the final pH, and the width of transition, we can see from the hypothetical reaction profiles below (X) that our fitting function is capable of extracting these data points with ease. Where k is time at (End-Start)/2, final absorption ratio$_{(450/405 \, nm)}$ (b_{end}), which can be converted to pH using our HPTS calibration curve (Figure 3.5), and n is the slope at k (m_k), which can be used as a relative indicator of transition width:
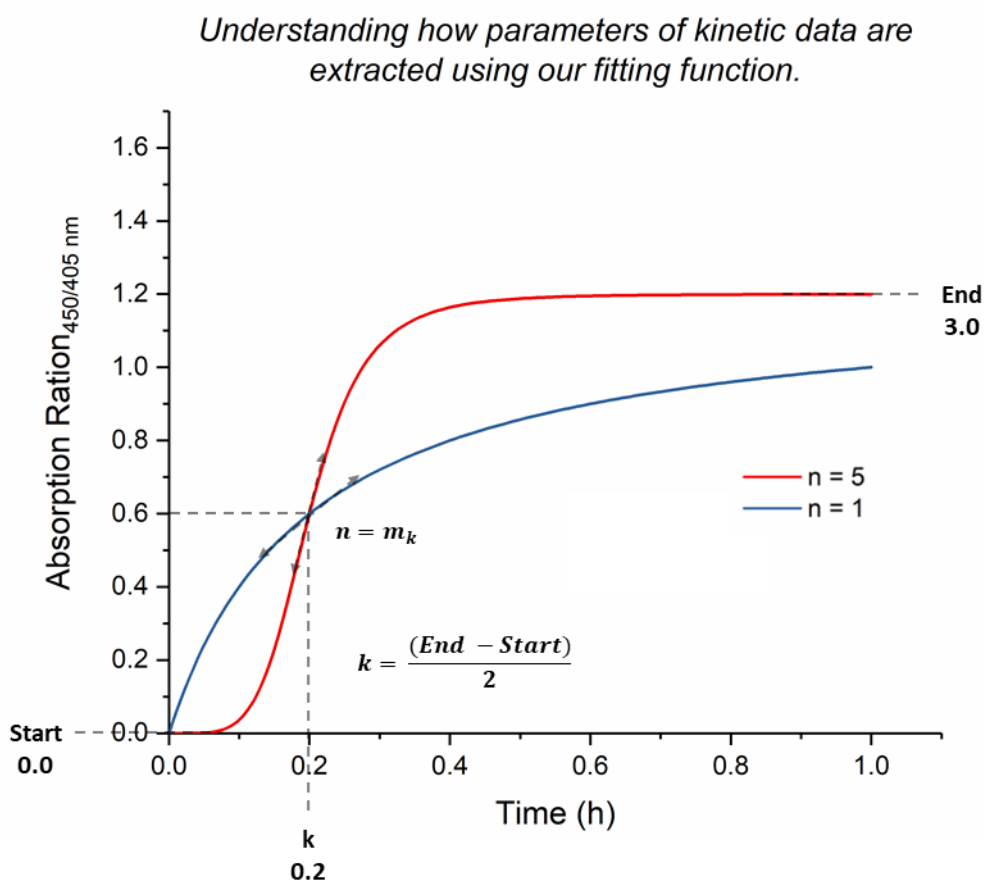
Figure 3.7. Hypothetical fitting scenario showing extractable parameters (clock time (k), final absorption ratio$_{450/405 \, nm}$ (End), and transition width (n)) when k and End remain constant, and n is varied (1 and 5).

To understand how this works on a practical level, the 200 nm vesicles at 250 μM phosphorus concentration from Figure 3.4 (Section 3.3.4) was taken and fitted with our chosen model (Equation 3.8). We can see here than our clock time is 35.1 minutes, our final absorption ratio is 0.499, which when converted to pH is 6.80, and our indicator of transition width is 1.86.
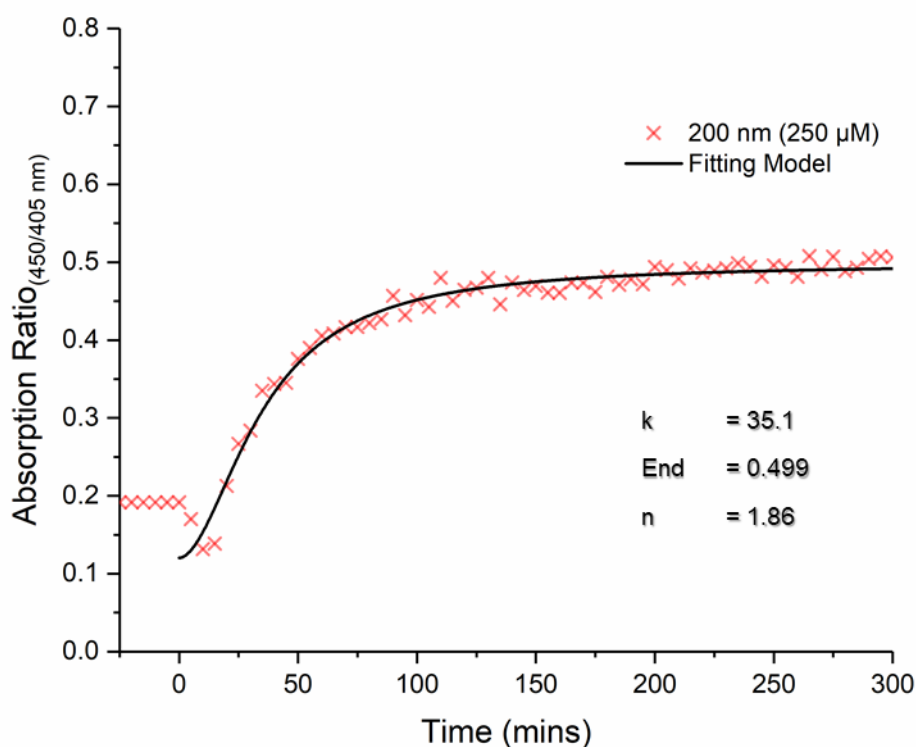
Figure 3.8. Exemplar plot showing fitting model and extractable parameters indicative of clock time (k), final absorption ratio (pH) (End), and transition width (n).

3.3.6   Post-Generation Stability

Lengthy production and purification time, in combination with the time taken to quantify the concentration of phosphorus and ensure samples are uniform, may raise questions regarding the post-generation stability of the vesicles, as well as their ability to house the reaction for an order of hours. As a result, it is natural to question whether the reaction profile we are seeing

is, as a matter of fact, the result of a confinement, or, whether we are seeing vesicular breakdown prior to characterisation, and, as such, witnessing a bulk reaction.

To test this experimentally, a sample of urease- and HPTS-encapsulating 200 nm DPhPC vesicles were produced, and diluted down to two identical samples (250 µM phosphorus concentration). One sample was ruptured using a detergent (Triton X-100), and the other was left untouched, and the absorption ratio was plotted over time, following the addition of urea (50 mM). As we can see (Figure 3.9), in the sample that had been "ruptured" using detergent, it can be assumed that either no pH switching has occurred, or that pH-switching is rapid (and weak), and has therefore not been picked up by the Ultraviolet-visible spectrometer. In both instances, given the comparison to pH-switching in "intact" vesicles, where a distinct reaction profile is shown, and the data in Figure 3.10, where, in bulk, negligible detergent-induced change in absorption, and zero reduction in urease activity, is witnessed, our suggestion that pH-switching is happening inside the lumen of our vesicles is reinforced.
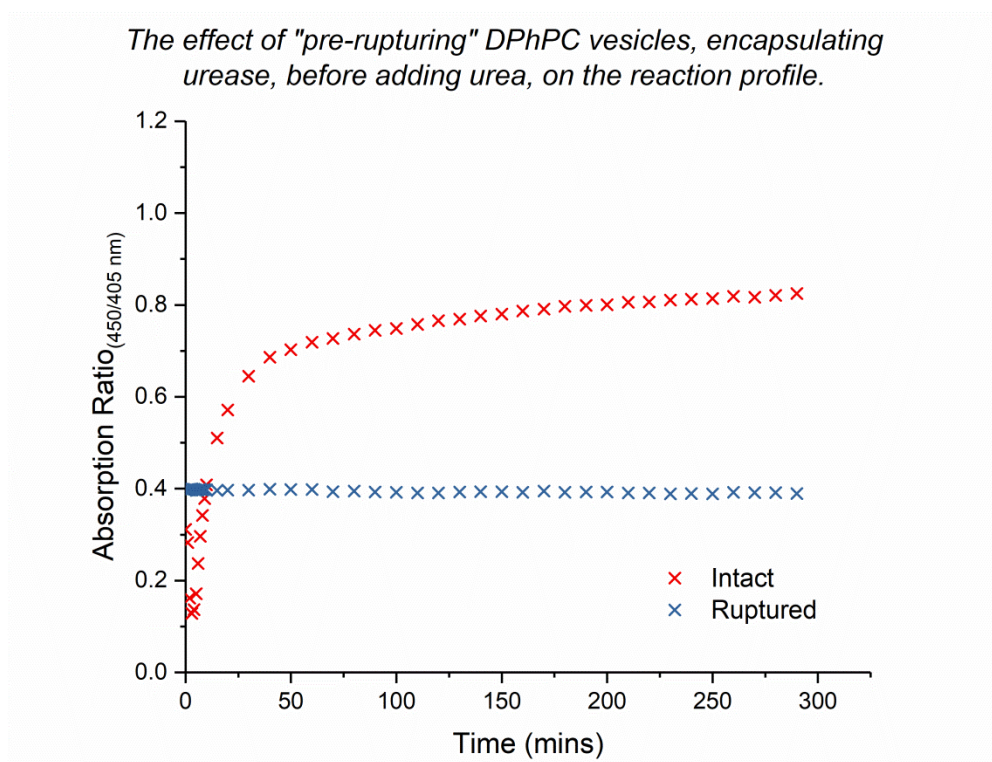
Figure 3.9. DPhPC vesicles (200 nm, 250 µM) encapsulating urease (10 µM) and HPTS (20 mM) where one sample was pre-ruptured using Triton X-100 (10% V/V), before adding urea (50 mM)
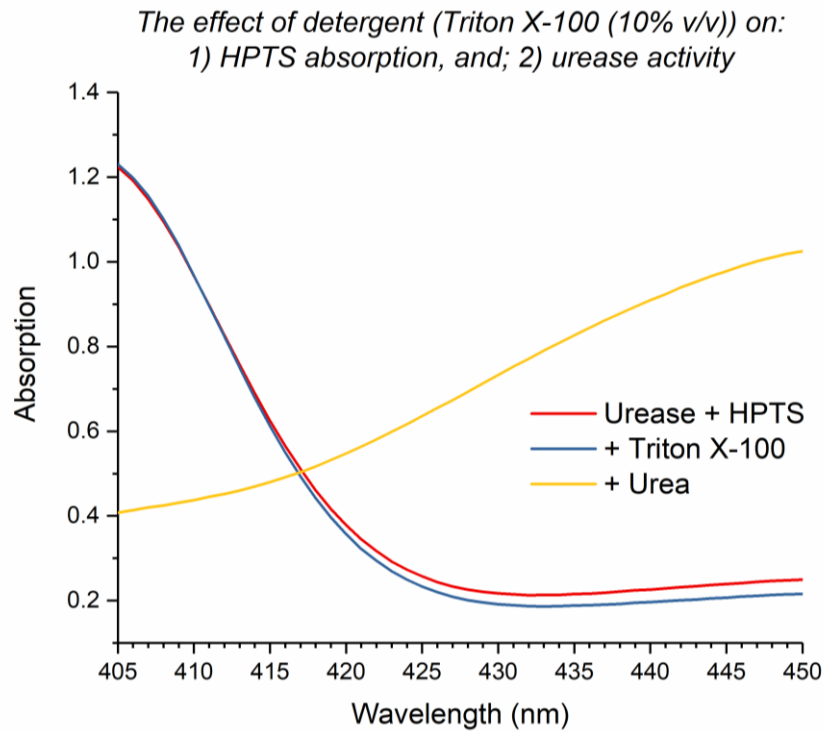
Figure 3.10. Absorption spectra between 450 and 405 nm, showing a) bulk urease (10 µM) and HPTS (50 µM), b) the sequential addition of Triton X-100 (10% v/v), and c) the sequential addition of urea (50 mM).

As well as reinforcing the locality of pH switching within the system, a major clue is unearthed within this data about the importance of confinement. The data shows, in both hypothetical scenarios, that confinement is actually causing pH switching (if we assume that no pH switching has occurred in the "ruptured" sample) or it is enhancing the strength of the switch (if we assume that pH switching is rapid and weak), with regards to the spatial distribution of urease. If we imagine the two samples in their most simple, representational form (Figure 3.11), we can quickly understand the importance of confinement, where, in "intact" vesicles, we see enzyme molecules in close spatial proximity, and, when we use a detergent to rupture the vesicles, the concentration of urease decreases, with respect to the total bulk volume.
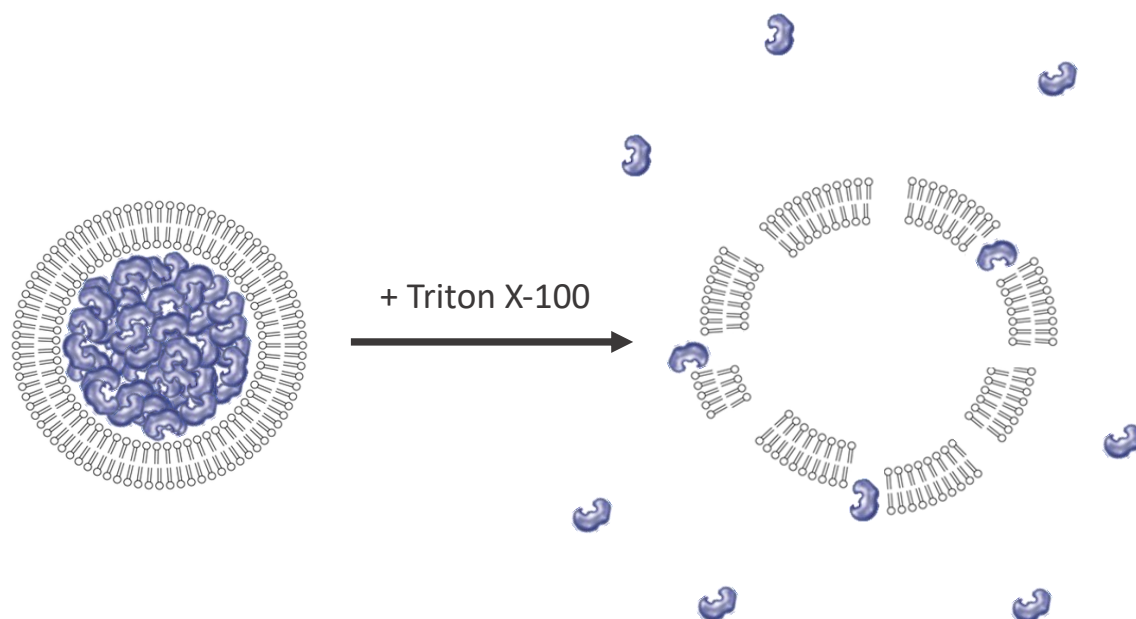
Figure 3.11. Spatial proximity of urease when in confinement and following the addition of a detergent.

3.4   Summary

Throughout this chapter, we have unearthed knowledge crucial to the understanding of our system. Through the comparison of pre-ruptured and intact vesicles, we have provided insight into the importance of confinement, where, owing to the overall concentration of urease present in our sample, localisation, forced through vesicular confinement, is now known to be needed for catalytic activity, where, rupture and subsequent dispersion into the bulk volume, is not sufficient, in terms of spatial distribution, to cause pH-switching. Similarly, through experiments tracking H^+/OH^- transport, a better understanding of cross-membrane chemical dynamics allows us to better design our experimental protocol, being mindful of internal and external pH, and ultimately achieve clock-like pH switching. Finally, we have generated a more robust calibration process, which, takes considerations of scattering and turbidity into account, and, thus, can allow us to more accurately compare reaction profiles across associated parameter space with ease and flexibility.

CHAPTER FOUR – GAINING CONTROL

4.1 Introduction

If nonlinear enzyme kinetics are to be used in the design of a temporally-controlled vesicular drug delivery system, a holistic understanding of how the system works, and how each parameter influences the reaction's kinetics is imperative. In this chapter, through the exploration of inter- and extra-lumen pH tracking, we begin on a path to better understanding how a confined reaction affects its local environment, and how, through the medium of membrane transport, this immediate effect is translated to the wider external environment. From this, we unearth interesting observations on reaction kinetics that are driven by the presence of a membrane not previously seen in bulk and begin to answer questions about how transport of substrates and products progresses over time, as the reaction proceeds.

In bulk conditions, the clock time can be controlled via three primary means, i.e., starting pH, urea concentration, and urease concentration. When we look to confine the reaction, we add additional parameter space to the matrices. Not only do we have considerations of vesicle size, and how that may be intrinsically linked to local urease concentration, but, we also have considerations of membrane composition, and how that may alter diffusion rates of reaction species. Naturally, it is most logical to explore the parameters which can be explored in bulk, i.e., acid concentration, urease concentration, etc., to better understand how the actual process of confinement, effects the reaction profile.

As such, controlling reaction kinetics through the manipulation of pH was investigated. By lowering the starting pH of the reaction, through suspension of urease and HPTS in increasingly concentrated solutions of HCl, we begin to see a pattern forming, correlating to its bulk counterpart, where clock time and transition width increase, and final pH decreases. Then the pH of the internal constituents loaded into their respective vesicles were tested, painting further colour on the internal working of our confined system. Owing to the buffering capabilities of proteins, our experiments show that the internal pH of each vesicle did not correlate to the expected pH, in fact, it was closer to neutral (pH 6.9) and therefore closer to the optimum activity pH for urease. This is an interesting observation, as one would expect instantaneous pH-switching in all cases, the presence of a clock is again indicative of an electrochemical movement towards a state of equilibrium with the lower pH external environment. To complete our comparison with bulk, a comprehensive survey of urea and urease concentration was undertaken, with the latter raising an interesting debate about the importance of protein copy number in a system that appears to be centralised around free diffusion across vesicular membranes.

Continuing with the theme of parameter space exploration, this chapter provides clarity on the impact of confinement-specific influencers such as vesicle size and membrane composition. If we take vesicle size, naturally, one would assume the larger the vesicle, the higher the protein copy number (in tune with Poisson statistics), and therefore, a more robust pH switch. However, similar to what we see in urease concentration, this assumption is not as clear-cut as first identified, adding further weight to the argument of inter-vesicle communication. Likewise, in a system where membrane transport is so important, the interchangeability of membrane composition between different lipids and polymers provides grounds of investigation to confirm our understanding, allowing cross-comparison with known diffusive properties, and again adds to our knowledge of the system in a holistic sense.

Finally, Chapter Four concludes by confirming a self-presented idea that instead of pH-switching being solely influenced by increased encapsulation of urease, we draw on what we know about membrane permeability and pH-switching outside the vesicle lumen to ask, "is the driving force of system-wide pH-switching determined by inter-vesicle communication?". We confirm this indication through the pH-switching of urease-deficient vesicles in the presence of urease-containing vesicles in the same population.

4.2 Experimental

4.2.1 Materials

The lipid, 1,2-diphytanoyl-sn-glycero-3-phosphocholine (DPhPC), 1-palmitoyl-2-oleoyl-sn-glycero-3-phosphocholine (POPC), 1,2-dipalmitoyl-sn-glycero-3-phosphocholine (DPPC), cholesterol, and the fluorescent lipid marker (1,2-dioleoyl-*sn*-glycero-3-phosphoethanolamine-N-(lissamine rhodamine B sulfonyl) (ammonium salt)) (Rhod-DOPE), were purchased from Avanti Polar Lipids Inc. Poly(butadiene)-poly(ethylene oxide) (PBD-PEO 1800 and 3800) were purchased from Polymer Source. The ratiometric pH probe 8-hydroxypyrene-1,3,6-trisulfonic acid trisodium salt (HPTS) and Urease from *Canavalia ensiformis* (Jack Bean) were purchased from Sigma-Aldrich.

4.2.2 Inside vs Outside

To compare how the pH changes inside and outside the vesicle lumen, two species of 200 nm DPhPC + Rh-DOPE (0.5 mol%) liposomes were prepared using "thin film hydration" (as outlined in Section 2.2.2) – the first encapsulating urease (10 µM) and HPTS (20 mM), and the second just encapsulating just 10 µM urease. Each sample was then purified via size-exclusion

chromatography using the corresponding solution used to suspend the urease and HPTS (0.20 mM HCl) as the mobile phase, again, outlined in Section 2.2.2. A phosphorus assay (Section 3.2.3.1) was used to determine the total phosphorus content of each sample. Sample one was diluted in HCl (0.2 mM) to a concentration of 500 μM, and sample two was diluted also diluted to 500 μM, in HCl (0.2 mM), but with 50 μM HPTS in the external environment. 250 μL of each sample was placed in a 550 μL micro-cuvette, and a Cary 100 ultraviolet-visible spectrometer was used to monitor changes in HPTS absorption ratio (450/405 nm), over time, when 250 μL urea (100 mM) was added. Three independent repeats were performed, and error was presented as ± standard deviation (SD).

4.2.3   Starting pH (HCl Concentration)

"Thin film rehydration", where the solutions used to suspend the urease (10 μM) and HPTS (20 mM) are of varying HCl concentration (0.10, 0.20, and 0.32 mM), was used to produce 200 nm DPhPC + Rh-DOPE (0.5 mol%) liposomes, which, in turn, were purified via size-exclusion chromatography, using the solution of dilute HCl used to suspend the urease and HPTS as the mobile phase (Section 2.2.2). A phosphorus assay (Section 3.2.3.1) was then used to determine the total phosphorus content of each sample, which, in turn, were diluted to 500 μM. 250 μL of each sample was placed in a 550 μL micro-cuvette, and a Cary 100 ultraviolet-visible spectrometer was used to monitor changes in HPTS absorption ratio (450/405 nm), over time, when 250 μL urea (100 mM) is added. Three independent repeats were performed, and error was presented as ± standard deviation (SD).

4.2.4   Balancing Internal and External pH

A pH meter was used to produce stock solutions of dilute HCl at pH 4, 5, and 6. Likewise, the sample pH meter was used to match a sample of urease (10 μM) and HPTS (20 mM) in dilute HCl to each corresponding pH (pH 4, 5, and 6). "Thin film rehydration" was used to produce 200 nm DPhPC + Rh-DOPE (0.5 mol%) liposomes, encapsulating each of the urease and HPTS solutions at different pH, which, in turn, were purified via size-exclusion chromatography using the corresponding stock solution of HCl as the mobile phase (Section 2.2.2). A phosphorus assay (Section 3.2.3.1) was used to determine the total phosphorus content of each sample, which, in turn, were diluted to 500 μM. 250 μL of each sample was placed in a 550 μL micro-cuvette, and a Cary 100 ultraviolet-visible spectrometer was used to monitor changes in HPTS absorption ratio (450/405 nm), over time, when 250 μL urea (100 mM) is added.

4.2.5 Urease, Urea, and Size

"Thin film rehydration" was used to produce DPhPC + Rh-DOPE (0.5 mol%) liposomes, of varying size (100, 200, and 400 nm), encapsulating HPTS (20 mM), and varying concentrations of urease (5, 10, and 20 µM), which, in turn, were purified via size-exclusion chromatography using the corresponding solution of dilute HCl (0.2 mM) used to suspend the urease and HPTS as the mobile phase (Section 2.2.2). A phosphorus assay (Section 3.2.3.1) was then used to determine the total phosphorus content of each sample, which, in turn, were diluted to 500 µM. 250 µL of each sample was placed in a 550 µL micro-cuvette, and a Cary 100 ultraviolet-visible spectrometer was used to monitor changes in HPTS absorption ratio (450/405 nm), over time, when 250 µL urea, at different concentrations (20, 100, and 500 mM) is added. Three independent repeats were performed, and error was presented as ± standard deviation (SD).

4.2.6 Membrane Composition

4.2.6.1 Lipids

"Thin film rehydration" was used to produce 200 nm liposomes, of varying membrane compositions (DPhPC, POPC, DPPC, and DPPC:Cholesterol (70:30) (all + Rh-DOPE (0.5 mol%)), encapsulating urease (10 µM) and HPTS (20 mM), which, in turn, were purified via size-exclusion chromatography using the corresponding solution of dilute HCl (0.2 mM) used to suspend the urease and HPTS (Section 2.2.2). A phosphorus assay (Section 3.2.3.1) was then used to determine the total phosphorus content of each sample, which, in turn, were diluted to 500 µM. 250 µL of each sample was placed in a 550 µL micro-cuvette, and a Cary 100 ultraviolet-visible spectrometer was used to monitor changes in HPTS absorption ratio (450/405 nm), over time, when 250 µL urea (100 mM) was added. Three independent repeats were performed, and error was presented as ± standard deviation (SD).

4.2.6.2 Polymers

Stock concentrations of DPhPC, PbD-PEO (1800) and PbD-PEO (3800) (all + Rh-DOPE (0.5 mol%) of 88.6 mM were dried under vacuum, and "thin film rehydration" (Section 2.2.2), was used to produce 200 nm vesicles, of corresponding membrane, encapsulating urease (10 µM) and HPTS (20 mM). These vesicles were purified using size-exclusion chromatography (Section 2.2.2), with the corresponding solution of dilute HCl (0.2 mM), used to suspend the urease and HPTS, as he mobile phase. 250 µL of each sample was placed in a 550 µL micro-cuvette, and a Cary 100 Ultraviolet-visible spectrometer was used to monitor changes in HPTS absorption ratio (450/405

nm), over time, when 250 μL urea (100 mM) was added. Three independent repeats were performed for PbD-PEO (1800), and error was presented as ± standard deviation (SD).

4.2.7 Temperature Control

"Thin film rehydration" was used to produce 200 nm DPhPC + Rh-DOPE (0.5 mol%) liposomes, encapsulating urease (10 μM) and HPTS (20 mM), which, in turn, were purified via size-exclusion chromatography, using the corresponding solution of dilute HCl (0.2 mM) used to suspend the urease and HPTS as the mobile phase (Section 2.2.2). Each sample was then subjected to heat treatment at 90°C for 1, 5, and 10 minutes, in a water bath. A phosphorus assay (Section 3.2.3.1) was then used to determine the total phosphorus content of each sample, which, in turn, were diluted to 500 μM. 250 μL of each sample was placed in a 550 μL micro-cuvette, and a Cary 100 ultraviolet-visible spectrometer was used to monitor changes in HPTS absorption ratio (450/405 nm), over time, when 250 μL urea (100 mM) was added.

4.2.8 Inter-Vesicle Communication

"Thin film rehydration" was used to produce two types of 200 nm DPhPC + Rh-DOPE (0.5 mol%) liposomes. The first type encapsulated urease (10 μM) only, and the second type encapsulated HPTS (20 mM) only. Each species were purified via size-exclusion chromatography, using Sephadex G-50 as the media, and where the corresponding solution of dilute HCl (0.2 mM) used to suspend the urease and HPTS was used as the mobile phase (Section 2.2.2). A phosphorus assay (Section 3.2.3.1) was then used to determine the total phosphorus content of each sample, and as single sample contained 500 μM of each species was produced. 250 μL of this sample was placed in a 550 μL micro-cuvette, and a Cary 100 Ultraviolet-visible spectrometer was used to monitor changes in HPTS absorption ratio (450/405 nm), over time, when 250 μL urea (100 mM) was added. This process was repeated to generate a third 200 nm DPhPC species, containing both urease (10 μM) and HPTS (20 mM), which was used as a control (phosphorus content; 500 μM, HCl; 0.2 mM, urea; 50 mM)

4.3 Results and Discussion

4.3.1 Inside vs Outside

Owing to the complexity of species-permeation between the lumen of the vesicle and the external environment (Section 1.6.2), it is important to understand how such exchange is affecting both internal and external pH. In an experiment where two vesicle samples differ only by the location of HPTS, i.e., inside or outside the vesicle lumen, a better understand of pH change can be obtained. It can be seen from Figure 4.1 that pH-switching in the external environment is instantaneous, i.e., pH begins to switch before a measurement can be registered by the equipment. If we compare bulk and confined conditions, with regards to the final pH (Figure 4.2) in which the reaction tends to, it may be expected that, since there is excess urea in the system, the urea-urease reaction should continue to proceed until a similar pH to that of bulk is achieved. However, the fact that the pH maxima tends toward a lower pH value than that of bulk, and that of the external environment, indicates that something within the system is having a repressive effect on the internal pH. Another interesting observation from the data is the initial drop in absorption ratio (450/405 nm) inside the vesicle (Figure 4.1), which corresponds to the sharp increase in absorption ratio (450/405 nm) outside the vesicle.

To aid our understanding, and to complement such experimental outcomes, the system was modelled by a collaborator, Dr Annette Taylor. The model, which considers the rate of enzyme catalysis (Equation 1.4), the associated equilibria that governs the internal and external pH (Table 4.1), and the net rate of species transfer across the membrane relative to the concentration gradient (Table 1.4), was used to simulate reaction kinetics.

Table 4.1. Rate constants (25°C) for reactions governing internal and external pH of confined urea-urease reaction, from [190, 191]. Note: acid included as H^+ rather than H_3O^+. Desorption of CO_2 or NH_3 (gas) from surrounding solution and H_2CO_3 (forms CO_2) are not included.

Reaction Equilibria	pK_a	Rate Equation	k_1 (s^{-1})	k_{-1} $(M^{-1} s^{-1})$
$NH_4^+ \rightleftharpoons NH_3 + H^+$	9.25	$k[NH_4^+] - k_r[NH_3][H^+]$	24	4.3×10^{10}
$CO_2 + H_2O \rightleftharpoons H^+ + HCO_3^-$	6.35	$k[CO_2] - k_r[HCO_3^-][H^+]$	3.7×10^{-2}	7.9×10^4
$HCO_3^- \rightleftharpoons H^+ + CO_3^{2-}$	10.25	$k[HCO_3^-] - k_r[CO_3^{2-}][H^+]$	2.8	5×10^{10}
$H_2O \rightleftharpoons H^+ + OH^-$	14	$k[H_2O] - k_r[OH^-][H^+]$	1×10^{-3}	1×10^{11}
$HPTS \cdot OH \rightleftharpoons HPTS \cdot O^- + H^+$	7.3	$k[HPTS \cdot OH] - k_r[OH^-][H^+]$	1	2.5×10^7

Although not shown in our experimental outcome, due to equipment restrictions, an instantaneous spike in pH is shown in the model – due to the very fast (k = 10^{10} mol L^{-1} s^{-1}) reaction rate between ammonia and acid. Where we see the absorption ratio (450/405 nm) decreasing, this is also mirrored in the simulation, and is owing to the rate of urea permeation towards the vesicle lumen being slower than the rate of ammonia transport out of the vesicle, until the internal concentration of urea has increased enough to reverse such a misbalance. Finally, the model shows that the internal pH does not reach the same pH as the external environment, because of an internal buffering effect caused by HPTS – when removed, the internal and external pH are similar.

This creates a novel scenario whereby the vesicle membrane is actually protecting the internal conditions from the very change in which it is eliciting outside the vesicle. So, with regards to enzyme kinetics, we have a situation where system self-induced lowering of pH, or sustaining the pH at a low value, maintains the enzymatic activity of urease below its optimum pH (pH 7) for longer, thereby increasing the clock time.
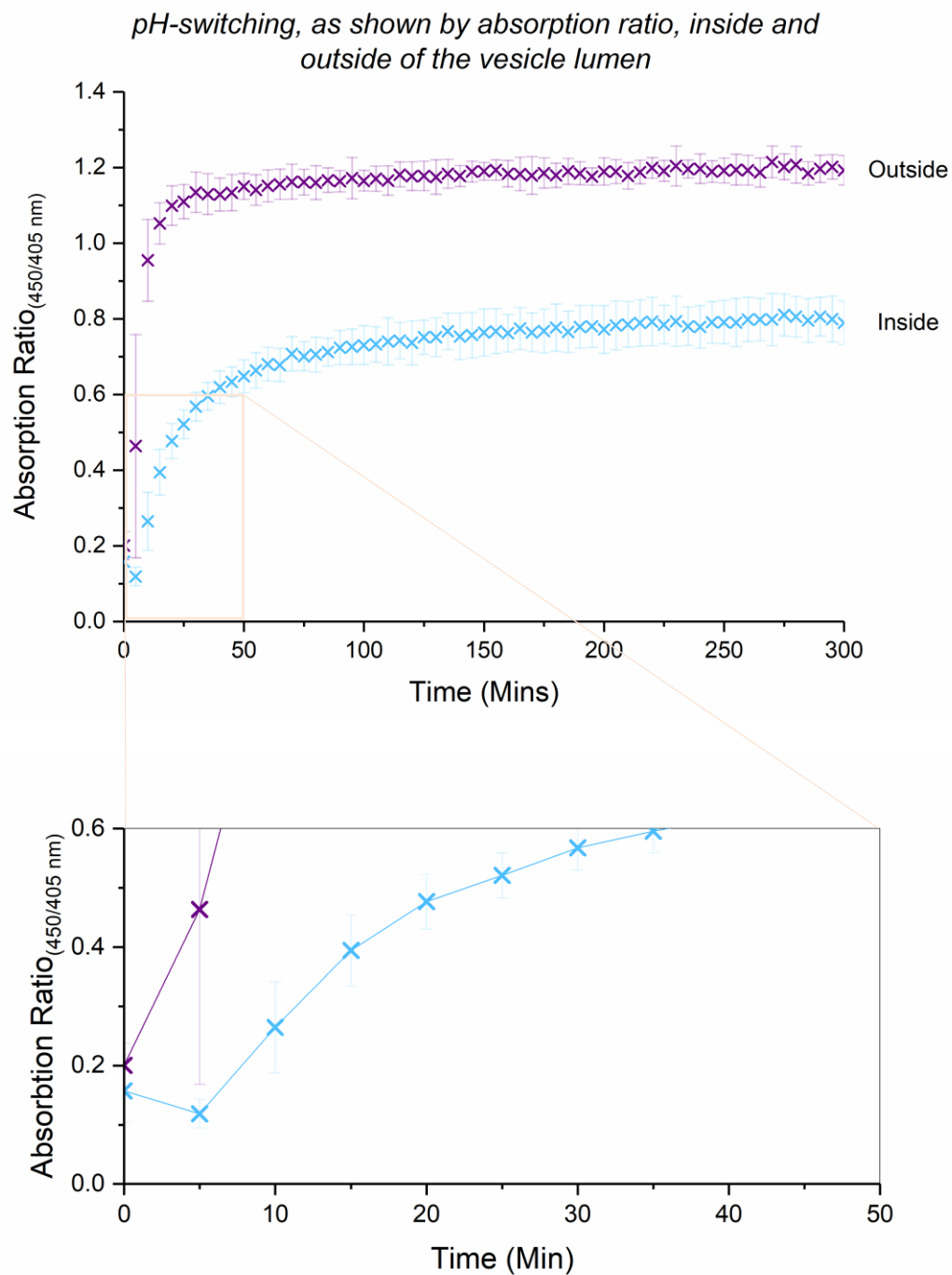
Figure 4.1. Change in absorption ratio (450/405 nm) inside and outside of the vesicle, when urea (50 mM) is added to urease (10 µM) encapsulating DPhPC vesicles (200 nm, 250 µM), including super-zoom on initial "dip" (n = 3, error = ± SD).
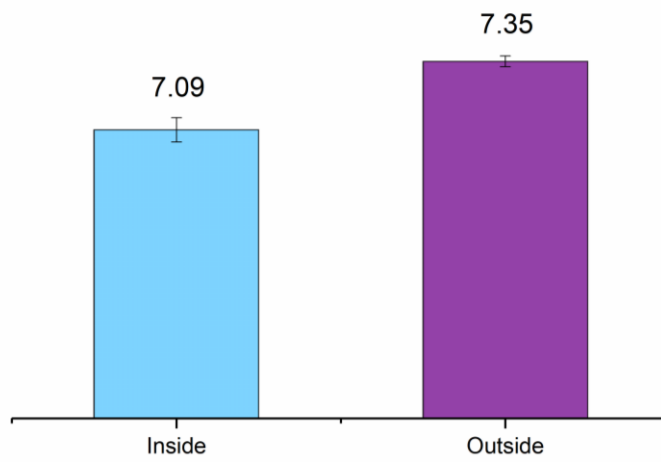
Figure 4.2. Internal and external pH of urease (10 μM)-encapsulating DPhPC vesicles (200 nm, 250 μM), following addition of urea (50 mM) (n = 3, error = ± SD).

4.3.2 Starting HCl Concentration

As previously mentioned, lowering the starting pH of the urea-urease reaction lowers the enzymatic activity of urease, meaning that, as the reaction proceeds towards pH-activity maximum (pH 7), the reaction will accelerate. In first instance, from the data shown in Figure 4.3, it can be seen that, likewise to bulk conditions (Figure 2.5), increasing starting acid concentration leads to an apparent and respective increase in clock time, a decrease in final pH, and a decrease in the robustness of pH-switching.
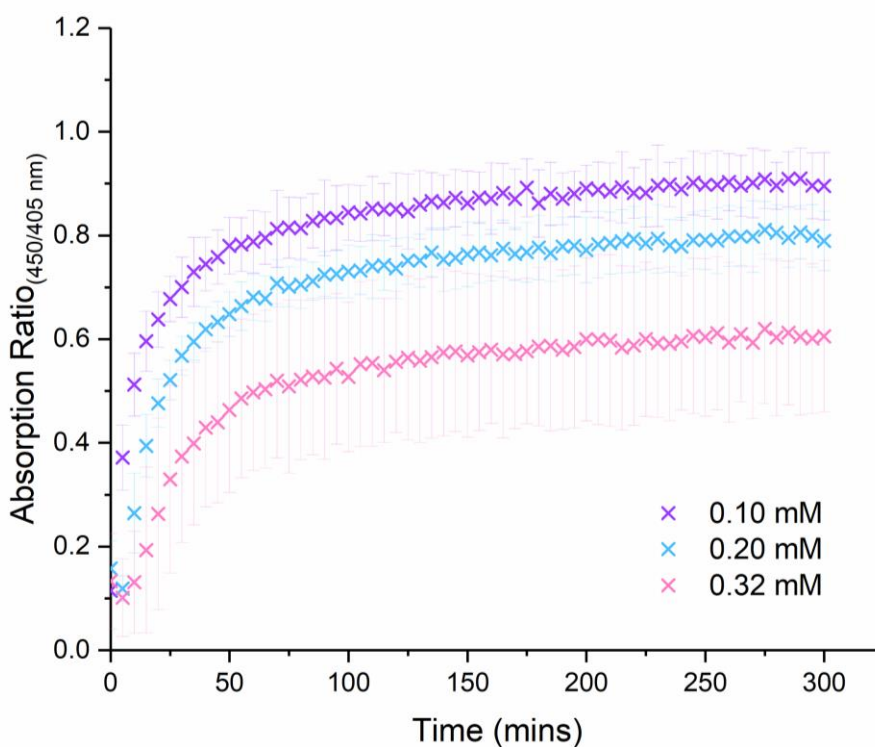
Figure 4.3. Change in absorption ratio (450/405 nm) for DPhPC vesicles (200 nm, 250 μM), encapsulating urease (10 μM) and HPTS (20 mM), when exposed to urea (50 mM), at different starting HCl concentrations (0.10 mM, 0.20 mM, 0.32 mM) (n = 3, error = ± SD).

Firstly, if we fix the concentration of urea at 10 mM (Figure 4.4), we can identify the effects of increasing HCl concentration (0.10, 0.20, 0.32 mM), and an unpaired t-test can help determine significance (95% confidence, denoted by an asterisk (*). Here, when we increase the initial concentration of HCl from 0.10 to 0.20 mM, we see a 160% increase in clock time, and a further

69.6% increase when HCl concentration is increased from 0.20 to 0.32 mM. With regards to final pH, increasing starting HCl concentration from 0.10 and 0.20 mM is shown to cause a shift in final pH from pH 6.96 ± 0.04 to pH 6.79 ± 0.05, however, further increasing HCl concentration from 0.20 to 0.32 mM is shown to have negligible effect (pH 6.79 ± 0.05 → pH 6.78 ± 0.10). Finally, for each incremental increase initial starting HCl concentration, an increase in transition width is witnessed (96.5% increase between 0.10 and 0.20 and 48.2% increase between 0.20 and 0.32 mM.

If we now increase urea concentration to 50 mM, we can assess if the relationship witnessed here can be strengthened through repeatability (Figure 4.4). As such, when we increase the initial concentration of HCl from 0.10 to 0.20 mM, and then 0.20 to 0.32 mM, we see an increase in clock time of 61.0% and 67.6%, respectively. With final pH, we see a decrease in the final pH when acid concentration is increased (0.10 to 0.20 to 0.32 mM = pH 7.20 ± 0.03 → pH 7.09 ± 0.05 → pH 6.91 ± 0.13).Similar to a fixed urea concentration of 10 mM, we see a positive relationship between increased acid concentration and increased transition width, where there is a 45.5% increase between 0.10 to 0.20 mM and a 26.6% increase between 0.20 to 0.32 mM.

Finally, if we fix the urea concentration at 250 mM, we see a similar pattern (Figure 4.4), whereby increasing acid concentration from 0.10 to 0.20 mM and from 0.20 to 0.32 mM produces an average, respective increase in clock time of 29.7% and 36.4%, respectively. A similar effect is seen in final pH, where an average decrease in pH is witnessed in respect to increasing acid concentration (pH 7.17 ± 0.04 → pH 7.12 ± 0.07 → pH 7.08 ± 0.03 when increasing from 0.10 → 0.20 → 0.32 mM, respectively). Likewise, with respect to transition width, we see an average increase of 18.6% and 12.7% in respect to increasing acid concentrations (0.10 to 0.20 mM and 0.20 to 0.32 mM, respectively).

Figure 4.4. Understanding the effect of HCl concentration (0.10, 0.20, 0.32 mM) on clock time, final pH, and transition width in DPhPC vesicles (size; 200 nm, phosphorus concentration; 250 μM, Urease; 10 μM, HPTS; 20 mM) at different concentrations of urea (10, 50, 250 mM) (n = 3, error = ± SD).

From this data, we see a consistent and expected relationship between increased acid concentration and our three measurable parameters, where, increasing acid concentration increases clock time and transition width, and reduces final pH. We also have first insight into the effect of urea, where at lower concentrations (10 mM) greater differences in clock time and transition width are witnessed, however, the degree of variability (error) is also increased. In contrast, at higher urea concentrations (250 mM) we see greater precision, however, the effect elicited through increasing HCl concentration is reduced, highlighting the overriding effect increased urea concentration may have. One thing to also notice here is that the HCl concentrations used, i.e., 0.10, 0.20, and 0.32 correspond to a pH of 4.0, 3.5, and 3.0, respectively. Given the reduced volume of urease, and the added effects of confinement, when comparing these results to bulk, one would expect that if the internal pH was truly pH 3.0, then the reaction vessel may not switch at all. This was investigated further in the next section.

4.3.3 Balancing Internal and External pH

Most proteins, and by extension, enzymes, hold buffering capabilities. To test the buffering capacity of urease, we took a dilute HCl solution (0.32 mM), and measured its pH using a pH meter (pH 3.63). We then added enough urease to give a 5 μM urease and tracked an increase in pH to pH 6.91. Finally, we added excess urea (1 M) to initiate the reaction and took the final reading (pH 9.10) (Figure 4.5).

pH, as measured by a pH meter, following sequential addition of urease (5 μM), and then urea (1 M), to a dilute HCl solution (0.20 mM)

Figure 4.5. Final pH, as tested by a pH meter, of a 0.2 mM dilute HCl solution, following sequential addition of urease (5 μM) and then urea (1 M)

The information at hand tells us something very important about the system we are working with. If, as the above experiment outlines, the addition of urease to dilute HCl causes an increase in the pH of that solution from acidic to near-neutral, we can assume that when the urease is loaded into the vesicle, under normal conditions, i.e., suspended in 0.2 mM HCl, the starting pH will be around pH 7. However, based on the experiment below (Figure 4.6), which compares vesicles made via our standard protocol (urease suspending in dilute HCl), to vesicles where the encapsulated volume has been pH-adjusted, using a pH meter, to pH 4, 5, and 6, respectively, we see this is not the case. Knowing what we know about the relationship between pH and final

pH, and pH and clock time, i.e., increased clock time and lower final pH, it may be safe to assume that the actual starting pH, although unknown, is around pH 5.5, meaning that during the process of vesicle generation, purification, and phosphorus quantification, there is a shift in luminal pH closer to that of the lower-pH external environment (0.20 mM HCl).

The effect of balancing internal and external pH, in comparison to resuspending urease in dilute HCl solution (0.2 mM)
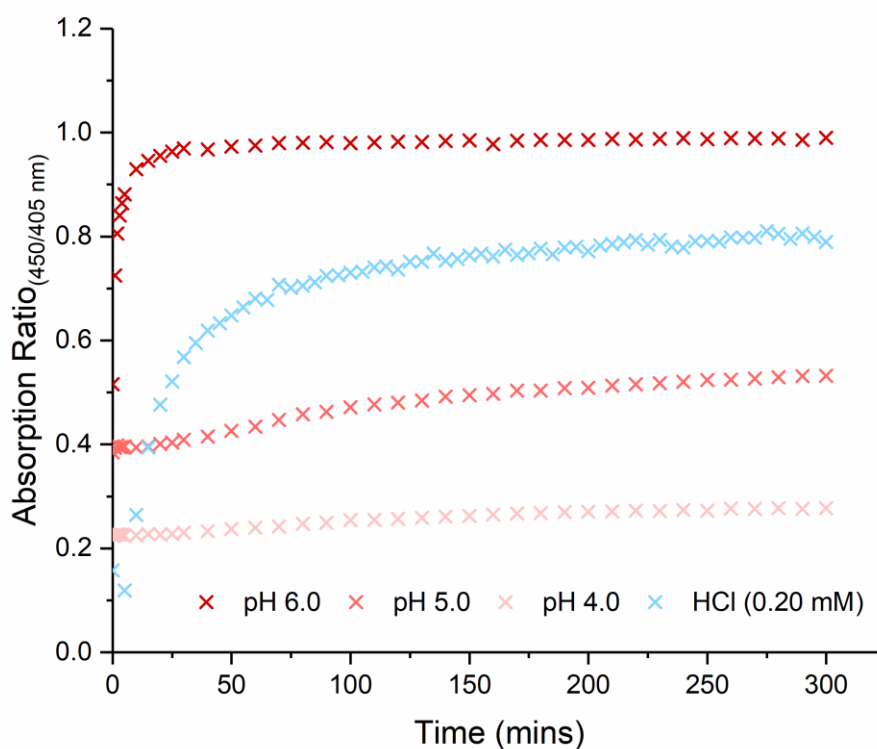
Figure 4.6. Comparison of reaction profile between standard experimental setup (urease in HCl (0.20 mM)) (blue), and internally and externally balanced pH (pH 4, 5, and 6) (red). Each sample contained 200 nm DPhPC vesicles (phosphorus concentration; 250 µM), encapsulating 10 µM urease and 20 mM HPTS, and the reaction was started with 50 mM urea.

4.3.4 Urease Concentration

If we fix the vesicle size at 100 nm (Figure 4.7), we can explore the effect of increasing urease concentration (5, 10, 20 µM), for three designated urea concentrations (10, 50, and 250 mM) (Figure 4.7). For 10 mM urea concentration, increasing urease concentration from 5 µM to 10 µM results in a 40.0% decrease in average clock time and doubling again from 10 µM to 20 µM produces a further 19.7% decrease. Likewise, at a urea concentration of 50 mM, a percentage decrease of 35.8% is witnessed from 5 to 10 µM, and a further 25.2% decrease is witnessed between 10 and 20 µM. At a urea concentration of 250 mM, a 62.9% decrease is witnessed between 5 µM and 10 µM, and a 22.8% decrease is witnessed between 10 µM and 20 µM, however, in both instances, there is large respective variability.

If we now consider final pH (Figure 4.7), at a urea concentration of 10 mM, we can see that increasing the concentration of urease from 5 to 10 µM, causes a respective increase in final pH (pH 6.83 ± 0.06 → pH 6.93 ± 0.02), however, although increasing further from 10 µM to 20 µM produces a further increase in average final pH, this increase is negligible (pH 6.93 ± 0.02 → pH 6.95 ± 0.07). Similarly, at 50 mM urea concentration, an initial increase in average final pH is witnessed when urease concentration is increased from 5 to 10 µM (pH 7.08 ± 0.06 → pH 7.15 ± 0.01), however, no further increase it witnessed when increasing from 10 to 20 µM (pH 7.15 ± 0.01 → pH 7.13 ± 0.03). At a urea concentration of 250 mM, there is no (or negligible) increase in final pH in response to increasing urease concentration from 5 to 10 µM (pH 7.16 ± 0.07 → pH 7.16 ± 0.04) or 10 to 20 µM (pH 7.16 ± 0.04 → pH 7.17 ± 0.07).

Finally, where width of transition is a determinant of the robustness of pH switching, we can see that for 10 mM urea concentration (Figure 4.7), increasing urease concentration, both from 5 µM to 10 µM and 10 µM to 20 µM, results in an average decrease in transition width (3.74 ± 1.32 → 2.00 ± 0.51 and 2.00 ± 0.51 → 1.87 ± 0.19, respectively). Similarly, for both 50 and 250 mM urea concentrations, a decrease in transition width is witnessed between 5 µM, 10 µM, and 20 µM (1.39 ± 0.24 → 1.33 ± 0.09 → 1.23 ± 0.03, and 1.26 ± 0.40 → 1.00 ± 0.23 → 0.96 ± 0.11, respectively).
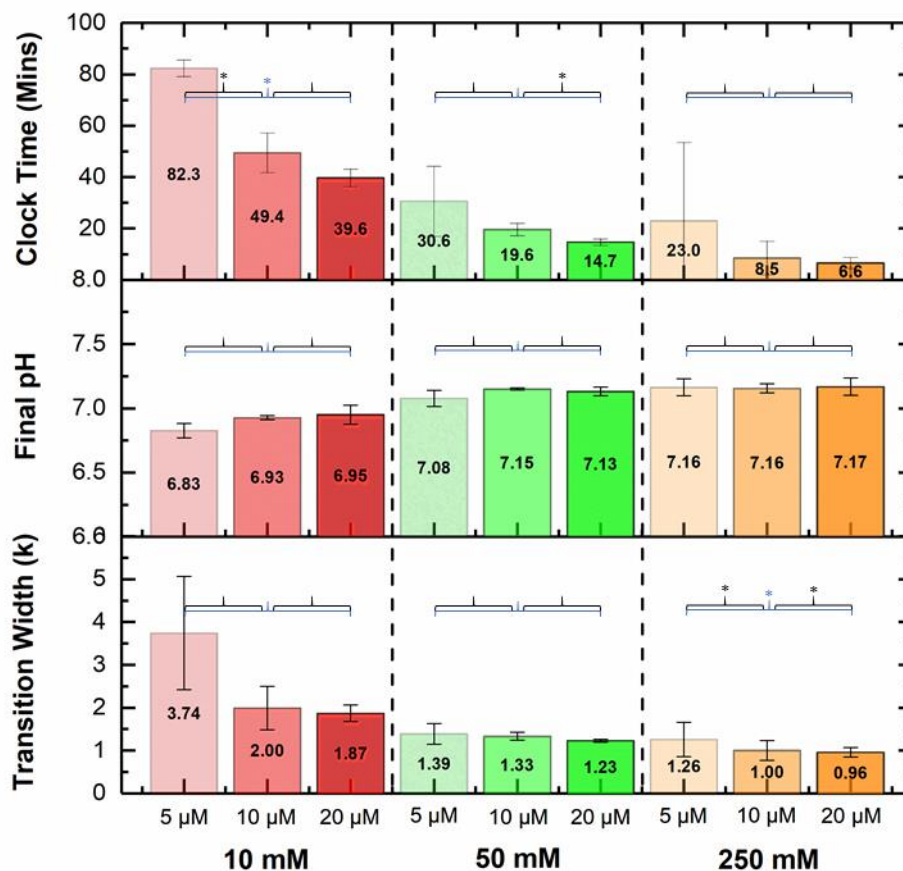
Figure 4.7. Understanding the effect of urease concentration (5, 10, 20 µM) on clock time, final pH, and transition width in DPhPC vesicles (size; 100 nm, phosphorus concentration; 250 µM, HPTS; 20 mM) at different concentrations of urea (10, 50, 250 mM) (n = 3, error = ± SD).

So, again, if we fix vesicle size at 200 nm (Figure 4.8), we can begin to extract the same information, with regards to clock time, final pH, and the width of transition, to see if these data are consistent with the data from 100 nm vesicles. For clock time, at all three of our tested urea concentrations (10, 50, and 250 mM), an inverse relationship exists between increased urease concentration (5 to 10 to 20 µM) and decreased clock time. With regards to final pH, it is difficult to infer a relationship with urease concentration. At 10 mM we see an unexpected decrease in final pH when urease concentration is increased from 5 to 10 µM, then pH increases again when urease concentrations is increased from 10 to 20 µM. At 50 mM we see an expected average increase in response to increasing urease concentrations, however, these increases are very

minimal. Finally, at 250 mM, we see no change between 5 and 10 μM, and then an unexpected drop in final pH when urease concentration is increased again to 20 μM. Finally, where transition width is concerned, for all tested urea concentrations (10, 50, and 250 mM), increasing urease concentration resulted in a consistent and expected decrease in transition width.
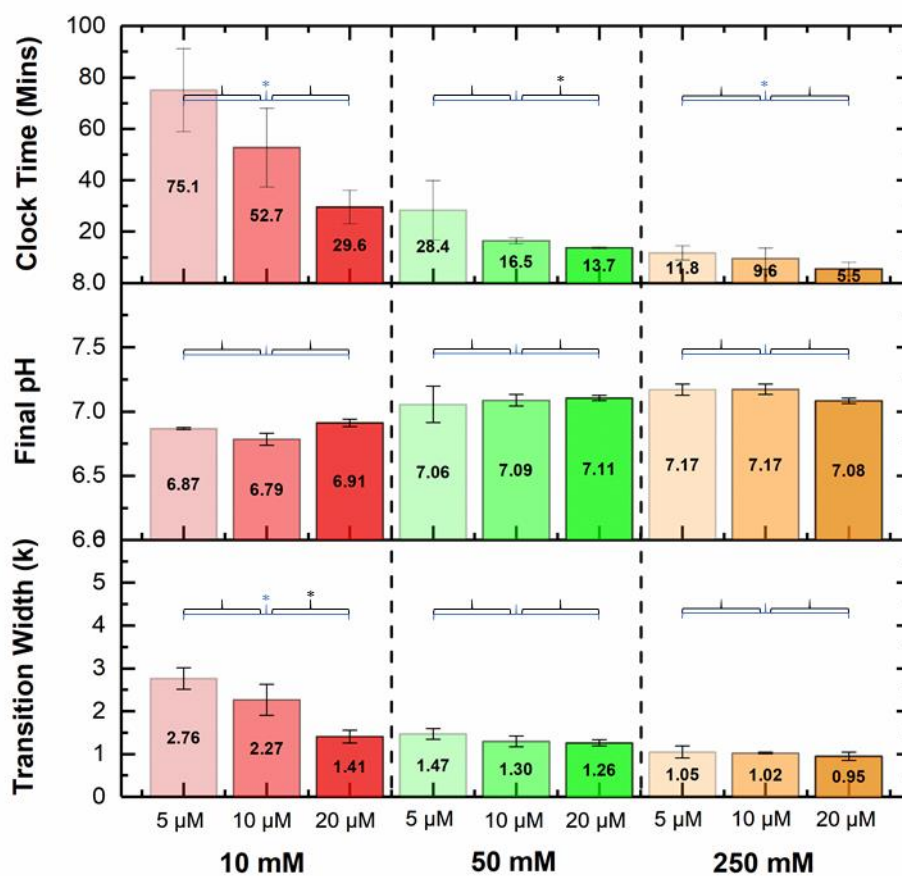
Figure 4.8. Understanding the effect of urease concentration (5, 10, 20 μM) on clock time, final pH, and transition width in DPhPC vesicles (size; 200 nm, phosphorus concentration; 250 μM, HPTS; 20 mM) at different concentrations of urea (10, 50, 250 mM) (n = 3, error = ± SD).

Finally, if we fix vesicle size at 400 nm (Figure 4.9), we add further insight to our understanding of the relationship between urease concentration and clock time, final pH, and the transition

width. At both 10 and 250 mM urea concentrations, we see a decrease in clock time when urease concentration is doubled from 5 to 10 µM, however, when it is doubled again, although we actually see a small increase in average clock time, there is no statistical difference between 10 and 20 µM (P = 0.7854 and P = 0.9196, respectively). However, at a urea concentration of 50 mM, we see the expected average decrease in clock time with respect to increasing urease concentrations. With regards to final pH, in the instance of 400 nm vesicles, we see a relationship inverse to what we would expect, where, increasing urease concentration is resulting in a decrease in final pH – likely to be attributed to enhanced protein buffering in the presence of increased protein copy number. Finally, for a urea concentration of 10 mM an average decrease in transition width is witnessed when increasing urease concentration from 5 to 10 µM, however, when the concentration of urease is doubled again, the average transition width actually increases, although large associated errors attached to the 20 µM sample makes it difficult to infer a statistical different between 10 and 20 µM (P = 0.6606). However, for both 50 and 250 mM urea concentrations, an expected an average gradual decrease is witnessed in relation to increased urease concentrations (5 to 10 to 20 µM).
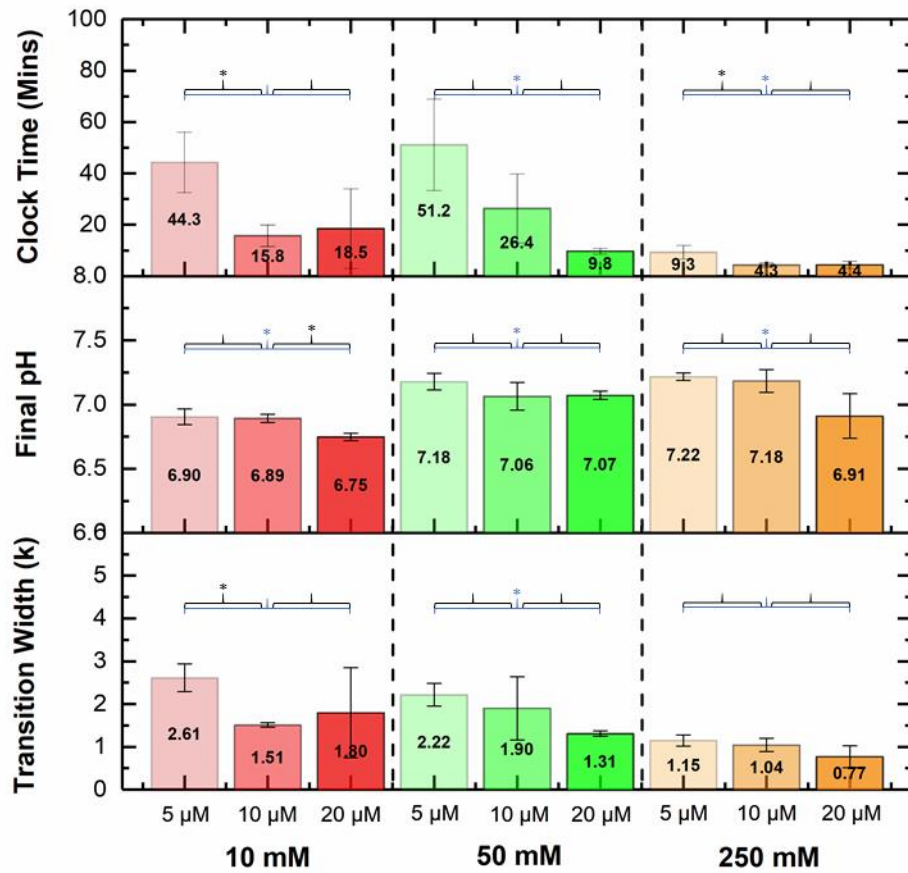
Figure 4.9. Understanding the effect of urease concentration (5, 10, 20 μM) on clock time, final pH, and transition width in DPhPC vesicles (size; 400 nm, phosphorus concentration; 250 μM, HPTS; 20 mM) at different concentrations of urea (10, 50, 250 mM) (n = 3, error = ± SD).

From the data at hand, across the range of vesicle sizes/urea concentrations, in the most, the average clock time and transition width is consistent with what is expected. However, where the theoretical number of urease copies each vesicle can hold doubles proportionally to doubling starting urease concentrations (Figure 4.10), you would expect this parameter to be one of the greatest contributors in enhanced kinetics. Instead, enhanced variability, increased experimental error, and overall lack of statistical significance highlights that urease concentration is not as strong a contributor as first predicted.

Figure 4.10. Calculated estimation of urease copy number when starting urease concentration is increased (5, 10, 20 µM), for different sized vesicles (100, 200, 400 nm)

Interestingly, this distribution amongst the sample does not follow typical Gaussian characteristics, but, instead, is Poisson in nature, meaning that the probability of vesicles containing a specific number of urease copies. i.e., 0, 1, 2, etc., is intrinsically linked to the initial concentration of urease and the capability of the vesicle lumen in terms of size to be able to house these copies (Figure 4.11).

This concept is no better explained than at 5 µM urease, in 100 nm vesicles, where the effects witnessed might not actually be because the concentration is not sufficient to cause a robust pH switch (in isolation), but because within the sample, the percentage of vesicles that contain a low protein copy number is increased, magnifying the stochasticity of the sample with regards to pH switching. At this concentration, we may create a scenario whereby some vesicles are switching more slowly than others, and potentially, even a small population of vesicles are not switching at all. This may explain why there is a larger percentage decrease in clock time, for each of the urea concentration (10, 50, 250 mM), when urease concentration is doubled from 5 µM to 10 µM (40.0%, 35.8%, 62.9%, respectively), than is when it is doubled again from 10 µM to 20 µM (19.7%, 25.2%, 22.8%, respectively). Similarly, it may be used to explain the interesting

behaviour of final pH at 400 nm, where, an increased internal enzyme concentration may negotiate a stronger protein-buffering capacity, resulting in a lower final pH when urease concentration is increased.
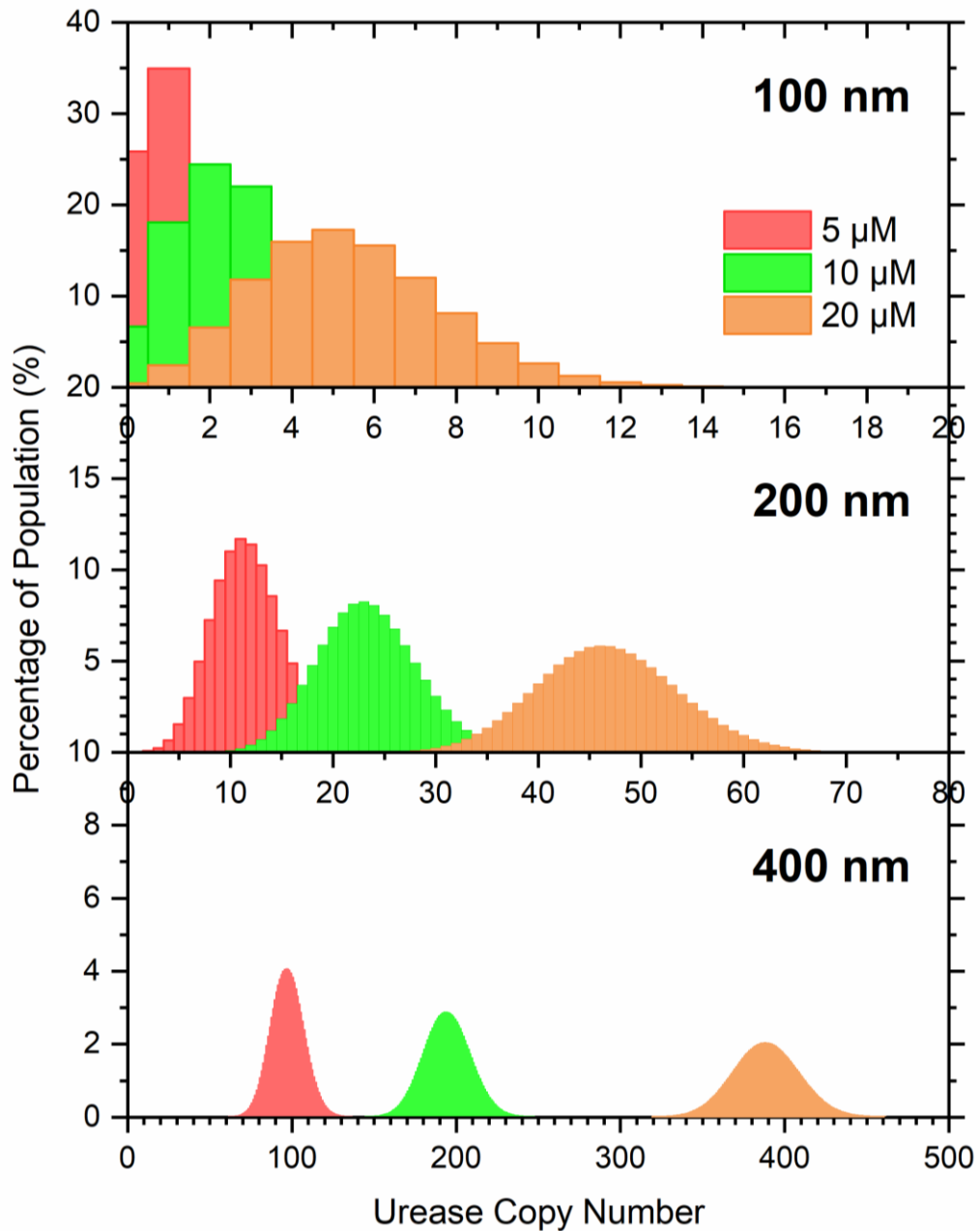
Figure 4.11. Poisson distribution for 5, 10, and 20 µM urease concentration in 100 nm (X; 1-20, γ = 1.35, 2.70, 5.41, respectively), 200 nm (X; 1-75, γ = 11.7, 23.4, 46.8, respectively), and 400 nm (X; 1-500, γ = 97.2, 194, 389, respectively), showing proportion of vesicles within the sample encapsulated urease.

4.3.5   Urea Concentration

Again, similar to what we have seen in bulk, where urea concentration can be manipulated to alter the reaction profile of the urea-urease reaction, this phenomenon can be replicated in confined conditions (Figure 4.12). So, to understand how alterations in urea concentration effect the system, in terms of urease concentration and vesicle size, the three measurable parameters, i.e., clock time, final pH, and transition width have been extracted for comparison below.
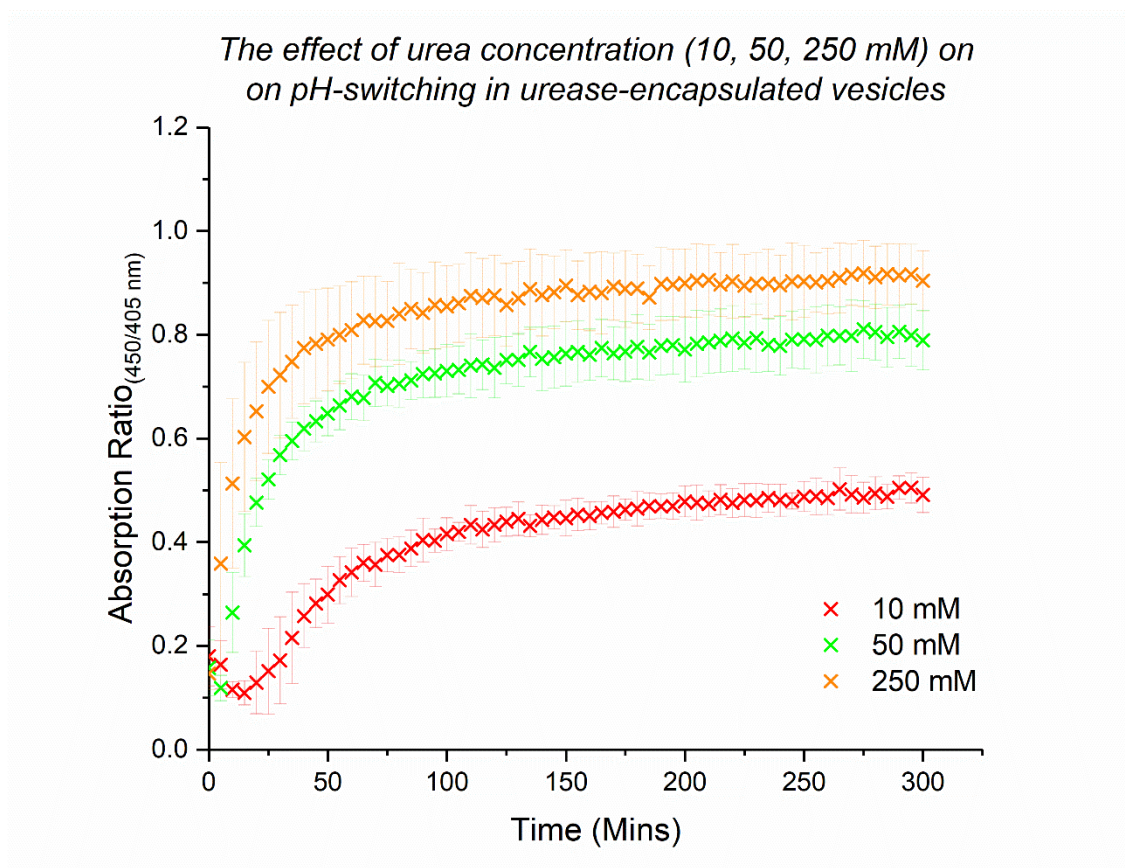
Figure 4.12. Absorption ratio (450/405 nm) of 200 nm DPhPC vesicles (phosphorus content; 250 μM), encapsulating urease (10 μM) and HPTS (20 mM), when the reaction is initiated by varying concentrations of urea (10, 50, 250 mM) (n = 3, error = ± SD).

Again, if we fix vesicle size at 100 nm (Figure 4.13), and explore the effect of increasing urea concentration (10, 50, 250 mM), we can see that for the three designated urease concentrations (5, 10, and 20 μM), if you increase urea concentration, an average decrease in clock time occurs. For all of the fixed urease concentrations tested (5, 10, and 20 μM), increasing urea

concentration five-fold, from to 10 to 50 mM was shown to produce a 62.8%, 60.2%, and 62.9% decrease in clock time, respectively, and increasing again a further five-fold, from 50 to 250 mM, was shown to decrease clock time by a further 24.7%, 56.6%, 55.2%, respectively. The overall decrease from 10 to 50, to 250 mM was 72.0%, 82.7%, and 83.4%, respectively. Similarly, if we consider final pH (Figure 4.13), for all three fixed urease concentrations (5, 10, and 20 µM), the average final pH increases incrementally with regards to increased urea concentration (10 to 50 to 250 mM), however, it is interesting to note that the difference in final pH is less when increasing from 50 to 250 mM, in comparison to 10 to 50 mM. Likewise, for all three fixed urease concentrations (5, 10, and 20 µM), the average width of transition decreases incrementally in response to increasing urea concentration (10 to 50 to 250 mM).
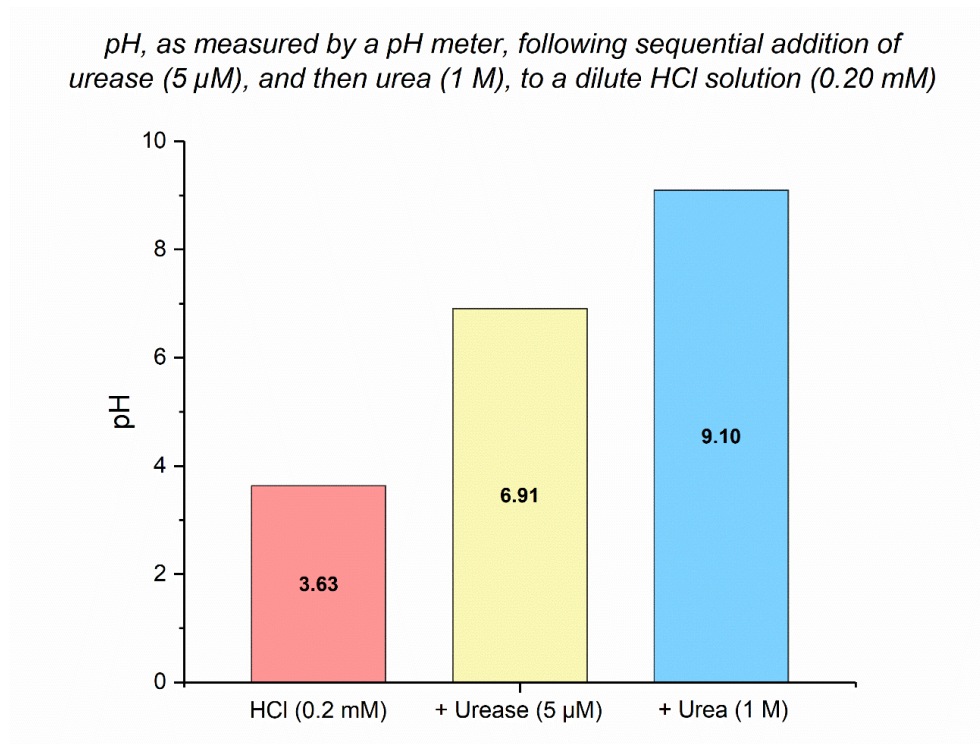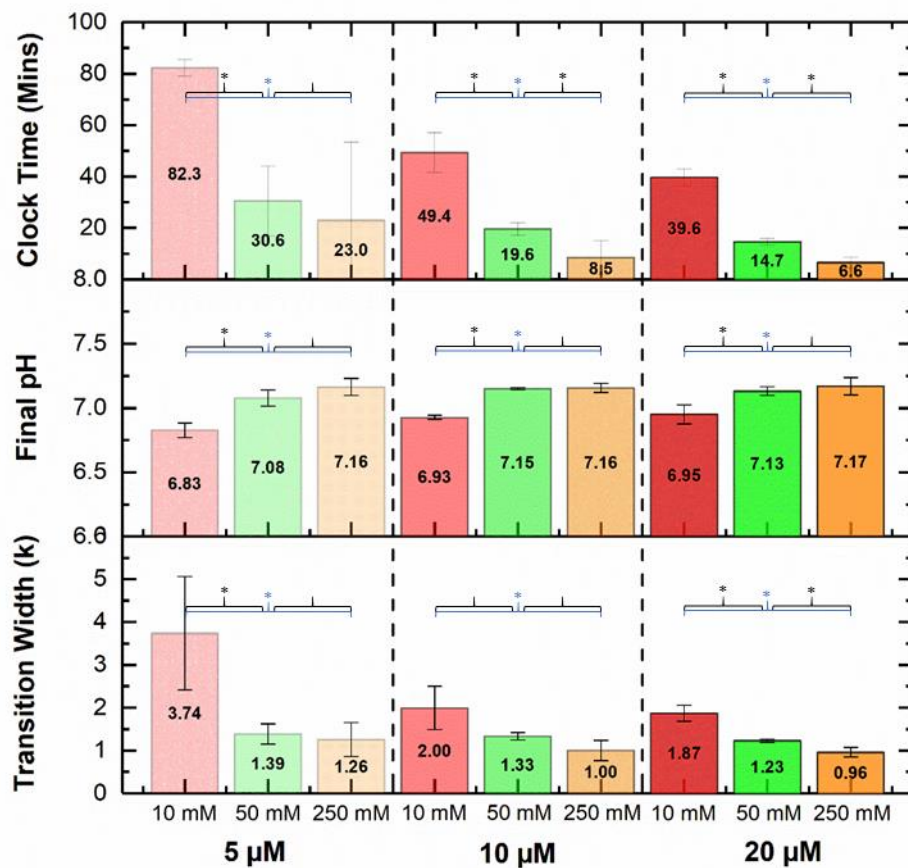

Figure 4.13. Understanding the effect of urea concentration (10, 50, 250 mM) on clock time, final pH, and transition width in DPhPC vesicles (size; 100 nm, phosphorus concentration; 250 µM, HPTS; 20 mM) at different concentrations of urease (5, 10, 20 µM) (n = 3, error = ± SD).

Likewise, if we fix vesicle size at 200 nm (Figure 4.14), a similarly strong relationship between urea concentration and average clock time exists. Again, for all three urease concentrations (5, 10, and 20 μM) we see an average decrease in clock time (62.2%, 68.7%, and 53.7%, respectively) when urea is increased from 10 mM to 50 mM, and a further average decrease (58.5%, 41.8%, and 59.9%, respectively) when urea concentration is increased from 50 to 250 mM. Similarly, if we consider final pH (Figure 4.13), for urease concentration fixed at 5 and 10 μM), the average final pH increases incrementally with regards to increased urea concentration (10 to 50 to 250 mM), however, when urease concentration is fixed at 20 μM, an increase is only witnessed when urea concentration is increased from 10 mM to 50 mM (but not when further increased to 250 mM). Likewise, for all three fixed urease concentrations (5, 10, and 20 μM), the average width of transition decreases incrementally in response to increasing urea concentration (10 to 50 to 250 mM).
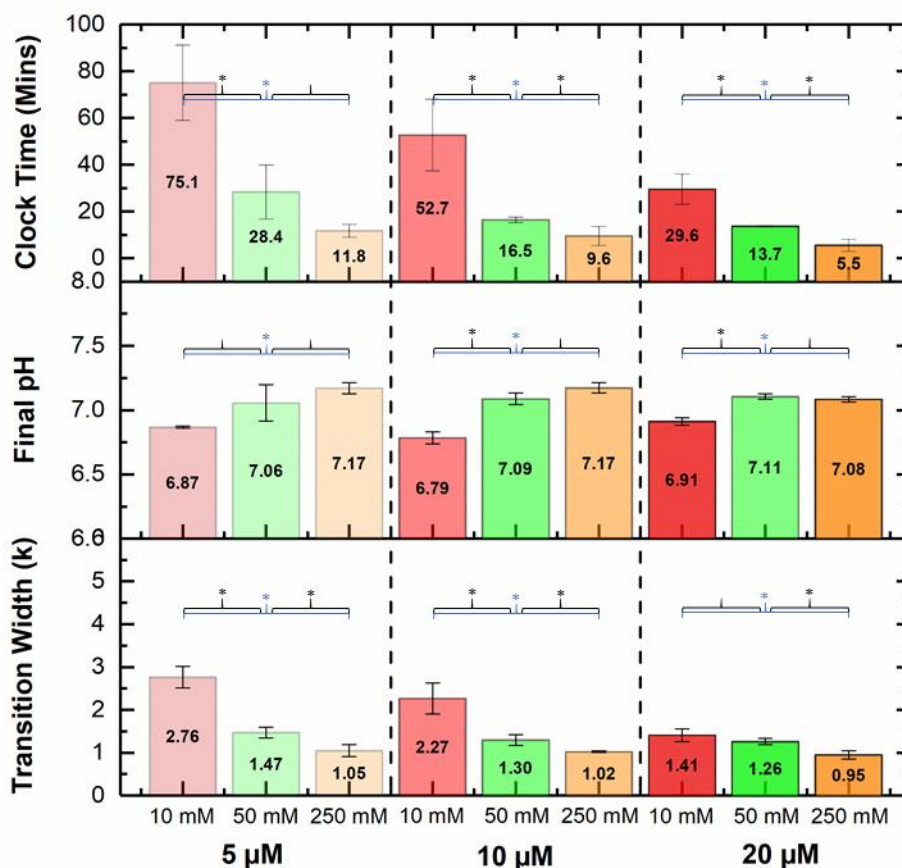
Figure 4.14. Understanding the effect of urea concentration (10, 50, 250 mM) on clock time, final pH, and transition width in DPhPC vesicles (size; 200 nm, phosphorus concentration; 250 μM, HPTS; 20 mM) at different concentrations of urease (5, 10, 20 μM) (n = 3, error = ± SD).

Finally, if vesicle size is fixed at 400 nm (Figure 4.15), for urease concentrations of 5 and 10 µM, we see an unexpected increase in clock time when urea concentration is increased from 10 mM to 50 mM, however, in each instance, there is large associated error. When comparing the clock time between 10 mM and 250 mM urea concentrations, however, a clear and expected relationship exists, where urea concentration is inversely proportional to clock time. In contrast, at a urease concentration of 20 µM, we see a clear, incremental decrease in average clock time. These results clearly highlight increased variability when there are opposing parameter extremities, i.e., larger vesicle (400 nm), low enzyme concentration (5 µM), however, when the parameters are respectively matched, e.g., by increasing urease concentration to 20 µM, resolution is reduced, but so is variability (in this example, i.e., 400 nm vesicles).

When it comes to final pH, at fixed urease concentrations of 5 and 10 µM, we witness what we seen in 100 and 200 nm vesicles, where, increasing urea concentration from 10 to 50 mM causes an increase with respect to increasing urea concentrations (10 to 50 to 250 mM). However, for 20 µM, like we have seen in previous examples, we see an increase in final pH when increasing urea concentration from 10 to 50 mM, but a decrease in final pH when further increasing urea from 50 to 250 mM – again, this could be attributed to a strengthened protein buffering capacity caused when larger vesicles contain a high concentration of enzymes.

Finally, with regards to transition width, for fixed urease concentrations of 5 and 20 µM, we see an expected relationship where increasing concentrations of urea (10 to 50 to 250 mM) results in a decrease in average transition width. For a urease concentration of 10 µM, although an anomalous result at 50 mM of urea is present, the overall relationship between urea concentration and transition width, i.e., increasing urea concentration from 10 to 250 mM, conforms to what is expected.
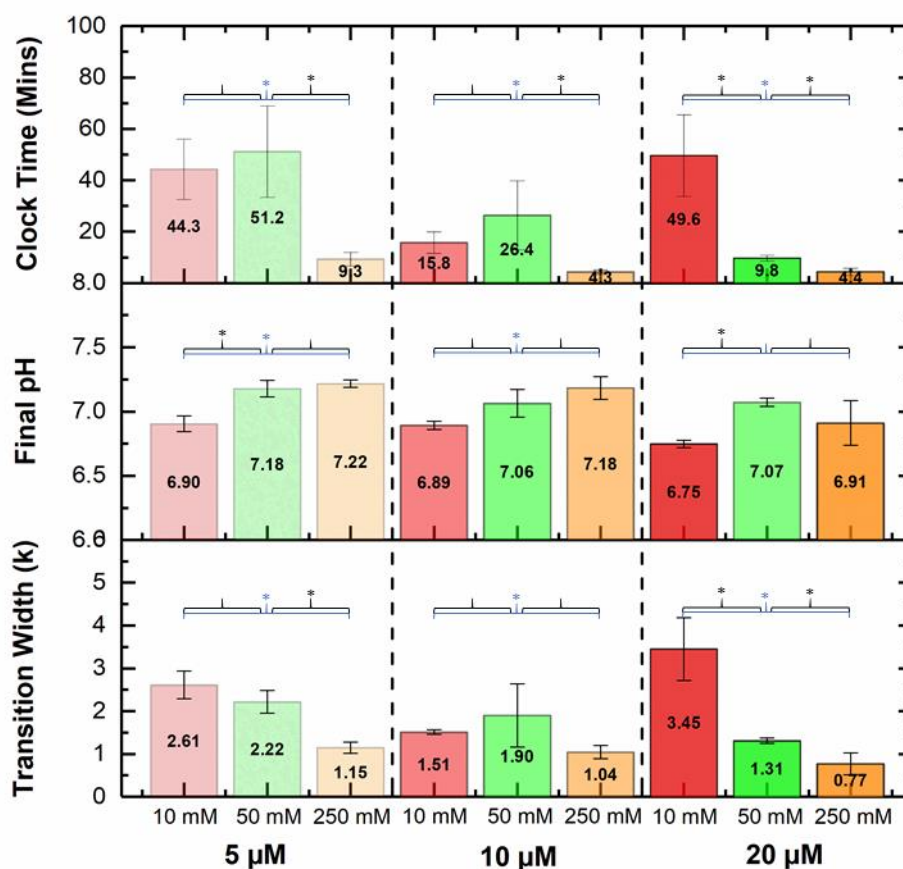
Figure 4.15. Understanding the effect of urea concentration (10, 50, 250 mM) on clock time, final pH, and transition width in DPhPC vesicles (size; 400 nm, phosphorus concentration; 250 μM, HPTS; 20 mM) at different concentrations of urease (5, 10, 20 μM) (n = 3, error = ± SD).

From the data above, you could infer that, especially at 10 mM, there is insufficient urea within the system to replicate the effects seen at the higher urea concentrations and in bulk. However, given the comparative concentrations between bulk (Figure 2.5) and confined (Figure 4.13, Figure 4.14, and Figure 4.15), it is hard to believe that in bulk conditions, where a greater urease copy number is present, when urea concentration remains constant, it is now insufficient in a confined system. Given that the concentration of urea is in excess in all scenarios, and the enzyme will likely be operating at V_{max} throughout, the positive relationship between urea concentration and our measurable parameters, is more likely to be attributed to concentration-based membrane diffusion, spatiotemporal correlations, or a combination there of.

Where urea concentration causes the most significant shifts in our measurable parameters, a clear relationship is beginning to unearth itself with regards to parameter concentrations. There is an increased variability when utilising 100 and 400 nm vesicle samples, especially when other parameter extremities are also employed. For example, in 100 nm vesicles, an initial increase in urea concentration from 10 to 50 mM gives a significant decrease in clock time at all urease concentrations, however, from 50 to 250 mM, a sequential reduction in P-value in response to increasing urease concentrations is indicative of an increased efficiency (less variability). Similarly, in both 100 and 400 nm vesicles, at low enzyme concentrations (5 µM), a lot of variability exists with regards to transition width – this is reduced when the urease concentration is increased to 20 µM. However, 200 nm vesicles, especially when in combination with other "middle" concentrations, i.e., 50 mM urea or 10 µM urease, give consistent, expected results, infer statistically significant relationships, and provide an appropriate resolution with regards to parameter manipulation. As such, this is likely to be considered our "baseline" in future experiments.

4.3.6 Vesicle Size

The effect of varying vesicle size on pH switching should, in theory, be simpler to predict, where variation in diameter, and as such, lumen volume, is relative to the theoretical number of urease copies each vesicle can hold (Figure 4.16). However, as seen with urease concentration, this distribution amongst the sample does not follow typical Gaussian characteristics, but, instead, is Poisson in nature (Figure 4.17). As such, if we are to assume that an increased number of protein copies equates to an increased probability that all vesicles within the sample are likely to contain a sufficient protein copy number to invoke robust pH switching, then we are likely to assume that larger vesicles should have a lower clock time, lower transition width, and a higher final pH.
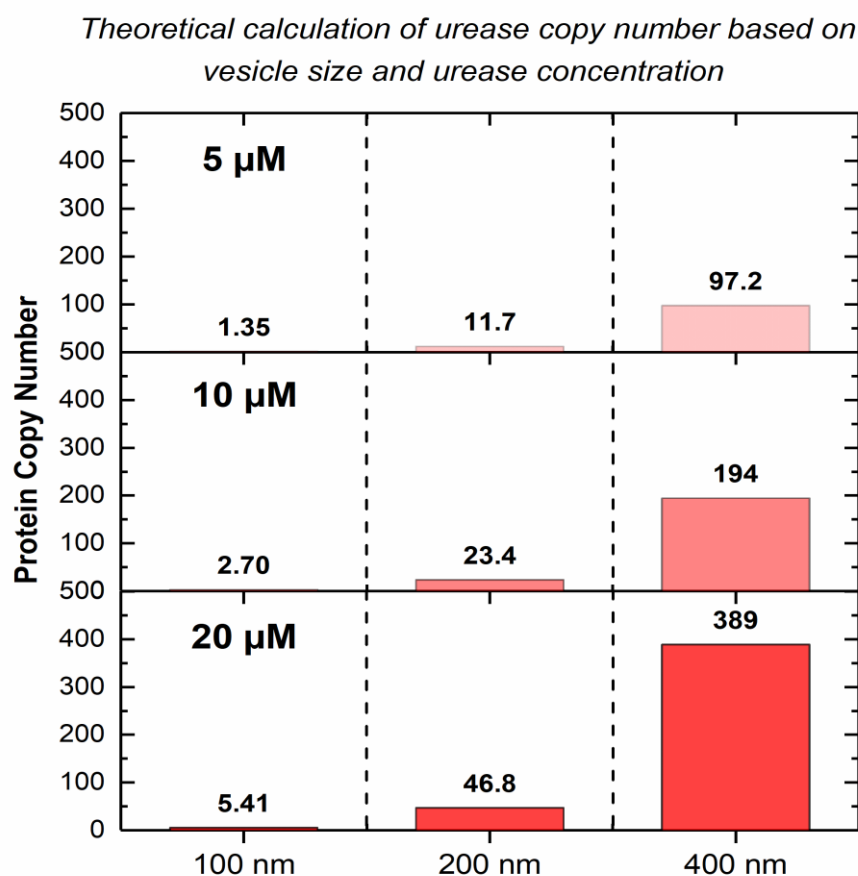
Figure 4.16. Calculated estimation, based on the size of the vesicle (400, 200, 100 nm), the respective volume of the lumen, and the concentration of urease (5, 10, 20 μM), of the total number of protein copies within each vesicle.

Poisson distribution: effect of vesicle size (100, 200, 400 nm) on respective urease copy number as a percentage of population
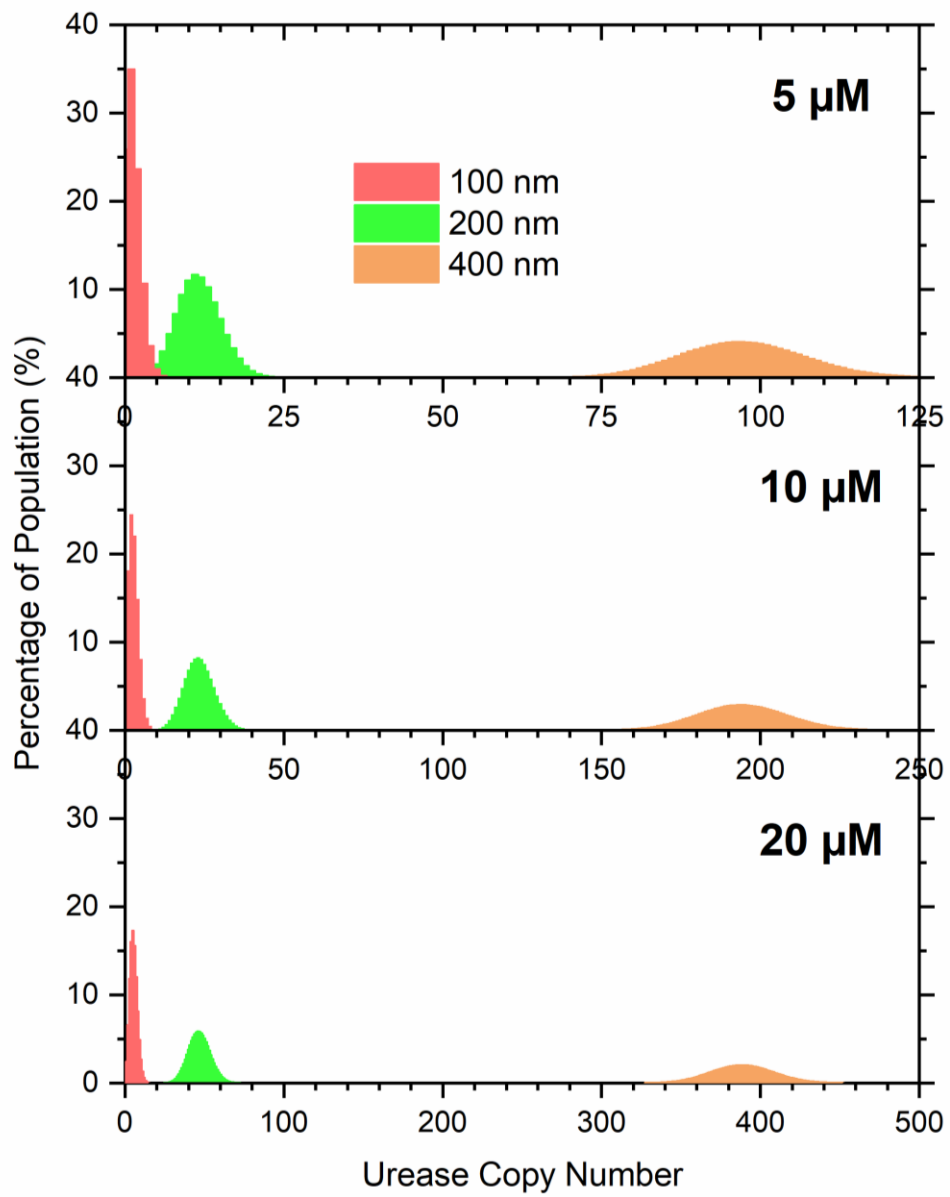
Figure 4.17. Poisson distribution for 100, 200, and 400 nm vesicles (X; 250, γ = 2.7, 23.4, and 194.3, respectively) extruded in the presence of urease (10 μM), showing percentage of vesicles within the samples encapsulating associated urease copy numbers.

Firstly, if we isolate the concentration of urea at 10 mM (Figure 4.18), which, thus far has been shown to have one of the biggest impacts on our extractable parameters, we can identify the effects of increasing vesicle size (100 to 200 to 400 nm) for each designated urease concentration (5, 10, and 20 µM). When working at urease concentrations of 5 and 20 µM, we see an expected and incremental decrease in clock time when increasing vesicle diameter from 100 nm to 200 nm (8.7% and 25.3%, respectively) and a further decrease when increasing from 200 nm to 400 nm (41.0% and 37.4%, respectively).

For a urease concentration of 10 µM, although an anomalous result at 50 mM of urea is present, where clock time increase (albeit with significant error), the overall relationship between urea concentration and clock time, i.e., increasing vesicle size from 100 to 200 nm, conforms to what is expected (68.0% decrease). With regards to final pH (Figure 4.18), it is hard to extract any sort of significant relationship to vesicle size, where, at 5 µM average final pH increases with respect to increasing size, at 20 µM we see the inverse, adding further weight to are argument that when vesicle size is increased at higher urease concentrations, increased protein buffering capacity may contribute to a reduced final pH, and at 10 µM we see a decrease when vesicle size is doubled from 100 to 200 nm but then an increase when diameter is doubled again (to 400 nm).

Similarly, it is difficult to infer a relationship between vesicle size and transition width (Figure 4.18), where at 5 µM we see we see an expected average decrease, albeit with overlapping variability, at 10 µM we see an increase in transition width between 100 and 200 nm, but a decrease between 200 and 400 nm, and at 20 µM, we see the opposite, where transition width decreases between 100 and 200 nm, but then increases again between 200 and 400 nm.
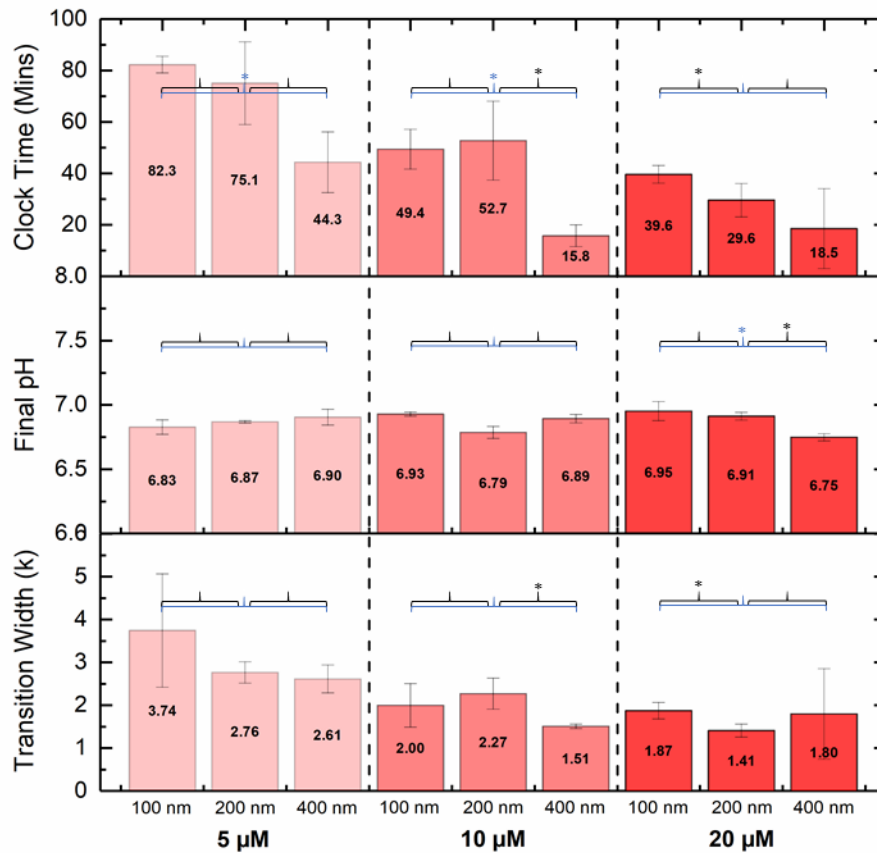
Figure 4.18. The effect of increasing vesicle size (100, 200, 400 nm) on clock time, final pH, and transition width for DPhPC vesicles encapsulating 5, 10, or 20 μM urease, and 20 mM HPTS, when 10 mM urea is added (n = 3, error = ± SD).

When urea concentration is fixed at 50 mM, for urease concentrations of 5 and 10 μM, variability in average clock time and a lack of precision in our triplicate repeats makes it difficult to infer any sort of correlative relationship with vesicle size (Figure 4.19). However, at 20 μM urease concentration, we see results more in line with what we would expect, where a consistent average decrease in clock time is linked to increasing vesicle size (evidence of reduced variability at higher systemic concentrations). For pH (Figure 4.19), at 5 μM urease, we see minimal decrease in final pH when increasing vesicles size from 100 nm to 200 nm, but then as vesicle size is doubled again (to 400 nm), the final pH then increases, given a net overall increase from 100 nm to 400 nm. Interestingly, for both 10 and 20 μM urease concentrations, a consistent decrease in final pH is witnessed in relation to increased vesicle size – this unexpected result adds further to the hypothesis of enhanced protein buffering where urease copy number is high. Finally, where increased vesicle size is intrinsically linked to increased protein copy number, you

would expect transition width to reduce in relation to increased vesicle size. However, what we see is the opposite, where for all three fixed urease concentrations (5, 10, and 20 µM), we see an incremental increase in transition width with respect to increasing vesicle size (100 to 200 to 400 nm) (Figure 4.19).
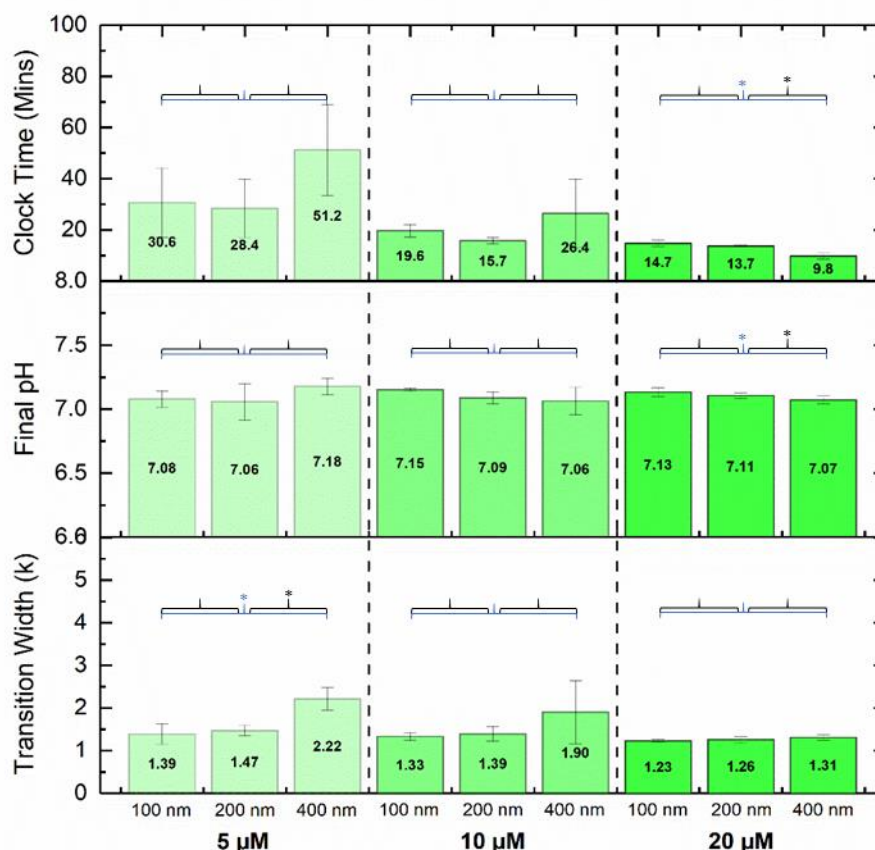
Figure 4.19. The effect of increasing vesicle size (100, 200, 400 nm) on clock time, final pH, and transition width for DPhPC vesicles encapsulating 5, 10, or 20 µM urease, and 20 mM HPTS, when 50 mM urea is added (n = 3, error = ± SD).

Finally, at a fixed urea concentration of 250 mM (Figure 4.20), there is a general trend between increased vesicle size and decreased clock time, however, given that we have already established urea concentration as a strong contributor towards kinetic output, the resolution is reduced to the point it is difficult to extract any statistical significance. With regards to pH, for both 5 and 10 µM urease concentrations, there is an overall increase in average final pH in

response to increasing vesicle size (from both 100 to 200 nm and 200 to 400 nm), however, these increases are negligible when considering the experimental precision. It could therefore be inferred that at this urea concentration, increasing vesicle size has no further impact on final pH (a maximum has been reached). As is a recurring observation, when urease concentration is increased to 20 µM, increasing vesicle size causes a relative decrease in final pH. Similarly, at 250 mM urea concentration, it is difficult to infer a relationship between vesicle size and transition width (Figure 4.18), where at 5 µM we see a decrease in transition width between 100 and 200 nm, but an increase between 200 and 400 nm, at 10 µM we see an average increase, albeit with overlapping variability, and at 20 µM we see the opposite, where transition width decreases in response to increasing vesicle size, albeit again with overlapping variability.
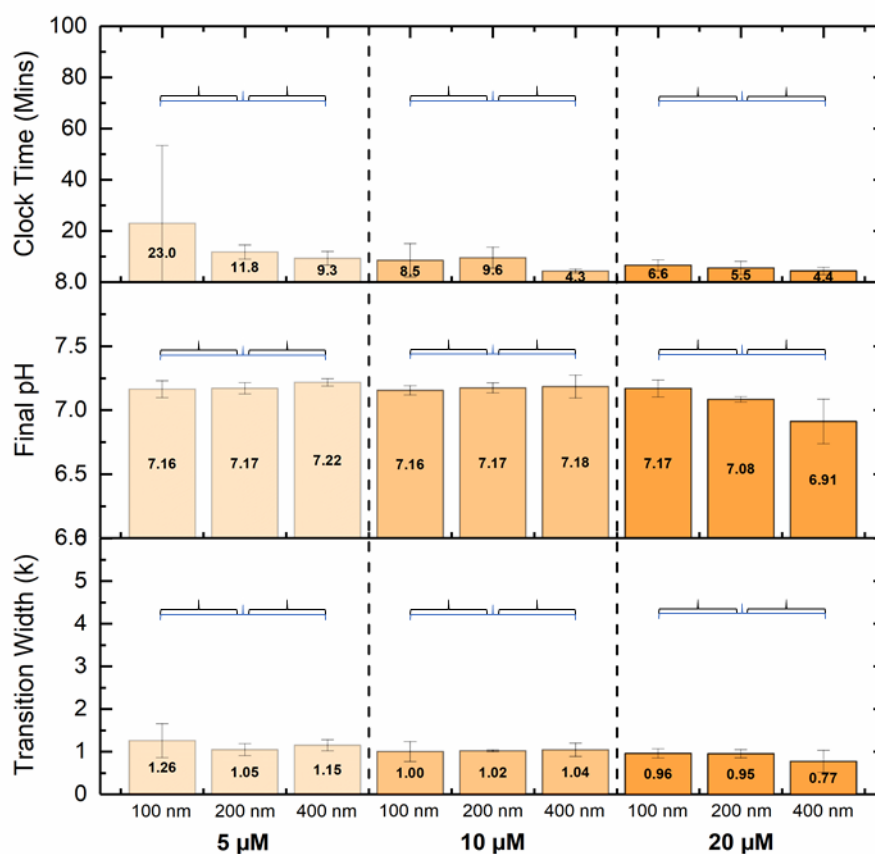
Figure 4.20. The effect of increasing vesicle size (100, 200, 400 nm) on clock time, final pH, and transition width for DPhPC vesicles encapsulating 5, 10, or 20 µM urease, and 20 mM HPTS, when 250 mM urea is added (n = 3, error = ± SD).

From the data at hand, across a range of different urea and urease concentration, we can establish that vesicle size, does not impact reaction kinetics as first predicted. Here, it is easy to think about a vesicle as a solitary reaction chamber, however, considerations of statistical encapsulation across a sample of vesicles complicates this issue. If, for example, we take 100 nm vesicles, the expected average number of urease molecules encapsulated within the at a urease concentration of 10 µM is 2.70 (Figure 4.16). When considered in terms of Poisson distribution (Figure 26), means that in probability, 70.9% of the vesicle population at this size and urease concentration will contain 3 or less protein molecules, with an estimated 6.7% of the population containing 0 ("urease-free"). Where no (or weak) relationship between vesicle size and our three parameters cannot be found, factoring in what we know about this relationship with urease copy number, this raises an interesting question about what is truly happening within the sample (as a collection of individual reaction chambers). Is pH switching stochastic in nature or do considerations of membrane permeability infer potential communication between vesicles, irrespective of protein copy number, ultimately leading to a deterministic form of permeability-induced pH switching?

4.3.7 Membrane Composition

4.3.7.1 Lipids

As we know from the literature, one of the key characteristics of lipid bilayers is the relative fluidity of the individual lipid molecules within it. This "fluidity" is dependent on the temperature, where, either side of the phase transition temperature (T_m (°C)), the bilayer can exist in a liquid ordered phase or a solid (gel) phase. It is worth noting that, in both phases, the individual lipids are restricted to the two-dimensional plane of the membrane, however, in the gel phase, the lipid molecules cannot freely diffuse within this plane. Exhibition of such phase behaviour is dependent on the corresponding characteristics of the lipid molecules with regards to the strength of attractive forces (Van der Waals) between adjacent lipid molecules. As such, the strength of interaction is intrinsically linked to the length of the lipid tail, where longer lipid tails have more area to interact. This means that at a designated temperature, a long-tailed lipid will exhibit less fluidity, and therefore have a higher T_m, than that of an otherwise identical short-tailed lipid.

Another factor, which has been shown to contribute to the fluidity of lipid bilayers, is the degree of unsaturation. A "kink" in the lipid tail, creating free space within the membrane, and ultimately permitting extra flexibility to the adjacent lipid chains, is created through the inclusion of one or more double bonds. It is this disruption that reduces packing efficiency and leads to a reduction in T_m. T_m is more sensitive to unsaturation than it is to chain length; decreasing chain length by one carbon is shown to produce an average reduction T_m of around 10°C, whereas inclusion of a single double bond is capable of reducing phase transition temperature by 50°C or more [192].

The relative permeability a lipid bilayer exhibits also has strong ties to 1) the degree of interaction between lipid chains, and; 2) the presence of defects (double bonds) within the membrane. For instance, a gel-like lipid membrane, which has high membrane rigidity and an increased packing density will exhibit the lowest permeability. If we consider the lipid structure of the three membrane compositions tested (Figure 4.21), then we can see that POPC (16:0-18:1), a common model lipid used to imitate chain disorder found in native membranes, is unsaturated, and, this is reflected in the T_m (-2°C). As such, you would therefore expect the relative permeability of POPC to be high. DPhPC (16:0), in contrast, has the benefit of being completely saturated, and, as a result, is more stable. However, the periodic inclusion of methyl groups along the acyl chains produces an (almost) energetic equivalence between the *trans* and one of the *gauche* rotamers [193]. A considerable disorder is therefore found in DPhPC lipid

membranes as a result of the steric requirements of these methyl branches preventing lateral packing efficiency between adjacent acyl chains. As a result, DPhPC does not exhibit a detectable gel to liquid crystalline phase transition between -120°C and +120°C [193]. Similar to DPhPC, DPPC (16:0) contains a 16-carbon acyl chain, however, the lack of a double bond, and the exclusion of chain methylation, means that the permission of lateral packing is strong between the adjacent chains. This is reflected in the T_m of DPPC, which is 41°C, meaning that at room temperature, DPPC exists as a gel, and should, hypothetically, have the lowest substrate permeability coefficient of any of the three membrane compositions tested.
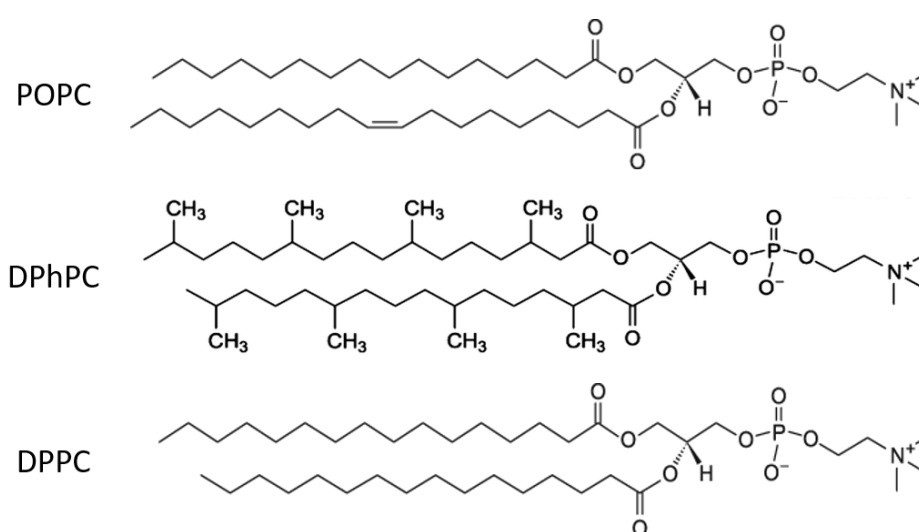
Figure 4.21. Chemical structure of POPC, DPhPC, and DPPC

When looking at the outcome of pH switching for different membrane compositions (Figure 4.22), we can immediately see that there has been either an apparent failure to successfully encapsulate urease in DPPC vesicles, or, exposure to prolonged temperatures above the T_m of DPPC (which is incidentally close to the denaturing point of urease (50°C)), could have caused inactivation. As a result, no pH switching was observed. Owing to the notoriety of pure DPPC membranes, cholesterol, a bidirectional regulator of membrane fluidity was added to DPPC at 30 mol% to generate DPPC:cholesterol (70:30) vesicles. However, much like pure DPPC vesicles, they were inefficient at producing a recognisable clock. Some preliminary data suggests that the low pH, caused by dilute HCl (0.2 mM), is affecting the ability of DPPC (and cholesterol) to form

vesicles capable of eliciting a reaction, but without information regarding the encapsulation efficiency of each vesicle membrane, it is difficult to identify the cause.
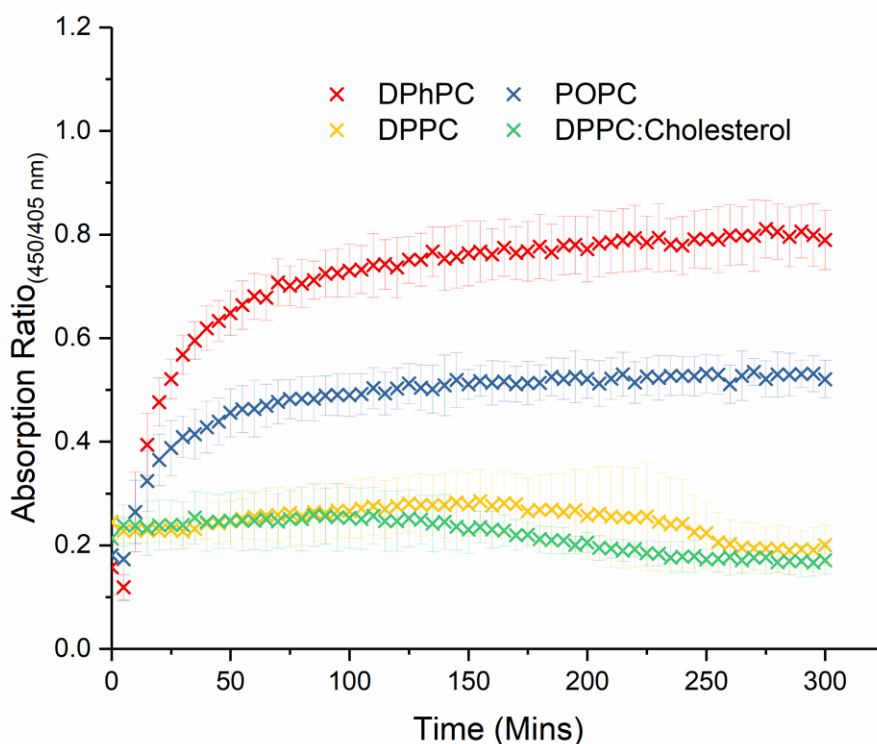
Figure 4.22. Change in absorption ratio (450/405 nm) for 200 nm lipid vesicles (phosphorus concentration; 250 µM) of differing membrane compositions (DPhPC, POPC, DPPC, and DPPC:cholesterol (70:30)), (urease (10 µM), HPTS (20 mM), urea (50 mM)) (n = 3, error = ± SD).

Firstly, if we compare the effect an increasing urea concentration has on the respective membrane compositions (Figure 4.23), we see that all three parameters, i.e., clock time, final pH, and transition width follow an expected trend, where increasing urea concentration results in a respective decrease in clock time and transition width, and a respective increase in final pH.

Now, if we are to take our three extractable parameters and compare the differences between POPC and DPhPC at set urea concentrations (Figure 4.23), we see an average decrease in clock time at a urea concentration of 10 mM (58.5 min vs 52.7 min, respectively, P = 0.62), another average decrease when urea concentration is 250 mM (11.0 min vs 9.6 min, respectively, P = 0.26), but an average increase when urea concentration is fixed at 50 mM (15.3 min vs 16.5 min, respectively, P = 0.78). For pH, at 10 mM urea concentration, final average pH is almost identical

between POPC and DPhPC (pH 6.80 vs pH 6.79, respectively, P = 0.62), however, at both 50 mM

and 250 mM, it is observed that POPC vesicles tend towards a lower average pH than their DPhPC

counterparts (8.85 vs 7.09, P = 0.00 and 7.02 vs 7.17, P = 0.25, respectively). Similarly, if we

compare the average transition width of our two species, it is clear that for all three urea

concentrations (10, 50, and 250 mM), POPC has a smaller width of transition in comparison to

DPhPC (P = 0.19, 0.03, and 0.03, respectively) – this highlights that although clock time is

considered (statistically) the same between the two differing lipid vesicles, the speed in which

they switch above 50 mM urea concentration is statistically quicker for POPC.
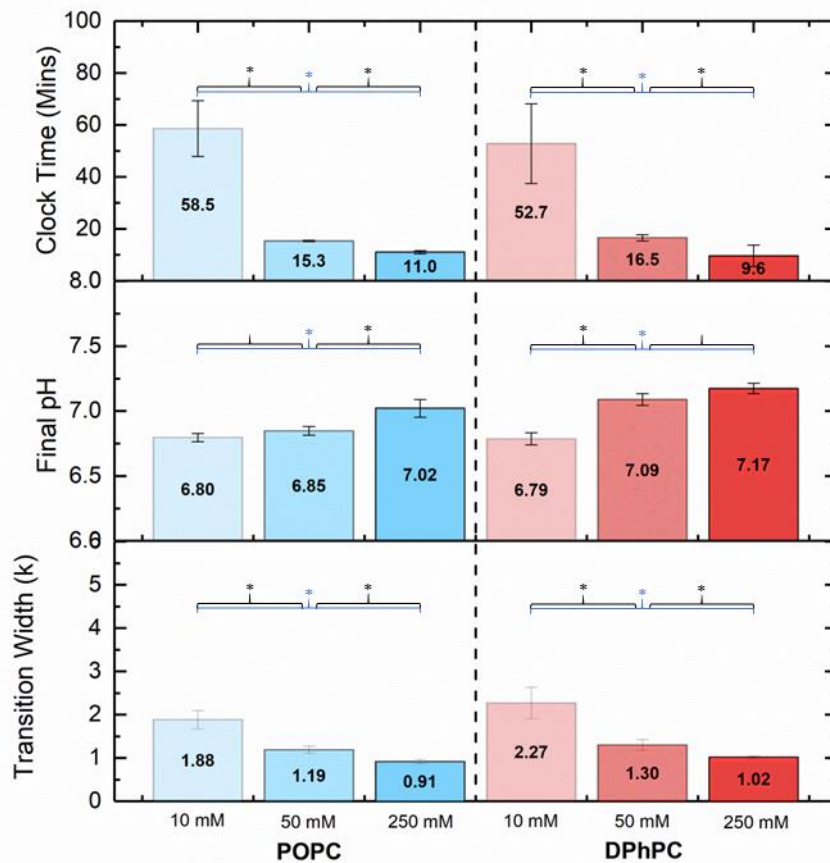
Figure 4.23. Comparing clock time, final pH, and transition width of POPC and DPhPC (size; 200 nm, phosphorus concentration; 250 µM, urease; 10 µM, HPTS; 20 mM) at different urea concentrations (10, 50, 250 mM) (n = 3, error = ± SD).

As previously touched upon, owing to the degree of unsaturation in POPC lipids, and therefore an increased permeability, in comparison to that of DPhPC, it could be concluded that the greater robustness in pH switching seen in POPC vesicles (Figure 4.23), may be attributed to an increased rate of urea permeability into the lumen, thereby overcoming the expulsion of pH (witnessed as ammonia is exchanged into the external environment) more efficiently. To add, hypothetically speaking, in terms of DPPC, if we consider the thickness of the non-polar region of the membrane to be one of the key contributors of permeability, then we would expect, because they are both straight, have an identical headgroup, and are shorter than 20 carbons in length [194], that the permeation rate of DPPC (16:0) and DPhPC (16:0) would be similar (according to the widely used solubility diffusion model). It has, however, been reported in various sources [194, 195], that the permeability of the branch-chained DPhPC lipid membrane is lower than that of its straight chained counterpart. This is likely due to restricted diffusion, brought on through the inclusion of methyl groups enhancing the energetic stability between *trans-gauche* rotamers, leading to an overall increase in structural stability [195], and, as a result, it is likely that the extracted parameters for DPPC would sit somewhere between POPC and DPhPC.

4.3.7.2 Polymers

As previously mentioned, polymersomes, by their nature, are very similar to liposomes, in that they self-assemble into a bilayer shell, encapsulating an aqueous core. However, amphiphilic block copolymers are typically much larger than the lipids that contribute to the formation of liposomes, and as a result, the hydrophobic portion of the membrane is much thicker. This associated thickness, in contribution to the viscous, mesh-like overlay of the hydrophobic polymer chains, means that polymer membranes are significantly less permeable than their lipid counterparts.

When trying to understand the effect a polymer membrane has on the reaction profile of the urea-urease reaction, a known lipid control must be incorporated. In this instance, DPhPC is used, however, because we cannot determine the phosphorus concentration of a polymersome sample, we must designate equal starting concentrations of each surfactant, and once subjected to the same purification techniques, we can assume that the final concentrations of each sample are roughly equal. In the example below (Figure 4.24), stock concentration of DPhPC, PbD-PEO (1800), and PbD-PEO (3800) was set at 88.6 mM, and, after purification with size-exclusion chromatography, and a likely dilution of 1 in 4, we can assume the final concentration of vesicles

in each sample is ~20 mM. It can be seen from first instance that, as the membrane thickness increases, from a lipid to a larger polymer, and then again to an even larger polymer, that we see some profound effects on the reaction profiles.
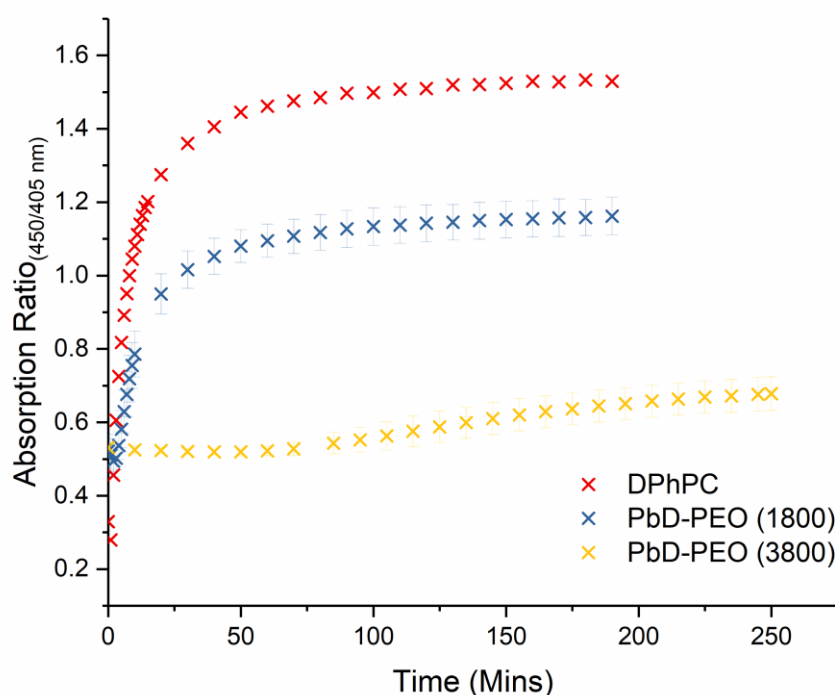
Figure 4.24. Change in absorption ratio (450/405 nm) for 200 nm vesicles (20 mM) of differing membrane compositions (DPhPC, PbD-PEO (1800), and PbD-PEO (3800)), encapsulating urease (10 µM) and HPTS (20 mM), following addition of urea (50 mM) (n = 3, error = ± SD).

However, if we are to look a little deeper, and extract our same three measurable parameters, i.e., clock time, final pH, and transition width (Figure 4.25), we can see some profound differences in the comparative values. Firstly, if we look at clock time, we see a 156% increase in clock time (4.7 min to 11.9 min) when switching from a lipid (DPhPC) membrane, to a polymer (PbD-PEO (1800)) membrane, and, a 1099% (11.9 min to 143.1 min) increase when the polymer membrane thickness is increase to PbD-PEO (3800). This means that, in first instance, clock time, when switching from DPhPC to PbD-PEO (3800) increases by 2966%. A similar trend is witnessed for transition width, where, following the same patterns, transition width increases by 55.9% (DPhPC to PbD-PEO (1800)) and a further 161.2% (PbD-PEO (3800)). However, a more significant difference in final pH, for DPhPC, PbD-PEO (1800), and PbD-PEO (3800), than seen in

137

comparative samples, i.e., 7.52, 7.33, and 7.00, respectively, raises questions about uniformity, in terms of encapsulation efficiency, and enzyme activity, where higher temperatures are used to resuspend the dried polymer film.

Theoretically, a thicker, more viscous membrane, and as such, a reduced permeability, should of course have an effect on the reaction profile, but, in these experiments, it is hard to extract whether the differences seen are due to the membrane type, or whether they are caused by variations in encapsulation efficiency, variations in sample concentrations, and/or variations in enzyme activity following more robust heating for PbD-PEO (3800). In likelihood, the heating of the PbD-PEO (3800) sample to 90°C, is likely to have affected the activity of urease, however, it does open questions as to whether clock time can be controlled in a post-generative fashion, using heat treatment.
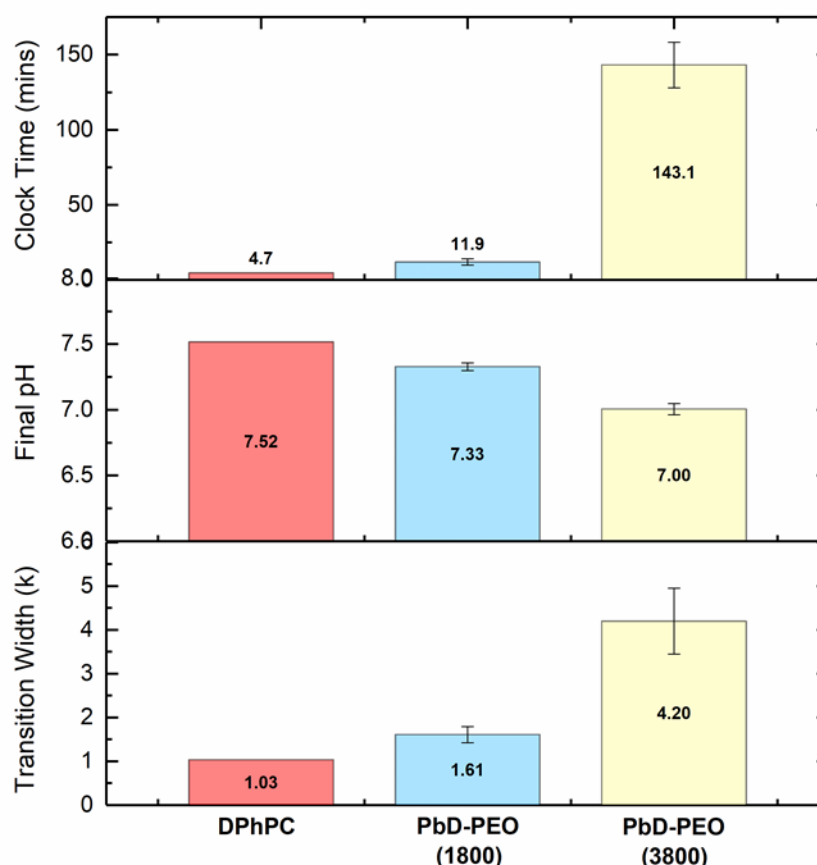
Figure 4.25. Comparing clock time, final pH, and transition width of DPhPC, PbD-PEO (1800), and PbD-PEO (3800) vesicles (size; 200 nm, surfactant concentration; 88.6 mM, urease; 10 μM, HPTS; 20 mM, urea; 50 mM) (n = 3, error = ± SD).

4.3.8 Temperature Control

In an experimental control, set up to better understand the effects seen with thick-membraned polymer vesicles (requiring robust heating in their generation), led to an idea, where heating above the temperature threshold of urease, for a controlled amount of time, could alter the reaction profile of a confined urea-urease reaction, in a post-generative fashion. In this experiment, three identical vesicle samples were all placed in a heater bath, and were sequentially removed after 1, 5, and 10 minutes. After purification, phosphate quantification, and dilution, the reaction was initiated through addition of urea, and the absorption ratio was monitored (Figure 4.26). As we can see from this initial data, increasing the duration of heating has a direct effect on the reaction profile witnessed.
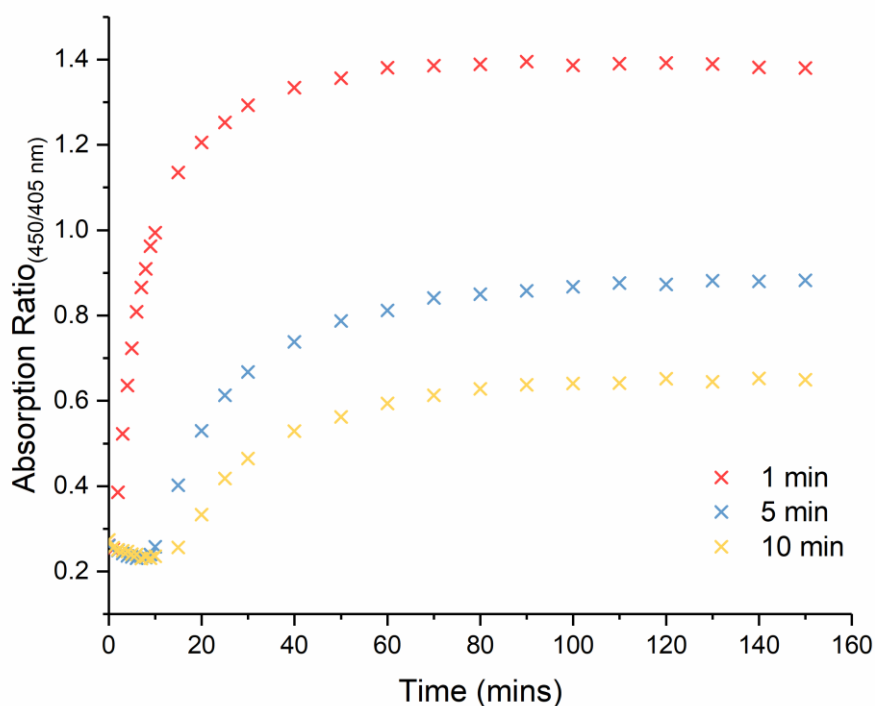
Figure 4.26. Change in absorption ratio (450/405 nm) for 200 nm DPhPC vesicles, encapsulating urease (10 μM) and HPTS (20 mM), which have been heat treated at 90°C for 1, 5, and 10 minutes, before addition of urea (50 mM)

If we are to look closer at our three standard parameters, i.e., clock time, final pH, and transition width (Figure 4.27), we see a considerable trend comparable to adjusting one of our standard starting concentrations, where a 297% increase in clock time (5.7 min to 22.5 min) was

witnessed when heating at 90°C is extended from 1 minute, to 5 minutes, and a further 30% increase (22.5 min to 29.2 min) was witnessed from 5 minutes to 10 minutes. A similar trend is observed for transition width, where, following the same patterns, transition width increases by 107% between 1 and 5 minutes, and a further 11.6% between 5 and 10 minutes. Finally, as we would expect, in instances where urease activity has been reduced, we see a relationship between final pH, and the amount of time spent under heated conditions. Extending the heating time from 1 minute to 5 minutes, and then 5 minutes to 10 minutes, produced a reduction in the final pH that the reaction tends towards of 4.01% and 2.63%, respectively. As is the pattern emerging, where, the greatest effect on each of the measurable parameters, occurs between 1 and 5 minutes of heating, it would appear that the affect heat has on the reaction profile is nonlinear, and, the greatest control over clock time may be achieved between 1 and 5 minutes.
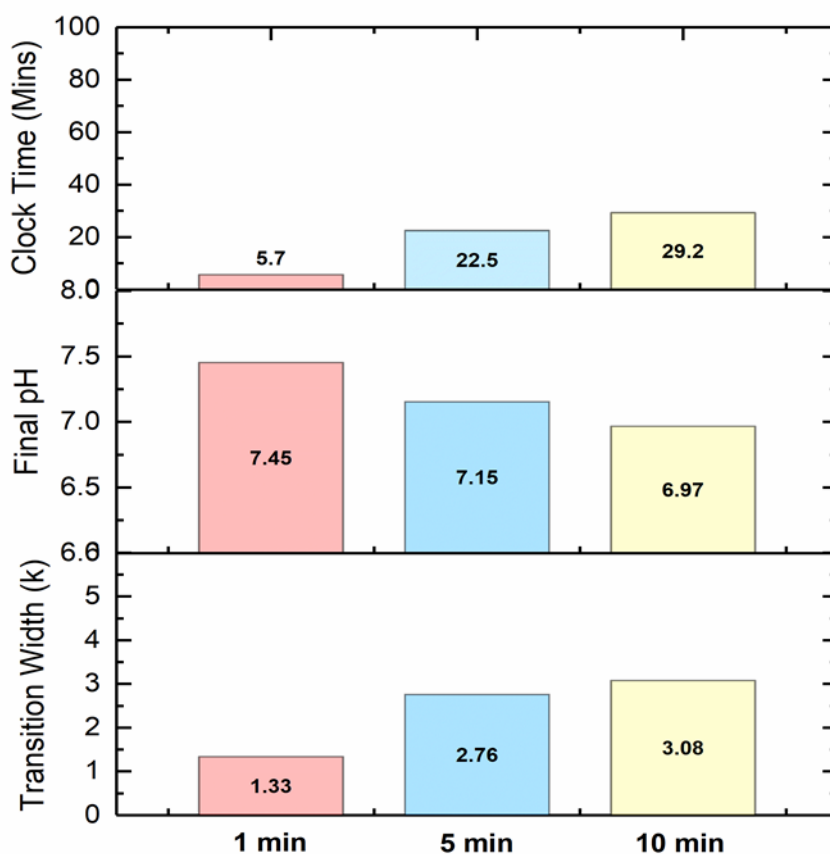
Figure 4.27. Comparing clock time, final pH, and transition width of heat treated (90°C for 1, 5, and 10 min) DPhPC vesicles (size; 200 nm, phosphorus concentration; 250 µM, urease; 10 µM, HPTS; 20 mM, urea; 50 mM)

4.3.9 Inter-Vesicle Communication

There is logic to assume that by increasing encapsulated urease concentration, or by increasing vesicle size, and as such, increasing the number of urease molecules encapsulated, that these parameters would have the greatest impact on the kinetics of our system, however, this has not been reciprocated. Given what we have learned from Section 1.6.2, 3.2.2, and 4.2.2, with regards to species permeation, and the differences between internal and external environments, a question has been raised about the possibility of inter-vesicle communication. To test this, we created two species of vesicles, one encapsulating urease-only and the other encapsulating HPTS-only. If communication is present, the products produced by the first species, upon initiation with urea, would cause a pH switch-like response in the second, HPTS-encapsulating species.

The first thing to point out is that pH-switch-like behaviour is present, confirming communicative behaviour (Figure 4.28). Interestingly, in system the pH-increasing ammonia permeates out of the vesicles as quickly as it is made, it may be a possibility that pH switching occurs outside the vesicle, and then the inside of our vesicle's lumens equilibrates to that of the outside. Secondly, when compared to our standard one-species system, we witness a greater robustness in pH-switching, more akin to what we see outside the vesicle in terms of final absorption ratio/pH (Figure 4.1) – an expected yield, where species one raises the pH of the external environment, and species two equilibrates to that. Another interesting thing to note is that there is a dip in pH, even in the urease-deficient vesicles, before the pH increases – this is believed to be attributed to a pH gradient being established across the membrane following addition of urea (presumably at a lower pH). Finally, it is interesting to note that where modelling predicted HPTS to be the reason why the pH inside the vesicle cannot reach that of the outside, here, we have stronger reason to believe this phenomenon is attributed to the buffering capacity of the enzyme.

Figure 4.28. Inter-vesicle communication between two species of 200 nm DPhPC vesicles (phosphorus concentration; 250 µM), where species one encapsulates urease (10 µM) and species two encapsulates HPTS (50 mM), following addition of urea (50 mM). A single species, encapsulating both HPTS and urease in the same concentration is added as a control.

4.4 Summary

Through the vast exploration of each available parameter, we have established a thorough understanding of the system, and how it can be controlled. Importantly, we have unearthed a relationship between the inside and outside of the vesicle, where, in the presence of internal buffering, changes in pH that originate in the vesicle lumen elicit a greater effect on the pH outside of the vesicle, in comparison to the inside. Likewise, we have established that through internal protein buffering, and pH transfer across the membrane, the pH on the inside when first encapsulated, isn't the pH on the inside once characterised, as they move towards equilibrium over time.

By way of an executive summary, we have established that decreasing starting pH, through increasing concentrations of HCl, results in an increase in clock time and transition width, and a decrease in final pH. Increasing urea and urease concentration causes a decrease in clock time and transition width, and an increase in final pH. Increasing urea concentration actually has the greatest effect on pH switching, however, unexpectedly, urease concentration is not a great influence. In fact, both urease concentration *and* vesicle size, two parameters predicted to have great effect on reaction kinetics, are not as important as once anticipated. There is evidence and logic to suggest that, because of inter-vesicle variation in protein copy number distribution within the sample, that increasing these two parameters would have a significant effect on our measurable parameters, however, because of the constant efflux and influx of reaction species in/out of the lumen, even in those potentially encapsulating no urease, it infers vesicular communication, and whole-sample, deterministic pH switching. For completeness, heat treating urea-containing vesicles is an attractive option for post-generation control of reaction kinetics, i.e., increasing the length of high heat treatment increases clock time and transition width, and decreases final pH.

Finally, from the data at hand, in instances of high and low vesicle size (100 and 400 nm) and urease concentration (5 and 20 µM), in combination with high and low urea concentration (10 and 250 mM) there is evidence of increased variability, when compared to 200 nm, 10 µM, and 50 mM. As such, these are defined as the optimum condition, and will be held as a baseline moving forward.

CHAPTER FIVE – DRUG RELEASE

5.1 Introduction

The potential of nanoreactors as drug delivery systems for low molecular weight drugs, proteins, nucleic acids, and other such molecules is huge. This potential, often driven by the enhancement of pharmacokinetic capabilities has seen more than ten liposomal-based drugs, e.g., Doxil™, put to clinical use [196, 197]. So, in this doctoral research, which has so far focused on understanding the effects of confinement and controlling the associated kinetics, the next goal is to combine nanoreactor technology and nonlinear enzyme kinetics to achieve temporal control over drug release.

In instances where passive-loading, i.e., loading during generation, is often associated with poor encapsulation efficiency, a major step in vesicle-based therapeutics was achieved through active-loading [196]; this is when drugs in a sufficient quantity to achieve therapeutic efficacy are loaded into preformed liposomes. The premise of this phenomenon takes advantage of the relative permeability of charged versus uncharged species, and as such, a suitable candidate for active loading must itself be capable of becoming ionised, where the degree of ionisation is intrinsically linked to the agent's pK_a and the pH of the surrounding environment. Not only this, but the molecule earmarked for encapsulation must also exhibit high solubility, and, as such, the only molecules that tend to fit such specific requirements are amphipathic weak acids or bases [196].

The first demonstration of active loading was achieved by Nichols and Deamer [198], where amphiphilic amines were loaded, down a pH gradient, into liposomes. Since then, this process has been improved upon, by way of producing pH and ion gradients through the salts of weak acids (e.g., acetate) or weak bases (e.g., ammonium) [199]. The associated ions can be present, depending on the pH of the surrounding solutions, as charged or uncharged species, where uncharged species are capable of crossing the liposomal membrane, capable of creating an ionic gradient leading to their exchange with amphipathic therapeutic entities [199].

With the internal and external pH maxima, in our case, being reached between pH 7.0 and 7.5, the ideal molecular profile of our drug would be a weak base with a pK_a around neutral. In this instance, the molecule will become ionised at low pH, becoming entrapped within the vesicle at the start of the reaction, however, once the reaction proceeds, and the pH of the system is increased, the therapeutic candidate will lose its charge, and will freely diffuse into the external environment.

One promising candidate, cimetidine (Figure 5.1), a histamine H_2-receptor antagonist, is an example of a weakly basic (pK_a; 6.9), water-soluble (0.938 mg/mL), and small-molecule drug (M_r;

252.3) used to treat gastrointestinal disorders such as gastric/duodenal ulcers, gastroesophageal reflux disease (GERD), and pathological hypersecretory conditions [200]. Just as *H. pylori* protects itself in the mucosal lining of the stomach, through the urease-catalysed conversion of urea (found in abundance in the stomach), to create a cloud of acid-neutralising byproducts, i.e., ammonia and carbon dioxide [201], one could imagine an instance where urease-encapsulating nanoreactors could not only be used to control the release of a compound, but to maintain that compound's therapeutic effect once released. This ideal may one day be translated out of the stomach, and into the acidic microenvironment of a urea-rich tumour, i.e., kidney. Here, the effect elicited by the urease-encapsulating nanoreactors on their external environment could be used to generate a more favourable microenvironment before the drug is even released, boosting efficacy, as well as helping to clear excess urea associated with tumour-related renal failure [202]. Similarly, another interesting avenue of exploration may be rooted in the treatment of dementia, where a build-up of urea in the brain is now known to be a primary contributor [203].
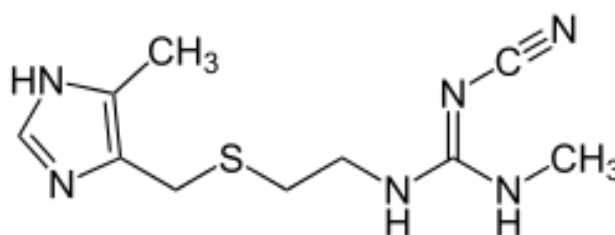
Figure 5.1. Chemical structure of cimetidine

Therefore, in this chapter, firstly, we are going to find an effective method of measuring cimetidine concentration whilst in a multi-component solution, whilst testing the capacity of cimetidine to be actively loaded down a pH gradient (HEPES; pH 7.4 → citrate buffer; pH 4.0). Next, we are going to leverage what we know about inter-vesicle communication, where one species of nanoreactors, housing urease, are responsible for neutralising the charge of cimetidine encapsulated in a second species of nanoreactors, to create a communicative drug release system.

5.2 Experimental

5.2.1 Materials

The lipid, 1,2-diphytanoyl-sn-glycero-3-phosphocholine (DPhPC), and the fluorescent lipid marker (1,2-dioleoyl-*sn*-glycero-3-phosphoethanolamine-N-(lissamine rhodamine B sulfonyl) (ammonium salt)) (Rhod-DOPE), were purchased from Avanti Polar Lipids Inc. Poly(butadiene)-poly(ethylene oxide) (PbD (1200)-PEO (600)) was purchased from Polymer Source. The ratiometric pH probe 8-hydroxypyrene-1,3,6-trisulfonic acid trisodium salt (HPTS), Urease from *Canavalia ensiformis* (Jack Bean), cimetidine, (4-(2-hydroxyethyl)-1-piperazineethanesulfonic acid) (HEPES), citric acid monohydrate, trisodium citrate dihydrate, and Slide-A-Lyzer™ MINI Dialysis Devices (2K MWCO, 0.1 mL) were purchased from Sigma-Aldrich.

5.2.2 Cimetidine Calibration

5.2.2.1 Cimetidine Only

Cimetidine (252.34 g/mol) was dissolved in dilute HCl (0.2 mM) to give a 1 mg/mL stock solution. This stock solution was serially diluted, giving cimetidine solutions, in dilute HCl (0.2 mM), of 0.0, 1.0, 2.5, 5.0, 10, 20, 30, 40, and 50 µg/mL. Each solution was placed into a quartz-standard microcuvette, and their absorption was measured (between 200 and 300 nm) using a Cary 100 Ultraviolet-visible spectrometer. A baseline correction was performed, and the resulting absorption at 219 nm was plotted as a calibration curve.

5.2.2.2 Cimetidine and DPhPC Vesicles

"Thin film rehydration" (Section 2.2.2), was used to produce 200 nm DPhPC and Rh-DOPE (0.5 mol%) liposomes, with dilute HCl (0.2 mM) both inside and outside of the vesicle lumen. A phosphorus assay (Section 3.2.3.1) was then used to determine the total phosphorus content of the sample. The cimetidine solutions outlined above (0.0, 1.0, 2.5, 5.0, 10, 20, 30, 40, and 50 µg/mL) were made again in the same way (Section 5.3.1.1), however, 250 µM of the DPhPC vesicles were present in each sample. Again, each solution was placed into a Quartz Standard microcuvette, and their absorption was read (between 200 and 300 nm) using a Cary 100 Ultraviolet-visible spectrometer. A baseline correction was performed, and the resulting absorption at 219 nm was plotted as a calibration curve.

5.2.2.3 Cimetidine and HPTS

A stock solution of HPTS (50 mM) was prepared. The cimetidine solutions outlined above (0.0, 2.5, 5.0, 10, 20, 30, 40, and 50 μg/mL) (Section 5.3.1.1) were made again, in the same way, however, this time, 50 μM of HPTS was present in each sample. Each solution was placed into a 3.5 mL Quartz Standard cuvette, and their absorption was read (between 200 and 300 nm) using a Cary 100 Ultraviolet-visible spectrometer. A baseline correction was performed, and the resulting absorption at 219 nm was plotted as a calibration curve.

5.2.3   Active Loading and Encapsulation Efficiency

Stock solutions (100 mL, 1 M) of citric acid monohydrate and trisodium citrate dihydrate were produced and used to create a citric acid buffer solution (100 mM, pH 4). Similarly, a 500 mL stock solution of HEPES buffer pH 7.4 (HEPES (20 mM) and NaCl (40 mM)) was produced.

"Thin film rehydration" (Section 2.2.2), was then used to produce 200 nm DPhPC and Rh-DOPE (0.5 mol%) liposomes, encapsulating citric acid buffer (100 mM, pH 4). The external citric acid buffer was exchanged for HEPES buffer, through size-exclusion chromatography (column: 1.5 x 15 cm, media: Sephadex G-50), using HEPES buffer as the mobile phase. Part (200 μL) of the sample was removed at this point and stored. To the remaining liposome solution, cimetidine was added to give a final concentration of 0.24 mg/mL, and the solution was stirred, using a 5 mm magnetic stirrer bar, for 30 minutes, to ensure complete dissolution. The cimetidine/liposome solution was then incubated at 65°C for 30 minutes, where the cimetidine would travel down the pH gradient, and become protonated (and therefore trapped) within the vesicle.

The same size-exclusion column with dilute HCl (0.2 mM) as the stationary and mobile phase, was used to remove unencapsulated cimetidine, and to exchange the external HEPES buffer. A phosphorus assay (Section 3.2.3.1) was then used to determine the total phosphorus content of each sample (pre- and post-cimetidine), and the "post-cimetidine" sample was diluted to 250 μM phosphorus content. The calibration curve above in Section 5.3.1.2 was used to determine the total cimetidine concentration in 250 μM of vesicles, which was multiplied by the dilution factor ("pre-cimetidine" vesicle concentration/250), and then calculated as a percentage of the initial cimetidine concentration (0.24 mg/mL).

5.2.4   Overcoming Buffering Potential via Vesicle-to-Vesicle Communication

Two species of 200 nm DPhPC and Rh-DOPE (0.5 mol%) vesicles were produced via "thin film rehydration" (Section 2.2.2). The first species encapsulated HPTS (20 mM) in citric acid buffer (100 mM, pH 4), where the external HPTS and citric acid buffer was removed/exchanged, through size-exclusion chromatography (column: 1.5 x 15 cm, media: Sephadex G-50, stationary phase: dilute HCl (0.2 mM)), using dilute HCl (0.2 mM) as the mobile phase. The second species encapsulated urease (10 µM) in dilute HCl (0.2 mM), and, again, size-exclusion chromatography was used to removed unencapsulated urease.

A phosphorus assay (Section 3.2.3.1) was then used to determine the total phosphorus content of each sample, and a solution containing 500 µM of each species was generated. An aliquot (250 µL) of this sample was placed in a 550 µL micro-cuvette, and a Cary 100 ultraviolet-visible spectrometer was used to monitor changes in HPTS absorption ratio (450/405 nm), over time, when 250 µL urea (100 mM) was added. Three independent repeats were performed, and error was presented as ± standard deviation (SD).

5.2.5   Drug Release

Two species of 200 nm DPhPC and Rh-DOPE (0.5 mol%) vesicles were produced via "thin film rehydration" (Section 2.2.2). The first species encapsulated urease (5 or 10 µM) and HPTS (20 mM) in dilute HCl (0.2 or 0.32 mM), where, size-exclusion chromatography, with the corresponding solution of HCl used to suspend the encapsulants, was used to removed unencapsulated urease and HPTS.

The second species encapsulated HPTS (20 mM) in citric acid buffer (100 mM, pH 4). The external citric acid buffer was exchanged for HEPES buffer, through size-exclusion chromatography, using HEPES buffer as the mobile phase. Cimetidine was added to give a final concentration of 1 mg/mL, and the solution was stirred, using a magnetic stirrer bar, for 30 minutes, to ensure complete dissolution. The cimetidine/liposome solution was then incubated at 65°C for 30 minutes, where the cimetidine would travel down the pH gradient, and become protonated (and therefore trapped) within the vesicle. A size-exclusion column, with a corresponding concentration of dilute HCl as the mobile phase, was used to remove unencapsulated cimetidine, and to exchange the external HEPES buffer, leaving cimetidine and citric acid (100 mM, pH 4)-encapsulating liposomes in dilute HCl.

A phosphorus assay (Section 3.2.3.1) was used to determine the total phosphorus content of each sample, and a "vesicle stock solution" containing 500 µM of each species was made. Simultaneously, in a 3.5 mL quartz cuvette, a magnetic stirrer bar is placed, and 2.85 mL of urea (10.1754 or 50.8772 mM) and HPTS (50.8772 µM) solution is made, and an aliquot (50 µL) is extracted. A Slide-A-Lyzer™ MINI Dialysis cup (2K MWCO, 0.1 mL) is placed in the top of the cuvette, sealed with parafilm, and the previously extracted 50 µL of urea and HPTS solution is placed inside the cup. The cuvette is placed inside a Cary 100 ultraviolet-visible spectrometer, and an absorption spectrum was obtained, between 200 and 450 nm, over time, when 50 µL of the aforementioned vesicle stock solution is added (total volume 2.9 mL, urea (10 or 50 mM), HPTS (50 µM)). As the pH switches, cimetidine is deprotonated and released, where it can diffuse from the dialysis cup, into the cuvette, and be read by the Ultraviolet-visible spectrometer. This value can then be converted to a concentration, using the calibration curve in Section 5.3.1.3.

5.3   Results and Discussion

5.3.1   Cimetidine Calibration

As we know, the absorption spectra of a chemical species are generated when a beam of electromagnetic energy (light) is passed through a sample, and a proportion of the photons within that beam are absorbed by the chemical species therein [204]. Here, we assume that absorbance (A) is directly proportional to both the concentration (c) of the solution, and the length of the light path (l), and through the inclusion of a proportionality constant (ϵ), Beer-Lambert law can be used to help determine the concentration of an analyte within a sample.

$$A = \epsilon c l$$

Equation 5.1. Beer-Lambert Law

5.3.1.1 Cimetidine Only

Thus, if we consider our compound of choice, cimetidine, it is important to ascertain whether it obeys Beer-Lambert's law, and for what concentration range. As such, an absorption spectrum of varying concentrations of cimetidine, between 0 and 100 µg/mL, dissolved in dilute HCl (0.2 mM), were originally taken, however, upon further analysis, it was shown that Beer-Lambert's law was only obeyed up to a maximum concentration of 50 µg/mL, and as such, it was only these values that are shown (Figure 5.2). A baseline correction was performed (Figure 5.3), and a calibration curve for cimetidine (@ 219 nm) was produced (Figure 5.4).

Concentration dependent absorption of cimetidine at 219 nm
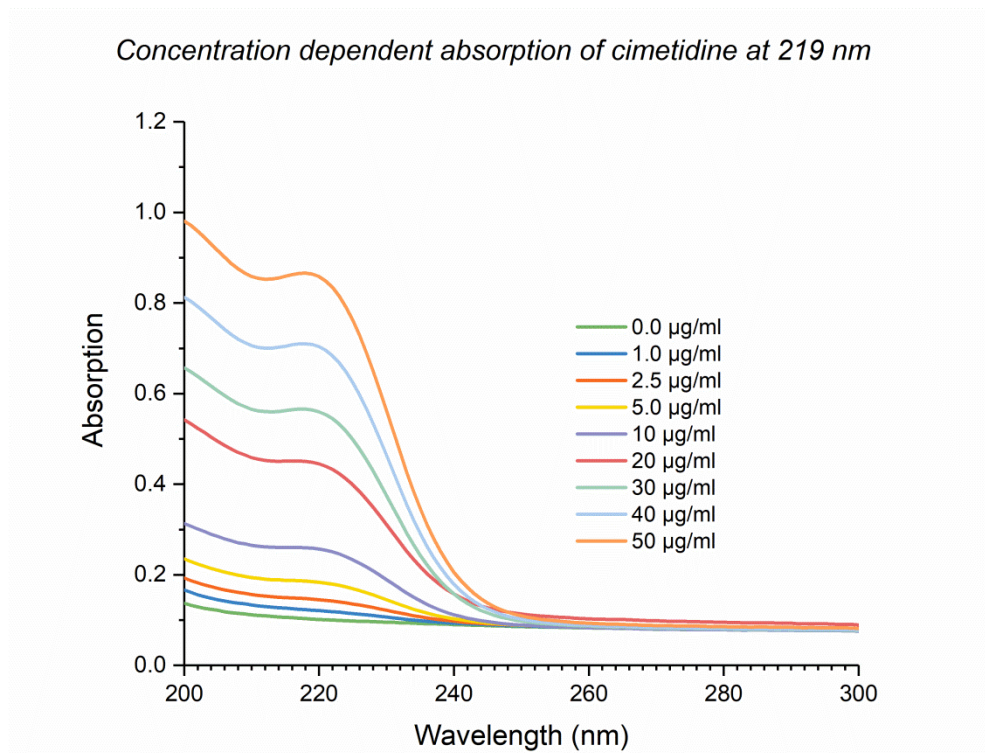
Figure 5.2. Absorption spectra for various cimetidine concentration (0 – 50 μg/mL) in dilute HCl (0.2 mM)

Concentration dependent absorption of cimetidine at 219 nm (baseline adjustment)
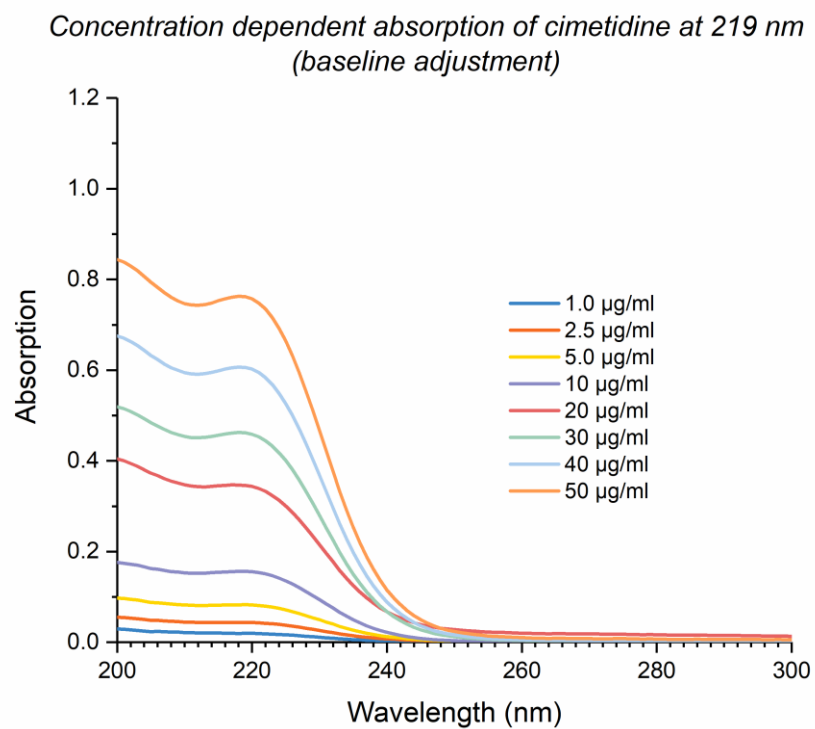
Figure 5.3. Baseline correction of cimetidine absorption for concentrations between 1 and 50 μg/mL

152
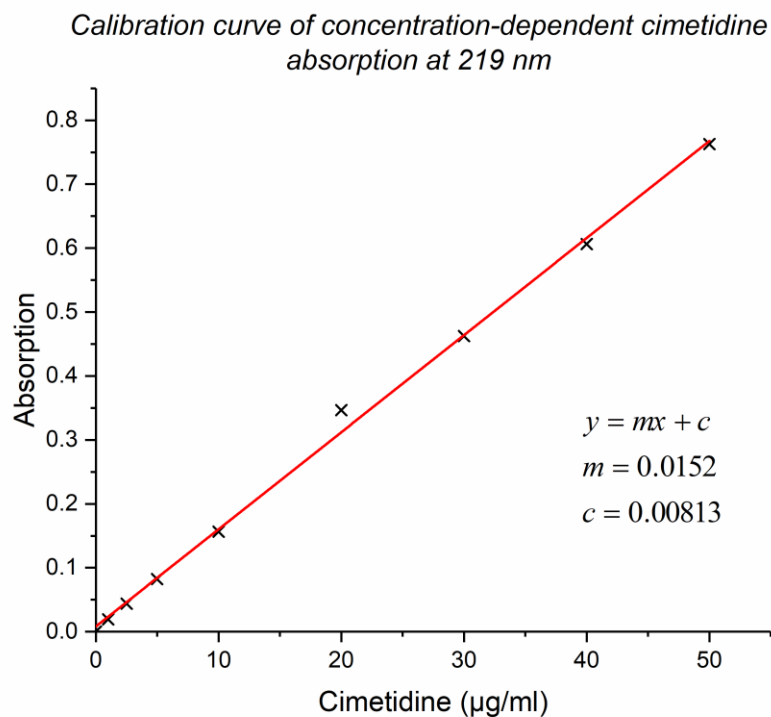
Figure 5.4. Calibration curve at 219 nm for cimetidine concentration, between 0 and 50 µg/mL, in dilute HCl (0.2 mM), showing conformation to Beers-Lambert law.

5.3.1.2 Cimetidine and DPhPC Vesicles

However, although we can comfortably appreciate that cimetidine in solution conforms to Beer-Lambert law, to test the encapsulation efficiency when subjected to active loading, a second calibration curve, which is mindful of the scattering effects talked about in Section 3.3.3, must be produced. In this instance, solutions of cimetidine, which conformed to the original concentrations outlined above (Section 5.3.1.1), were produced in the presence of 250 µM (phosphorus concentration) of DPhPC vesicles, and their absorption spectra was taken (Figure 5.5). Although clear scattering effects were present, a baseline correction (Figure 5.6) showed clear conformation to Beer-Lambert law, and an appropriate calibration curve, at 219 nm, was produced (Figure 5.7).
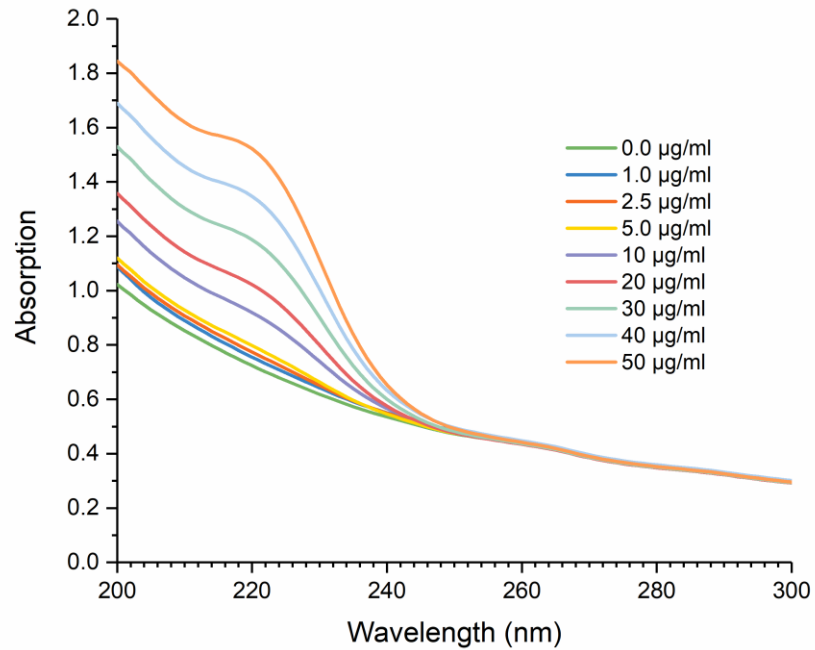
Figure 5.5. Absorption spectra for various cimetidine concentration (0 – 50 μg/mL), in the presence of DPhPC vesicles (250 μM phosphorus concentration), in dilute HCl (0.2 mM)

Figure 5.6. Baseline correction of cimetidine absorption, in the presence of 250 μM (phosphorus content) of DPhPC vesicles, for concentrations between 1 and 50 μg/mL
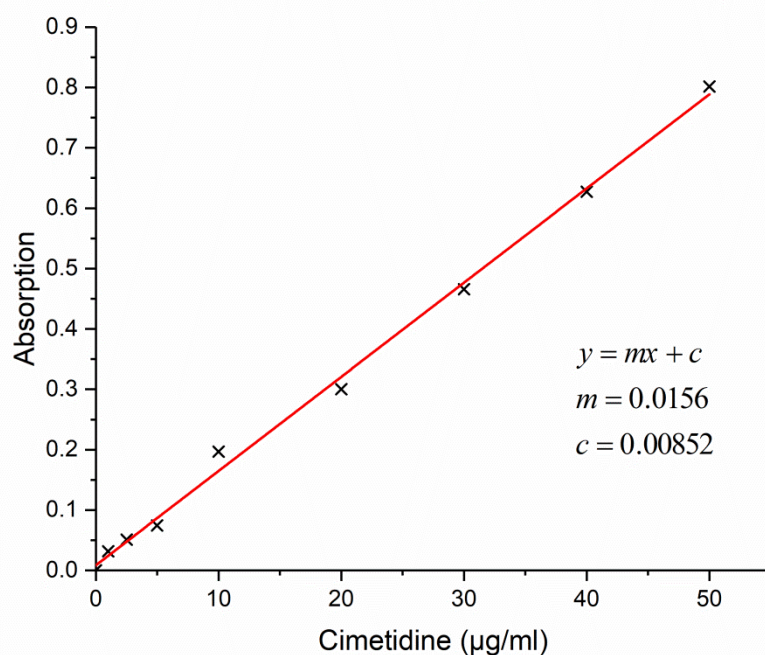
Figure 5.7. Calibration curve, at 219 nm, for cimetidine (0 – 50 μg/mL) in presence of DPhPC vesicles (250 μM phosphorus content)

5.3.1.3 Cimetidine and HPTS

Finally, for the experiment outlined in Section 5.2.5, where a Slide-A-Lyzer™ MINI Dialysis cup (2K MWCO, 0.1 mL), holding two species of vesicles capable of communicative drug-release, is placed inside a 3.5 mL cuvette, thus allowing the transfer of cimetidine into the HPTS-containing cuvette, a third calibration curve must be generated. This time, solutions of cimetidine, which conformed to the original concentrations outlined above (Section 5.3.1.1), were produced in the presence of HPTS (50 μM) (Figure 5.8). Although clear interference of HPTS was present, a baseline correction (Figure 5.9) showed clear conformation to Beer-Lambert law, and an appropriate calibration curve, at 219 nm, was produced (Figure 5.10), thus allowing us to monitor both pH change, in terms of absorption ratio, and cimetidine release, for our drug release experiments.
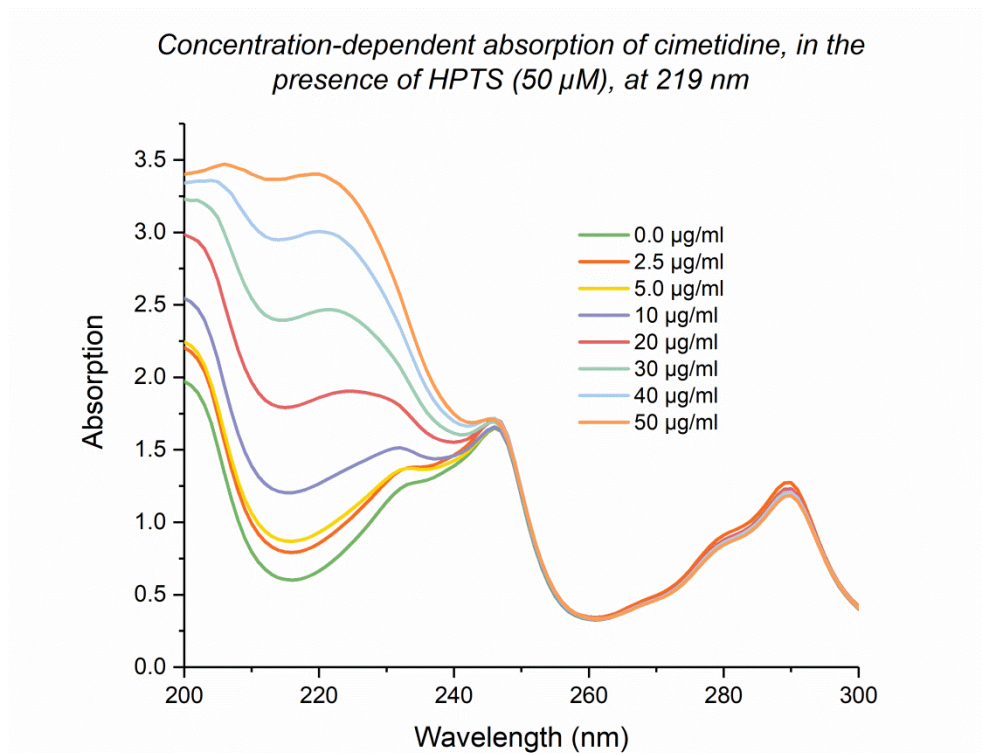
Figure 5.8. Absorption spectra for various cimetidine concentration (0 – 50 μg/mL), in the presence of HPTS (50 μM), in dilute HCl (0.2 mM)
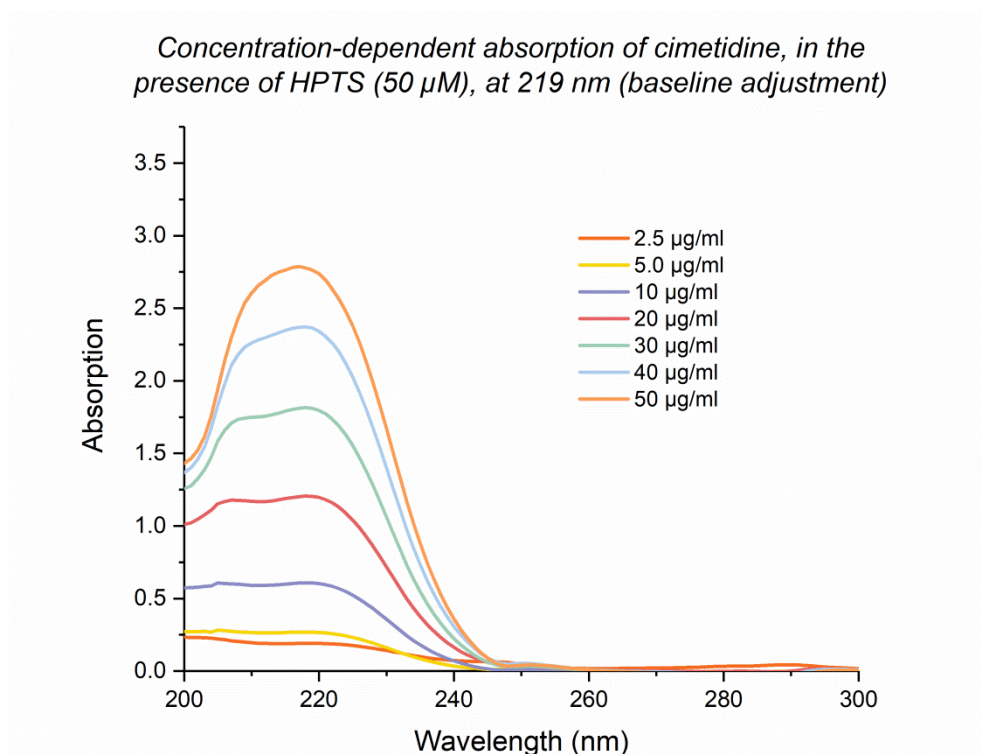
Figure 5.9. Baseline correction of cimetidine absorption, in the presence of 50 μM HPTS, for concentrations between 1 and 50 μg/mL
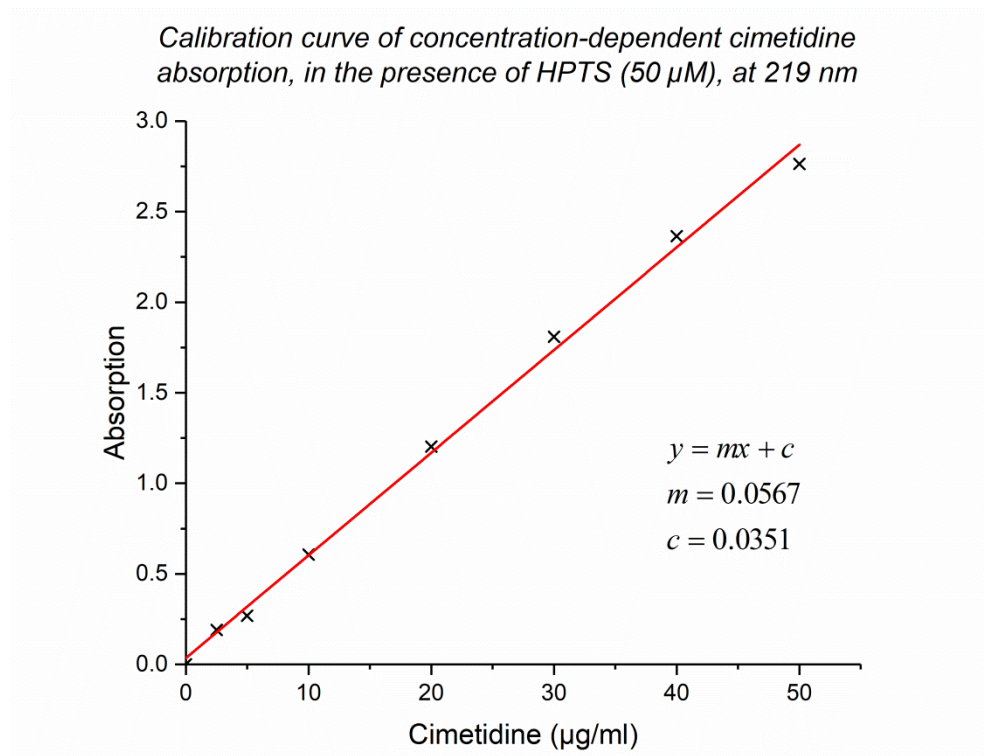
Figure 5.10. Calibration curve, at 219 nm, for cimetidine (0 – 50 µg/mL) in presence of HPTS (50 µM)

5.3.2 Active Loading and Encapsulation Efficiency

To determine the capability of our vesicles in encapsulating cimetidine, and to understand the encapsulating efficiency of our methodology, a sample of DPhPC vesicles encapsulating citrate buffer was purified via size exclusion chromatography, with HEPES buffer as the mobile phase, and 3 mL of the eluent was collected. Out of this 3 mL, 1 mL was separated and designated "pre-cimetidine", and the remaining 2 mL, designated "post-cimetidine" underwent active loading, as described above. A phosphorus assay of each sample was conducted, reporting the average concentration of "pre-cimetidine" to be 1384 ± 95 µM, and the average concentration of "post-cimetidine" to be 889 ± 42 µM. Each sample was diluted to 250 µM, and their absorption was read between 200 and 300 nm. A baseline reduction ("post-cimetidine" minus "pre-cimetidine") was conducted, and the resulting spectrum plotted (Figure 5.11). Using our calibration curve above (Figure 5.7), a concentration value of 39.81 µg/mL was extracted, and using our known dilution factor, 5.54, i.e., 1384/250, and our starting cimetidine concentration (240 µg/mL), we can successfully determine our encapsulation efficiency to be approximately 92% (((39.81 x 5.54)/240)*100).

Figure 5.11. Absorption of cimetidine in 250 µM (phosphorus concentration) DPhPC vesicles (200 nm), following baseline correction, showing concentration equivalent as 39.82 µg/mL

5.3.3 Overcoming Buffering Potential via Vesicle-to-Vesicle Communication

For our drug to be released in a communicative fashion, the pH of the cimetidine-containing vesicles must be increased, to neutralise the drug. In chapter four, we discussed the potential of inter-vesicular communication to affect the luminal pH of HPTS-only containing vesicles, however, in this instance, a new question is asked; is inter-vesicle communication strong enough to overcome the internal buffering potential of citrate buffer (needed for active loading)?

To simulate the conditions needed for our drug release studies, we adapted the communication experiments seen in Chapter Four. Two species of vesicles; one containing urease in dilute HCl (0.2 mM), and the other containing HPTS in citrate buffer (100 mM, pH 4) were generated, and upon addition of urea, it becomes evident that overcoming buffering potential, through communicative means, is possible (Figure 5.12). It is likely, given what we know about how the system works, where the external pH rapidly switches in relation to rapid ammonia transport out of the lumen, that overcoming the internal buffering potential of the vesicles in this scenario is aided by the disparity in volume between the vesicle lumen and the external environment,

and, by association, the strength of the pH gradient across the membrane. It is also worth mentioning that, as expected, pH-switching is comparatively slower under buffered conditions, than what was witnessed under non-buffered conditions in Chapter Four, however, the characteristic "dip" in pH at the beginning of the reaction is still present (due to urea addition at a lower pH of system's universal pH).
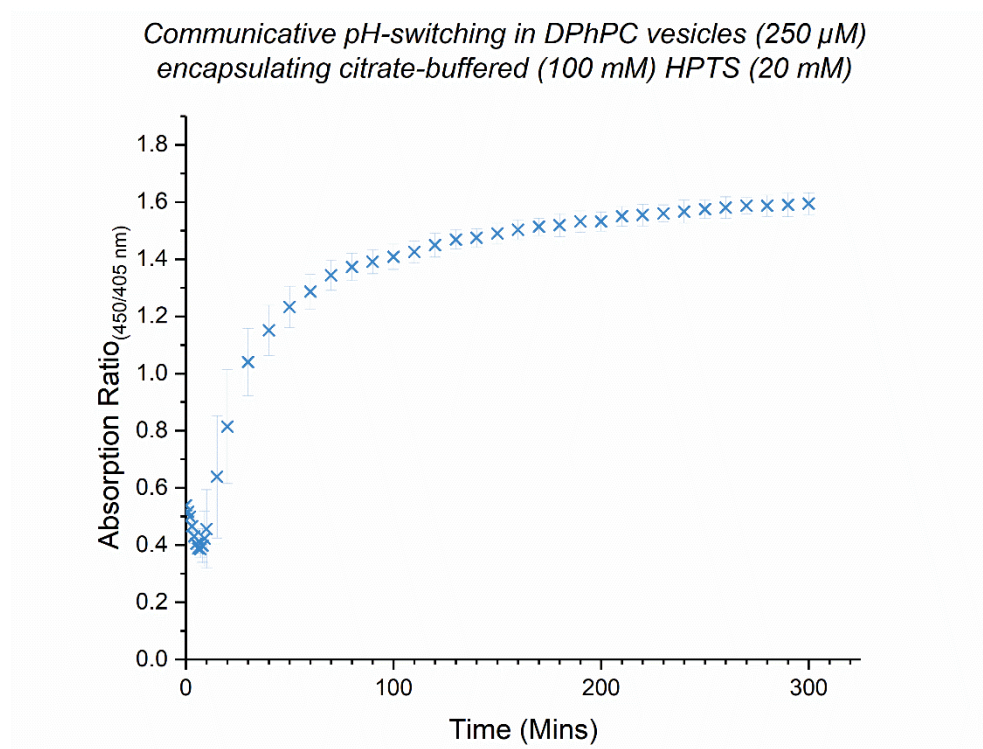
Figure 5.12. Communicative pH-switching between a urease (10 µM) in HCl (0.2 mM)-encapsulating species and a HPTS (20 mM) in citrate buffer (100 mM, pH 4)-encapsulating species of DPhPC vesicles (250 µM phosphorus content, 200 nm) (n = 3, error = ± SD).

5.3.4 Drug Release

Here, in a creative experimental setup (Figure 5.13), where, to a quartz cuvette containing urea and HPTS in dilute HCl, a dialysis cup, partially filled with equally concentrated urea and HPTS in dilute HCl, was inserted. This way, when the reaction is initiated by introducing our two species of vesicles, i.e., urease encapsulating and drug encapsulating, into the dialysis cup, the subsequent urea-urease reaction will raise the pH of the external solution, thus allowing us to

monitor the change in pH over time, and, as a consequence, the neutralised cimetidine, now capable of freely diffusing across the vesicular membrane, can also diffuse across the dialysis membrane, to also allow for drug concentration monitoring.
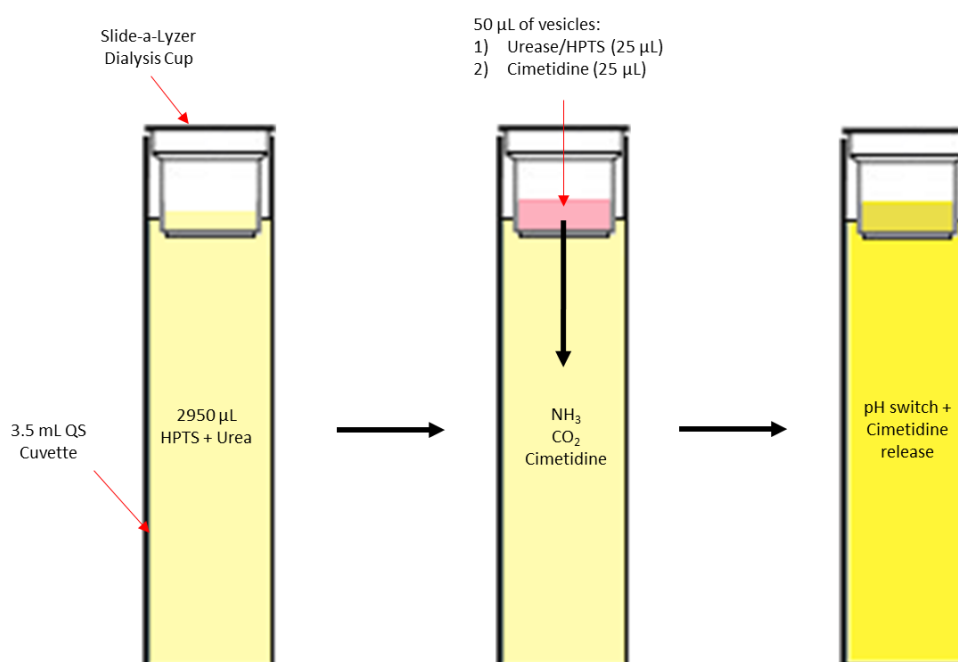
Figure 5.13. Experimental setup for drug release experiments, showing a Slide-a-Lyzer dialysis cup placed inside a 3.5 mL QS cuvette. Once the communicative vesicles are added to the cup/cuvette containing urea and HPTS, the reaction is initiated, and the associated NH_3 and CO_2 raises the pH of the whole cuvette, altering the permeability of cimetidine, which is subsequently released.

5.3.4.1 Control and Standard

To gain a better understanding of the natural rate of cimetidine release from DPhPC vesicles, a control experiment, where 250 μM (phosphorus concentration) of vesicles encapsulating cimetidine in citrate buffer were added to the dialysis cup, and the absorption values of the sample were monitored at 219, 405, and 450 nm for 10 hours (Figure 5.14). In this example, as we would expect, without the presence of a urease-containing species capable of invoking communicative release, the pH (represented by absorption ratio) does not increase, and as such, neutralisation of encapsulated cimetidine, and triggered release, is not achieved.

Cimetidine release from DPhPC vesicles without the assistance of a second, pH-switch-causing population of vesicles
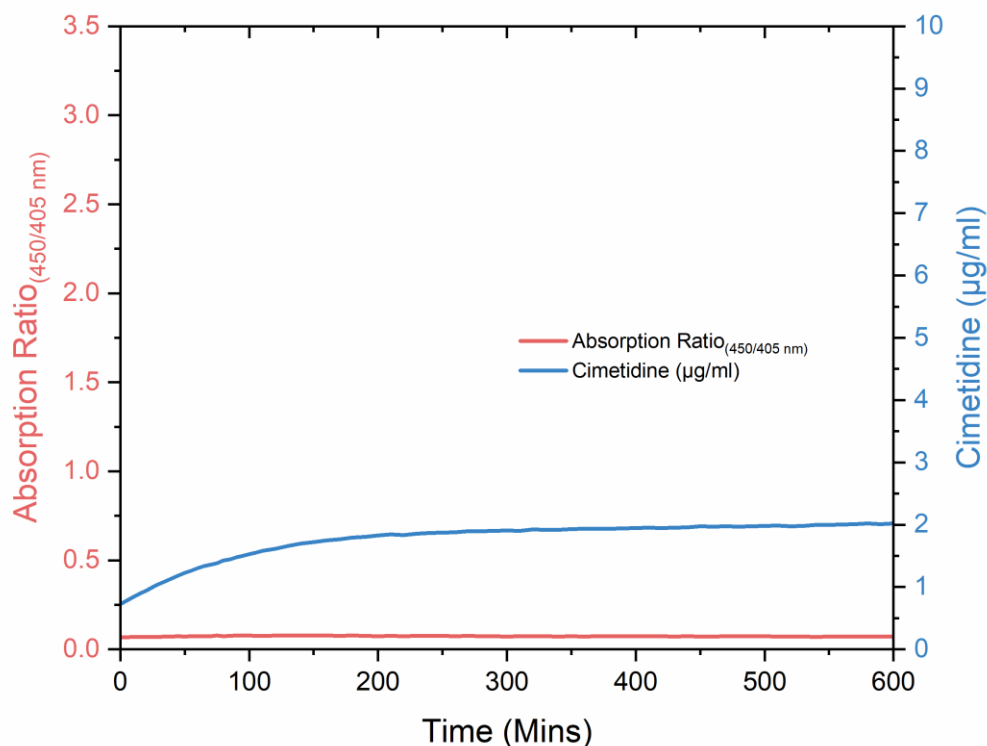
Figure 5.14. Drug release control, where only cimetidine in citrate buffer (100 mM, pH 4)-encapsulating DPhPC vesicles (200 nm, 250 μM phosphorus content) are added to the dialysis cup, without the presence of a communication-linked triggering species.

However, if we are to take our standard parameters, outlined at the end of Chapter Four, i.e., DPhPC (200 nm, 250 μM phosphorus concentration), urease (10 μM), urea (50 mM), and HCl (0.2 mM), we can ascertain a "typical" release profile for our drug release experiments (Figure 5.15). The first thing to notice, upon initial examination, is that the profile of each measured parameter is very similar, and conforms to our initial prediction, where increased pH would lead to increased cimetidine neutralisation, and therefore release. If we are to then apply our standard fitting parameter (Hill1), first discussed in Section 4.2.3, to each profile, i.e., the reaction profile of pH switching, and the reaction profile of drug release, we can more accurately compare the "clock time" (time taken to reach half maximum), and thus the relationship, between the two. Here, the clock time for pH switching is 28.9 min, and the clock time for cimetidine release is 29.9 min, inferring a strong correlation between the two.
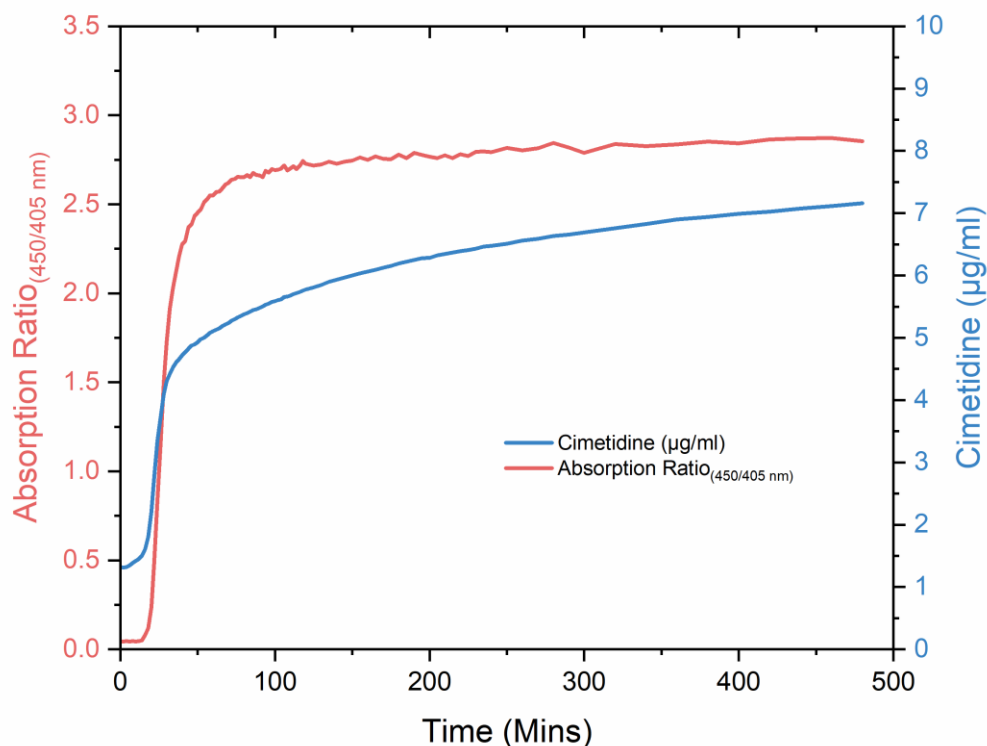
Figure 5.15. Drug release, where DPhPC vesicles (200 nm, 250 µM phosphorus content) encapsulating urease (10 µM) in HCl (0.2 mM) are used communicatively trigger cimetidine release from DPhPC vesicles (200 nm, 250 µM phosphorus content) encapsulating cimetidine in citrate buffer (100 mM, pH 4), in the presence of 50 mM urea.

5.3.4.2 Urea Concentration

Although we have achieved (approximately) a 30-minute delay in drug release using our "standard" concentrations, given what we learned in Chapter Four through our extensive parameter space exploration, it is likely that we can adjust said parameters to extend/control drug release, in a chronotherapeutic capacity. In this example, all the parameters are held constant, barring the concentration of urea, which is reduced from 50 mM to 10 mM. Here, upon first examination, we can see a comparable increase in the time taken for both the pH to switch and the drug to be released (Figure 5.16). In fact, for all our measurable parameters extracted from our fitting function, we see a predictable change, where clock time and transition width increase, and final pH (represented in this example by absorption ratio) decreases (Table 5.1) – this relationship between pH and drug release adds strong further evidence that drug release is triggered by the urease clock.

Table 5.1. Clock time, final absorption ratio(450/405 nm), and transition width for pH-switching and drug release, following adjustment of urea concentration (50 - 10 mM), when other experimental parameters are held constant (DPhPC (200 nm), urease (10 µM), HCl (0.2 mM))

	Absorption Ratio/AR (450/405 nm)		Cimetidine Concentration (µg/mL)	
Urea Concentration	50 mM	10 mM	50 mM	10 mM
Clock Time (min)	28.1	63.5	29.9	60.1
Final AR	2.74	2.61		
Transition Width	4.56	5.05	1.32	2.71
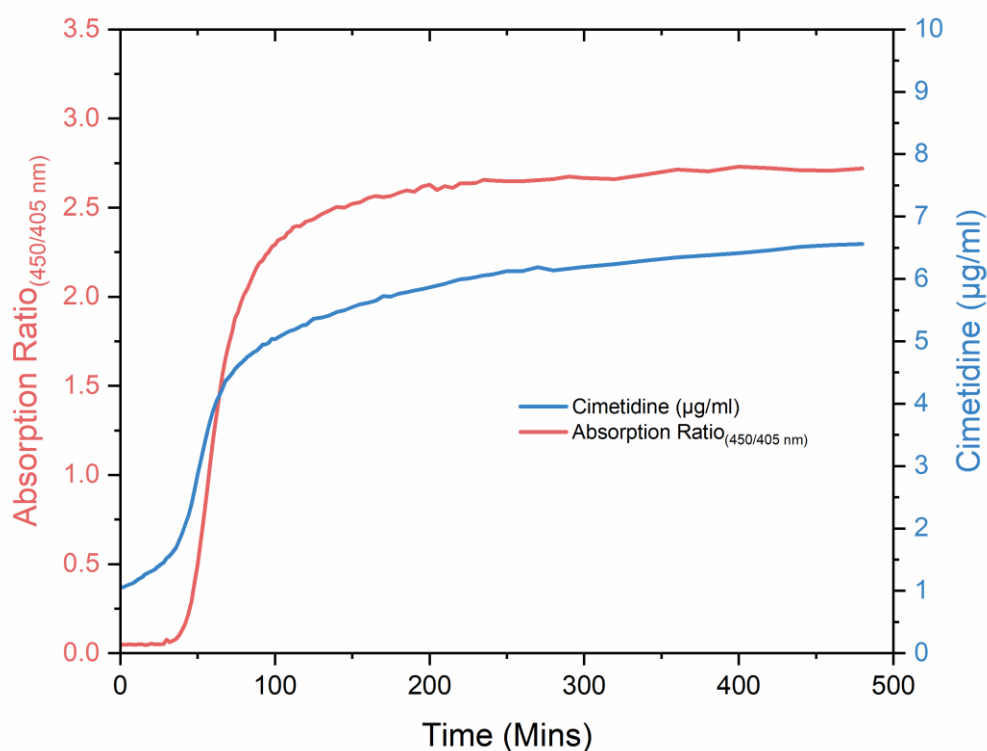
Figure 5.16. Drug release, where DPhPC vesicles (200 nm, 250 µM phosphorus content) encapsulating urease (10 µM) in HCl (0.2 mM) are used communicatively trigger cimetidine release from DPhPC vesicles (200 nm, 250 µM phosphorus content) encapsulating cimetidine in citrate buffer (100 mM, pH 4), in the presence of 10 mM urea.

5.3.4.3 Urease Concentration

Similarly, if we again hold all the standard parameters constant, but change the concentration of urease from 10 μM to 5 μM, we can see a comparable increase in the time taken for the pH to switch, the drug to be released, and, like we have seen before, the width of transition also increases (Figure 5.17). In fact, similarly to when we decrease urea concentration, all our measurable parameters alter in an expected way, i.e., clock time and transition width increase, and final pH (represented in this example by absorption ratio) decreases (Table 5.2).

Table 5.2. Clock time, final absorption ratio$_{(450/405\ nm)}$, and transition width for pH-switching and drug release, following adjustment of urease concentration (10 to 5 μM), when other experimental parameters are held constant, i.e., DPhPC (200 nm), urea (50 mM), HCl (0.2 mM)

	Absorption Ratio/AR (450/405 nm)		Cimetidine Concentration (μg/mL)	
Urease Concentration	10 μM	5 μM	10 μM	5 μM
Clock Time (min)	28.1	221.0	29.9	180.4
Final AR	2.74	1.98		
Transition Width	4.56	5.25	1.32	3.31
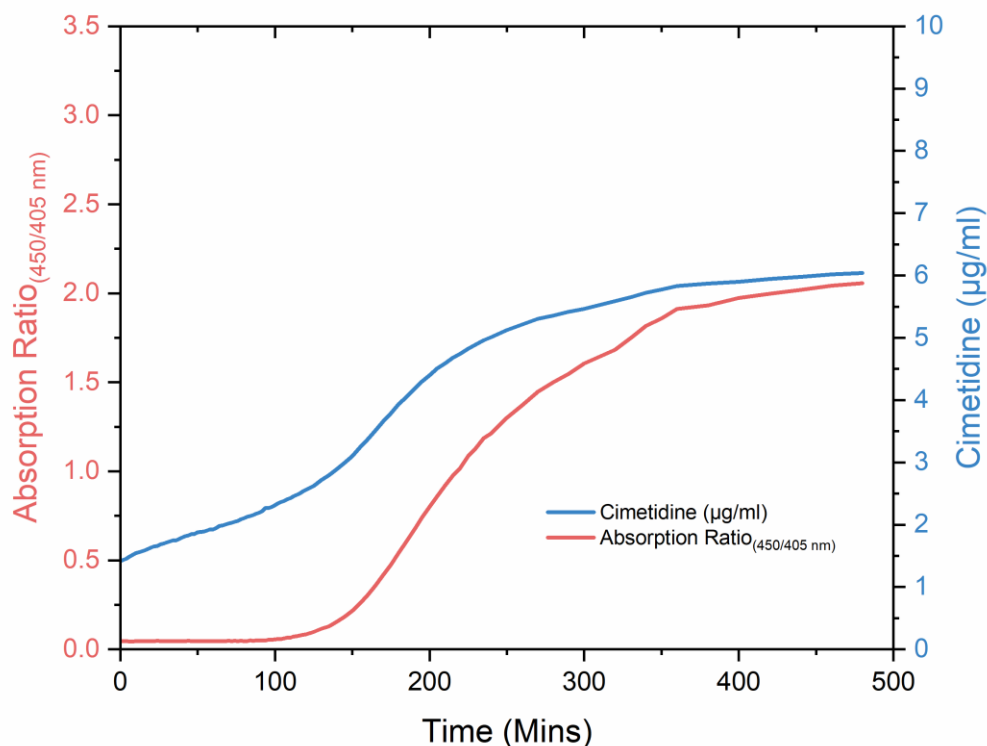
Figure 5.17. Drug release, where DPhPC vesicles (200 nm, 250 μM phosphorus content) encapsulating urease (5 μM) in HCl (0.2 mM) are used to communicatively trigger release from DPhPC vesicles (200 nm, 250 μM phosphorus content) encapsulating cimetidine in citrate buffer (100 mM, pH 4), in the presence of 50 mM urea.

5.3.4.4 Acid Concentration

Now, if we hold all our standard parameters constant, but adjust the concentration of HCl both used to suspend our encapsulants and as the mobile phase in size-exclusion chromatography, from 0.20 mM to 0.32 mM (pH 3.7 to pH 3.5), we see some remarkable results (Figure 5.18). Firstly, from 0 – 50 minutes, we see a passive rate of cimetidine diffusion across the membrane, then, as the urea-urease reaction begins to proceed, at around 100 minutes, we see a corresponding increase in the rate of release. Finally, although we cannot see the full reaction to completion, although we can assume the clock time would be somewhere around 600 minutes, we see a corresponding increase in cimetidine release, that mirrors the reaction profile of the pH of the cell.
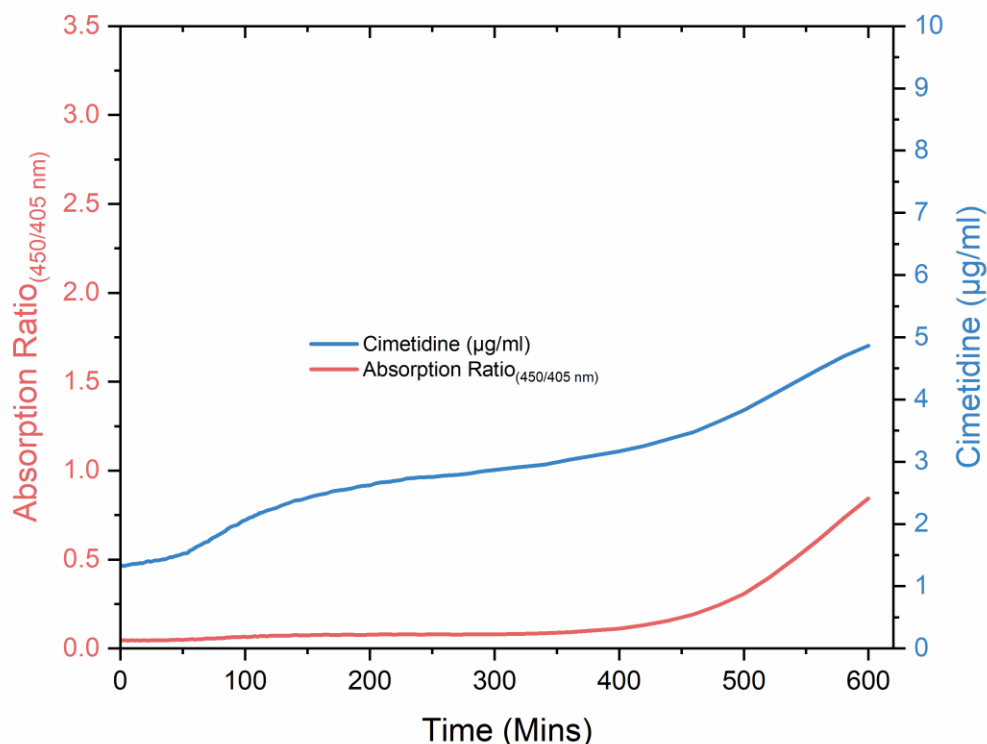
Figure 5.18. Drug release, where DPhPC vesicles (200 nm, 250 μM phosphorus content) encapsulating urease (10 μM) in HCl (0.32 mM) are used communicatively trigger cimetidine release from DPhPC vesicles (200 nm, 250 μM phosphorus content) encapsulating cimetidine in citrate buffer (100 mM, pH 4), in the presence of 50 mM urea.

5.4   Summary

Through the manipulation of charge, we have successfully loaded our model compound (cimetidine), and, utilised vesicle-to-vesicle communication and parameter space manipulation to create a tuneable, feedback-controlled drug delivery system. As previously described, the potential of chemical feedback in next-generation nanomedicine cannot be understated, and here, we have achieved a first demonstration of feedback-controlled drug delivery. As such, the significance of this finding, given its potential, is vast. However, not only have we devised a system capable of temporal control, but, in likeliness to *H. pylori* creating a cloud of acid-neutralising byproducts for protection, we have a drug delivery system capable of clearing urea, whilst generating a favourable external environment for drug release, be it in a protective capacity, or to boost efficacy.

CHAPTER SIX – ENZYMATIC PROPULSION OF NANOREACTORS

6.1 Introduction

The exploitation and conversion of chemical free energy into mechanical work is ubiquitous across all systems within nature, and is a vital component of survival in all organisms of varying complexity. From locomotion to vesicle transportation, phagocytosis to cell division, examples of substrate-driven mechanical work are commonplace within biological systems [205], and, in most instances, enzymes that are capable of converting substrates with specificity and efficiency provide the engine. Whether it be energy production via the dephosphorylation of ATP by ATPase, or the synthesis of DNA by DNA polymerase, countless examples of enzymes acting as biological workhorses exist [206]. In fact, in a more recent overview, enzymes themselves are effectively considered a type of nanomotor, given the revelation of enhanced diffusion (on a single molecule level) in response to catalytic activity [207-209].

In similarity to the discovery of nanoreactors, discussed in Section 1.6, the discovery of synthetic nanomotors grew from a similar seed; an endeavour to mimic their biological counterpart, with a hope to better understand their fundamentals and a view to control their use for wider application [210]. Since their first demonstration in 2004, nanomotors have received great attention for their potential applications in smart drug delivery [211], bio-nanotheragnostics [212], environmental remediation [213], etc. It is, therefore, not only important to understand and appreciate their fundamental biocatalytic processes, but to also ascertain a full understanding of enzymes themselves as "swimmers", and as a result, begin to unravel their contribution towards motility in more complex structures, i.e., vesicles. As such, a deeper understanding of the mechanism of enzymatic propulsion, may lead to the creation of more advanced nanomotor architectures, and technological advancement within the fields they are rooted.

Therefore, given the slightly tangential nature of this chapter, this introduction will seek to provide a focused, mini-review on enzymes as molecular machines, as well as their propelling contribution to nanomotors, when combined with synthetic machines, i.e., inorganic [214, 215] or polymeric [216] entities. This section will be focused on the fundamental mechanisms of enzymatic catalysis, and how such reactions can be used to convert biocatalytic energy into propulsive power.

6.1.1 Enzymes as Motors

At the cellular level, enzymatic catalysis of substrates to products is responsible for most forms of biological motion. For example, the movement of myosin along an actin filament [217], or,

similarly, the movement of kinesin or dynein along a microtubule track [218], represent the three primary, cellular molecular motors. Their movement, attributed to the energy generated when ATPase hydrolyses, and, as a result, dephosphorylates ATP into ADP (ATP + $H_2O \rightarrow$ ADP + Pi (inorganic phosphate)), has been reported to generate forces varying between 1 and 10 pN [219-221].

Single enzymes can also perform decoupled intracellular motion, for example, the rotation of ATPase. In this example, ATPase catalytic proteins are embedded within organelle membranes, and contribute to either ATP synthesis, through the electron transport chain-facilitated generation of an electrochemical proton gradient (F-ATPase) [222], or the acidification of intra- or -extracellular compartments (V-ATPase) [223]. Although first hypothesised in 1979 [224], the rotary phenomena of ATPase, now known to be attributed to conformational changes in differing subunits [225], was not empirically observed until 1997 [226], and realisation that ATPase was capable of generating a force was not realised until 2002 [227].

In addition to these more well-understood accounts of intracellular motion, it has been hypothesised that the self-diffusion of enzymes located within the cytoplasm plays a vital role in the transduction of intracellular signals [228]. It wasn't until 2010, that empirical evidence of this phenomena was first demonstrated, where, enhanced diffusion of urease was shown to be highly reliant on urea concentration and enhanced diffusion of catalase was shown in the presence of hydrogen peroxide. However, enhanced diffusion was not the only interesting finding. In fact, in both cases, free enzymes presented with a preferential movement up their respective concentration gradients, and towards increasing substrate concentrations – regarded as a form of molecular chemotaxis [208].

Although such findings have opened a whole new field of scientific discovery, where energy released by enzymes is harnessed as fuel for nanomotors, the underlying mechanism in which enzymatic motion is achieved has yet to be agreed upon. The first idea, suggested by Golestanian, claims that a self-diffusiophoresis mechanism is accountable for enhanced enzymatic diffusion, where, an asymmetric release of products creates an interfacial force in relation to osmotic gradients, charges, or other such properties [229, 230]. This idea, simplified via the notion that self-propulsive forces are generated through enzymatic interactions with the local gradient of the product they release, was echoed in 2014 [231].

However, it has also been suggested, that enhanced diffusion is actually the result of repeat conformational changes, in response to substrate catalysis, that actually results in a phenomenon called "stochastical swimming" [229, 232-234]. The mechanisms behind this

swimming phenomena, i.e., the energetics that drive conformational change in response to substrate binding, were investigated in 2016 with adenylate kinase, an enzyme responsible for cellular homeostasis through the interconversion of ATP, ADP, and AMP (ATP + AMP → 2ADP), using single-molecule force spectroscopy (optical tweezers) [235].

Likewise, although it may seem simplistic to suggest that an increase in temperature, attributed to catalysis-induced heat release, is responsible for enhanced diffusion, it has been explored. In this instance, it was suggested that motion was the result of asymmetric pressure waves being generated through the transient displacement of the centre-of-mass of the enzyme (chemo-acoustic effect) [209], however, this idea is still under debate. As such, Golestanian [229] investigated four distinct mechanisms of motion (stochastic swimming, self-thermophoresis, collective heating, and boosting kinetic energy) in the temperature-driven enhanced diffusion of enzymes observed by Riedel et al [209]. However, his findings were inconclusive, stating that there was not enough evidence to suggest self-thermophoresis or a boost in kinetic energy is responsible for effective diffusion, and instead, suggested that enhanced motility in enzymes responsible for the catalysis of exothermic reactions is likely to be connected to a systemic increase in temperature and/or conformational changes that enhance the relative diffusion coefficient [229].

Although no such agreement has been reached, understanding the underlying mechanism of single-enzyme motion is likely to be critical to the advancement of biocompatible, enzyme-powered nanomachinery. It is likely that the answer to this question lies in sophisticated experimental design, negating the combining effects described above, and ultimately helping in the design and implementation of nanomotors to drive complex artificial systems.

6.1.2   Enzyme-Powered Nanomotors

One of the classic, most-simple, self-propulsive systems involves the exposure of platinum-silica (Pt-SiO$_2$) Janus spheres to H$_2$O$_2$, where catalytic decomposition of H$_2$O$_2$ on the Pt face, causes diffusiophoretic movement in relation to the newly established concentration gradient, and nucleation of oxygen on the Pt surface resulted in microbubble propulsion [236]. However, just as enzymes power motion in biological structures, their ability to provide adequate force to propel larger synthetic entities has been investigated [209, 214, 216, 237]. Of course, as is the toxicity and inefficiency of Pt, catalase was identified as a suitable replacement [238], and through the immobilisation of catalase inside a tubular micromotor (25 μm), ultrafast propulsion was achieved through via microbubble expulsion. Other research looked to demonstrate proof-

of-concept applications for microbubble-propelled micromotors, which included drug delivery [239], decontamination [240], testing water quality [241], and sensory applications [242]. Likewise, the conjugation of catalase onto one face of a Janus particle, produced microbubbles sufficient enough to drive the particle away from the biocatalytic face [209, 243, 244]. Of course, although microbubble propulsion holds several advantages over phoretic motion, such as directional movement and higher propulsive velocity, the use of H_2O_2 as fuel presents realistic limitations in terms of high oxidative activity and biotoxicity.

The benefit of efficiency in replacing Pt-based microbubble systems with enzyme-based systems was again exemplified, firstly, in 500 nm stomatocytes (a cell which has lost its biconcave morphology, and presents in three dimensions as a "bowl"), where, when loaded with catalase, or catalase and glucose oxidase, self-propulsion was achieved through the expulsion of gas through small openings in the structures [216], and, secondly, in the work of Pantarotto and co-workers [237], where microbubble-propulsion was achieved when 20 nm glucose oxidase/catalase-conjugated carbon nanotubes were exposed to glucose and oxygen. In likelihood, this increase in efficiency is likely to be attributed to the highly efficient and rapid catalytic conversion of substrates exhibited by the enzymes, but, also through the localisation of catalytic activity within micro/nanomotor cavities, resulting in an accumulation of product, which is subsequently expelled as a "jet" [216].

In another example [214], where propulsion occurred through chemophoretic mechanisms, 400 nm Janus nanomotors were created by conjugating three different enzymes (catalase, urease, and glucose oxidase), onto one "face" of the hollow mesoporous silica nanoparticles (HMSNPs). It was shown, that upon exposure to their respective substrates (H_2O_2, urea, and glucose), enhanced diffusion of all nanomotors was present, and a measurable driving force of around 60 fN was reported. A similar enhancement in diffusion of Janus silica particles was also reported by Schattling and co-workers [245], who immobilised both catalase and glucose oxidase onto one face of the particles.

Another method, using various enzymes (glucose oxidase, catalase, horseradish peroxidase, glutamate oxidase, xanthine oxidase) conjugated onto polypyrrole-gold nanorods, enhanced diffusion was found, and reported to be the result of self-electrophoresis based on a bioelectrochemical mechanism ($2H^+ +2e^- + H_2O_2 \rightarrow 2H_2O$; $2O_2 \rightarrow 2O_2^{\bullet-}+ 2e^-$) [246, 247]. Bioelectrochemical propulsion was also achieved, this time by Mano and Heller [248], through the conjugation of glucose oxidase and bilirubin oxidase onto a macroscale carbon fibre, and subsequent exposure to glucose. Mechanical force was generated through bioelectrochemical

means, via the oxidation of β-D-glucose to δ-glucono-1,5-lactone (β-D-glucose + ½O_2 → δ-glucono-1,5-lactone + H_2O), which resulted in propulsion at the air-liquid interface.

Enhanced diffusion of polystyrene beads, explained by a thermal effect, was reported by Dey and co-workers [215] when both catalase and urease where conjugated around the whole surface of the polystyrene structures. It was reported that, following exposure to their respective substrates, the exothermic enzymatic reaction that ensued was sufficient to drive particle motility, however, it was pointed out, in the same paper, that this hypothesis needs further investigation.

In this section, thus far, we have described the potential of nanomotors, and shown their feasibility of utilising biocompatible fuel sources, however, micro/nanomotors do not operate in the same regime in which we live, and, as such, the outcomes of physical laws on this scale differ significantly. Within this regime, the effect of viscous drag, coupled with Brownian motion and its subsequent randomisation on movement, has a profound and deterministic effect on motion [249]. With regards to viscous drag, each object, i.e., a vesicle or a person, can be designated a Reynolds number (Re), relating to the ratio between inertial and viscous forces (Equation 6.1) [250]:

$$Re = \frac{pVl}{\mu} = \frac{Inertial\ Forces}{Viscous\ Forces}$$

Equation 6.1. Reynolds number.

In this equation, p represents the density of the fluid, V is indicative of the velocity of the particle, l can be defined as the length of the object in question, and μ is the dynamic viscosity of the external medium. By way of an example, a human swimming through a swimming pool of water has a high (10^4) Reynolds number, and in most instances in the macroscopic world, inertial forces dominate over viscous forces, resulting in turbulent flow. By contrast, a bacterium swimming through the same pool would have a Reynolds number of 10^{-4}, where viscous forces are dominant [249]. This means, at low Re numbers, the immediate counteraction of viscous

drag means that inertia is no longer sufficient in sustaining motion, flow is laminar, and, as such, the importance of continuous force is imperative for micro/nanomotor motion.

In recent times, a fully biocompatible, urease-conjugated, hollow mesoporous silica Janus micromotor (2.3 µm) was shown to exhibit fast (>10 µms⁻¹), long-lasting, and long-range (>100 µm) motion at physiological urea concentrations, thus highlighting its potential for biotherapeutic applications [251]. Such findings, i.e., self-diffusiophoresis-driven propulsion, adds weight to what was claimed above by Golestanian, where asymmetric release of catalytic products results in phoretic motion in enzyme-conjugated Janus particles [230]. However, considerations of conformational changes in enzyme structure and systemic temperature increases may potentiate the enhancement of Brownian motion. Brownian motion is described as the randomisation of particle motion in response to thermally driven collisions between solvent and colloidal molecules, and given by the diffusion coefficient (D) extracted from the Stokes-Einstein relationship (Equation 6.2) [252]:

$$D = \frac{k_B T}{6\pi n r}$$

Equation 6.2. Stokes-Einstein Equation

In this instance, k_B represents the Bolztmann constant, T is the absolute temperature, n is defined as the viscosity, and r is the particle radius. The rate of diffusion, represented by the diffusion coefficient, is therefore related to the thermal energy within the system and the size of the particle in question. Consequentially, the interference of Brownian motion, in terms of randomisation of directionality, increases as the size of the particle decreases [249]. As such, when designing a micro/nanomotor-based system for future application, especially in terms of biotherapeutics, control over motion is paramount.

Such control of micro/nanomotor movement can be achieved through external means, where, in one example, one-dimensional guidance of both solitary enzymes (urease and catalase) [208] and enzyme-conjugated systems was achieved in a microfluidic system [215] - these enzymatic micro/nanomotors were shown to have preferential movement towards areas of high substrate

concentration (chemotaxis). Another common strategy, based on the incorporation of a magnetic entity, e.g., Ni or Fe, into the micro/nanomotor structure, is remote magnetic guidance. In this example, the directional orientation of enzymatic motors was achieved through the application of a guided magnetic field [243, 251, 253]. It is also worth mentioning, that as well as directional guidance, propulsion velocity was also tuned through the manipulation of enzymatic activity, using known urease inhibitors, such as the Ag^+ or Hg^{2+} [251]. This concept was applied to water quality sensing, by observing inhibited propulsion in micromotor systems [240, 241].

6.1.3 Overview of Chapter

We seek to achieve motility in a novel way, where the enzymes responsible for providing propulsive energy are encapsulated within a phase-separated hybrid (lipid/polymer) vesicle. In this instance, we combine two assumptions. Firstly, that the permeability of a lipid domain on a phase-separated vesicle is higher than that of the remaining polymer domain, thus directing propulsion away from the lipid domain (Figure 6.1), and, secondly, building off the work of Nam and co-workers [254], that the size of the lipid domain can be controlled through composition ratio. Through this technique, we seek to control propulsive velocity through the manipulation of domain size, hypothesising that the smaller the domain, the more focused, and therefore, powerful, the jet of propulsive force will be, whilst creating a system, where enzymatic nanomotors are protected from hypothetical physiological macroenvironments.
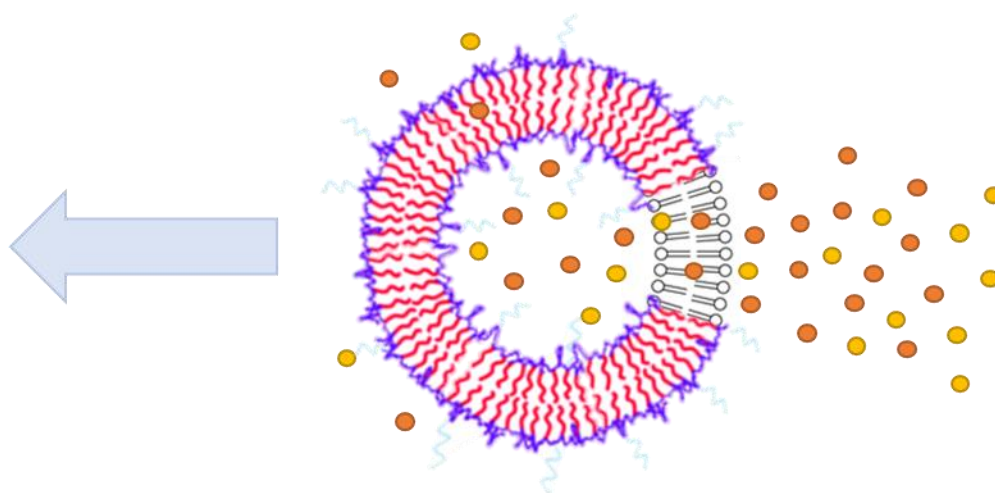
Figure 6.1. Hypothesised mechanism of propulsive velocity, where, owing to the superior permeability of lipids to polymers, phase separated vesicles should result in a focused efflux of catalytic byproducts, and as such, propel the vesicle away from the lipid domain.

6.2 Experimental

6.2.1 Materials

The lipid, 1-palmitoyl-2-oleoyl-sn-glycero-3-phosphocholine (POPC), cholesterol, and the fluorescent lipid marker (1,2-dioleoyl-*sn*-glycero-3-phosphoethanolamine-N-(lissamine rhodamine B sulfonyl) (ammonium salt)) (Rhod-DOPE), were purchased from Avanti Polar Lipids Inc. poly(butadiene)-poly(ethylene oxide) (PBD-PEO (3500)) was purchased from Polymer Source. The ratiometric pH probe 8-hydroxypyrene-1,3,6-trisulfonic acid trisodium salt (HPTS), urease from *Canavalia ensiformis* (Jack Bean), and urea were purchased from Sigma-Aldrich.

6.2.2 Motility

"Thin film rehydration" (Section 2.2.2) was used to produce PbD-PEO (3500):POPC:cholesterol + Rh-DOPE (0.5 mol%) vesicles, at varying molar ratios of the constituents (3:5:2, 1:1:1, 5:3:3, and 0:6:4), and of varying sizes (100, 200, 400 nm), depending on which parameter was being tested. The HPTS concentration encapsulated in each vesicle was held constant (20 mM), but the concentration of urease could vary (0, 10, 30 µM). Each sample was purified via size-exclusion chromatography, using 0.20 mM HCl (used to suspend the urease and HPTS) as the mobile phase. To an 850 µL micro-cuvette, 1000 µL of the sample being tested was added. At the same time, a solution of urea (0.21, 1.05, or 2.10 M, depending on the experiment in mind) was prepared. A Malvern Zetasizer was programmed to take reading every 5 minutes and immediately after the first reading was complete, 50 µL of the specified urea solution was added, making the final volume 1050 µL, and the final urea concentrations, 10, 50, and 100 mM, respectively. Three independent repeats were performed, and error was presented as ± standard deviation (SD).

6.3 Results and Discussion

6.3.1 Motility

Due to the simplicity of its underlying principles, where a laser beam of light is shone into a sample and the resulting scattered photons are detected at a known scattering angle (θ) by a photon detector, dynamic light scattering (DLS) [255] has proved to be a popular technique in the size determination of colloids, nanoparticles, polymers, vesicles, micelles, proteins, and emulsions.

In this nano/microscopic regime, the fluctuation of light scattered by particles provides information about their motion, in terms of intensity, and, from this, information about their size, through the processing of fluctuating intensity with an autocorrelation function, and the subsequent extraction of the autocorrelation function as a function of delay time (τ), can be determined [256].

Earlier in this chapter, we seen the relationship between size and the diffusion coefficient, through the Stoke-Einstein equation (Equation 6.2). By simple rearrangement, we can determine the hydrodynamic diameter (m), D_h, of our particles through the Stokes-Einstein relationship:

$$D_h = \frac{k_B T}{3\pi n D_t}$$

Equation 6.3. Stokes-Einstein Relationship

Where, D_t now represents the diffusion coefficient (m^2 s^{-1}), and, as we know, k_B, T, n, represent the Bolztmann constant, absolute temperature (K), and viscosity (Pa·s), respectively, if we measure the apparent average diameter of a urease-loaded vesicle, over time (using DLS), following the addition of urea, and assume that vesicle size *and* all other parameters, i.e., heat and viscosity, remain constant, we can use the Stokes-Einstein relationship to measure the associated diffusion coefficient (μm^2 s^{-1}) (D_v) of our sample in response to changing experimental conditions, i.e., increased urease concentration:

$$D_v = \left(\frac{k_B T}{3\pi n D_h}\right) \times 10^{12}$$

Equation 6.4. Diffusion coefficient extracted from Stokes-Einstein relationship.

6.3.1.1 Membrane Composition

In our initial hypothesis, we sought to enhance diffusion through the manipulation of lipid domain size, where, a smaller lipid domain would result in a more focused "jet" of exponents, and, as such, greater diffusion. Building off the work off Nam and co-workers [254], who found that through manipulation of PbD-PEO:POPC:cholesterol membrane composition from 3:5:2, to 1:1:1, to 5:3:3, sequentially smaller lipid domains on phase separated vesicles could be attained, we loaded 200 nm PbD-PEO:POPC:cholesterol vesicles, at membrane compositions of 0:6:4 (lipid and cholesterol only), 3:5:2, 1:1:1, and 5:3:3, with either HPTS (20 mM) (control), or urease (10 µM) and HPTS (20 mM), and determined their apparent diffusion coefficient (Table 6.1) by recording their average diameter over 5 minute increments, following exposure to urea (50 mM), and translating the data using the aforementioned equation (Equation 6.4).

To allow for a more representational measurement, the diffusion coefficient recorded at each time increment was converted to percentage change with respect to the diffusion coefficient at t_0 min (Figure 6.2). For our control, i.e., when internal urease concentration is 0 µM, we can see that for all three of our phase separated vesicle compositions (3:5:2, 1:1:1, and 5:3:3), there is no significant percentage change in diffusion coefficient between t_0 min and t_{30} min (6.1 ± 3.3, 5.0 ± 0.4, and 4.2 ± 1.0 % change in $\mu m^2\,s^{-1}$, respectively), following the addition of urea (50 mM) (Figure 6.2). In the case of our lipid and cholesterol-only vesicle, apparent diffusion coefficient increases by 13.2 ± 1.8 % following the addition of urea, indicating that the apparent diffusion of these homogenous vesicles is naturally higher in the presence of urea, than their polymer-containing counterpart, even without the presence of an appropriate nanomotor (enzyme) (Figure 6.2).

Membrane Composition	Diffusion Coefficient ($\mu m^2\ s^{-1}$)	
	t_0	t_{30}
0:6:4	2.63 ± 0.12	2.98 ± 0.13
3:5:2	3.08 ± 0.24	3.27 ± 0.24
1:1:1	3.06 ± 0.20	3.22 ± 0.22
5:3:3	3.08 ± 0.17	3.21 ± 0.21

Percentage change in diffusion coefficient ($\mu m^2\ s^{-1}$) in empty (0 µM) PbD-PEO:POPC:chol vesicles of varying membrane composition
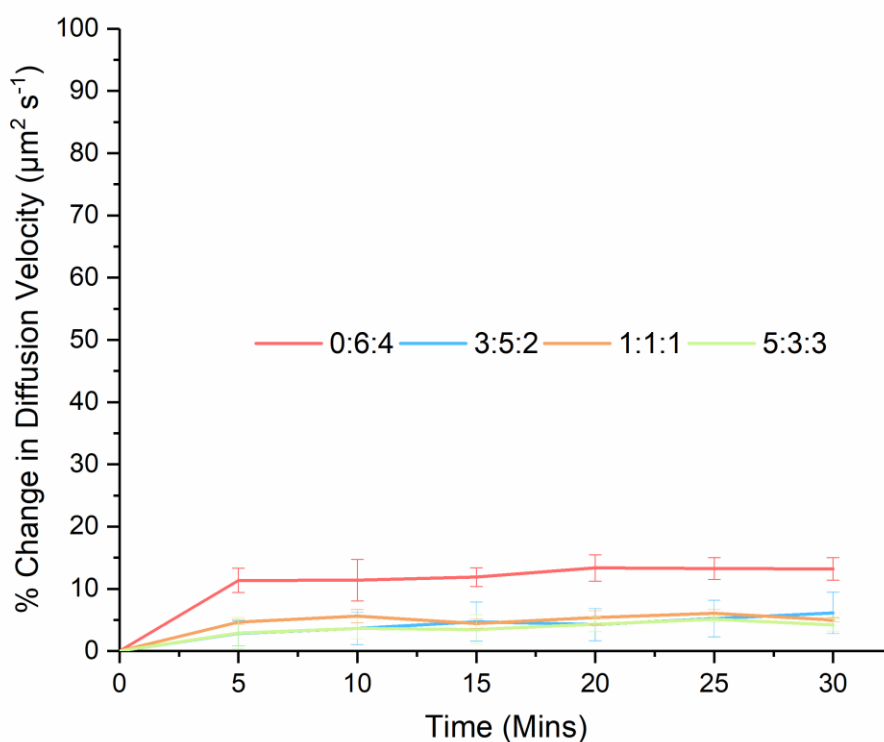
Figure 6.2. Percentage change in diffusion coefficient ($\mu m^2\ s^{-1}$) in urease-deficient (0 µM) 200 nm PbD-PEO:POPC:Cholesterol vesicles, at membrane compositions of 0:6:4, 3:5:2, 1:1:1, and 5:3:3, when exposed to urea (50 mM) *(n = 3, error = ± SD).*

Now, if we take the same vesicle compositions as above, and give them an "engine", by way of 10 µM encapsulated urease, we test our hypothesis of enhanced diffusion in relation to different permeability characteristics of phase separated vesicles. As for the control, if we take our absolute values (Table 6.2), and plot them as percentage change in apparent diffusion coefficient over time (Figure 6.3), a better comparison can be made. Here, when our lipid composition is at 50 mol% (3:5:2), and our lipid domain is theoretically at its largest, the percentage change in diffusion coefficient between t_0 min and t_{30} min is significantly lower (12.3 ± 2.6 % change in μm^2 s^{-1}) than our other smaller-lipid-domain vesicle species (1:1:1 and 5:3:3). Although this supports our "jet" hypothesis, the same cannot be said when comparing the percentage change in apparent diffusion coefficient (t_{30} min) between 1:1:1 and 5:3:3, where the theoretically larger lipid domain of 1:1:1 has a higher apparent change in diffusion coefficient (21.6 ± 0.7 % change in μm^2 s^{-1}) than a membrane composition of 5:3:3 (18.8 ± 1.4 % change in μm^2 s^{-1}). However, given the mol% compositions of both 1:1:1 and 5:3:3, in terms of lipid contribution (33.3% and 27.3%, respectively), in comparison to the 50% of 3:5:2, it may be easy to appreciate, given their similarity, why their apparent diffusion coefficient is similar.

Likewise, it may be strange at first instance to see a non-phase separated, lipid and cholesterol-only vesicle (0:6:4), displaying evidence of comparatively increased diffusion coefficient, in a scenario where diffusion of catalytic byproducts, i.e., ammonia and CO_2, is not focused through heterogeneities in membrane constituent properties. One answer, which may be influencing our above data, is encapsulation efficiency. We know already that the encapsulation efficiency of liposomes is greater than that of polymersomes/hybrid vesicles, so, what if, we are entering into a regime where, although more focused propulsion is being achieved with reduced lipid composition, the encapsulation of urease, i.e., the engine that powers our nanomotor, is being reduced with it. Although potentially offering an explanation as to why lipid and cholesterol vesicles display enhanced apparent diffusion coefficient in comparison to their polymer-containing counterparts, it does not explain why directional apparent propulsion is being witnessed in a system where homogenous diffusion of catalytic byproducts is present.

Table 6.2. Diffusion coefficient ($\mu m^2\ s^{-1}$) in 200 nm PbD-PEO:POPC:Cholesterol vesicles, at membrane compositions of 0:6:4, 3:5:2, 1:1:1, and 5:3:3, loaded with urease (10 μM) and HPTS (20 mM), and exposed to urea (50 mM)

Membrane Composition	Diffusion coefficient ($\mu m^2\ s^{-1}$)	
	t_0	t_{30}
0:6:4	2.35 ± 0.22	3.23 ± 0.18
3:5:2	3.04 ± 0.08	3.45 ± 0.03
1:1:1	2.84 ± 0.03	3.46 ± 0.03
5:3:3	2.92 ± 0.03	3.46 ± 0.03

Percentage change in diffusion coefficient ($\mu m^2\ s^{-1}$) of PbD-PEO:POPC:chol vesicles when membrane composition (0:6:4. 3:5:2, 1:1:1, 5:3:3) is tuned
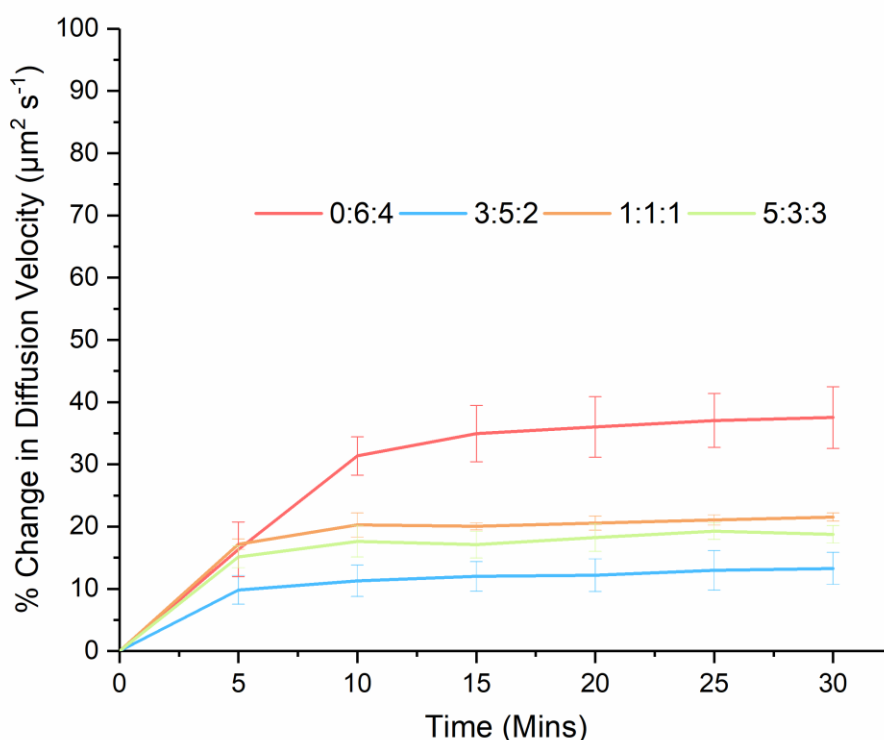
Figure 6.3. Percentage change in diffusion coefficient ($\mu m^2\ s^{-1}$) in 200 nm PbD-PEO:POPC:Cholesterol vesicles, at membrane compositions of 0:6:4, 3:5:2, 1:1:1, and 5:3:3, loaded with urease (10 μM) and HPTS (20 mM), and exposed to urea (50 mM) (n = 3, error = ± SD).

6.3.1.2 Urease Concentration

To test our assumption, that the bigger the "engine" the faster the diffusion, we sought to encapsulate differing concentrations of urease (0, 10, 30 µM) within our lipid/cholesterol only vesicles. Again, if we take our absolute values (Table 6.3), and plot them as percentage change in apparent diffusion coefficient over time (Figure 6.5), we can see, that the change in diffusion coefficient increases by 13.2 ± 1.8 % change in µm^2 s^{-1}, 37.5 ± 4.9 % change in µm^2 s^{-1}, and finally, nearly doubling, 90.2 ± 6.3 % change in µm^2 s^{-1} at t_{30} min, for 0, 10, and 30 µM, respectively, in response to activation with urea (50 mM). This confirms what we already assume, that the higher the concentration of enzyme encapsulated within, the more propulsive power the vesicle has in terms of motility, however, it does not explain why we get propulsion despite symmetrical diffusion of catalytic byproducts, alluding to the idea that transmembrane substrate diffusion is not the primary driver of enhanced diffusion.

In the previously mentioned work of Dey and colleagues [215], enhanced diffusion in symmetric enzyme-coated beads was reported to be attributed to the strongly exothermic catalysis of urease/catalase, and the associated collective heating of the sample. However, if we take our 30 µM urease sample, which displays an apparent percentage increase in diffusion coefficient of 90.2 ± 6.3 % at t_{30}, we start with vesicle population, at t_0, with an average diameter of 285.9 ± 14.2 nm, at a temperature of 298.15 K and water viscosity of 8.891 x 10^{-4} Pa*s, and, as such, the initial diffusion coefficient of this sample is 1.722 µm^2 s^{-1}. Then, if we are to assume that size remains constant, but an increase in temperature, and associated effect on water viscosity, is resulting in the extremity of enhanced diffusion coefficient (to 3.272 µm^2 s^{-1}). Then, in this instance, the temperature within the sample would have had to rise to 327.09 K (increase of 28.94°C), inclusive of a decrease in water viscosity to 4.388 x 10^{-4} Pa*s.

To validate this, the catalytically-induced local rise in the temperature was modelled by our collaborator, Dr Annette Taylor. Here, the vesicles are just assumed to be well-mixed spherical reactors of volume (V), surface area (A), and radius (r) in a bath of urea solution (at T_0). By adding an equation for temperature, relating to the internal reaction enthalpy and the heat lost to the external environment, the change in temperature could be determined:

$$\frac{dT_i}{dt} = \frac{1}{pVc}\left(V * (-\Delta H_r) * v - L * A * (T_i - T_0)\right)$$

Equation 6.5. Rate of temperature change inside the vesicle

Where v is the enzyme rate in mol dm^{-3}, ΔH_r is the enthalpy of the reaction (-59850 J/mol), L is the heat transfer coefficient across a lipid bilayer, p is the density of water, and c is the specific heat capacity of water. For the surrounding solution, we have, where d is the dilution factor of vesicles (n x V_i) in volume of external environment (V_s):

$$\frac{dT_0}{dt} = d * \frac{1}{pVc}\left(L * A * (T_i - T_0)\right)$$

Equation 6.6. Rate of temperature change in the surrounding solution

The model shows that, where an initial temperature of 298 K is concerned, the temperature rises to 298.002 K in the vesicles, and similar in the surrounding solution, after 33 minutes. Likewise, if no heat is transferred to the surrounding solution, the maximum theoretical temperature rise was approximately 4 K after 30 minutes – reaffirming that the increased motility witnessed is not solely contributed for by an increase in local or systemic temperature.

If we are to consider other mechanisms of motility, firstly, micro-swimming, where actuation of the enzyme in response to catalytic activity is achieved through iterative conformational changes in the protein's active site, and, secondly, self-diffusiophoresis, where instant redistribution of catalytic products causes fluctuations in velocity, then we still have a scenario where no net oriental propulsion should theoretically be achieved. However, for this to be true, we would have to assume that enzyme distribution is even/symmetrical around the whole internal circumference of the vesicle. It is difficult at this point to identify what breaks the symmetry and provides this "directionality". Is propulsion driven by asymmetry in product diffusion across the membrane, or are vesicles being "pushed" internally by asymmetric enzyme clustering (Figure 6.4)? Is there cause to suggest that such an asymmetric phenomenon is caused by a self-generating, environmental gradient of products to substrates, which may contribute to a degree of molecular chemotaxis? These are all highly theoretical suggestions, which are in need of further investigation.
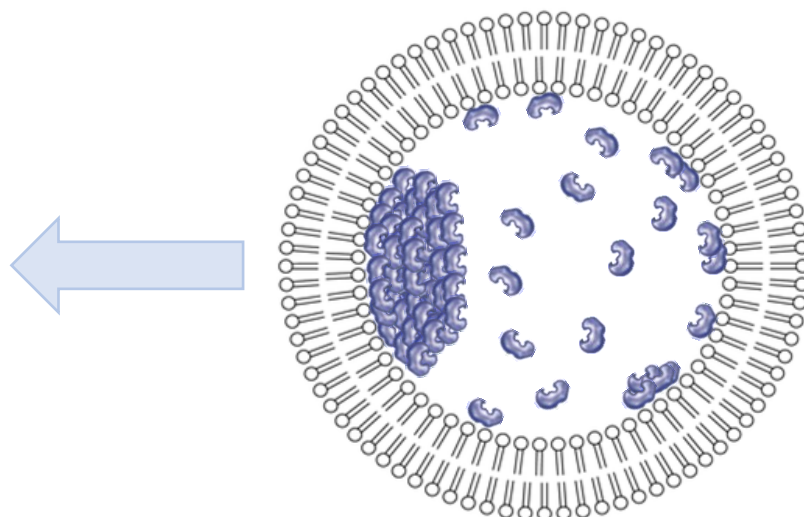
Figure 6.4. Proposed mechanism of motility in enzyme-driven nanomotor, where enzymes are encapsulated within the lumen of a homogenous POPC:cholesterol vesicle.

Table 6.3. Diffusion coefficient (μm² s⁻¹) in 200 nm POPC:cholesterol (6:4) vesicles, loaded with different concentrations of urease (0, 10, 30 μM) and HPTS (20 mM), when exposed to urea (50 mM)

Urease Concentration	Diffusion coefficient (μm^2 s^{-1})	
	t_0	t_{30}
0 μM	2.63 ± 0.12	2.98 ± 0.13
10 μM	2.35 ± 0.22	3.23 ± 0.18
30 μM	1.72 ± 0.09	3.27 ± 0.07

Figure 6.5. Percentage change in diffusion coefficient (μm² s⁻¹) in 200 nm POPC:cholesterol (6:4) vesicles, loaded with varying concentrations of urease (0, 10, 30 μM) and HPTS (20 mM), when exposed to urea (50 mM) (n = 3, error = ± SD).

6.3.1.3 Urea Concentration

To conduct a thorough examination, and help us better understand this system in terms of its variables, the effect of urea concentration was also investigated, where all other parameters, i.e., size (200 nm), urease concentration (10 µM), membrane composition (POPC:cholesterol, 6:4), were held constant. If we take our absolute values (Table 6.4), and plot them as percentage change in apparent diffusion coefficient over time (Figure 6.6), we can see, that the apparent increase in diffusion coefficient does not increase in response to increased urea concentration from 1 mM to 10 mM (5.5 ± 2.3 % and 4.6 ± 2.1 %, respectively). There is, however, a percentage increase in apparent diffusion coefficient is witnessed when increasing to 50 mM urea concentrations (20.3 ± 4.0 %), and, again, when further increased to 100 mM (27.4 ± 5.4 %), albeit not as significant (over our recorded timeframe, i.e., 30 min). From this data, we can assume that the standard concentration of urea that we have been using (50 mM) is perfect for the conditions at hand, and, evidence is added to the suggestion that "engine size" is the most important driving force behind enhanced diffusion coefficient.

Table 6.4. Diffusion coefficient (µm² s⁻¹) in 200 nm POPC:cholesterol (6:4) vesicles, loaded urease (10 µM) and HPTS (20 mM), when exposed to varying concentrations of urea (1, 10, 50, 100 mM)

Urea Concentration	Diffusion coefficient (µm² s⁻¹)	
	t_0	t_{30}
1 mM	2.46 ± 0.05	2.59 ± 0.07
10 mM	2.48 ± 0.05	2.59 ± 0.02
50 mM	2.46 ± 0.05	2.96 ± 0.13
100 mM	2.45 ± 0.09	3.12 ± 0.13

Percentage change in diffusion coefficient (µm² s⁻¹) of POPC:cholesterol vesicles when urea concentration is increased (1, 10, 50, 100 mM)
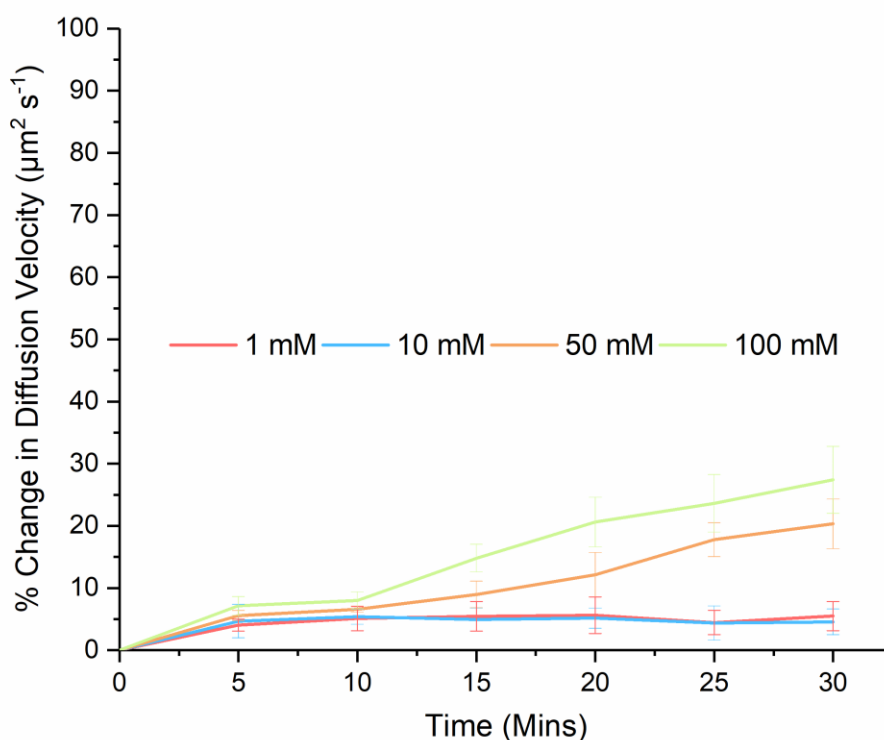
Figure 6.6. Percentage change in apparent diffusion coefficient (µm² s⁻¹) in 200 nm POPC:cholesterol (6:4) vesicles, loaded urease (10 µM) and HPTS (20 mM), when exposed to varying concentrations of urea (1, 10, 50, 100 mM) (n = 3, error = ± SD).

6.3.1.4 Size

Finally, to determine the contribution of vesicle size, all experimental parameters were held constant, i.e., urease (10 µM), membrane composition (POPC:cholesterol, 6:4), urea (50 mM), and the size of the nanopore filter in which it was extruded was adjusted (100, 200, 400 nm). You may hypothesise, from what we know about theoretical encapsulation from our nanoreactor work (Section 4.3.6, Figure 4.17), and from what we have seen here in terms of urease concentration, that the larger the vesicle, and, subsequently, the greater the amount of encapsulated urease molecules, the more enhanced apparent diffusion coefficient will appear. The diffusion coefficient of our vesicles, in terms of Brownian motion, is higher the smaller they are, however, if we are then to plot these values as percentage change in apparent diffusion coefficient over time (Figure 6.7), we can see, that the apparent increase in the diffusion coefficient does not significantly change in response to increasing nanopore filter size from 100 to 200 nm (22.1 ± 4.2 % to 21.4 ± 4.0 % (at t_{30}). However, a significant finding presents itself when we increase size further, utilising a 400 nm nanopore filter. In this instance, we see no change at all, at t_{30}, (0.7 ± 1.4 %), when exposed to urea, again, leading us to the assumption that "engine" size is a more profound contributor to motility, and that above a certain size threshold, the potential of nanomotor-driven vesicle diffusion, via this methodology, becomes unattainable.

Table 6.5. Changes in absolute vesicle diameter (nm) and absolute apparent diffusion coefficient (µm² s⁻¹) in POPC:cholesterol (6:4) vesicles of varying size (100, 200, 400 nm), loaded urease (10 µM) and HPTS (20 mM), and exposed to 50 mM urea.

Vesicle Size	Diffusion Coefficient ($\mu m^2 \ s^{-1}$)	
	t_0	t_{30}
100 nm	3.04 ± 0.12	3.71 ± 0.21
200 nm	2.56 ± 0.17	3.11 ± 0.26
400 nm	1.10 ± 0.10	1.10 ± 0.11

Percentage change in diffusion coefficient (µm² s⁻¹) of POPC:cholesterol vesicles when vesicle diameter is increased (100, 200, 400 nm)
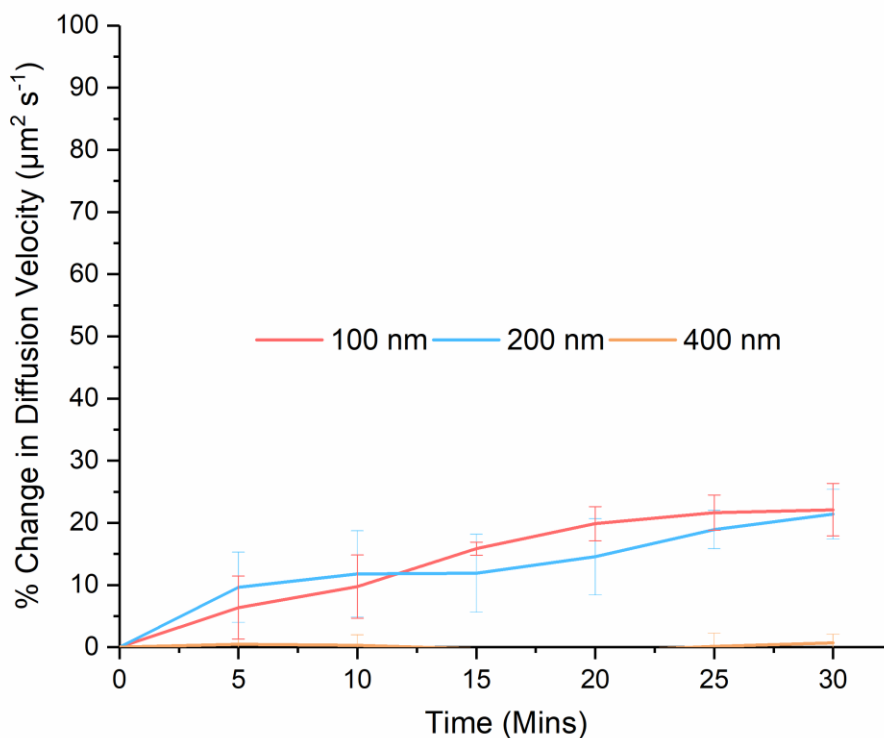
Figure 6.7. Percentage change in apparent diffusion coefficient (µm² s⁻¹) in POPC:cholesterol (6:4) vesicles of varying size (100, 200, 400 nm), loaded urease (10 µM) and HPTS (20 mM), and exposed to 50 mM urea (n = 3, error = ± SD).

6.4 Summary

In this chapter, we place the foundations for enzyme-driven nanomotors in a new light. Through the encapsulation of urease within the lumen of a phase separated vesicle (PbD-PEO:POPC:cholesterol), and the subsequent manipulation of the lipid domain size through membrane composition (3:5:2, 1:1:1, 5:3:3), we have unearthed initial findings that suggests a smaller lipid domain enhances vesicle diffusion, adding to the idea of directional motility through channel-focused byproduct diffusion. However, it is worth highlighting that DLS can only measure an increase in diffusion, rather than the direction of movement, meaning that there may be no net displacement of vesicles. Likewise, given what we subsequently discovered about "engine power", i.e., encapsulated urease concentration, and what we already know about the encapsulation efficiency of polymersomes/hybrid vesicles, more investigation is needed to truly support our hypothesis.

As previously mentioned, in the process of determining the effects of parameter manipulation, the effect of increasing urease concentration enhanced nanomotor diffusion was unearthed. Diffusion of symmetrically coated vesicles, where propulsion is generated from conjugation of enzymes onto the surface, was previously reported to be the work of a catalytically-induced exothermic release of heat, repeated actuation of the enzyme in response to catalytic activity, or the contribution of phoretic movement. However, in this work, we have dismissed heat production as the primary contributor to increased diffusion coefficient, opening further discussion on internally-propelled nanomotors from a different outlook.

CHAPTER SEVEN – CONCLUSION & FUTURE WORK

7.1   Conclusion

The fundamentals of this doctoral thesis, and our initial aim, was to draw together two areas of considerable scientific attention, nanoreactor technology and non-linear enzyme kinetics, to create a temporally-controlled drug delivery system. Within our first two results chapters, the focus was on building our platform from a bottom-up perspective, and circumventing the associated nuances of the system. In Chapter Two, we sought to optimise our system before loading urease. We tested the suitability and efficiency of our pH probe HPTS in tracking pH switching in our primary reaction, and calibrated the relevant spectroscopic equipment to allow for easy conversion between absorption ratio and pH. Likewise, we tested the robustness of our experimental constituents to the conditions presented in vesicle generation, i.e., freeze-thaw cycling, concluding that the urease enzyme is capable of withstanding such conditions, with minimal effect on catalytic activity. Finally, owing to the large relative mass of urease, we investigated a suitable and convenient method of sample purification, ultimately discovering that although our urease enzyme is outside the molecular cut-off weight (~30 kDa), Sephadex G-50 actually provided an efficient means separation.

In Chapter Three, we generated a more robust calibration process, adjusting for considerations of scattering and turbidity, to allow for a more accurate comparison of reaction profiles across associated parameter space. It was also within Chapter Three, that we really began to unearth knowledge crucial to our understanding of the system. Through the comparison of pre-ruptured and intact vesicles, we have provided insight into the importance of confinement, where, owing to the overall concentration of urease present in our sample, localisation, forced through vesicular confinement, is now known to be needed for catalytic activity, where, rupture and subsequent dispersion into the bulk volume, is not sufficient, in terms of spatial distribution, to cause pH-switching. Likewise, through experiments tracking pH transport, a better understanding of cross-membrane electrochemical dynamics allowed us to better design our experimental protocol to balance internal and external pH, ultimately allowing us to achieve a first example of "clock-like" pH-switching inside a vesicular system.

And so, by fully optimising our confined urea-urease reaction, whilst circumventing any potential caveats, a platform was built to efficiently and accurately explore our associated parameter space, i.e., acid concentration, urease concentration, etc., gaining control over the reaction kinetics, and providing a deeper holistic understanding of the cross-membrane dynamics of our system. Here, we uncovered a system more complicated than first anticipated, but helped paint a more clear picture of system dynamics, where changes in pH that originate from within the vesicle lumen are capped as a result of internal buffering capacity (enzyme and probe), but elicit

a greater effect, in terms of pH-switching, on the external environment. Likewise, through the unexpected lack of comparative influence both urease concentration *and* vesicle size had on reaction kinetics, in combination with an advanced understanding of system dynamics, we raised and answered the question of inter-vesicle communication- showing through clear experimental means, that two distinct species of vesicles are able to communicate with one another through reactant and product permeability through the membrane.

It is this organic discovery, and ultimate understanding, that has allowed us to extend our reach, and push the functionality of our novel system, e.g., drug delivery, inter-vesicle communication, and vesicular motility. Firstly, within Chapter Five, our primary aim was realised. Here, we successfully loaded our model drug (cimetidine), and, utilised principles founded throughout this doctoral thesis, such as vesicle-to-vesicle communication and parameter space manipulation, to create the first demonstration of a tuneable, feedback-controlled vesicular drug delivery system. We theorise that the systems potential goes beyond that of temporal control, and extends to a drug delivery system capable of generating a favourable external environment capable of protecting sensitive constituents or boosting therapeutic efficacy.

In the final results chapter, through the manipulation of different membrane permeabilities in phase-separated vesicles, we laid the foundations for a new-perspective on enzyme-driven nanomotors. In this instance, we have unearthed initial findings to suggest that a smaller lipid domain provides more focused membrane diffusion, and therefore potential for enhanced directional motility. Likewise, an investigation was conducted to determine the effect of parameter space manipulation on nanomotor diffusion, yielding the most profound differences in response to an increase in enzyme concentration, i.e., engine size. These findings provide a new perspective into the argument of nanomotor motility, dismissing heat production as the primary contributor to increased diffusion, where, a population of enzymes is driving, in a directional fashion, a larger supramolecular assembly.

7.2   Future Work

7.2.1   Giant Unilamellar Vesicles

Moving forward, there are large segments of this doctoral thesis that can be further expanded upon. Throughout, we have investigated the reaction kinetics of a nanoscale system, which provides whole-sample information through spectroscopic means. However, by upsizing our reaction vessel, not only would we have the reassurance of visualisation, alleviating initial concerns about membrane stability, reaction location, etc., but we could also ascertain a better understanding of pH-switching on a vesicle-to-vesicle basis.

One of the most obvious and appropriate methods of producing GUVs for this purpose, and mentioned in Section 1.6.3, is the Inverted Emulsion Technique. Here, water-in-oil emulsion droplets, formed when our aqueous encapsulants are agitated in an appropriate oil, are driven through a surfactant-water interface, to pick up a secondary monolayer. This allows encapsulants to be held distinct from the hosting solution throughout the entire process, an obvious benefit when working with sensitive biological compounds.

As part of an initial movement towards realising this aim, an investigation into the optimisation of this technique (outlined by Pautot and colleagues [106]) was conducted. Firstly, the size of the emulsion droplets produced were sought to be controlled by the agitation technique initiated. When comparing two techniques, pipetting and sonication, the results were as follows. Pipetting for 90 seconds yielded emulsion droplets with a diameter of approximately 80 μm (Figure 7.1), however, no GUVs were formed following centrifugation through the secondary monolayer, likely because the emulsion droplets were in too large to pick up a second layer of lipids, either because the lipid interface could not replenish its lipids fast enough, or the amount of lipids needed to coat the vesicle was insufficient, leading to gaps in the membrane, and therefore, structural deficiencies. Increasing pipetting time to 5 minutes was shown to reduce the average size of the emulsion droplets to diameters ranging between 10 μm and 30 μm, which subsequently produced GUVs, but was labour intensive, and sonication for 2 minutes produced emulsion droplets with a diameter ranging between 5 μm and 20 μm, again producing GUVs. These initial experiments confirmed that GUV size is inversely linked to the strength of agitation, however, there is a question of how urease would respond to being sonicated.
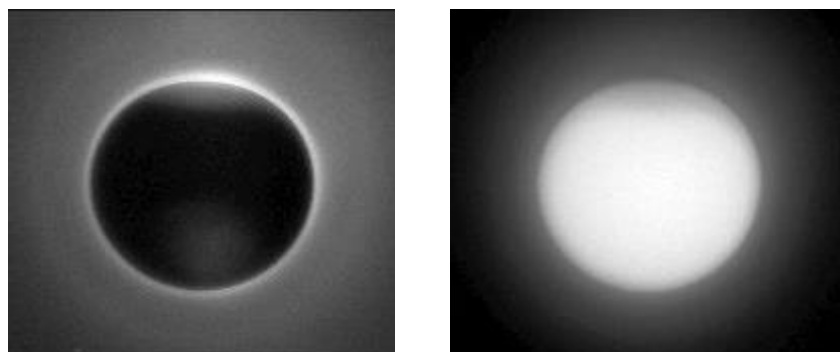
Figure 7.1. DPhPC + 0.5 mol% Rhod-DOPE inverted emulsion droplets (~80 μm): a) fluorescent rhodamine monolayer (green light), and; b) fluorescent encapsulated carboxyfluorescein (blue light).

Although GUVs were obtained through the aforementioned agitation techniques, yield was very low. To improve vesicle yield, reducing the collection volume (from 3 mL to 2 mL) to increase concentration and increasing encapsulant density by replacing carboxyfluorescein with HEPES-buffered sucrose *and* carboxyfluorescein and osmotically balancing the external environment to cause "sinking" (Figure 7.2), were investigated, but yield was not significantly increased.

However, emulsion droplets found in the intermediate phase following centrifugation necessitated the investigation into centrifugation time/speed. Maintaining centrifugation speed at 700 rpm, but increasing time to 60 minutes produced a noticeable, yet largely unimpressive yield, however, maintaining centrifugation duration and increasing centrifugation speed to 1500 rpm resulted in a considerable increase (Figure 7.2)
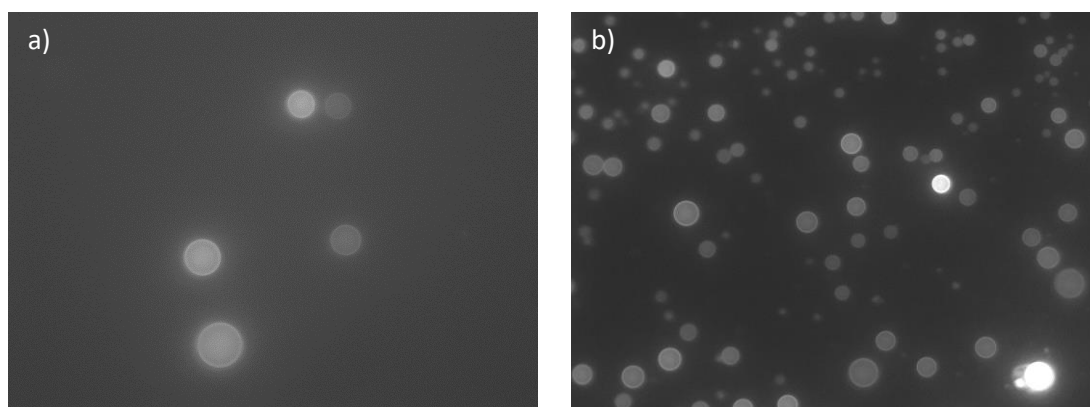
Figure 7.2. Improving GUV yield: a) increasing luminal density and osmotically balancing exterior, and; b) increasing centrifugation speed to 1500 rpm.

Polymer GUVs, usually produced in this manner with toluene as the solvent, were investigated using squalene oil instead. Following the same experimental protocol outlined above for their lipid counterpart [106], GUVs were successfully produced, and shown to efficiently encapsulate carboxyfluorescein via confocal microscopy (Figure 7.3)
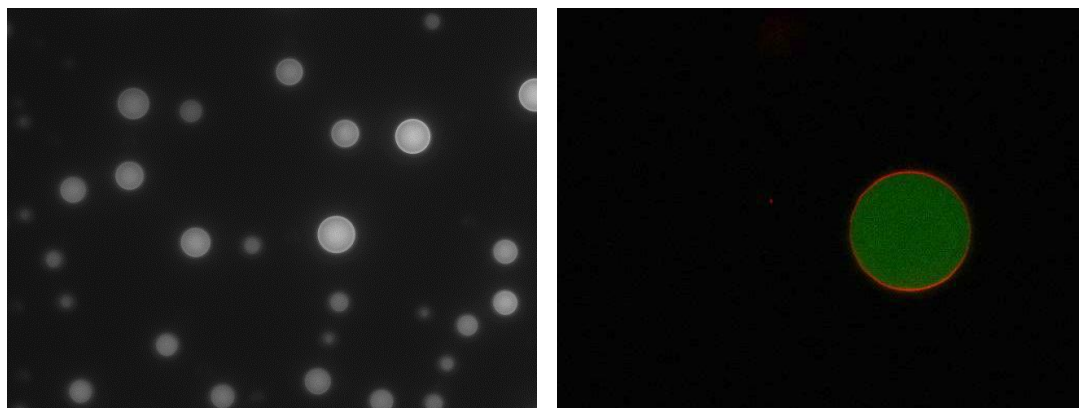
Figure 7.3. PBd-PEO polymersomes + 0.5 mol% Rhod-DOPE: a) fluorescent microscopy image showing a relatively high yield when using squalene as the solvent, and; b) confocal microscopy image showing encapsulation of HEPES-buffered sucrose + CF.

Unfortunately, owing to time restrictions, no initial data was obtained for the confinement of the urea-urease reaction in microscale. Of course, confocal microscopy can be used to obtain qualitative and quantitative data regarding pH-switching within vesicles on a singular level and can help us understand the effects of confinement under a different size regime, however, additional considerations must be employed. In solution, vesicles are free flowing, so, viewing the behaviour of a single GUV over a period of time, especially when urea is added, is problematic without tethering. A common solution is through the biotin-containing lipid into the vesicular membrane, and coating the well plate with avidin, allowing tethering to occur through the formation of the avidin-biotin complex, without any experimental interference [257].

7.2.2 Negative Feedback

As previously mentioned, the need for advanced chronotherapeutics is not only necessitated by the strong association between certain diseases and biological rhythms, but, a greater therapeutic efficacy can also be achieved when the compound aims to mimic the pulsatile release of endogenous peptides. However, to generate a truly pulsatile and autonomous drug delivery system, characteristic feedback behaviour must be installed. Throughout this thesis, we have provided an in-depth review and analysis of confined enzymatic (positive) feedback, however, despite this demonstration, to function as a pH oscillator, a negative feedback loop, capable of removing OH⁻, will have to be incorporated.

One of the most discernible options, moving forward, would be to utilise acid-catalysed feedback, showing similar characteristics, but, where pH switching occurs in the opposite direction (from high to low). An example of acid-catalysed feedback, which would ultimately remove OH⁻ ions from the system, is the glucose-glucose oxidase reaction (Equation 7.1). This particular reaction has been subject to great attention in recent years, owing to its potential as the autonomous "brain" of responsive insulin release. In this reaction, we see the glucose oxidase-driven catalytic conversion of glucose into hydrogen peroxide and D-glucono-δ-lactone, which subsequently hydrolyses into gluconic acid. It is this sequential drop in pH that is taken advantage of in terms of insulin release, where pH responsive smart materials, i.e., hydrogels, polymers, or polymersomes, are caused to degrade, swell, or increase permeability, in response to a reduction in pH [258].

$$C_6H_{12}O_6 \rightarrow C_6H_{10}O_6 + H_2O_2$$

$$C_6H_{10}O_6 \rightarrow C_6H_{12}O_7$$
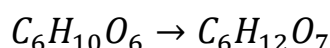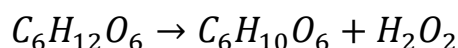
Equation 7.1. Enzyme catalysed conversion of glucose to D-glucono-δ-lactone and subsequent hydrolyses to gluconic acid

Glucose oxidase, in a similar fashion to urease, displays the principally autocatalytic characteristic of a bell-shaped rate-pH with a maximum activity at pH 7. This means that if the pH was increased, for example by the urea-urease reaction (positive feedback), a hypothetical

clock time would be witnessed, before rapid pH switching back to an acidic pH (negative feedback). Of course, this form of negative feedback may theoretically work to remove the autocatalyst, however, as we have elucidated towards, for oscillation to arise as a result of kinetic instability, negative feedback must be delayed in relation to positive feedback [34].

There is a case to state that because of the spatiotemporal distribution of nanoreactors within the system, that this delay may be provided, however, in more typical circumstances, such behaviour usually occurs in a limited parameter space only and, therefore, requires tight control of the concentrations of all reagents. Obviously, the vast majority of techniques used for vesicle generation yield heterogeneity in terms of size and encapsulation (stochastic distribution), hindering this control. However, through microfluidics, there is an option to hold greater control over these parameters, including spatial distribution in multicompartment vesicles, which may provide a solution.

As such, the natural next step would be to investigate the confinement of the glucose-glucose oxidase reaction, repeating what we have seen within this doctoral thesis, to gain control over reaction kinetics and obtain a holistic understanding of the system in totality. From this, we may uncover particular nuances that may better position us to design a positive/negative feedback system, with a novel reaction profile, capable of initiating a secondary response.

7.2.3 Drug Delivery

Where drug delivery is concerned, a platform has been created to allow for the testing of a whole variety of drugs, providing they fit the defined criteria, i.e., suitable pK_a, etc, and this choice will only be broadened, to include weakly basic compounds, if negative feedback (Section 7.2.2) is achieved. This can be expanded to cause a secondary effect, for example, the antibacterial effects of weakly basic (pK_a 7.2) trimethoprim could be explored following delayed release.

Obviously, where our drug delivery system is concerned, two separate species of vesicles must communicate to elicit a secondary response, however, can this process function in a single vesicle? In an experiment, where two sets of vesicles each encapsulating urease and HPTS suspended in differing concentrations of pH 4 citrate buffer (10 mM and 100 mM), but where the external environment is dilute HCl (0.2 mM), some potential was shown (Figure 7.4). Here, we see that for the lower concentration of buffer, a very small switch in pH occurs, which raises the question of whether an optimal parameter combination between buffer strength and starting pH can be established to control clock time in internally buffered vesicles. As part of a

Master's research project, under the supervision of myself, Eleanor McKeating successfully explored this space, loaded cimetidine down a pH gradient into a vesicle containing urease, and demonstrated the first example of a single species drug delivery system to use these novel components.
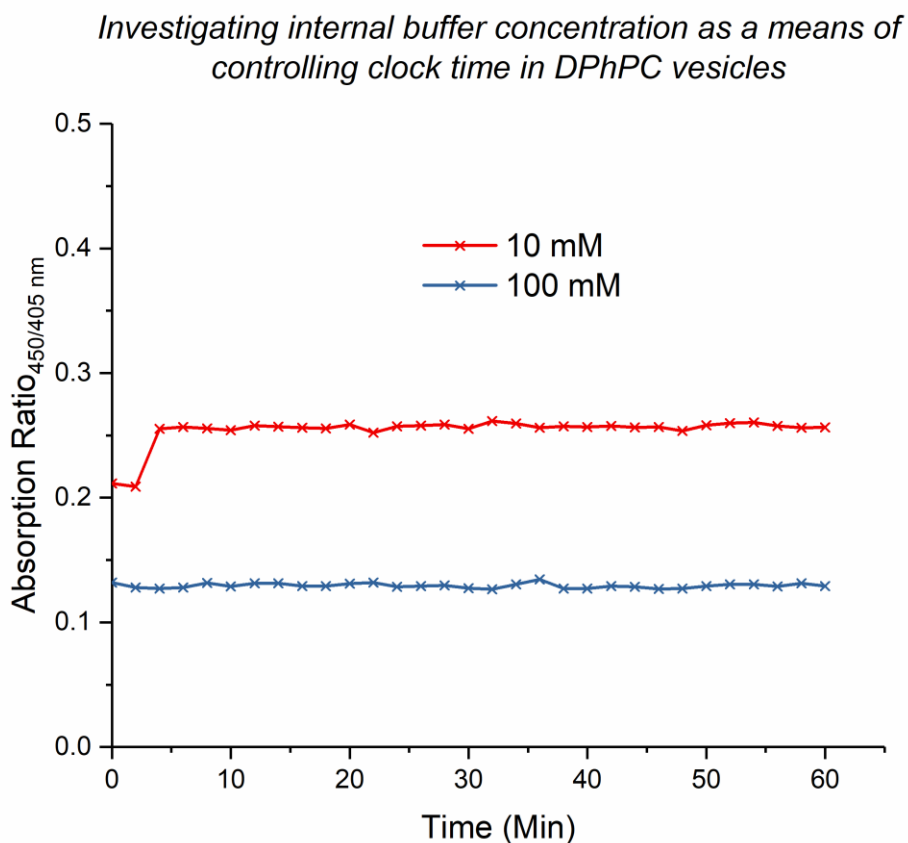
Figure 7.4. Absorption ratio of 200 nm DPhPC vesicles (phosphorus content; 250 μM) encapsulating urease (10 μM) and HPTS (20 mM) in pH 4 citrate buffer (10 mM or 100 mM), when urea (50 mM) is added (external environment is dilute HCl (0.2 mM).

However, the true potential of this system could lie in the ability to neutralise a biological microenvironment, ultimately releasing a drug into a more efficacious surrounding. For example, although blood/tissue is usually maintained at pH around 7.4 in mammals, the extracellular pH drops below 6.5 in solid cancer nests. Such acidic environments are capable of decreasing intracellular pH, interfering with a number of enzymes with pH-sensitive catalytic activity, and ultimately disrupt cellular function. In a lot of cases, target molecules of anti-cancer

drugs are these pH-sensitive enzymes, suggesting that the efficacy of anti-cancer drugs varies as pH changes. Of course, with a system such as ours, there is potential to not only release the drug in a temporal fashion, but to benefit the conditions it is being released into, and this notion deserves further investigation.

7.2.4 Nanomotors

As we have discussed, the design of smart drug delivery systems is not only necessitated by the need to be biocompatibility, biodegradability, and show appropriate pharmacokinetics, but, be able to deliver a defined payload to a specific location, whilst minimising adverse effects on nearby tissues. Of course, in many instances, drug delivery systems rely on the use of passive nanoparticles, which has been reported to have low efficacy [259]. Where we have a drug delivery system capable of temporally-controlled drug release, which has also shown enhanced motility in the presence of urea, it would be interesting to test this improved efficacy, by determining the cellular uptake kinetic profile in *in vitro* assays. To add further, work on fuel-dependent targeting and cell uptake and in situ guidance methods, i.e., chemotaxis, to attract and guide these nanomotor-based drug delivery systems, need to be addressed, both *in vitro* and *in vivo*, however, such work may lay the foundations for the development of smart, self-propelled, enzyme-catalysed drug delivery vehicles.

Similarly, and as previously suggested, further investigation should be made to determine the mechanism of propulsion, i.e., what break symmetry, in internally-driven nanomotor assemblies. As a final recommendation, given what we discovered about "engine power", and its effect on enhanced motility, to truly test our hypothesis that a smaller lipid domain, and therefore more focused membrane permeation, results in greater propulsion, a more in-depth investigation, taking greater consideration of vesicle size and encapsulation efficiency may be conducted.

CHAPTER EIGHT - REFERENCES

1.   Rades, T. and Y. Perrie, *Pharmaceutics: drug delivery and targeting*. 2 ed. 2012, London: Pharmaceutical Press.

2.   Santos, R., et al., *A comprehensive map of molecular drug targets.* Nat Rev Drug Discov, 2017. **16**(1): p. 19-34.

3.   Levine, M.M. and M.B. Sztein, *Vaccine development strategies for improving immunization: the role of modern immunology.* Nat Immunol, 2004. **5**(5): p. 460-464.

4.   Tiwari, G., et al., *Drug delivery systems: An updated review.* International Journal of Pharmaceutical Investigation, 2012. **2**(1): p. 2-11.

5.   Steinijans, V.W., *Pharmacokinetic characterization of controlled-release formulations.* Eur J Drug Metab Pharmacokinet, 1990. **15**(2): p. 173-81.

6.   Liechty, W.B., et al., *Polymers for Drug Delivery Systems.* Annual review of chemical and biomolecular engineering, 2010. **1**: p. 149-173.

7.   Misra, G.P. and R.A. Siegel, *Multipulse drug permeation across a membrane driven by a chemical pH-oscillator.* Journal of Controlled Release, 2002. **79**(1–3): p. 293-297.

8.   Zhao, Y.-N., et al., *A Drug Carrier for Sustained Zero-Order Release of Peptide Therapeutics.* Scientific Reports, 2017. **7**: p. 5524.

9.   Zhang, L., et al., *Zero-order release of poorly water-soluble drug from polymeric films made via aqueous slurry casting.* European Journal of Pharmaceutical Sciences, 2018. **117**: p. 245-254.

10.   Kawasaki, E., *Type 1 Diabetes and Autoimmunity.* Clinical Pediatric Endocrinology, 2014. **23**(4): p. 99-105.

11.   Siegel, R.A., *Autonomous rhythmic drug delivery systems based on chemical and biochemomechanical oscillators*, in *NATO Science for Peace and Security Series A: Chemistry and Biology*. 2009. p. 175-201.

12.   Smolensky, M.H. and N.A. Peppas, *Chronobiology, drug delivery, and chronotherapeutics.* Advanced Drug Delivery Reviews, 2007. **59**(9): p. 828-851.

13.   Nunemaker, C.S. and L.S. Satin, *Episodic hormone secretion: a comparison of the basis of pulsatile secretion of insulin and GnRH.* Endocrine, 2014. **47**(1): p. 49-63.

14.   Bruguerolle, B., A. Boulamery, and N. Simon, *Biological rhythms: a neglected factor of variability in pharmacokinetic studies.* J Pharm Sci, 2008. **97**(3): p. 1099-108.

15.   Brabant, G., K. Prank, and C. Schofl, *Pulsatile patterns in hormone secretion.* Trends Endocrinol Metab, 1992. **3**(5): p. 183-90.

16.   Coy, D.H. and A.V. Schally, *Gonadotrophin releasing hormone analogues.* Ann Clin Res, 1978. **10**(3): p. 139-44.

17.   Leyendecker, G., L. Wildt, and M. Hansmann, *Pregnancies following chronic intermittent (pulsatile) administration of Gn-RH by means of a portable pump ("Zyklomat")--a new approach to the treatment of infertility in hypothalamic amenorrhea.* J Clin Endocrinol Metab, 1980. **51**(5): p. 1214-6.

18.   Kala, R., et al., *Nitroglycerin ointment effective for seven hours in severe angina pectoris.* Acta Med Scand, 1983. **213**(3): p. 165-70.

19.	Crean, P.A., et al., *Failure of transdermal nitroglycerin to improve chronic stable angina: a randomized, placebo-controlled, double-blind, double crossover trial.* Am Heart J, 1984. **108**(6): p. 1494-500.

20.	Sullivan, M., et al., *Failure of transdermal nitroglycerin to improve exercise capacity in patients with angina pectoris.* J Am Coll Cardiol, 1985. **5**(5): p. 1220-3.

21.	Parker, J.O., et al., *Intermittent transdermal nitroglycerin therapy in angina pectoris. Clinically effective without tolerance or rebound. Minitran Efficacy Study Group.* Circulation, 1995. **91**(5): p. 1368-74.

22.	Stanislaus, D., et al., *Mechanisms mediating multiple physiological responses to gonadotropin-releasing hormone.* Mol Cell Endocrinol, 1998. **144**(1-2): p. 1-10.

23.	Li, Y. and A. Goldbeter, *Frequency specificity in intercellular communication. Influence of patterns of periodic signaling on target cell responsiveness.* Biophysical Journal, 1989. **55**(1): p. 125-145.

24.	Baraldo, M., *The influence of circadian rhythms on the kinetics of drugs in humans.* Expert Opin Drug Metab Toxicol, 2008. **4**(2): p. 175-92.

25.	Kwon, I.C., Y.H. Bae, and S.W. Kim, *Electrically erodible polymer gel for controlled release of drugs.* Nature, 1991. **354**(6351): p. 291-3.

26.	Edelman, E.R., et al., *Regulation of drug release from polymer matrices by oscillating magnetic fields.* J Biomed Mater Res, 1985. **19**(1): p. 67-83.

27.	Kost, J., K. Leong, and R. Langer, *Ultrasound-enhanced polymer degradation and release of incorporated substances.* Proc Natl Acad Sci U S A, 1989. **86**(20): p. 7663-6.

28.	Arunothayanun, P., T. Sooksawate, and A.T. Florence, *Extrusion of niosomes from capillaries: approaches to a pulsed delivery device.* J Control Release, 1999. **60**(2-3): p. 391-7.

29.	Sunil, S.A., et al., *Chronotherapeutic drug delivery systems: an approach to circadian rhythms diseases.* Curr Drug Deliv, 2011. **8**(6): p. 622-33.

30.	Hu, G., et al., *Base-catalyzed feedback in the urea-urease reaction.* J Phys Chem B, 2010. **114**(44): p. 14059-63.

31.	Novak, B. and J.J. Tyson, *Design principles of biochemical oscillators.* Nat Rev Mol Cell Biol, 2008. **9**(12): p. 981-91.

32.	Turing, A.M., *The chemical basis of morphogenesis.* Philosophical Transactions of the Royal Society of London. Series B, Biological Sciences, 1952. **237**(641): p. 37.

33.	Ludlow, R.F. and S. Otto, *Systems chemistry.* Chem Soc Rev, 2008. **37**(1): p. 101-8.

34.	Kovacs, K., et al., *pH oscillations and bistability in the methylene glycol-sulfite-gluconolactone reaction.* Phys Chem Chem Phys, 2007. **9**(28): p. 3711-6.

35.	Giannos, S.A., S.M. Dinh, and B. Berner, *Temporally Controlled Drug Delivery Systems: Coupling of pH Oscillators with Membrane Diffusion.* Journal of Pharmaceutical Sciences, 1995. **84**(5): p. 539-543.

36.	Epstein, I.R., *Nonlinear oscillations in chemical and biological systems.* Physica D: Nonlinear Phenomena, 1991. **51**(1): p. 152-160.

37.	Yashin, V.V. and A.C. Balazs, *Pattern Formation and Shape Changes in Self-Oscillating Polymer Gels.* Science, 2006. **314**(5800): p. 798-801.

38.   Dhanarajan, A.P., G.P. Misra, and R.A. Siegel, *Autonomous Chemomechanical Oscillations in a Hydrogel/Enzyme System Driven by Glucose.* The Journal of Physical Chemistry A, 2002. **106**(38): p. 8835-8838.

39.   Misra, G.P. and R.A. Siegel, *Multipulse drug permeation across a membrane driven by a chemical pH-oscillator.* J Control Release, 2002. **79**(1-3): p. 293-7.

40.   Ryan, A.J., et al., *Responsive brushes and gels as components of soft nanotechnology.* Faraday Discuss, 2005. **128**: p. 55-74.

41.   Vanag, V.K., D.G. Míguez, and I.R. Epstein, *Designing an enzymatic oscillator: Bistability and feedback controlled oscillations with glucose oxidase in a continuous flow stirred tank reactor.* The Journal of Chemical Physics, 2006. **125**(19): p. -.

42.   Hauser, M.J.B. and L.F. Olsen, *Mixed-mode oscillations and homoclinic chaos in an enzyme reaction.* Journal of the Chemical Society, Faraday Transactions, 1996. **92**(16): p. 2857-2863.

43.   Bagyan, S., et al., *Glycolytic oscillations and waves in an open spatial reactor: Impact of feedback regulation of phosphofructokinase.* Biophysical Chemistry, 2005. **116**(1): p. 67-76.

44.   Krajewska, B., *Ureases I. Functional, catalytic and kinetic properties: A review.* Journal of Molecular Catalysis B: Enzymatic, 2009. **59**(1): p. 9-21.

45.   Maroney, M.J. and S. Ciurli, *Nonredox Nickel Enzymes.* Chemical Reviews, 2014. **114**(8): p. 4206-4228.

46.   Zamble, D., et al., *The Biological Chemistry of Nickel*. 2017.

47.   Estiu, G. and K.M. Merz, *Competitive Hydrolytic and Elimination Mechanisms in the Urease Catalyzed Decomposition of Urea.* The Journal of Physical Chemistry B, 2007. **111**(34): p. 10263-10274.

48.   Krajewska, B., R. van Eldik, and M. Brindell, *Temperature- and pressure-dependent stopped-flow kinetic studies of jack bean urease. Implications for the catalytic mechanism.* J Biol Inorg Chem, 2012. **17**(7): p. 1123-34.

49.   Kappaun, K., et al., *Ureases: Historical aspects, catalytic, and non-catalytic properties – A review.* Journal of Advanced Research, 2018. **13**: p. 3-17.

50.   Krajewska, B. and S. Ciurli, *Jack bean (Canavalia ensiformis) urease. Probing acid-base groups of the active site by pH variation.* Plant Physiol Biochem, 2005. **43**(7): p. 651-8.

51.   Wrobel, M.M., *pH-driven instabilities in chemical systems*, in *School of Chemistry*. 2012, University of Leeds.

52.   Callahan, B.P., Y. Yuan, and R. Wolfenden, *The Burden Borne by Urease.* Journal of the American Chemical Society, 2005. **127**(31): p. 10828-10829.

53.   Follmer, C., et al., *PIXE analysis of urease isoenzymes isolated from Canavalia ensiformis (jack bean) seeds.* Nuclear Instruments and Methods in Physics Research Section B: Beam Interactions with Materials and Atoms, 2002. **189**(1): p. 482-486.

54.   Lubbers, M.W., et al., *Purification and characterization of urease from Schizosaccharomyces pombe.* Canadian Journal of Microbiology, 1996. **42**(2): p. 132-140.

55.   Sumner, J.B. and D.B. Hand, *THE ISOELECTRIC POINT OF CRYSTALLINE UREASE1.* Journal of the American Chemical Society, 1929. **51**(4): p. 1255-1260.

56.   Krajewska, B. and W. Zaborska, *The effect of phosphate buffer in the range of pH 5.80–8.07 on jack bean urease activity.* Journal of Molecular Catalysis B: Enzymatic, 1999. **6**(1): p. 75-81.

57.   Wrobel, M.M., et al., *pH wave-front propagation in the urea-urease reaction.* Biophysical journal, 2012. **103**(3): p. 610-615.

58.   Bellomo, E.G., et al., *Stimuli-responsive polypeptide vesicles by conformation-specific assembly.* Nat Mater, 2004. **3**(4): p. 244-8.

59.   Hu, G., et al., *Base-Catalyzed Feedback in the Urea–Urease Reaction.* The Journal of Physical Chemistry B, 2010. **114**(44): p. 14059-14063.

60.   Follmer, C., et al., *Canatoxin, a toxic protein from jack beans (Canavalia ensiformis), is a variant form of urease (EC 3.5.1.5): biological effects of urease independent of its ureolytic activity.* Biochemical Journal, 2001. **360**(1): p. 217.

61.   Carlini, C.R., et al., *Biological Effects of Canatoxin in Different Insect Models: Evidence for a Proteolytic Activation of the Toxin by Insect Cathepsinlike Enzymes.* Journal of Economic Entomology, 1997. **90**(2): p. 340-348.

62.   Carlini, C.R., J.A. Guimarães, and J.M.C. Ribeiro, *Platelet release reaction and aggregation induced by canatoxin, a convulsant protein: evidence for the involvement of the platelet lipoxygenase pathway.* British Journal of Pharmacology, 1985. **84**(2): p. 551-560.

63.   Benjamin, C.F., C.R. Carlini, and C. Barja-Fidalgo, *Pharmacological characterization of rat paw edema induced by canatoxin, the toxic protein from Canavalia ensiformis (jack bean) seeds.* Toxicon, 1992. **30**(8): p. 879-885.

64.   Becker-Ritt, A.B., et al., *Antifungal activity of plant and bacterial ureases.* Toxicon, 2007. **50**(7): p. 971-983.

65.   Carlini, C.R. and R. Ligabue-Braun, *Ureases as multifunctional toxic proteins: A review.* Toxicon, 2016. **110**: p. 90-109.

66.   Defferrari, M.S., et al., *Insecticidal effect of Canavalia ensiformis major urease on nymphs of the milkweed bug Oncopeltus fasciatus and characterization of digestive peptidases.* Insect Biochemistry and Molecular Biology, 2011. **41**(6): p. 388-399.

67.   Mulinari, F., et al., *Jaburetox-2Ec: An insecticidal peptide derived from an isoform of urease from the plant Canavalia ensiformis.* Peptides, 2007. **28**(10): p. 2042-2050.

68.   Piovesan, A.R., et al., *Canavalia ensiformis urease, Jaburetox and derived peptides form ion channels in planar lipid bilayers.* Archives of Biochemistry and Biophysics, 2014. **547**: p. 6-17.

69.   Micheletto, Y.M.S., et al., *Interaction of jack bean (Canavalia ensiformis) urease and a derived peptide with lipid vesicles.* Colloids and Surfaces B: Biointerfaces, 2016. **145**: p. 576-585.

70.   Marsh, D., *CRC handbook of lipid bilayers*. 1990, Boca Raton: CRC Press.

71.   Walter, H., *Consequences of phase separation in cytoplasm.* Int Rev Cytol, 2000. **192**: p. 331-43.

72.   Graff, A., M. Winterhalter, and W. Meier, *Nanoreactors from Polymer-Stabilized Liposomes.* Langmuir, 2001. **17**(3): p. 919-923.

73.   Palivan, C.G., et al., *Protein-polymer nanoreactors for medical applications.* Chem Soc Rev, 2012. **41**(7): p. 2800-23.

74.   Karlsson, M., et al., *Biomimetic nanoscale reactors and networks.* Annu Rev Phys Chem, 2004. **55**: p. 613-49.

75.   Vriezema, D.M., et al., *Self-assembled nanoreactors.* Chem Rev, 2005. **105**(4): p. 1445-89.

76.   Barenholz, Y., *Doxil(R)--the first FDA-approved nano-drug: lessons learned.* J Control Release, 2012. **160**(2): p. 117-34.

77.   Diniz, I.M.A., et al., *Pluronic F-127 hydrogel as a promising scaffold for encapsulation of dental-derived mesenchymal stem cells.* Journal of Materials Science. Materials in Medicine, 2015. **26**(3): p. 153.

78.   Langowska, K., C.G. Palivan, and W. Meier, *Polymer nanoreactors shown to produce and release antibiotics locally.* Chemical Communications, 2013. **49**(2): p. 128-130.

79.   Tanner, P., et al., *Enzymatic cascade reactions inside polymeric nanocontainers: a means to combat oxidative stress.* Chemistry, 2011. **17**(16): p. 4552-60.

80.   Axthelm, F., et al., *Antioxidant nanoreactor based on superoxide dismutase encapsulated in superoxide-permeable vesicles.* J Phys Chem B, 2008. **112**(28): p. 8211-7.

81.   Tanner, P., et al., *Polymeric Vesicles: From Drug Carriers to Nanoreactors and Artificial Organelles.* Accounts of Chemical Research, 2011. **44**(10): p. 1039-1049.

82.   De Vocht, C., et al., *Polymeric nanoreactors for enzyme replacement therapy of MNGIE.* J Control Release, 2010. **148**(1): p. e19-20.

83.   Nardin, C., et al., *Nanoreactors based on (polymerized) ABA-triblock copolymer vesicles.* Chemical Communications, 2000(15): p. 1433-1434.

84.   Kumar, M., et al., *Highly permeable polymeric membranes based on the incorporation of the functional water channel protein Aquaporin Z.* Proceedings of the National Academy of Sciences, 2007. **104**(52): p. 20719-20724.

85.   Graff, A., et al., *Virus-assisted loading of polymer nanocontainer.* Proc Natl Acad Sci U S A, 2002. **99**(8): p. 5064-8.

86.   Walde, P. and S. Ichikawa, *Enzymes inside lipid vesicles: preparation, reactivity and applications.* Biomolecular Engineering, 2001. **18**(4): p. 143-177.

87.   WorldsChoiceProducts. *Liposome*. 2015 [cited 2015; Available from: http://worldschoiceproducts.com/images//liposomal/liposome.png.

88.   Discher, D.E. and A. Eisenberg, *Polymer vesicles.* Science 2002. **297**(5583): p. 967-973.

89.   Blanazs, A., et al., *Synthesis of pH-responsive amphiphilic ABC block copolymers: The generation of asymmetric vesicle membranes and their cell uptake kinetics.* Abstr Pap Am. Chem Soc., 2008. **236**: p. 393.

90.   Kita-Tokarczyk, K., et al., *Block copolymer vesicles—using concepts from polymer chemistry to mimic biomembranes.* Polymer, 2005. **46**(11): p. 3540-3563.

91.   Antonietti, M. and S. Förster, *Vesicles and Liposomes: A Self-Assembly Principle Beyond Lipids.* Advanced Materials, 2003. **15**(16): p. 1323-1333.

92.   Gunkel-Grabole, G., et al., *Polymeric 3D nano-architectures for transport and delivery of therapeutically relevant biomacromolecules.* Biomaterials Science, 2015. **3**(1): p. 25-40.

93.   Klibanov, A.L., et al., *Amphipathic polyethyleneglycols effectively prolong the circulation time of liposomes.* FEBS Lett, 1990. **268**(1): p. 235-7.

94. Allen, T.M., et al., *Liposomes containing synthetic lipid derivatives of poly(ethylene glycol) show prolonged circulation half-lives in vivo.* Biochim Biophys Acta, 1991. **1066**(1): p. 29-36.

95. Blume, G. and G. Cevc, *Molecular mechanism of the lipid vesicle longevity in vivo.* Biochim Biophys Acta, 1993. **1146**(2): p. 157-68.

96. Southall, N.T., K.A. Dill, and A.D.J. Haymet, *A View of the Hydrophobic Effect.* The Journal of Physical Chemistry B, 2002. **106**(3): p. 521-533.

97. Nagarajan, R., *Molecular Packing Parameter and Surfactant Self-Assembly: The Neglected Role of the Surfactant Tail.* Langmuir, 2002. **18**(1): p. 31-38.

98. Small, D.M., *Lateral chain packing in lipids and membranes.* J Lipid Res, 1984. **25**(13): p. 1490-500.

99. Lodish, H., et al., *Diffusion of Small Molecules across Phospholipid Bilayers*, in *Molecular Cell Biology*. 2000, W.H. Freeman: New York.

100. Paula, S., et al., *Permeation of protons, potassium ions, and small polar molecules through phospholipid bilayers as a function of membrane thickness.* Biophysical Journal, 1996. **70**(1): p. 339-348.

101. Torchilin, V., *Handbook of Nanobiomedical Research*. Handbook of Nanobiomedical Research.

102. Bangham, A.D., M.M. Standish, and J.C. Watkins, *Diffusion of univalent ions across the lamellae of swollen phospholipids.* J Mol Biol, 1965. **13**(1): p. 238-52.

103. Bangham, A.D., M.M. Standish, and G. Weissmann, *The action of steroids and streptolysin S on the permeability of phospholipid structures to cations.* J Mol Biol, 1965. **13**(1): p. 253-9.

104. Qiao, H., et al., *Encapsulation of Nucleic Acids into Giant Unilamellar Vesicles by Freeze-Thaw: a Way Protocells May Form.* Orig Life Evol Biosph, 2016.

105. Meure, L., N. Foster, and F. Dehghani, *Conventional and Dense Gas Techniques for the Production of Liposomes: A Review.* AAPS PharmSciTech, 2008. **9**(3): p. 798-809.

106. Pautot, S., B.J. Frisken, and D.A. Weitz, *Production of Unilamellar Vesicles Using an Inverted Emulsion.* Langmuir, 2003. **19**(7): p. 2870-2879.

107. Ulrich, A.S., *Biophysical aspects of using liposomes as delivery vehicles.* Biosci Rep, 2002. **22**(2): p. 129-50.

108. Monteiro, N., et al., *Liposomes in tissue engineering and regenerative medicine.* J R Soc Interface, 2014. **11**(101): p. 20140459.

109. Egli, S., et al., *Biocompatible Functionalization of Polymersome Surfaces: A New Approach to Surface Immobilization and Cell Targeting Using Polymersomes.* Journal of the American Chemical Society, 2011. **133**(12): p. 4476-4483.

110. Grzelakowski, M., et al., *Immobilized Protein–Polymer Nanoreactors.* Small, 2009. **5**(22): p. 2545-2548.

111. Tanner, P., et al., *Specific His6-tag attachment to metal-functionalized polymersomes relies on molecular recognition.* J Phys Chem B, 2012. **116**(33): p. 10113-24.

112. Torchilin, V.P., *Recent advances with liposomes as pharmaceutical carriers.* Nat Rev Drug Discov, 2005. **4**(2): p. 145-60.

113. Broz, P., et al., *Cell targeting by a generic receptor-targeted polymer nanocontainer platform.* J Control Release, 2005. **102**(2): p. 475-88.

114. van Dongen, S.F.M., et al., *Cellular Integration of an Enzyme-Loaded Polymersome Nanoreactor.* Angewandte Chemie International Edition, 2010. **49**(40): p. 7213-7216.

115. Baumann, P., et al., *Light-responsive polymer nanoreactors: a source of reactive oxygen species on demand.* Nanoscale, 2013. **5**(1): p. 217-24.

116. Broz, P., et al., *Inhibition of macrophage phagocytotic activity by a receptor-targeted polymer vesicle-based drug delivery formulation of pravastatin.* J Cardiovasc Pharmacol, 2008. **51**(3): p. 246-52.

117. Slingerland, M., H.J. Guchelaar, and H. Gelderblom, *Liposomal drug formulations in cancer therapy: 15 years along the road.* Drug Discov Today, 2012. **17**(3-4): p. 160-6.

118. Sakai, H. and E. Tsuchida, *Hemoglobin-vesicles for a Transfusion Alternative and Targeted Oxygen Delivery.* Journal of Liposome Research, 2007. **17**(3-4): p. 227-235.

119. Chang, T.M., *From artificial red blood cells, oxygen carriers, and oxygen therapeutics to artificial cells, nanomedicine, and beyond.* Artif Cells Blood Substit Immobil Biotechnol, 2012. **40**(3): p. 197-9.

120. Arifin, D.R. and A.F. Palmer, *Polymersome encapsulated hemoglobin: a novel type of oxygen carrier.* Biomacromolecules, 2005. **6**(4): p. 2172-81.

121. Lee, J.C., et al., *Preparation, stability, and in vitro performance of vesicles made with diblock copolymers.* Biotechnol Bioeng, 2001. **73**(2): p. 135-45.

122. Rameez, S., H. Alosta, and A.F. Palmer, *Biocompatible and biodegradable polymersome encapsulated hemoglobin: a potential oxygen carrier.* Bioconjug Chem, 2008. **19**(5): p. 1025-32.

123. Dobrunz, D., et al., *Polymer nanoreactors with dual functionality: simultaneous detoxification of peroxynitrite and oxygen transport.* Langmuir, 2012. **28**(45): p. 15889-99.

124. Sakai, H., et al., *Haemoglobin-vesicles as artificial oxygen carriers: present situation and future visions.* J Intern Med, 2008. **263**(1): p. 4-15.

125. Li, T., X. Jing, and Y. Huang, *Polymer/hemoglobin assemblies: biodegradable oxygen carriers for artificial red blood cells.* Macromol Biosci, 2011. **11**(7): p. 865-75.

126. Taguchi, K., T. Maruyama, and M. Otagiri, *Pharmacokinetic properties of hemoglobin vesicles as a substitute for red blood cells.* Drug Metab Rev, 2011. **43**(3): p. 362-73.

127. Tsuchida, E., et al., *Artificial Oxygen Carriers, Hemoglobin Vesicles and Albumin–Hemes, Based on Bioconjugate Chemistry.* Bioconjugate Chemistry, 2009. **20**(8): p. 1419-1440.

128. Sakai, H., et al., *Review of hemoglobin-vesicles as artificial oxygen carriers.* Artif Organs, 2009. **33**(2): p. 139-45.

129. Noor, R., S. Mittal, and J. Iqbal, *Superoxide dismutase--applications and relevance to human diseases.* Med Sci Monit, 2002. **8**(9): p. Ra210-5.

130. Luisa Corvo, M., et al., *Superoxide dismutase entrapped in long-circulating liposomes: formulation design and therapeutic activity in rat adjuvant arthritis.* Biochim Biophys Acta, 2002. **1564**(1): p. 227-36.

131. Corvo, M.L., et al., *Superoxide Dismutase Enzymosomes: Carrier Capacity Optimization, in Vivo Behaviour and Therapeutic Activity.* Pharm Res, 2014.

132. Onaca, O., et al., *SOD antioxidant nanoreactors: influence of block copolymer composition on the nanoreactor efficiency.* Macromol Biosci, 2010. **10**(5): p. 531-8.

133. Slemmer, J.E., et al., *Antioxidants and free radical scavengers for the treatment of stroke, traumatic brain injury and aging.* Curr Med Chem, 2008. **15**(4): p. 404-14.

134. Droege, W., *Oxidative stress in HIV infection.* Oxid Stress, Dis Cancer, 2006: p. 885-895.

135. Bechet, D., et al., *Nanoparticles as vehicles for delivery of photodynamic therapy agents.* Trends Biotechnol, 2008. **26**(11): p. 612-21.

136. Sibani, S.A., et al., *Photosensitiser delivery for photodynamic therapy. Part 2: systemic carrier platforms.* Expert Opin Drug Deliv, 2008. **5**(11): p. 1241-54.

137. Donnelly, R.F., P.A. McCarron, and D. Woolfson, *Drug delivery systems for photodynamic therapy.* Recent Pat Drug Deliv Formul, 2009. **3**(1): p. 1-7.

138. Sharman, W.M., C.M. Allen, and J.E. van Lier, *Photodynamic therapeutics: basic principles and clinical applications.* Drug Discovery Today, 1999. **4**(11): p. 507-517.

139. Perera, R.H., et al., *Nitric Oxide Synthase Encapsulation in Liposomes: a Potential Delivery Platform to (Nitric Oxide)-Deficient Targets.* Electroanalysis, 2012. **24**(1): p. 37-41.

140. Hirano, M., et al., *Thymidine phosphorylase deficiency causes MNGIE: an autosomal recessive mitochondrial disorder.* Nucleosides Nucleotides Nucleic Acids, 2004. **23**(8-9): p. 1217-25.

141. Both, G.W., *Gene-directed enzyme prodrug therapy for cancer: a glimpse into the future?* Discov Med, 2009. **8**(42): p. 97-103.

142. Huysmans, G., et al., *Encapsulation of therapeutic nucleoside hydrolase in functionalised nanocapsules.* J Control Release, 2005. **102**(1): p. 171-9.

143. Parker, W.B., et al., *Metabolism and metabolic actions of 6-methylpurine and 2-fluoroadenine in human cells.* Biochem Pharmacol, 1998. **55**(10): p. 1673-81.

144. Tanner, P., et al., *Can polymeric vesicles that confine enzymatic reactions act as simplified organelles?* FEBS Lett, 2011. **585**(11): p. 1699-706.

145. Ben-Haim, N., et al., *Cell-Specific Integration of Artificial Organelles Based on Functionalized Polymer Vesicles.* Nano Letters, 2008. **8**(5): p. 1368-1373.

146. Balasubramanian, V., et al., *A surprising system: polymeric nanoreactors containing a mimic with dual-enzyme activity.* Soft Matter, 2011. **7**(12): p. 5595-5603.

147. Rasoulianboroujeni, M., et al., *Development of a DNA-liposome complex for gene delivery applications.* Materials Science and Engineering: C, 2017. **75**(Supplement C): p. 191-197.

148. Dalby, B., et al., *Advanced transfection with Lipofectamine 2000 reagent: primary neurons, siRNA, and high-throughput applications.* Methods, 2004. **33**(2): p. 95-103.

149. Ding, Y., F. Wu, and C. Tan, *Synthetic Biology: A Bridge between Artificial and Natural Cells.* Life, 2014. **4**(4): p. 1092.

150. Malinova, V., et al., *Synthetic biology, inspired by synthetic chemistry.* FEBS Letters, 2012. **586**(15): p. 2146-2156.

151. Blain, J.C. and J.W. Szostak, *Progress Toward Synthetic Cells.* Annual Review of Biochemistry, 2014. **83**(1): p. 615-640.

152. Gibson, D.G., et al., *Creation of a Bacterial Cell Controlled by a Chemically Synthesized Genome.* Science, 2010. **329**(5987): p. 52-56.

153. Mann, S., *Systems of Creation: The Emergence of Life from Nonliving Matter.* Accounts of Chemical Research, 2012. **45**(12): p. 2131-2141.

154. Dzieciol, A.J. and S. Mann, *Designs for life: protocell models in the laboratory.* Chemical Society Reviews, 2012. **41**(1): p. 79-85.

155. Solé, R.V., *Evolution and self-assembly of protocells.* The International Journal of Biochemistry & Cell Biology, 2009. **41**(2): p. 274-284.

156. Schoonen, L. and J.C. van Hest, *Compartmentalization Approaches in Soft Matter Science: From Nanoreactor Development to Organelle Mimics.* Adv Mater, 2016. **28**(6): p. 1109-28.

157. Tu, Y., et al., *Mimicking the Cell: Bio-Inspired Functions of Supramolecular Assemblies.* Chemical Reviews, 2016. **116**(4): p. 2023-2078.

158. Buddingh', B.C. and J.C.M. van Hest, *Artificial Cells: Synthetic Compartments with Life-like Functionality and Adaptivity.* Accounts of Chemical Research, 2017. **50**(4): p. 769-777.

159. W., P.R.J.R., et al., *Cascade Reactions in Multicompartmentalized Polymersomes.* Angewandte Chemie International Edition, 2014. **53**(1): p. 146-150.

160. Yu, W., et al., *Synthesis of functional protein in liposome.* Journal of Bioscience and Bioengineering, 2001. **92**(6): p. 590-593.

161. Ishikawa, K., et al., *Expression of a cascading genetic network within liposomes.* FEBS Letters, 2004. **576**(3): p. 387-390.

162. Shin, J. and V. Noireaux, *An E. coli cell-free expression toolbox: application to synthetic gene circuits and artificial cells.* ACS Synth Biol, 2012. **1**(1): p. 29-41.

163. Garamella, J., et al., *The All E. coli TX-TL Toolbox 2.0: A Platform for Cell-Free Synthetic Biology.* ACS Synthetic Biology, 2016. **5**(4): p. 344-355.

164. Osellame, L.D., T.S. Blacker, and M.R. Duchen, *Cellular and molecular mechanisms of mitochondrial function.* Best practice & research. Clinical endocrinology & metabolism, 2012. **26**(6): p. 711-723.

165. Meeuwissen, S.A., et al., *Cofactor regeneration in polymersome nanoreactors: enzymatically catalysed Baeyer–Villiger reactions.* Journal of Materials Chemistry, 2011. **21**(47): p. 18923-18926.

166. Graff, A., et al., *Amphiphilic Copolymer Membranes Promote Nadh:Ubiquinone Oxidoreductase Activity: Towards an Electron-Transfer Nanodevice.* Macromol Chem Physic, 2010. **211**: p. 229-238.

167. Nardin, C., et al., *Amphiphilic block copolymer nanocontainers as bioreactors.* The European Physical Journal E, 2001. **4**(4): p. 403-410.

168. Noireaux, V. and A. Libchaber, *A vesicle bioreactor as a step toward an artificial cell assembly.* Proceedings of the National Academy of Sciences of the United States of America, 2004. **101**(51): p. 17669-17674.

169. Kurihara, K., et al., *Self-reproduction of supramolecular giant vesicles combined with the amplification of encapsulated DNA.* Nature Chemistry, 2011. **3**: p. 775.

170. W., P.R.J.R., N. Marlies, and v.H.J.C. M., *Reversibly Triggered Protein–Ligand Assemblies in Giant Vesicles.* Angewandte Chemie International Edition, 2015. **54**(33): p. 9614-9617.

171. Li, M., et al., *Electrostatically gated membrane permeability in inorganic protocells.* Nature Chemistry, 2013. **5**: p. 529.

172. Gardner, P.M., K. Winzer, and B.G. Davis, *Sugar synthesis in a protocellular model leads to a cell signalling response in bacteria.* Nature Chemistry, 2009. **1**: p. 377.

173. Sun, S., et al., *Chemical Signaling and Functional Activation in Colloidosome-Based Protocells.* Small, 2016. **12**(14): p. 1920-7.

174. Muzika, F., et al., *A bistable switch in pH in urease-loaded alginate beads.* Chem Commun (Camb), 2014. **50**(76): p. 11107-9.

175. Scott, D.R., et al., *Mechanisms of acid resistance due to the urease system of Helicobacter pylori.* Gastroenterology, 2002. **123**(1): p. 187-195.

176. Overly, C.C., et al., *Quantitative measurement of intraorganelle pH in the endosomal-lysosomal pathway in neurons by using ratiometric imaging with pyranine.* Proc Natl Acad Sci U S A, 1995. **92**(8): p. 3156-60.

177. Wrobel, M.M., *pH-driven instabilities in chemical systems*, in *School of Chemistry*. 2012, University of Leeds. p. 176.

178. Rowland, R.N. and J.F. Woodley, *The stability of liposomes in vitro to pH, bile salts and pancreatic lipase.* Biochimica et Biophysica Acta (BBA) - Lipids and Lipid Metabolism, 1980. **620**(3): p. 400-409.

179. Sila, M., S. Au, and N. Weiner, *Effects of Triton X-100 concentration and incubation temperature on carboxyfluorescein release from multilamellar liposomes.* Biochimica et Biophysica Acta (BBA) - Biomembranes, 1986. **859**(2): p. 165-170.

180. Colletier, J.-P., et al., *Protein encapsulation in liposomes: efficiency depends on interactions between protein and phospholipid bilayer.* BMC Biotechnology, 2002. **2**(1): p. 9.

181. Gasteiger, E., et al., *Protein Identification and Analysis Tools on the ExPASy Server*, in *The Proteomics Protocols Handbook*, J.M. Walker, Editor. 2005, Humana Press: Totowa, NJ. p. 571-607.

182. Leiding, T., et al., *Precise detection of pH inside large unilamellar vesicles using membrane-impermeable dendritic porphyrin-based nanoprobes.* Analytical biochemistry, 2009. **388**(2): p. 296-305.

183. Paxton, W.F., et al., *Monitoring and modulating ion traffic in hybrid lipid/polymer vesicles.* Colloids and Surfaces B: Biointerfaces, 2017. **159**(Supplement C): p. 268-276.

184. Seneviratne, R., et al., *A reconstitution method for integral membrane proteins in hybrid lipid-polymer vesicles for enhanced functional durability.* Methods, 2018.

185. Abad, J.P., *Proton Motive Force*, in *Encyclopedia of Astrobiology*, M. Gargaud, et al., Editors. 2011, Springer Berlin Heidelberg: Berlin, Heidelberg. p. 1355-1356.

186. Mirafzali, Z. *The number of lipid molecules per liposome*. 2009 [cited 2017; Available from: http://www.liposomes.org/2009/01/number-of-lipid-molecules-per-liposome.html.

187. Lyubartsev, A.P. and A.L. Rabinovich, *Force Field Development for Lipid Membrane Simulations.* Biochimica et Biophysica Acta (BBA) - Biomembranes, 2016. **1858**(10): p. 2483-2497.

188. Harrison, P., C. Gardiner, and I. Sargent, *Extracellular Vesicles in Health and Disease*. 2014: New York: Pan Stanford.

189. Novales, B., *Diffraction in Particle Size Analysis*, in *Encyclopedia of Analytical Chemistry*. 2006, John Wiley & Sons, Ltd.

190. Eigen, M., *Proton Transfer, Acid-Base Catalysis, and Enzymatic Hydrolysis. Part I: ELEMENTARY PROCESSES.* Angewandte Chemie International Edition in English, 1964. **3**(1): p. 1-19.

191. Wang, X., et al., *Comprehensive study of the hydration and dehydration reactions of carbon dioxide in aqueous solution.* J Phys Chem A, 2010. **114**(4): p. 1734-40.

192. Eze, M.O., *Phase transitions in phospholipid bilayers: Lateral phase separations play vital roles in biomembranes.* Biochemical Education, 1991. **19**(4): p. 204-208.

193. Hung, W.C., F.Y. Chen, and H.W. Huang, *Order–disorder transition in bilayers of diphytanoyl phosphatidylcholine.* Biochimica et Biophysica Acta (BBA) - Biomembranes, 2000. **1467**(1): p. 198-206.

194. Paula, S., et al., *Permeation of protons, potassium ions, and small polar molecules through phospholipid bilayers as a function of membrane thickness.* Biophys J, 1996. **70**(1): p. 339-48.

195. Purushothaman, S., J. Cama, and U.F. Keyser, *Dependence of norfloxacin diffusion across bilayers on lipid composition.* Soft Matter, 2016. **12**(7): p. 2135-44.

196. Zucker, D., et al., *Liposome drugs' loading efficiency: a working model based on loading conditions and drug's physicochemical properties.* J Control Release, 2009. **139**(1): p. 73-80.

197. Barenholz, Y., *Relevancy of drug loading to liposomal formulation therapeutic efficacy.* J Liposome Res, 2003. **13**(1): p. 1-8.

198. Nichols, J.W. and D.W. Deamer, *Catecholamine uptake and concentration by liposomes maintaining pH gradients.* Biochimica et Biophysica Acta (BBA) - Biomembranes, 1976. **455**(1): p. 269-271.

199. Gubernator, J., *Active methods of drug loading into liposomes: recent strategies for stable drug entrapment and increased in vivo activity.* Expert Opin Drug Deliv, 2011. **8**(5): p. 565-80.

200. DrugBank. *Cimetidine*. 2017 [cited 2018; Available from: https://www.drugbank.ca/drugs/DB00501.

201. Foundation, T.H. *H. Pylori*. General 2006 [cited 2018; Available from: http://studio.helicobacter.com/h_general.html.

202. Ochocki, J.D., et al., *Arginase 2 Suppresses Renal Carcinoma Progression via Biosynthetic Cofactor Pyridoxal Phosphate Depletion and Increased Polyamine Toxicity.* Cell Metabolism, 2018. **27**(6): p. 1263-1280.e6.

203. Handley, R.R., et al., *Brain urea increase is an early Huntington's disease pathogenic event observed in a prodromal transgenic sheep model and HD cases.* Proceedings of the National Academy of Sciences, 2017. **114**(52): p. E11293-E11302.

204. Clark, J. and G. Gunawardena. *The Beer-Lambert Law*. Chemistry 2013 [cited 2018; Available from: https://chem.libretexts.org/Core/Physical_and_Theoretical_Chemistry/Spectroscopy/Electronic_Spectroscopy/Electronic_Spectroscopy_Basics/The_Beer-Lambert_Law.

205. Alberts, B.J., A.; Lewis, J.; Morgan, D.; Raff, M.; Roberts, K.; Walter, P., *Molecular Biology of the Cell, 6th ed.*, ed. G. Science. 2014, New York.

206. Lehninger, A.L.N., D. L.; Cox, M. M., *Principles of Biochemistry, 6th ed*, ed. W. Publishers. 2013, New York.

207. Muddana, H.S., et al., *Substrate Catalysis Enhances Single-Enzyme Diffusion.* Journal of the American Chemical Society, 2010. **132**(7): p. 2110-2111.

208. Sengupta, S., et al., *Enzyme Molecules as Nanomotors.* Journal of the American Chemical Society, 2013. **135**(4): p. 1406-1414.

209. Riedel, C., et al., *The heat released during catalytic turnover enhances the diffusion of an enzyme.* Nature, 2015. **517**(7533): p. 227-30.

210. Wang, J., *Nanomachines. Fundamentals and Applications*. 2013: WILEY-VCH Verlag.

211. Abdelmohsen, L.K.E.A., et al., *Micro- and nano-motors for biomedical applications.* Journal of Materials Chemistry B, 2014. **2**(17): p. 2395-2408.

212. Chalupniak, A., E. Morales-Narvaez, and A. Merkoci, *Micro and nanomotors in diagnostics.* Adv Drug Deliv Rev, 2015. **95**: p. 104-16.

213. Soler, L. and S. Sanchez, *Catalytic nanomotors for environmental monitoring and water remediation.* Nanoscale, 2014. **6**(13): p. 7175-82.

214. Ma, X., et al., *Enzyme-Powered Hollow Mesoporous Janus Nanomotors.* Nano Letters, 2015. **15**(10): p. 7043-7050.

215. Dey, K.K., et al., *Micromotors Powered by Enzyme Catalysis.* Nano Letters, 2015. **15**(12): p. 8311-8315.

216. Abdelmohsen, L.K.E.A., et al., *Dynamic Loading and Unloading of Proteins in Polymeric Stomatocytes: Formation of an Enzyme-Loaded Supramolecular Nanomotor.* ACS Nano, 2016. **10**(2): p. 2652-2660.

217. Tyska, M.J. and D.M. Warshaw, *The myosin power stroke.* Cell Motil Cytoskeleton, 2002. **51**(1): p. 1-15.

218. Tsao, D.S. and M.R. Diehl, *Molecular motors: myosins move ahead of the pack.* Nat Nanotechnol, 2014. **9**(1): p. 9-10.

219. Schliwa, M. and G. Woehlke, *Molecular motors.* Nature, 2003. **422**(6933): p. 759-65.

220. Butler, P.J., K.K. Dey, and A. Sen, *Impulsive Enzymes: A New Force in Mechanobiology.* Cell Mol Bioeng, 2015. **8**(1): p. 106-118.

221. Spudich, J.A., et al., *Optical traps to study properties of molecular motors.* Cold Spring Harb Protoc, 2011. **2011**(11): p. 1305-18.

222. Yoshida, M., E. Muneyuki, and T. Hisabori, *ATP synthase--a marvellous rotary engine of the cell.* Nat Rev Mol Cell Biol, 2001. **2**(9): p. 669-77.

223. Forgac, M., *Vacuolar ATPases: rotary proton pumps in physiology and pathophysiology.* Nat Rev Mol Cell Biol, 2007. **8**(11): p. 917-29.

224. Boyer, P.D., *The Binding-Change Mechanism of ATP Synthesis.* Membrane Bioenergetics, 1979.

225. Itoh, H., et al., *Mechanically driven ATP synthesis by F1-ATPase.* Nature, 2004. **427**(6973): p. 465-8.

226.   Noji, H., et al., *Direct observation of the rotation of F1-ATPase.* Nature, 1997. **386**(6622): p. 299-302.

227.   Montemagno, C. and G. Bachand, *Constructing nanomechanical devices powered by biomolecular motors*. Vol. 10. 1999. 225.

228.   Takahashi, K., S.N. Arjunan, and M. Tomita, *Space in systems biology of signaling pathways--towards intracellular molecular crowding in silico.* FEBS Lett, 2005. **579**(8): p. 1783-8.

229.   Golestanian, R., *Enhanced Diffusion of Enzymes that Catalyze Exothermic Reactions.* Phys Rev Lett, 2015. **115**(10): p. 108102.

230.   Golestanian, R., T.B. Liverpool, and A. Ajdari, *Propulsion of a molecular machine by asymmetric distribution of reaction products.* Phys Rev Lett, 2005. **94**(22): p. 220801.

231.   Colberg, P.H. and R. Kapral, *Nanoconfined catalytic Angstrom-size motors.* J Chem Phys, 2015. **143**(18): p. 184906.

232.   Golestanian, R. and A. Ajdari, *Mechanical Response of a Small Swimmer Driven by Conformational Transitions.* Physical Review Letters, 2008. **100**(3): p. 038101.

233.   Osuna, S., et al., *Molecular Dynamics Explorations of Active Site Structure in Designed and Evolved Enzymes.* Accounts of Chemical Research, 2015. **48**(4): p. 1080-1089.

234.   Luk, L.Y., E.J. Loveridge, and R.K. Allemann, *Protein motions and dynamic effects in enzyme catalysis.* Phys Chem Chem Phys, 2015. **17**(46): p. 30817-27.

235.   Pelz, B., et al., *Subnanometre enzyme mechanics probed by single-molecule force spectroscopy.* Nat Commun, 2016. **7**: p. 10848.

236.   Ke, H., et al., *Motion analysis of self-propelled Pt-silica particles in hydrogen peroxide solutions.* J Phys Chem A, 2010. **114**(17): p. 5462-7.

237.   Pantarotto, D., W.R. Browne, and B.L. Feringa, *Autonomous propulsion of carbon nanotubes powered by a multienzyme ensemble.* Chem Commun (Camb), 2008(13): p. 1533-5.

238.   Sanchez, S., et al., *Dynamics of Biocatalytic Microengines Mediated by Variable Friction Control.* Journal of the American Chemical Society, 2010. **132**(38): p. 13144-13145.

239.   Wu, Z., et al., *Biodegradable Protein-Based Rockets for Drug Transportation and Light-Triggered Release.* ACS Applied Materials & Interfaces, 2015. **7**(1): p. 250-255.

240.   Sattayasamitsathit, S., et al., *Dual-enzyme natural motors incorporating decontamination and propulsion capabilities.* RSC Advances, 2014. **4**(52): p. 27565-27570.

241.   Orozco, J., et al., *Artificial Enzyme-Powered Microfish for Water-Quality Testing.* ACS Nano, 2013. **7**(1): p. 818-824.

242.   Singh, V.V., et al., *Nanomotors responsive to nerve-agent vapor plumes.* Chem Commun (Camb), 2016. **52**(16): p. 3360-3.

243.   Wu, Y., et al., *Self-Propelled Polymer Multilayer Janus Capsules for Effective Drug Delivery and Light-Triggered Release.* ACS Applied Materials & Interfaces, 2014. **6**(13): p. 10476-10481.

244.   Simmchen, J., et al., *Asymmetric hybrid silica nanomotors for capture and cargo transport: towards a novel motion-based DNA sensor.* Small, 2012. **8**(13): p. 2053-9.

245. Schattling, P., B. Thingholm, and B. Städler, *Enhanced Diffusion of Glucose-Fueled Janus Particles.* Chemistry of Materials, 2015. **27**(21): p. 7412-7418.

246. Pavel, I.-A., et al., *Nanorods with Biocatalytically Induced Self-Electrophoresis.* ChemCatChem, 2014. **6**(3): p. 866-872.

247. Bunea, A.I., et al., *Modification with hemeproteins increases the diffusive movement of nanorods in dilute hydrogen peroxide solutions.* Chem Commun (Camb), 2013. **49**(78): p. 8803-5.

248. Mano, N. and A. Heller, *Bioelectrochemical Propulsion.* Journal of the American Chemical Society, 2005. **127**(33): p. 11574-11575.

249. Sánchez, S., L. Soler, and J. Katuri, *Chemically Powered Micro- and Nanomotors.* Angewandte Chemie International Edition, 2015. **54**(5): p. 1414-1444.

250. Purcell, E.M., *Life at low Reynolds number.* American Journal of Physics, 1977. **45**(1): p. 3-11.

251. Ma, X., et al., *Motion Control of Urea-Powered Biocompatible Hollow Microcapsules.* ACS Nano, 2016. **10**(3): p. 3597-3605.

252. Ma, X., et al., *Reversed Janus Micro/Nanomotors with Internal Chemical Engine.* ACS Nano, 2016. **10**(9): p. 8751-8759.

253. Idili, A., A. Vallée-Bélisle, and F. Ricci, *Programmable pH-Triggered DNA Nanoswitches.* Journal of the American Chemical Society, 2014. **136**(16): p. 5836-5839.

254. Nam, J., T.K. Vanderlick, and P.A. Beales, *Formation and dissolution of phospholipid domains with varying textures in hybrid lipo-polymersomes.* Soft Matter, 2012. **8**(30): p. 7982-7988.

255. Phelps, C.F., *Dynamic light scattering, with application to chemistry, biology and physics: B. J. Berne & R. Pecora. Pp. 376. John Wiley 1976. £14.00 or $27.00.* Biochemical Education, 1977. **5**(1): p. 22-22.

256. Scientific, H. *Dynamic Light Scattering*. [cited 2018; Available from: http://www.horiba.com/scientific/products/particle-characterization/technology/dynamic-light-scattering/.

257. Briand, E., et al., *An OEGylated thiol monolayer for the tethering of liposomes and the study of liposome interactions.* Talanta, 2010. **81**(4-5): p. 1153-61.

258. Wu, Y., et al., *Glucose-regulated insulin release from acid-disintegrable microgels covalently immobilized with glucose oxidase and catalase.* Macromol Rapid Commun, 2012. **33**(21): p. 1852-60.

259. Shi, J., et al., *Cancer nanomedicine: progress, challenges and opportunities.* Nature Reviews Cancer, 2016. **17**: p. 20.

CHAPTER NINE – APPENDIX

9.1 APPENDIX 1 – CHAPTER ONE – INTRODUCTION

9.1.1 Urea Urease Reaction

9.1.1.1 pH dependence of the reaction

The reaction shows a typical bell-shaped curve which can be explained by the presence of 2 acid equilibria giving inactive forms of enzyme [44, 57]:

$$EH \rightleftharpoons E^- + H^+ \qquad\qquad K_{e1}$$

$$EH_2^+ \rightleftharpoons EH + H^+ \qquad\qquad K_{e2}$$
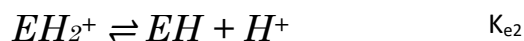
Equation 9.1. Acid equilibria which leads to inactive form of enzyme

and inactive forms of enzyme-substrate complex:

$$EHU \rightleftharpoons EU^- + H^+ \qquad\qquad K_{es1}$$

$$EH_2U \rightleftharpoons EHU + H^+ \qquad\qquad K_{es2}$$
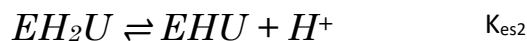
Equation 9.2. Acid equilibria which leads to inactive form of enzyme-substrate complex

As mentioned (Section 1.5.2), it is found that K_M changes little with acid concentration implying that $K_{e1} = K_{es1}$ and $K_{e2} = K_{es2}$, i.e., the protonation equilibria do not change in the presence of the substrate. Taking this into consideration, the rate expression becomes [44, 57]:

$$V = \frac{V_{max} U}{(K_M + U)\left(1 + \dfrac{K_{es2}}{H^+} + \dfrac{H^+}{K_{es1}}\right)}$$

Equation 9.3. Modified Michaelis-Menten rate expression for urease activity, taking into consideration acid-induced inactivation

9.1.1.2 Product inhibition

The ammonium ion is also found to inhibit the reaction through non-competitive means [44, 57]:

$$EH + P + S \rightleftharpoons EHPS \qquad\qquad K_p$$

Equation 9.4. Equilibria of enzyme product inhibition.

This equilibrium may be incorporated into the Michaelis rate expression to give [44, 57]:

$$V = \frac{V_{max} U}{(K_M + U)\left(1 + \dfrac{P}{K_p}\right)}$$

Equation 9.5. Modified Michaelis-Menten rate expression for urease activity, taking into consideration product inhibition.

9.1.1.3 Substrate inhibition

The urea inhibits the reaction by an uncompetitive mechanism [44, 57]:

$$EHS + S \rightleftharpoons EHS_2 \qquad\qquad K_s$$

Equation 9.6. Equilibria of enzyme substrate inhibition.

This equilibrium may be incorporated into the rate expression to give [44, 57]:

$$V = \frac{V_{max}U}{\left(K_M + U\left(1 + \dfrac{U}{K_s}\right)\right)}$$

Equation 9.7. Modified Michaelis-Menten rate expression for urease activity, taking into consideration substrate inhibition.

9.2 APPENDIX 2 – CHAPTER FOUR – GAINING CONTROL

9.2.1 Starting pH (HCl Concentration)

Table 9.1. The effect of increasing starting HCl concentration (0.10, 0.20, 0.32 mM) on clock time, final pH, and transition width, in 200 nm DPhPC vesicles (phosphorus concentration; 250 µM), when urea (10, 50, 250 mM) is added.

Urea Concentration	HCl Concentration	Clock Time (min)	Final pH	Transition Width
10 mM	0.10 mM	20.3 ± 3.1	6.96 ± 0.04	1.16 ± 0.10
	0.20 mM	52.7 ± 15.3	6.79 ± 0.05	2.27 ± 0.36
	0.32 mM	89.4 ± 20.4	6.78 ± 0.10	3.36 ± 0.51
50 mM	0.10 mM	10.2 ± 0.3	7.20 ± 0.03	0.89 ± 0.03
	0.20 mM	16.5 ± 1.1	7.09 ± 0.05	1.30 ± 0.12
	0.32 mM	27.7 ± 6.9	6.91 ± 0.13	1.64 ± 0.18
250 mM	0.10 mM	7.4 ± 0.4	7.17 ± 0.04	0.86 ± 0.04
	0.20 mM	9.6 ± 3.1	7.12 ± 0.07	1.02 ± 0.01
	0.32 mM	13.1 ± 3.0	7.08 ± 0.03	1.15 ± 0.10

9.1.2 Urease Concentration

Table 9.2. The relative effect of increasing urease concentration (5 to 10 to 20 µM) on clock time, final pH, and transition width, in 100 nm DPhPC vesicles (phosphorus concentration; 250 µM), when urea (10, 50, 250 mM) is added.

Urea Concentration	Urease Concentration	Clock Time	Final pH	Transition Width
10 mM	5 µM	82.3 ± 3.2	6.83 ± 0.06	3.74 ± 1.32
	10 µM	49.4 ± 7.7	6.93 ± 0.02	2.00 ± 0.51
	20 µM	39.6 ± 3.4	6.95 ± 0.07	1.87 ± 0.19
50 mM	5 µM	30.6 ± 13.6	7.08 ± 0.06	1.39 ± 0.24
	10 µM	19.6 ± 2.4	7.15 ± 0.01	1.33 ± 0.09
	20 µM	14.7 ± 1.2	7.13 ± 0.03	1.23 ± 0.03
250 mM	5 µM	23.0 ± 30.4	7.16 ± 0.07	1.26 ± 0.40
	10 µM	8.5 ± 6.5	7.16 ± 0.04	1.00 ± 0.23
	20 µM	6.6 ± 2.2	7.17 ± 0.07	0.96 ± 0.11

Table 9.3. The relative effect on clock time, final pH, and transition width for increasing urease concentrations (5 to 10 to 20 µM) in 200 nm DPhPC vesicles (phosphorus concentration; 250 µM), when urea (10, 50, 250 mM) is added.

Urea Concentration	Urease Concentration	Clock Time	Final pH	Transition Width
10 mM	5 µM	75.1 ± 16.1	6.87 ± 0.01	2.76 ± 0.25
	10 µM	52.7 ± 15.3	6.79 ± 0.05	2.27 ± 0.36
	20 µM	29.6 ± 6.5	6.91 ± 0.03	1.41 ± 0.15
50 mM	5 µM	28.4 ± 11.5	7.06 ± 0.14	1.47 ± 0.12
	10 µM	16.5 ± 1.1	7.09 ± 0.05	1.30 ± 0.12
	20 µM	13.7 ± 0.2	7.11 ± 0.02	1.26 ± 0.07
250 mM	5 µM	11.8 ± 2.7	7.17 ± 0.04	1.05 ± 0.14
	10 µM	9.6 ± 4.1	7.17 ± 0.04	1.02 ± 0.02
	20 µM	5.5 ± 2.6	7.08 ± 0.02	0.95 ± 0.10

Table 9.4. The relative effect on clock time, final pH, and transition width for increasing urease concentrations (5 to 10 to 20 μM) in 400 nm DPhPC vesicles (phosphorus concentration; 250 μM), when urea (10, 50, 250 mM) is added.

Urea Concentration	Urease Concentration	Clock Time	Final pH	Transition Width
10 mM	5 μM	44.3 ± 11.8	6.90 ± 0.06	2.61 ± 0.33
	10 μM	15.8 ± 4.2	6.89 ± 0.03	1.51 ± 0.05
	20 μM	18.5 ± 15.5	6.75 ± 0.03	1.80 ± 1.06
50 mM	5 μM	51.2 ± 17.7	7.18 ± 0.06	2.22 ± 0.27
	10 μM	26.4 ± 13.4	7.06 ± 0.11	1.90 ± 0.74
	20 μM	9.8 ± 1.1	7.07 ± 0.03	1.31 ± 0.06
250 mM	5 μM	9.3 ± 2.6	7.22 ± 0.03	1.15 ± 0.13
	10 μM	4.3 ± 0.8	7.18 ± 0.09	1.04 ± 0.16
	20 μM	4.4 ± 1.4	6.91 ± 0.17	0.77 ± 0.26

9.1.3 Urea Concentration

Table 9.5. The relative effect on clock time, final pH, and transition width for increasing urea concentrations (10 to 50 to 250 mM)) when added to 100 nm DPhPC vesicles (phosphorus concentration; 250 µM), encapsulating urease (5, 10, 20 µM).

Urease Concentration	Urea Concentration	Clock Time	Final pH	Transition Width
5 µM	10 mM	82.3 ± 3.2	6.83 ± 0.06	3.74 ± 1.32
	50 mM	30.6 ± 13.6	7.08 ± 0.06	1.39 ± 0.24
	250 mM	23.0 ± 30.4	7.16 ± 0.07	1.26 ± 0.40
10 µM	10 mM	49.4 ± 7.7	6.93 ± 0.02	2.00 ± 0.51
	50 mM	19.6 ± 2.4	7.15 ± 0.01	1.33 ± 0.09
	250 mM	8.5 ± 6.5	7.16 ± 0.04	1.00 ± 0.23
20 µM	10 mM	39.6 ± 3.4	6.95 ± 0.07	1.87 ± 0.19
	50 mM	14.7 ± 1.2	7.13 ± 0.03	1.23 ± 0.03
	250 mM	6.6 ± 2.2	7.17 ± 0.07	0.96 ± 0.11

Table 9.6. The relative effect on clock time, final pH, and transition width for increasing urea concentrations (10 to 50 to 250 mM)) when added to 200 nm DPhPC vesicles (phosphorus concentration; 250 µM), encapsulating urease (5, 10, 20 µM).

Urease Concentration	Urea Concentration	Clock Time	Final pH	Transition Width
5 µM	10 mM	75.1 ± 16.1	6.87 ± 0.01	2.76 ± 0.25
	50 mM	28.4 ± 11.5	7.06 ± 0.14	1.47 ± 0.12
	250 mM	11.8 ± 2.7	7.17 ± 0.04	1.05 ± 0.14
10 µM	10 mM	52.7 ± 15.3	6.79 ± 0.05	2.27 ± 0.36
	50 mM	16.5 ± 1.1	7.09 ± 0.05	1.30 ± 0.12
	250 mM	9.6 ± 4.1	7.17 ± 0.04	1.02 ± 0.02
20 µM	10 mM	29.6 ± 6.5	6.91 ± 0.03	1.41 ± 0.15
	50 mM	13.7 ± 0.2	7.11 ± 0.02	1.26 ± 0.07
	250 mM	5.5 ± 2.6	7.08 ± 0.02	0.95 ± 0.10

Table 9.7. The relative effect on clock time, final pH, and transition width for increasing urea concentrations (10 to 50 to 250 mM)) when added to 400 nm DPhPC vesicles (phosphorus concentration; 250 µM), encapsulating urease (5, 10, 20 µM).

Urease Concentration	Urea Concentration	Clock Time	Final pH	Transition Width
5 µM	10 mM	44.3 ± 11.8	6.90 ± 0.06	2.61 ± 0.33
	50 mM	51.2 ± 17.7	7.18 ± 0.06	2.22 ± 0.27
	250 mM	9.3 ± 2.6	7.22 ± 0.03	1.15 ± 0.13
10 µM	10 mM	15.8 ± 4.2	6.89 ± 0.03	1.51 ± 0.05
	50 mM	26.4 ± 13.4	7.06 ± 0.11	1.90 ± 0.74
	250 mM	4.3 ± 0.8	7.18 ± 0.09	1.04 ± 0.16
20 µM	10 mM	49.6 ± 15.9	6.75 ± 0.03	3.45 ± 0.74
	50 mM	9.8 ± 1.1	7.07 ± 0.03	1.31 ± 0.06
	250 mM	4.4 ± 1.4	6.91 ± 0.17	0.77 ± 0.26

9.2.1 Vesicle Size

Table 9.8. The raw data obtained, for clock time, final pH, and transition width, when the size of DPhPC vesicles encapsulating 5, 10, or 20 µM urease and 20 mM HPTS, is increased (100, 200, and 400 nm) following the addition of 10 mM urea.

Urease Concentration	Vesicle Size	Clock Time	Final pH	Transition Width
5 µM	100 nm	82.3 ± 3.2	6.83 ± 0.06	3.74 ± 1.32
	200 nm	75.1 ± 16.1	6.87 ± 0.01	2.76 ± 0.25
	400 nm	44.3 ± 11.8	6.90 ± 0.06	2.61 ± 0.33
10 µM	100 nm	49.4 ± 7.7	6.93 ± 0.02	2.00 ± 0.51
	200 nm	52.7 ± 15.3	6.79 ± 0.05	2.27 ± 0.36
	400 nm	15.8 ± 4.2	6.89 ± 0.03	1.51 ± 0.05
20 µM	100 nm	39.6 ± 3.4	6.95 ± 0.07	1.87 ± 0.19
	200 nm	29.6 ± 6.5	6.91 ± 0.03	1.41 ± 0.15
	400 nm	18.5 ± 15.5	6.75 ± 0.03	1.80 ± 1.06

Table 9.9. The raw data obtained, for clock time, final pH, and transition width, when the size of DPhPC vesicles encapsulating 5, 10, or 20 µM urease and 20 mM HPTS, is increased (100, 200, and 400 nm) following the addition of 50 mM urea

Urease Concentration	Vesicle Size	Clock Time	Final pH	Transition Width
5 µM	100 nm	30.6 ± 13.6	7.08 ± 0.06	1.39 ± 0.24
	200 nm	28.4 ± 11.5	7.06 ± 0.14	1.47 ± 0.12
	400 nm	51.2 ± 17.7	7.18 ± 0.06	2.22 ± 0.27
10 µM	100 nm	19.6 ± 2.4	7.15 ± 0.01	1.33 ± 0.09
	200 nm	15.7 ± 1.2	7.09 ± 0.05	1.39 ± 0.17
	400 nm	26.4 ± 13.4	7.06 ± 0.11	1.90 ± 0.74
20 µM	100 nm	14.7 ± 1.2	7.13 ± 0.03	1.23 ± 0.03
	200 nm	13.7 ± 0.2	7.11 ± 0.02	1.26 ± 0.07
	400 nm	9.8 ± 1.1	7.07 ± 0.03	1.31 ± 0.06

Table 9.10. The raw data obtained, for clock time, final pH, and transition width, when the size of DPhPC vesicles encapsulating 5, 10, or 20 µM urease and 20 mM HPTS, is increased (100, 200, and 400 nm) following the addition of 250 mM urea

Urease Concentration	Vesicle Size	Clock Time	Final pH	Transition Width
5 µM	100 nm	23.0 ± 30.4	7.16 ± 0.07	1.26 ± 0.40
	200 nm	11.8 ± 2.7	7.17 ± 0.04	1.05 ± 0.14
	400 nm	9.3 ± 2.6	7.22 ± 0.03	1.15 ± 0.13
10 µM	100 nm	8.5 ±6.5	7.16 ± 0.04	1.00 ± 0.23
	200 nm	9.6 ± 4.1	7.17 ± 0.04	1.02 ± 0.02
	400 nm	4.3 ± 0.8	7.18 ± 0.09	1.04 ± 0.16
20 µM	100 nm	6.6 ± 2.2	7.17 ± 0.07	0.96 ± 0.11
	200 nm	5.5 ± 2.6	7.08 ± 0.02	0.95 ± 0.10
	400 nm	4.4 ± 1.4	6.91 ± 0.17	0.77 ± 0.26

9.2.1 Membrane Composition

9.2.5.1 Lipids

Table 9.11. Absolute values, including error, allowing comparison of clock time, final pH, and transition width for POPC and DPhPC at set concentrations of urea

Urea	Lipid	Clock Time	Final pH	Transition Width
10 mM	POPC	58.5 ± 10.7	6.80 ± 0.03	1.88 ± 0.22
	DPhPC	52.7 ± 15.3	6.79 ± 0.05	2.27 ± 0.36
50 mM	POPC	15.3 ± 0.3	6.85 ± 0.03	1.19 ± 0.08
	DPhPC	16.5 ± 1.1	7.09 ± 0.05	1.30 ± 0.12
250 mM	POPC	11.0 ± 0.6	7.02 ± 0.07	0.92 ± 0.05
	DPhPC	9.6 ± 4.1	7.17 ± 0.04	1.02 ± 0.02